



*HiSOR*



**ACTIVITY REPORT**

2007

**Hiroshima Synchrotron Radiation Center, HSRC  
Hiroshima University**



# HiSOR ACTIVITY REPORT

2007

Hiroshima Synchrotron Radiation Center, HSRC

Hiroshima University

Edited by

T. Hori, M. Nakatake

The annual report is available from  
Hiroshima Synchrotron Radiation Center  
Hiroshima University  
2-313 Kagamiyama, Higashi-Hiroshima 739-0046  
JAPAN

Phone: +81-82-424-6293

Fax: +81-82-424-6294

e-mail: [hisor@hiroshima-u.ac.jp](mailto:hisor@hiroshima-u.ac.jp)

URL: <http://www.hsrb.hiroshima-u.ac.jp/>

## Preface

Hiroshima Synchrotron Radiation Center is a common facility opened for outside users. The light source operated at 700 MeV with a critical energy of 873 eV has 14 photon beam ports on the bending sections and two on the straight sections with a linear and a helical undulators. In 2007, the light source has been operated for 1950 hours, and used for 1550 hours for user experiments with the beam lifetime of about 8 hours at 300 mA accumulation current under the operation of two undulators.

A total of 13 beamlines has been constructed so far; three normal-incidence monochromators, seven grazing-incidence monochromators, two double crystal monochromators and an apparatus for white beam irradiation. In particular, resolutions of energy and momentum in angle-resolved photoemission spectroscopy experiments have been significantly improved to 600-700  $\mu\text{eV}$  and  $4 \times 10^{-3} \text{ \AA}^{-1}$ , respectively, at excitation photon energy of  $h\nu \sim 8 \text{ eV}$  on helical undulator beamline. The low-energy tunable excitation-photons have enabled us to resolve a very small nodal bilayer splitting, unmasking the intrinsic quasi-particle scattering rate, and to observe precisely a small electronic structure change due to an oxygen isotope effect, in nearly optimally doped  $\text{Bi}_2\text{Sr}_2\text{CaCu}_2\text{O}_{8+\delta}$ . A part of the research has been presented at The 9th International Conference on Synchrotron Radiation Instrumentation as a plenary talk.

In 2007, new end station for polarization-dependent angle-resolved photoemission spectroscopy (ARPES) has been designed. ARPES with *s*- or *p*-polarization geometry, which determines symmetry of the initial-state wave function, will soon be possible. On the soft x-ray beamline, an *in situ* system for fabrication of magnetic ultrathin films with monatomic layer control by means of MBE technique and their characterization by Auger electron spectroscopy, low energy electron diffraction and reflection high-energy electron diffraction, has been introduced. After the fabrication and characterization of magnetic films, the soft x-ray magnetic circular dichroism experiments are available on the grown films.

In addition to electronic and spin structures of solids above, activities are going up in the field of photochemistry such as photo-fragmentation, analysis on chemical states of catalyst for automobile emission, secondary-structural analysis of denatured protein, electronic structure determination by inverse-photoemission and direct observation of nano-structure by STM.

We will continue to develop the performance of HiSOR facility and utilize the environment of HiSOR for training of students and young scientists.

June 2008



Masaki Taniguchi

Director of Hiroshima Synchrotron Radiation Center



# Table of Contents

## Preface

## Current Status of HiSOR

*Status of the HiSOR storage ring and future plan of HSRC* . . . . . 1  
A. Miyamoto, K. Goto, H. Tsutsui, T. Hori

*Beamlines* . . . . . 11

## Research Activities

*New end station for the linear undulator beamline BL-1* . . . . . 17  
K. Shimada, M. Higashiguchi, N. Tobita, S. Fukuda, K. Tanaka, J. Jiang, H. Hayashi, H. Namatame,  
M. Taniguchi

*Angle-resolved photoemission study of the Shockley state in Au(110)* . . . . . 18  
M. Higashiguchi, K. Shimada, Y. Miura, N. Tobita, Y. Aiura, H. Namatame, M. Taniguchi

*Angle-resolved photoemission study of Pt (111)* . . . . . 22  
N. Tobita, S. Fukuda, N. Nakajima, N. Ishimatsu, H. Maruyama, H. Hayashi, K. Tanaka, J. Jyan,  
M. Higashiguchi, K. Shimada, H. Namatame, M. Taniguchi

*Angle-resolved photoemission study of Cr (110)* . . . . . 24  
S. Fukuda, N. Tobita, N. Nakajima, N. Ishimatsu, H. Maruyama, H. Hayashi, K. Tanaka, J. Jyan,  
M. Higashiguchi, K. Shimada, H. Namatame, M. Taniguchi

*High-resolution angle-resolved photoemission study of the surface-derived state  
in Al(100) single crystal* . . . . . 25  
J. Jiang, K. Shimada, M. Higashiguchi, N. Tobita, K. Tanaka, S. Fukuda, H. Hayashi, Y. Aiura,  
H. Namatame, M. Taniguchi

*High-resolution angle-resolved photoemission spectroscopy of Rh(100)* . . . . . 30  
H. Hayashi, K. Shimada, K. Tanaka, M. Higashiguchi, N. Tobita, J. Jyan, S. Fukuda, H. Namatame,  
M. Taniguchi

*High-resolution angle-resolved photoemission spectroscopy of Rh(111)*. . . . . 32  
K. Tanaka, K. Shimada, N. Tobita, S. Fukuda, H. Hayashi, J. Jiang, Y. Aiura, H. Namatame, M. Taniguchi

*Angle resolved photoemission spectroscopy measurements of VO<sub>2</sub> thin films* . . . . . 34  
K. Saeki, Y. Muraoka, T. Wakita, M. Hirai, T. Yokoya, R. Eguchi, S. Shin, K. Shimada

<i>Carrier-doping effects on Cr-doped perovskite-type titanates <math>\text{Sr}_{1-(x+y)}\text{La}_{x+y}\text{Ti}_{1-x}\text{Cr}_x\text{O}_3</math> studied by photoemission spectroscopy</i> . . . . .	36
H. Iwasawa, S. Kaneyoshi, K. Kurahashi, T. Saitoh, T. Katsufuji, Y. Miura, M. Higashiguchi, K. Shimada, H. Namatame, M. Taniguchi	
<i>ARPES study of Fermi surface of <math>T^*</math>-phase high-<math>T_c</math> cuprate <math>\text{SmLa}_{0.8}\text{Sr}_{0.2}\text{CuO}_4</math></i> . . . . .	39
Y. Nakashima, H. Anzai, T. Fujita, A. Ino, M. Higashiguchi, N. Tobita, J. Jiang, K. Tanaka, S. Fukuda, K. Shimada, M. Arita, H. Namatame, M. Taniguchi, T. Kakeshita, S. Adachi, S. Tajima	
<i>Annealing effect on the chemical structure of diamondlike carbon (DLC) by C 1s photoelectron spectroscopy</i> . . . . .	40
S. Takabayashi, K. Shimada, K. Okamoto, T. Nakatani, H. Sakaue, T. Takahagi	
<i>NEXAFS, XPS and AFM studies of Rh deposited on <math>\text{Al}_2\text{O}_3</math> thin film/NiAl(100)</i> . . . . .	42
T. Nomoto, S. Yagi, K. Soda, H. Namatame, M. Taniguchi	
<i>Adsorption and oxidation reaction of sulfur on Rh/<math>\text{Al}_2\text{O}_3</math>/NiAl(100) studied by XPS and NEXAFS</i> . . . . .	46
T. Nomoto, S. Yagi, K. Soda, H. Namatame, M. Taniguchi	
<i>Cl K-edge NEXAFS and AFM study of Pd(PVP) nanoparticle by means of He path system</i> . . . . .	50
S. Yagi, T. Kodera, T. Nomoto, G. Kutluk, H. Namatame, M. Taniguchi	
<i>Pd <math>L_3</math>-edge NEXAFS study of Pd(PVP) nanoparticle by means of He path system</i> . . . . .	54
S. Yagi, T. Kodera, T. Nomoto, G. Kutluk, H. Namatame, M. Taniguchi	
<i>Reaction study of L-cysteine on Rh(PVP) nanoparticle surface in the aqueous solution environment</i> . . . . .	56
S. Gohd, T. Ashid, S. Yagi, H. Namatame, M. Taniguchi	
<i>Dissociation reaction of <math>(\text{CH}_3)_2\text{S}</math> adsorbed on Pd nanoparticles fabricated by gas evaporation method using NEXAFS and in-situ XPS</i> . . . . .	60
M. Morihara, K. Miura, T. Nomoto, S. Yagi, G. Kutluk, H. Namatame, M. Taniguchi	
<i>Site- and state-selective dissociation of core-excited organic molecules: Deuterium-labeled methyl acetate</i> . . . . .	63
R. Kawasaki, T. Yamanaka, H. Yoshida, K. Tabayashi	
<i>Hydrogen-bond interactions of small ammonia clusters observed with inner-shell excitation spectroscopy at the nitrogen K-edge</i> . . . . .	65
T. Yamanaka, T. Maruyama, H. Yoshida, K. Tabayashi	
<i>Dissociation dynamics of multiply-charged <math>\text{CF}_4</math> and <math>\text{CHF}_3</math> by momentum imaging spectroscopy</i> . . . . .	66
Y. Kimura, I. Miyagami, Y. Kawakami, H. Kawabata, H. Yoshida, A. Hiraya	
<i>Study on symmetries of core-excited states in <math>\text{CF}_4</math> and <math>\text{CHF}_3</math></i> . . . . .	67
I. Miyagami, Y. Kimura, Y. Kawakami, H. Kawabata, H. Yoshida, A. Hiraya	

<i>Dissociation dynamics of multiply-charged CH<sub>2</sub>F<sub>2</sub> by momentum imaging spectroscopy . . . . .</i>	68
Y. Kawakami, Y. Kimura, I. Miyagami, H. Kawabata, H. Yoshida, A. Hiraya	
<i>Dissociation dynamics of multiply-charged SF<sub>6</sub> by momentum imaging spectroscopy. . . . .</i>	69
H. Kawabata, Y. Kimura, I. Miyagami, Y. Kawakami, H. Yoshida, A. Hiraya	
<i>Photoemission study of fluorescein isothiocyanate isomer 1 (FITC) monolayer on platinum . . . . .</i>	70
T. Maeda, M. Nakatake, H. Namatame, M. Taniguchi, T. Ishibashi	
<i>Core-level photoemission spectra and glass-forming ability in Pd<sub>42.5</sub>Ni<sub>7.5</sub>Cu<sub>30</sub>P<sub>20</sub> bulk metallic glass. . . . .</i>	72
S. Hosokawa, M. Nakatake, H. Sato, N. Hoppo, T. Ichitsubo, E. Matsubara, N. Nishiyama	
<i>Electronic states in Zr<sub>70</sub>Ni<sub>20</sub>Al<sub>10</sub> Bulk Metallic Glass . . . . .</i>	76
T. Nasu, S. Hosokawa, M. Nakatake, H. Sato, W. Zhang, A. Inoue	
<i>Angle-resolved photoemission spectroscopy of SrSi<sub>2</sub>/Si(111) . . . . .</i>	80
H. Maso, H. Kurihara, Y. Tatsukawa, H. Sato, M. Nakatake, H. Namatame, M. Taniguchi	
<i>The constant volume dilution effect of Eu site in EuPd<sub>2</sub>Si<sub>2</sub>: Eu 4d-4f resonant photoemission study. . . . .</i>	82
K. Mimura, D. Okumura, T. Ishizu, M. Nakatake, T. Kuwai, H. Namatame, M. Taniguchi, Y. Taguchi, K. Ichikawa	
<i>Temperature-dependent angle-resolved photoemission spectra of TlInSe<sub>2</sub>: specification of incommensurate and commensurate phases . . . . .</i>	84
K. Mimura, T. Nogami, K. Abe, K. Wakita, M. Arita, N. Mamedov, G. Orudzhev, J. Takasu, Y. Yonehira, H. Namatame, M. Taniguchi, Y. Taguchi, K. Ichikawa	
<i>Fermi surface and CDW gap of 2H-TaS<sub>2</sub> studied by angle resolved photoemission spectroscopy. . . . .</i>	87
M. Arita, H. Sato, Y. Utsumi, H. Namatame, M. Taniguchi, M. Sasaki	
<i>Primary role of the barely occupied states in the charge density wave formation of NbSe<sub>2</sub> . . . . .</i>	88
D. W. Shen, Y. Zhang, L. X. Yang, J. Wei, H. W. Ou, J. K. Dong, B. P. Xie, C. He, J. F. Zhao, B. Zhou, M. Arita, K. Shimada, H. Namatame, M. Taniguchi, J. Shi, D. L. Feng	
<i>Superconducting coherence peak in the electronic excitations of a single layer cuprate superconductor Bi<sub>2</sub>Sr<sub>1.6</sub>La<sub>0.4</sub>CuO<sub>6+δ</sub> . . . . .</i>	90
J. Wei, Y. Zhang, H. W. Ou, B. P. Xie, D. W. Shen, J. F. Zhao, L. X. Yang, M. Arita, K. Shimada, H. Namatame, M. Taniguchi, Y. Yoshida, H. Eisaki, D. L. Feng	
<i>Novel electronic structure induced by a highly strained oxide interface with incommensurate crystal fields . . . . .</i>	92
H.W. Ou, J.F. Zhao, Y. Zhang, B.P. Xie, D.W. Shen, Y. Zhu, Z.Q. Yang, J.G. Che, X.G. Luo, X.H. Chen, M. Arita, K. Shimada, H. Namatame, M. Taniguchi, C.M. Cheng, K.D. Tsuei, D.L. Feng	

<i>Observation of the multibands and superconducting gaps in the trilayer high-<math>T_c</math> cuprate superconductor <math>\text{Bi}_2\text{Sr}_2\text{Ca}_2\text{Cu}_3\text{O}_{10+\delta}</math>.</i> . . . . .	94
S. Ideta, K. Takashima, M. Hashimoto, T. Yoshida, A. Fujimori, A. Ino, H. Anzai, T. Fujita, Y. Nakashima, M. Arita, H. Namatame, M. Taniguchi, K. M. Kojima, S. Uchida	
<i>Impurity effect of nodal fine quasiparticle structure of <math>\text{Bi}_2\text{Sr}_{1.6}(\text{La,Gd})_{0.4}\text{CuO}_{6+\delta}</math> studied by low-energy synchrotron-radiation ARPES.</i> . . . . .	98
T. Fujita, T. Kamo, H. Anzai, A. Ino, M. Arita, H. Namatame, M. Taniguchi, A. Fujimori, Z.-X. Shen, K. Fujita, S. Uchida	
<i>Doping- dependence of gap anisotropy of <math>\text{Bi}_2\text{Sr}_2\text{CaCu}_2\text{O}_{8+\delta}</math> studied by low-energy ARPES</i> . . . . .	99
H. Anzai, T. Kamo, T. Fujita, A. Ino, M. Arita, H. Namatame, M. Taniguchi, M. Ishikado, A. Fujimori, S. Uchida, Z. -X. Shen	
<i>ARPES study of the quantum size effects in atomically uniform Pb films on Si(111)-7<math>\times</math>7</i> . . . . .	101
S. He, Z. Zeng, M. Arita, M. Sawada, K. Shimada, S. Qiao, G. Li, X. Liu, W.-X. Li, Y.-F. Zhang, J. Jia, Q.-K. Xue, H. Namatame, M. Taniguchi	
<i>Optimization of fluorescence XAFS spectroscopy for L edge measurements of Pd nano particles supported onto <math>\text{ZrO}_x</math>.</i> . . . . .	105
S. Hayakawa, H. Koga, H. Sumida, H. Namatame, T. Hirokawa	
<i>Molecular chain effect in photon stimulated ion desorption of self-assembled monolayers induced by carbon core excitation</i> . . . . .	106
A. Hirano, I. Ohyama, Y. Tanikawa, S. Wada, K. Tanaka	
<i>Adsorption of <math>\text{HS}(\text{CH}_2)_2\text{COOCH}_3</math> on Cu(111) surface studied by XPS and NEXAFS spectroscopy.</i> . . . . .	108
K. Yufu, K. Watanabe, K. Matsushita, S. Wada, K. Tanaka	
<i>Site-selective ion desorption of fluorine substituted self-assembled monolayers by core electron excitations</i> . . . . .	111
S. Wada, N. Kushima, T. Yamamoto, K. Tanaka	
<i>In-situ XMCD measurement system for magnetic ultrathin films at BL14</i> . . . . .	114
M. Sawada	
<i>Structural and magnetic properties of Cr/Fe/Cu(001)</i> . . . . .	117
S. Tohoda, M. Sawada, M. Nagira, T. Ueno, T. Tagashira, A. Kimura, H. Namatame, M. Taniguchi	
<i>Fabrication and in-situ XMCD study of Fe/Pd multilayers on Pd(001)</i> . . . . .	119
T. Ueno, M. Sawada, M. Nagira, S. Tohoda, T. Tagashira, A. Kimura, H. Namatame, M. Taniguchi	
<i>XMCD study of orbital contribution to perpendicular magnetization in <math>\text{Co}_{80}\text{Pt}_{20}</math> Thin-Films</i> . . . . .	123
N. Ishimatsu, R. Ogasawara, T. Sone, Y. Tsutsui, H. Maruyama, N. Nakajima, M. Sawada, H. Namatame	

<i>L<sub>2,3</sub> XAFS spectroscopy as a probe for the local symmetry of dopants (Nb, Ti) in LiNi<sub>1-x</sub>Co<sub>x</sub>O<sub>2</sub></i> . . . . .	.124
S. Hayakawa, R. Hasuno, T. Hayashi, T. Sako, M. Sawada, H. Namatame, T. Hirokawa	
<i>Improved sequence-based prediction of protein secondary structures by combining vacuum-ultraviolet circular dichroism spectroscopy with neural network</i> . . . . .	.125
K. Matsuo, H. Watanabe, K. Gekko	
<i>Secondary-structure analysis of intermediate states of apo-myoglobin and pepsin using a vacuum-ultraviolet circular dichroism spectroscopy</i> . . . . .	.129
H. Watanabe, K. Matsuo, H. Namatame, M. Taniguchi, K. Gekko	
<i>Secondary-structure analysis of disulfide variants of lysozyme by vacuum-ultraviolet circular dichroism spectroscopy</i> . . . . .	.131
K. Matsuo, H. Watanabe, S. Tate, H. Tachibana, K. Gekko	
<i>Vacuum-ultraviolet circular dichroism analysis of glycosaminoglycans by synchrotron-radiation spectroscopy</i> . . . . .	.133
K. Matsuo, H. Namatame, M. Taniguchi, K. Gekko	
<i>Secondary-structure analysis of human serum albumin and <math>\alpha</math>-chymotrypsinogen at trifluoroethanol-denatured state using a vacuum-ultraviolet circular dichroism spectroscopy</i> . .	.136
K. Matsuo, S. Yoshie, H. Namatame, M. Taniguchi, K. Gekko	
<i>Structural analysis of <math>\gamma</math>-polyglutamic acids by vacuum-ultraviolet circular dichroism spectroscopy</i> . . . . .	.138
K. Gekko, K. Matsuo, Y. Nogusa	
<i>Spin- and angle-resolved photoemission study of ultrathin Bi films on a silicon substrate</i> . . . .	.139
T. Hirahara, K. Miyamoto, A. Kimura, Y. Niinuma, G. Bihlmayer, E. V. Chulkov, T. Nagao, I. Matsuda, S. Qiao, K. Shimada, H. Namatame, M. Taniguchi, S. Hasegawa	
<i>Spin polarization of spin-orbit induced electronic structures of Bi(111)</i> . . . . .	.143
R. Nishimura, K. Miyamoto, T. Kadono, K. Kanomaru, A. Kimura, K. Shimada, S. Qiao, H. Namatame, T. Taniguchi	
<i>Unveiling spin characters of spin-orbit induced surface states</i> . . . . .	.144
K. Miyamoto, R. Nishimura, T. Kadono, K. Kanomaru, K. Iori, A. Kimura, S. Qiao, K. Shimada, H. Namatame, M. Taniguchi	
<i>Spin-resolved ARPES of Sb(111) single crystal surface</i> . . . . .	.146
T. Kadono, K. Miyamoto, R. Nishimura, K. Kanomaru, M. Nagano, T. Shishidou, T. Oguchi, S. Qiao, K. Shimada, H. Namatame, A. Kimura, M. Taniguchi	
<i>Spin- and angle- resolved photoemission spectroscopy of a Si(111)<math>\sqrt{3}\times\sqrt{3}</math>-Sb surface</i> . . . . .	.147
K. Kanomaru, K. Miyamoto, T. Kadono, R. Nishimura, A. Kimura, S. Qiao, K. Shimada, H. Namatame, M. Taniguchi	

<i>Unoccupied band structure of 1T-TaS<sub>2</sub> investigated by angle-resolved inverse-photoemission spectroscopy</i> . . . . .	148
Y. Utsumi, Y. Mukaegawa, M. Arita, H. Sato, M. Sasaki, A. Ohnishi, H. Namatame, M. Taniguchi	
<i>Surface electronic structures of ferromagnetic Ni(111) studied by scanning tunneling microscopy and spectroscopy</i> . . . . .	150
Y. Nishimura, H. Narita, M. Takeya, M. Higashiguchi, Y. Miura, M. Nakatake, A. Kimura, K. Shimada, H. Namatame, M. Taniguchi	
<i>Atomic and local electronic structure of Co and CoSi<sub>2</sub> clusters</i> . . . . .	151
H. Narita, K. He, T. Okuda, A. Kakizaki, I. Matsuda, Y. Cui, A. Kimura, M. Nakatake, H. Namatame, M. Taniguchi	
<i>Co-induced nano-structures on Si (111) surface</i> . . . . .	153
Y. T. Cui, T. Xie, M. Yea, A. Kimura, S. Qiao, H. Namatame, M. Taniguchi	
<i>Graphene epitaxially grown on the step with unit-cell height of 4H-SiC(0001) substrate</i> . . . . .	157
M. Ye, Y. T. Cui, S. Qiao, A. Kimura, M. Sawada, H. Namatame, M. Taniguchi	

## Appendices

Organization . . . . .	161
List of Publications . . . . .	166
Symposium . . . . .	172
Plan of the Building . . . . .	173
Location . . . . .	174

# Current Status of HiSOR



# Status of the HiSOR storage ring and future plan of HSRC

A. Miyamoto, K. Goto, H. Tsutsui<sup>†</sup>, T. Hori

Hiroshima Synchrotron Radiation Center, Hiroshima University

2-313 Kagamiyama, Higashi-Hiroshima, 739-0046 Japan

<sup>†</sup>Sumitomo Heavy Industries, Ltd.

1-1, Yato-cho 2-chome, Tanashi, Tokyo 188-8585, Japan

## 1. Introduction

HiSOR is a synchrotron radiation (SR) source of Hiroshima Synchrotron Radiation Center, Hiroshima University, established in 1996<sup>[1]</sup>. HiSOR is a compact racetrack-type storage ring having 21.95 m circumference, therefore its natural emittance  $400\pi$  nmrad is not so small compared with the other medium~large storage rings. The most outstanding advantage of the facility lies in good combination with beamlines (BL's) for high-resolution photoelectron spectroscopy in energy range of VUV ~ soft X-ray. The principal parameters are shown in Table 1.

Table 1: Main parameters of the HiSOR Storage ring.

Circumference	21.95 m
Type	Racetrack
Bending radius	0.87 m
Beam energy at Injection	150 MeV
at Storage	700 MeV
Magnetic field at Injection	0.6 T
at Storage	2.7 T
Injector	150 MeV Racetrack Microtron
Betatron tune ( $\nu_x, \nu_y$ )	(1.72, 1.84)
RF frequency	191.244 MHz
Harmonic number	14
RF voltage	200 kV
Stored current (nominal)	350 mA
Natural emittance	$400 \pi$ nmrad
Beam life time	~10 hours@200 mA
Critical wavelength	1.42 nm
Photon intensity (5 keV)	$1.2 \times 10^{11}$ /sec/mr <sup>2</sup> /0.1%b.w./300mA

The designed current of HiSOR is 300 mA, however, after the completion of both upgrade of the control system and improvement of the RF system in 2003, HiSOR has been in

operation with 350 mA stored current since then. Fig. 1 shows an example of recent one-day operation. Beam injection for HiSOR is operated twice a day, at about 9:00 and 14:30.

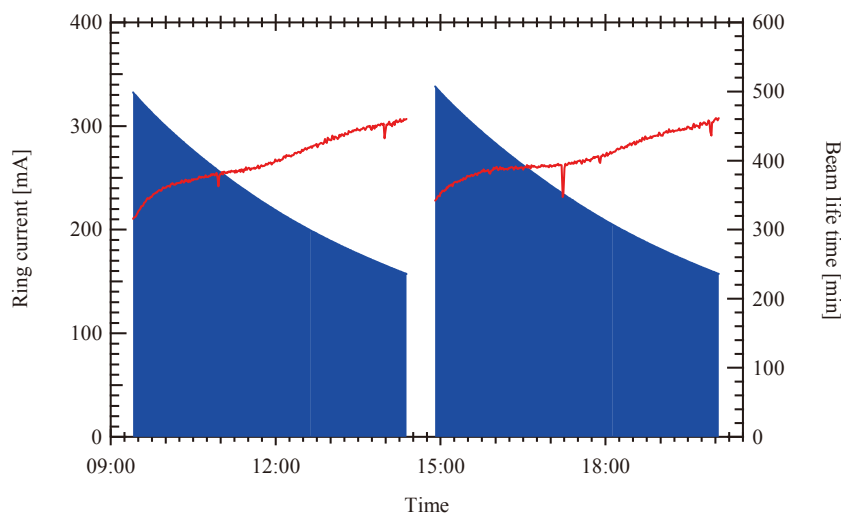


Fig. 1: Typical daily operation status.

HiSOR has two 180-deg. bending magnets which generate 2.7 T magnetic fields with normal conductivity. This storage ring has two undulators, linear and helical, in each straight section. The fundamental parameters of these undulators are shown in Table 2. The photon energy spectra of the SR from HiSOR are shown in Fig. 2.

Table 2: Main parameters of the undulators.

<b>Linear undulator (BL-1)</b>	
Total length	2354.2 mm
Periodic length $\lambda_u$	57 mm
Periodic number	41
Pole gap	30-200 mm
Maximum magnetic field	0.41 T
Magnetic material	Nd-Fe-B (NEOMAX-44H)
<b>Helical undulator (BL-9A,B)</b>	
Total length	1828.6 mm
Periodic length $\lambda_u$	100 mm
Periodic number	18
Pole gap	30-200 mm
Maximum magnetic field	0.347 T (helical mode) 0.597 T (linear mode)
Magnetic material	Nd-Fe-B (NEOMAX-44H)

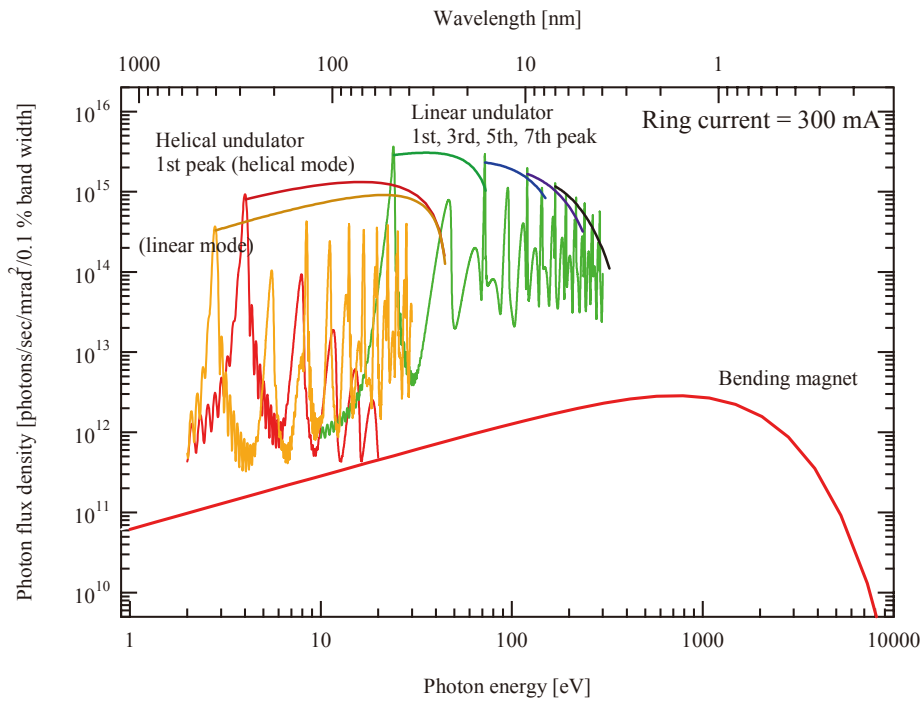


Fig. 2: Photon energy spectra of the SR from HiSOR.

## 2. Operation status in FY 2007

Fig. 3 shows operation time of HiSOR storage ring in FY 2007. HiSOR is stopped for a long term to have routine inspection every year in summer. In 2007, the serious trouble did not occur and was able to digest a schedule on schedule. Therefore the user time achieved 1546 hours and it exceeded one of last year more than 100 hours, though we did not extend the machine time after 20:00.

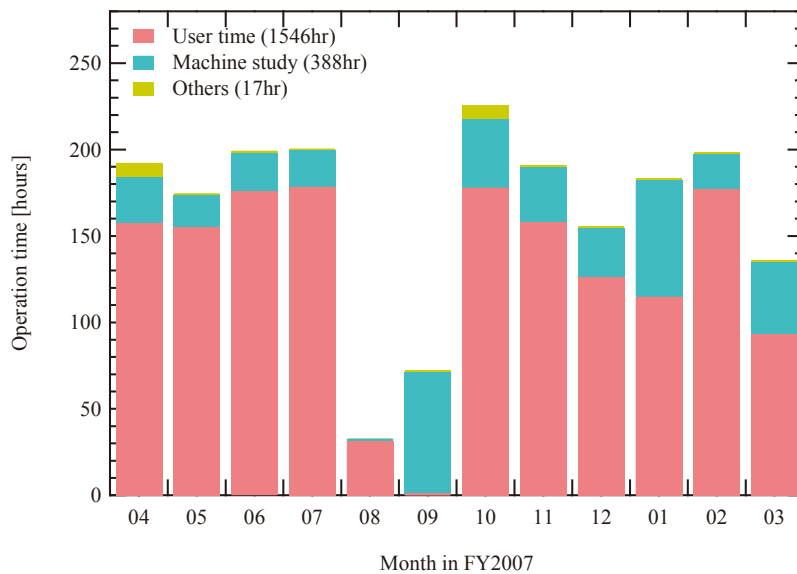


Fig. 3: Monthly operation time in FY 2007.

Further because there was not serious trouble, the storage time of HiSOR increased and

recorded the longest time in last year. A change of operation time of storage ring and Microtron from FY 2002 to FY 2007 is shown in Fig. 4.

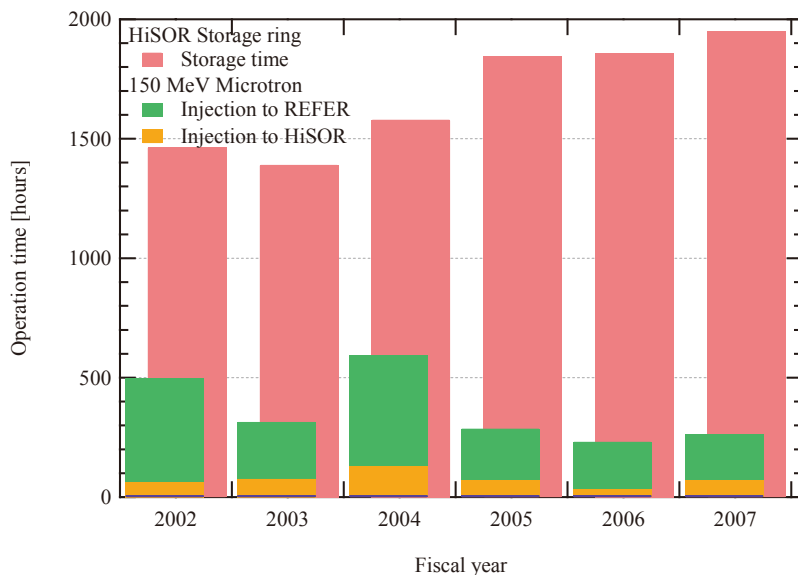


Fig. 4: Annually operation time of Storage ring and Microtron.

### 3. Future plan of HSRC, ‘HiSOR-II’

The emittance of the existing ring is not small because HiSOR is a compact synchrotron light source when we compare it with the third generation light sources. In addition, there are 14 BL’s available in the bending section, but only two straight lines for undulators which are obviously not enough as a current SR facility. Therefore, we are planning a compact storage ring, ‘HiSOR-II’<sup>2,3</sup>, where undulators are dominant light sources as a next plan in HSRC.

#### 3.1 Outline of HiSOR-II

We refer to electron storage ring MAX-III<sup>4</sup> (in Lund, Sweden) as the outstanding models with same scale to design of HiSOR-II. This storage ring is designed that the circumference is equal to or less than 50m so that it can be build in the site of HSRC, it has several straight sections for undulators, and its emittance is about 14nmrad. The main parameters of HiSOR-II are shown in Table 3, and the schematic view is shown in Fig. 5.

A booster ring to have top-up injection is built the inside of HiSOR-II. This ring accelerates the electron beam to 700 MeV for full energy injection to HiSOR-II storage ring. The details of the injector to the booster ring are considering, but we plan either 150MeV Microtron which is operating as injector to HiSOR now or 15MeV linac (this detail is described later).

This booster has to be smaller than storage ring because it is arranged in the inside of compact storage ring. Further, it is placed in sublevel lower than the storage ring, this is convenient that we can thin radiation shield walls.

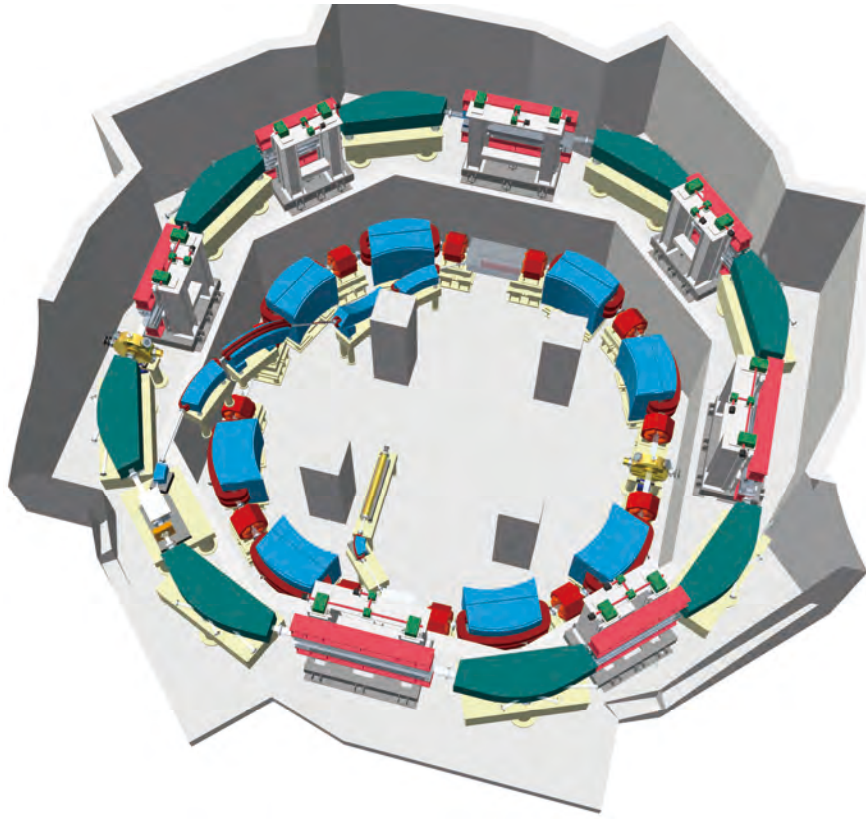


Fig. 5: Schematic draw of HiSOR-II storage ring and booster ring.

Table 3: Main parameters of HiSOR-II.

Beam energy	700 [MeV], $B\rho=2.335$ [Tm]
Circumference [m]	40.079
Betatron tune	3.761, 2.846
Natural emittance [nmrad]	13.57
Momentum spread	$5.79e-04$
Momentum compaction factor	0.0319
Bunch length [mm]	37.0
Harmonic number	7
RF Frequency [MHz]	52.4
Radiation dumping time [msec]	L:11.44 H: 8.57 V:14.70
Touschek lifetime [hour]	2.7
Straight sections	$3.4\text{ m} \times 4$ $2.0\text{ m} \times 4$

The quadrupole magnets of HiSOR-II are combined magnets that occurring quadrupole and sextupole field as well as MAX-III. Further the bending magnets have focusing force, and sextupole component occurs by curved surface of edge of magnetic pole. Fortunately, we could reduce the number of magnet and were able to plan ring miniaturization. The design of

these magnets that complicated shapes is calculated with 2D and 3D electromagnetic code. Fig. 6 shows optical functions of the unit cell of HiSOR-II.

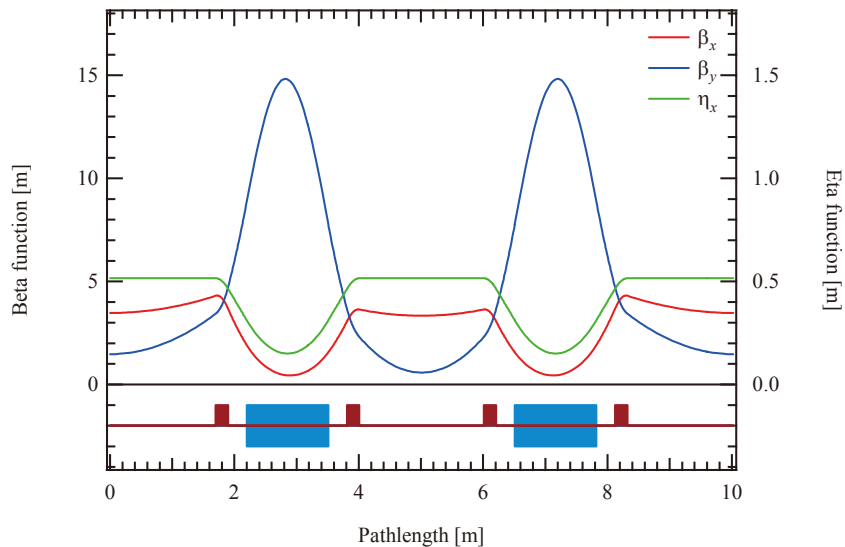


Fig. 6: Beta and dispersion functions of HiSOR-II.

### 3.2 Spectra of synchrotron radiation

Fig. 7 shows radiation spectra from bending magnets, linear and helical undulators of HiSOR-II at 300mA stored current. For comparison, the spectra of HiSOR are carried by fine lines. It was assumed that the linear and helical undulators are the same that are used in HiSOR now.

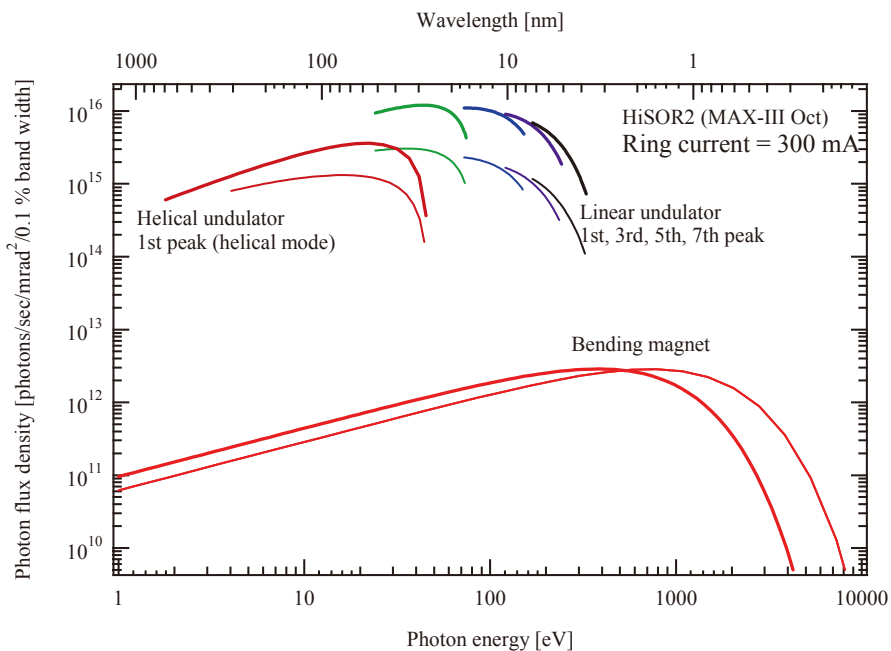


Fig. 7: Spectra of radiation from HiSOR and HiSOR-II at 300 mA current. Bold lines show spectra from HiSOR-II, and fine lines from HiSOR.

### 3.3 Layout of accelerator complex of HSRC

A layout plan of accelerator complex of HSRC including HiSOR-II is shown in Fig. 8. But the layout which is different from this may be adopted because this plan is not yet decision. The building installing HiSOR-II storage ring and booster ring is built newly in this plan. The arrangement of the ring is considered to be able to lengthen a straight section as much as possible, and the beam is injected from the inside of the ring not to reduce beam line.

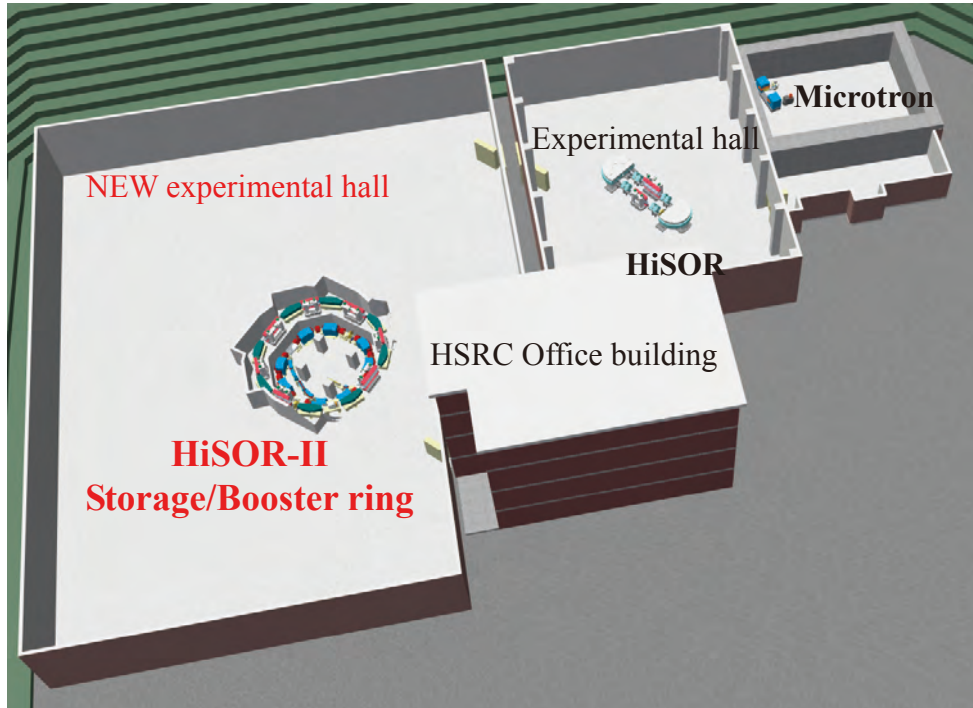


Fig. 8: Layout plan of accelerator complex of HSRC.

### 3.4 Conversion to booster ring from NAR

We are planning that converts the second generation synchrotron radiation ring into booster ring of HiSOR-II to save a construction cost of new accelerators. This ring is NAR<sup>5</sup> of the NTT synchrotron radiation facility, and middle class SR ring in about 53m circumference. The magnets of NAR are separate function type, but we expect that it is necessary to convert it into the combined function type on converting it into very compact booster ring. The outline of the 700 MeV booster ring that is converted from NAR is shown in Fig. 9, and Fig. 10 shows the optical functions of the booster ring. Circumference of this ring is 29.23 m, betatron tune ( $\nu_x, \nu_y$ ) is (2.31, 1.20).

About injector to the booster ring, it is considered two plans. One is 150 MeV Microtron operating as injector to HiSOR now. However, we cannot have injection to HiSOR if we install Microtron in the inside of the booster. Still, it is expected that that the construction of long beam transport line by way of the underground tunnels from Microtron to the booster ring is difficult. The other is a plan to transfer 15 MeV Linac which was injector to NAR. In this case, the electron will be accelerated from 15 MeV to 700 MeV at the booster ring, the

conquest of many problems such as the injection to the ring by the low energy becomes required. Even if either plan is put into execution, enough studies are necessary.

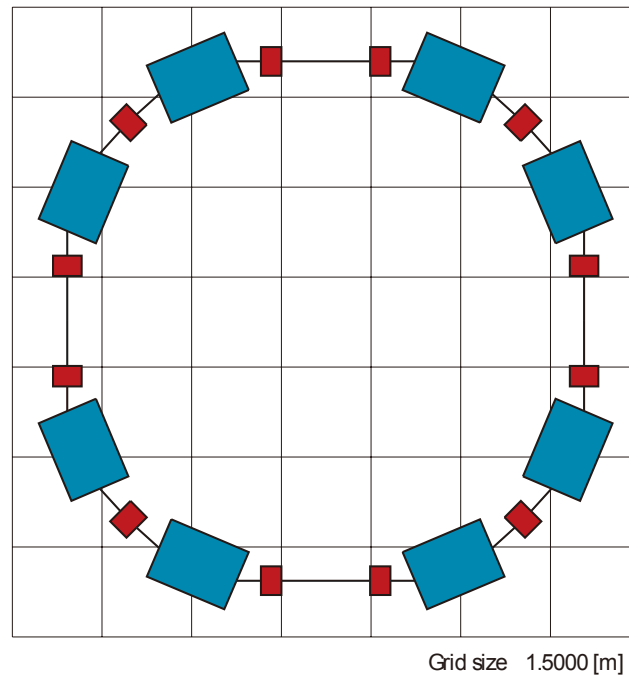


Fig. 9: Outline of the 700 MeV booster ring for HiSOR-II.

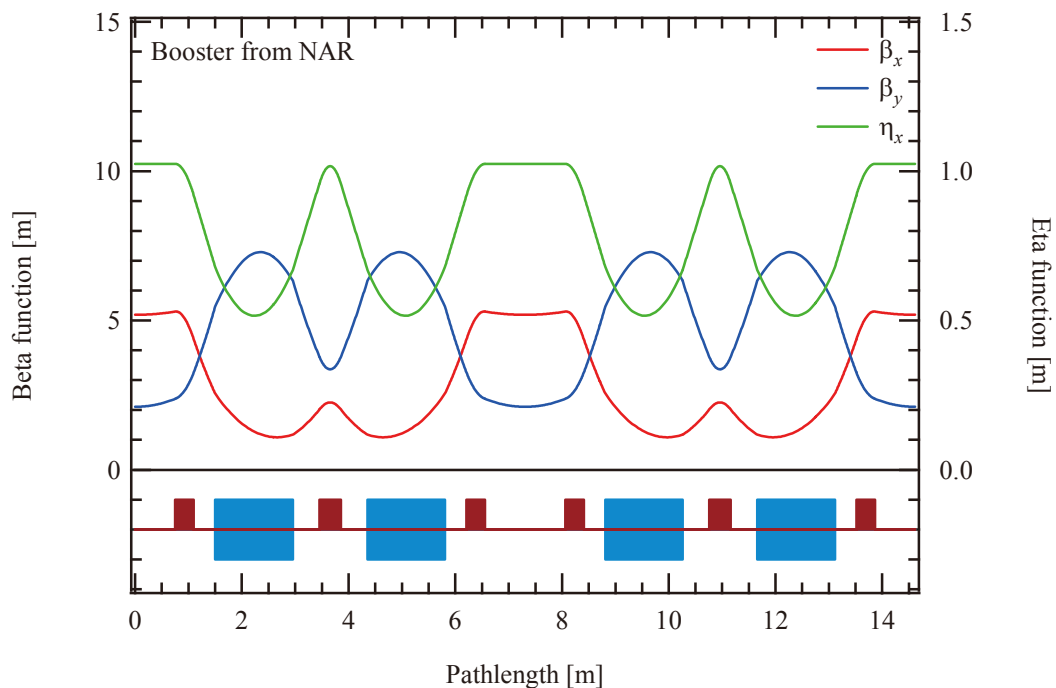


Fig. 10: Optical functions of 700 MeV booster ring.

### 3.5 REFER-II to study of injection / extraction of booster ring

The booster ring installed inward of the storage rings has short straight section for beam injection or extraction. Therefore it is expected that the ordinary beam injection which we

used septum for is difficult. Thus we proceed with plan using pulse sextupole magnet for beam injection, we want to have the testing at the place where REFER is installed in.

REFER (Relativistic Electron Facility for Education and Research) is a very compact multipurpose electron ring using the 150MeV electron beam from Microtron, and it is used for experiments using electron stored in the ring with internal target and extracted beam from the ring. It is necessary to give ability same as REFER in REFER-II which is the test ring of the booster to maintain these activity. Therefore we decided to find space to arrange the instrument which was necessary for beam injection or extractions by extending two straight section of the booster ring. Fig. 11 shows the overview of REFER-II, for comparison of the size, the booster ring is drawn in the figure in a watermark, too. The circumference of this ring is 35.23 m, and 6 m are longer than it of the booster ring.

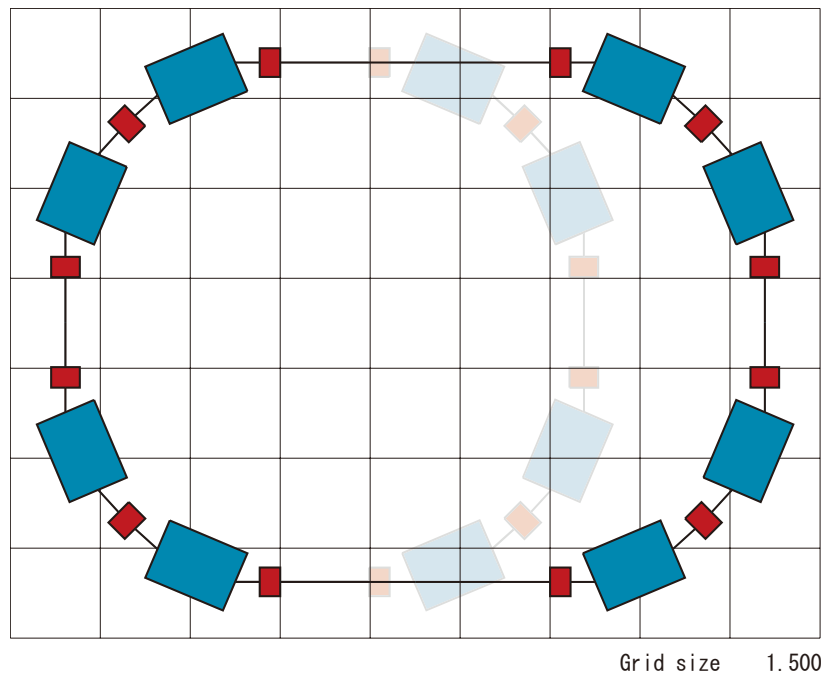


Fig. 11: Outline of REFER-II.

Because the study of the magnets is performed in REFER-II, this ring consist of the magnets totally same as the booster ring. Furthermore, the lattice of this ring is assembled with magnetic field strength same as the magnets of the booster ring. The optical functions of the completed lattice in that way are shown in Fig. 12. The betatron tune ( $\nu_x$ ,  $\nu_y$ ) in this Lattice is (2.31, 1.20).

Because the design of REFER-II still began, there will be many parts which you must consider. Problems such as the injector of the booster ring will solve it in future by considering about the injection using pulse sextupole magnets enough.

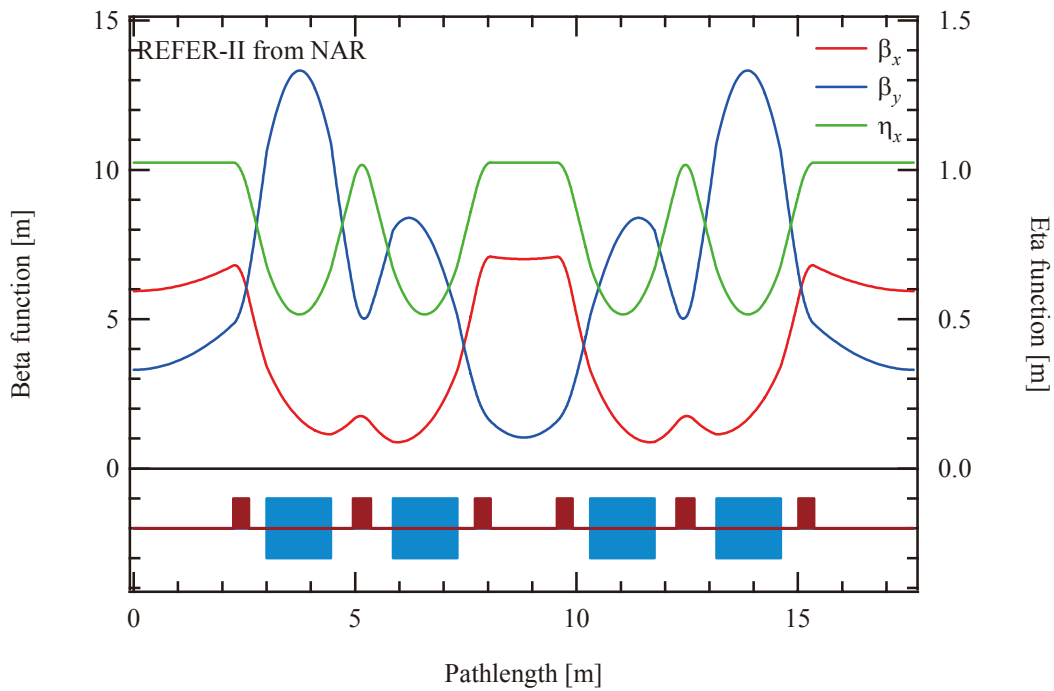


Fig. 12: Optical functions of REFER-II

<sup>1</sup> K. Yoshida, et al., “Commissioning of a Compact Synchrotron Radiation Source at Hiroshima University”, APAC’98, KEK (1998) pp.653-657.

<sup>2</sup> Sumitomo Heavy Industries, Ltd., “MAX-III/UVSOR-II type ring basic design examination for HiSOR-II”, (2006). (in Japanese)

<sup>3</sup> A. Miyamoto, et al., “Status of the HiSOR storage ring and future plan of HSRC”, HiSOR activity report 2007.

<sup>4</sup> G. LeBlanc et al., “MAX-III, a 700 MeV Storage Ring for Synchrotron Radiation”, EPAC2000, Vienna (2000).

<sup>5</sup> S. Shibayama, et al., “NTT normal-conducting accelerating ring”, Rev. Sci. Instrum. 60 (1989) pp.1779-1782.

## Beamlines

A total of 13 beamlines has been constructed so far; three normal-incidence monochromators, seven grazing-incidence monochromators, two double crystal monochromators and an apparatus for white beam irradiation. Table 1 lists the beamlines at present together with the main subject, energy range and monochromators.

At present, nine beamlines BL1, BL3, BL6, BL7, BL9(A), BL11, BL13, BL14 and BL15 have been opened for users. Furthermore, two off-line systems, spin- and angle-resolved photoemission (SARPES) spectrometer and inverse-photoemission spectrometers have also opened for users. Research proposals are regularly submitted in the beginning of every year or additionally any time on demand of users not only in Japan but also in worldwide countries. In 2007, 66 research proposals and 7 improvement proposals were approved. At the undulator beamlines BL1 and BL9A dedicated to the photoemission and angle-resolved photoemission spectroscopies, the experiments with a total energy resolution of 0.66-15 meV at 6-100 eV are now possible.

In 2007, new end station at BL1 for polarization-dependent angle-resolved photoemission spectroscopy (ARPES) has been designed. ARPES with *s*- or *p*-polarization geometry, which determines symmetry of the initial-state wave function, will soon be possible. At the soft x-ray beamline BL14, in situ system for fabrication of magnetic ultrathin films in monatomic layer control by MB and their characterization by means of Auger electron spectroscopy, low energy electron diffraction and high energy electron diffraction, has been introduced. After the fabrication and characterization of magnetic films, the soft x-ray magnetic circular dichroism experiments on the grown films are available. The similar fabrication system has been introduced for the SARPES spectrometer and several in situ SARPES data have been obtained on magnetic atoms on simple metals.

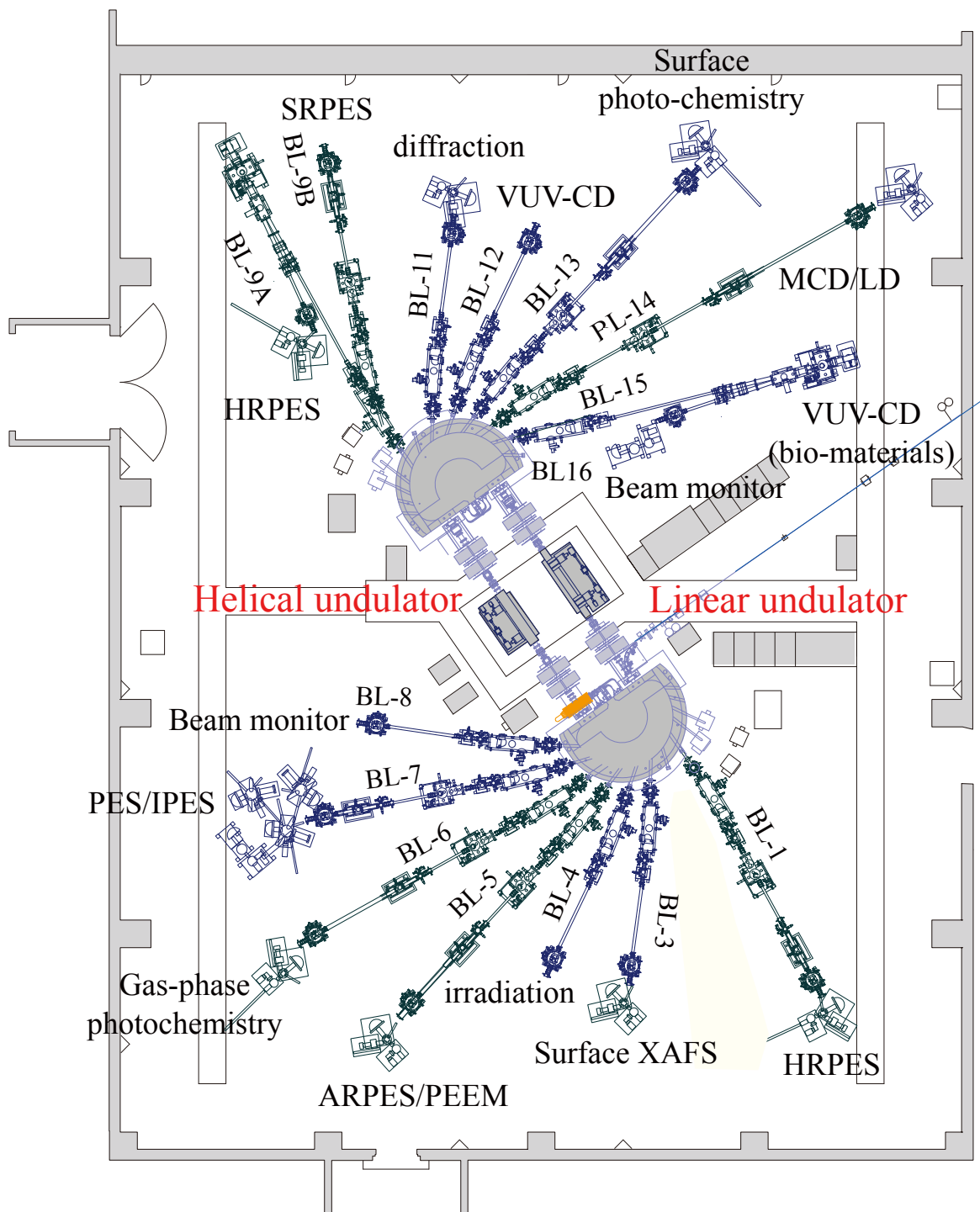


Fig. 1. Schematical view of the experimental hole.

Table I. List of Beamlines

beam line	source	monochromator	subject	energy range (eV)	status
BL1	LU	GIM	High-resolution PES and ARPES	26-300	in use
BL3	BM	DCM	Surface XAFS	1800-3200	in use
BL4	BM		White beam irradiation		in use
BL5	BM	GIM	ARPES and PEEM	40-220	in use
BL6	BM	GIM	Gas-phase photochemistry	200-1200	in use
BL7	BM	GIM	PES and IPES	20-380	in use
BL8	BM		Beam monitor		
BL9A	HU/LU	NIM	High-resolution PES and ARPES	5-35	in use
BL9B	HU/LU	GIM	Spin-resolved PES (in future)	16-300	testing
BL11	BM	DCM	X-ray diffraction	2000-5000	in use
BL12	BM	NIM	VUV-CD of biomaterials	2-10	testing
BL13	BM	GIM	Surface photochemistry	60-1200	in use
BL14	BM	GIM	Soft x-ray MCD	400-1200	in use
BL15	BM	NIM	VUV-CD of biomaterials	4-40	in use
BL16	BM		Beam monitor		

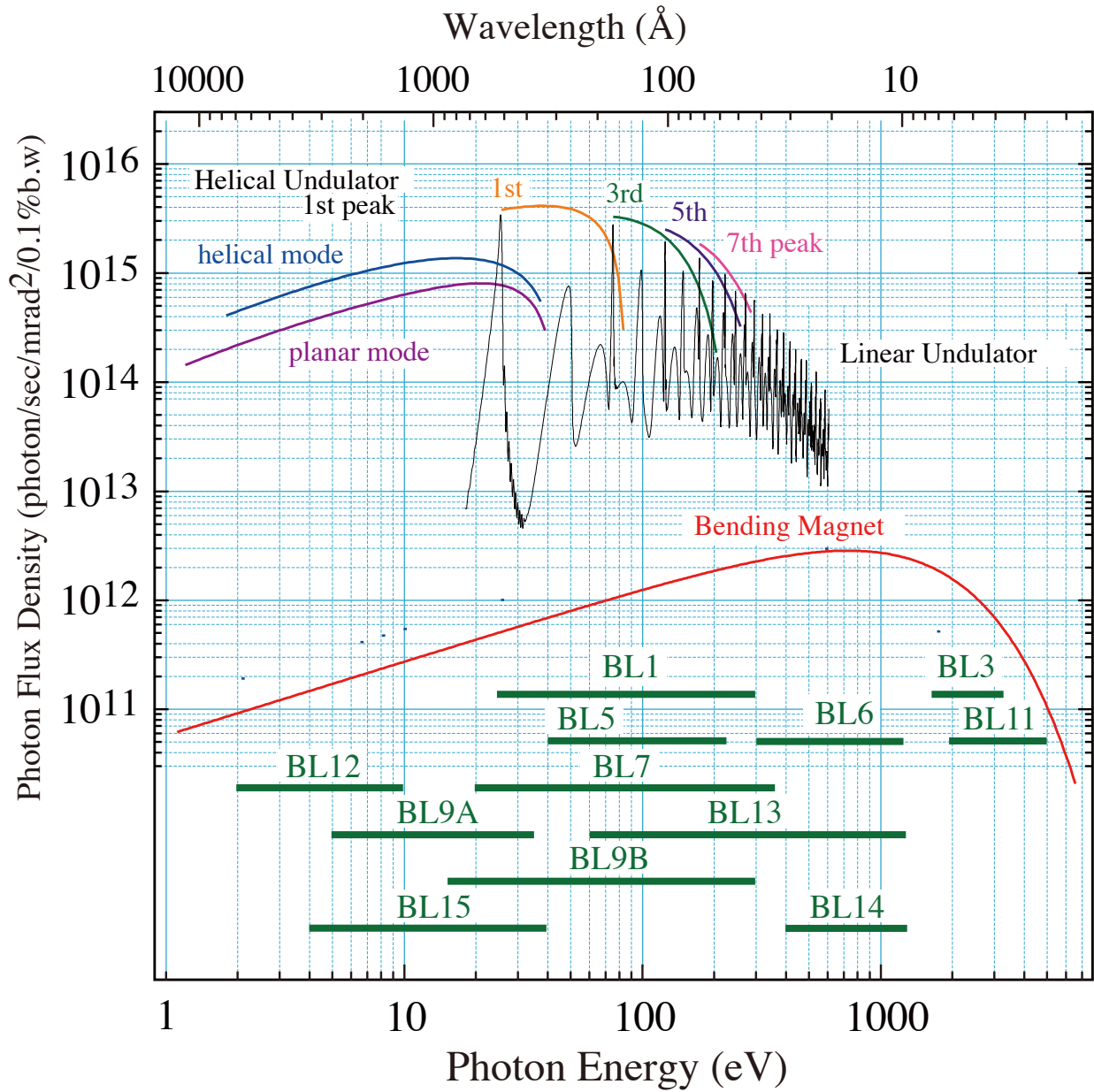


Fig. 2. Energy ranges of beamlines with spectra of HiSOR.

# Research Activities



## New end station for the linear undulator beamline BL-1

K. Shimada<sup>a</sup>, M. Higashiguchi<sup>b</sup>, N. Tobita<sup>b</sup>,  
S. Fukuda<sup>b</sup>, K. Tanaka<sup>b</sup>, J. Jiang<sup>b</sup>, H. Hayashi<sup>b</sup>, H. Namatame<sup>a</sup>, M. Taniguchi<sup>a,b</sup>

<sup>a</sup>*Hiroshima Synchrotron Radiation Center, Hiroshima University*

<sup>b</sup>*Graduate School of Science, Hiroshima University*

In year 2007, we have designed new end station for BL-1 in order to perform polarization-dependent angle-resolved photoemission spectroscopy (ARPES). In the new system, the electron analyzer can be rotated around the light axis, which enables us to examine ARPES spectra with s- or p-polarization geometry. It is indispensable to determine symmetry of the initial-state wave function.

Figure 1 shows the final design of the rotatable frame. High-resolution angle-resolved photoemission spectrometer (VG-SCIENIA, R4000), main chamber with a  $\mu$ -metal chamber inside, and multi-axes low-temperature goniometer (*i*-GONIO) will be rotated with the frame. Differentially pumped rotary feedthroughs will be installed between the main chamber and the beamline, and the main chamber and the preparation chamber. We will use a high-precision goniometer with in-plane motion for Fermi surface mapping. New system will be installed in year 2008.

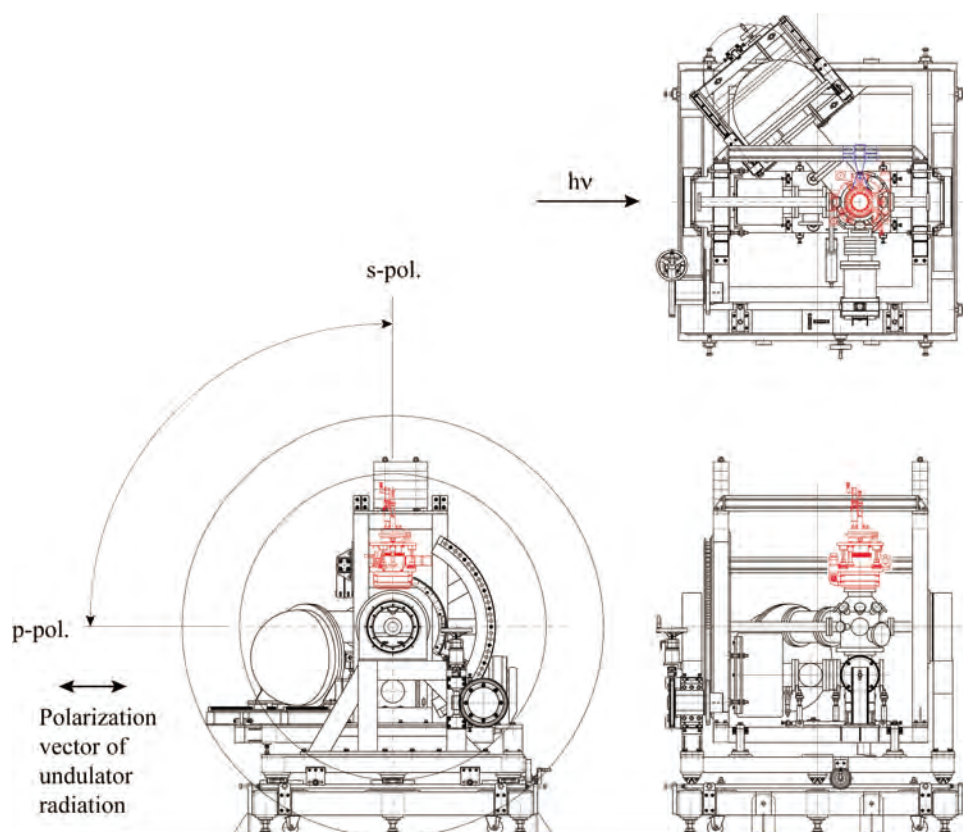


Fig. 1. Final design of the rotatable frame for new BL-1 end station.

## Angle-resolved photoemission study of the Shockley state in Au(110)

Mitsuharu Higashiguchi<sup>1</sup>, Kenya Shimada<sup>2</sup>, Yuichi Miura<sup>1</sup>, Naohisa Tobita<sup>1</sup>, Yoshihiro Aiura<sup>3</sup>,  
Hirofumi Namatame<sup>2</sup>, Masaki Taniguchi<sup>1,2</sup>

<sup>1</sup>*Graduate School of Science, Hiroshima University*

<sup>2</sup>*Hiroshima Synchrotron Radiation Center, Hiroshima University*

<sup>3</sup>*National Institute of Advanced Industrial Science and Technology*

In the present study, we have examined the electronic states of the Shockley state (SS) in Au(110) by means of high-resolution angle-resolved photoemission spectroscopy (ARPES). Although Au(110) surface is known to have the “(2×1) missing-row” reconstructed structure as Fig. 1(b) shows [1-3], we have obtained the (1×1) unreconstructed structure (Fig. 1(a)) judging from the Fermi surface (FS) mapping. Figure 1(c) shows the relation between the bulk Brillouin zone (BBZ) and surface Brillouin zone (SBZ) of the (110) plane without reconstruction. If the (2×1) surface reconstruction occurs, a new zone boundary is formed midway between the  $\bar{\Gamma}$  and  $\bar{Y}$  points as Fig. 1(d) shows. In this case, the  $\bar{\Gamma}$  and  $\bar{Y}$  points become essentially identical.

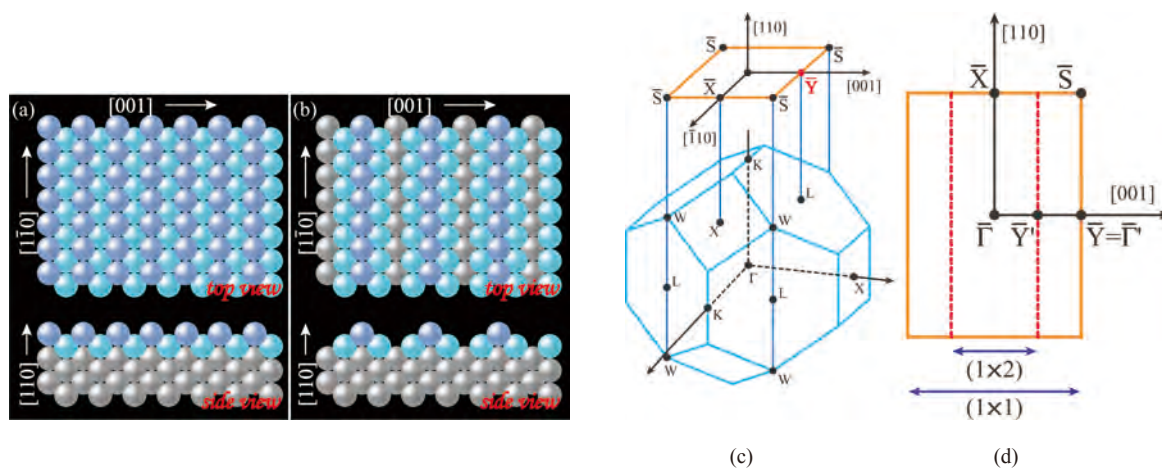


Figure 1. Schematic view of the (1×1) unreconstructed surface of (110) plane (a), and the (2×1) reconstructed surface of (110) plane (missing-row structure) (b). (c) The relation between BBZ and SBZ of (110) plane. (d) The SBZ with and without reconstruction.

High-resolution ARPES measurements were carried out using an angular mode of a hemispherical electron-energy analyzer (ESCA200, SCIEN TA) installed at the linear

undulator beamline BL-1. The total energy resolution was set at  $\Delta E=10$ - $17$  meV, and the angular resolution at  $\Delta\theta= \pm 0.15^\circ$  ( $\Delta k_{\parallel}=0.016$ - $0.02 \text{ \AA}^{-1}$ ). A single crystal of Au(110) (99.999%) was cleaned by repeated cycles of  $\text{Ar}^+$  ion sputtering (the beam energy, 1-2kV) and subsequent annealing at  $400^\circ\text{C}$ . The amounts of impurities such as C, O on the surface were found to be below the detection limit of Auger electron spectroscopy and ultraviolet photoemission spectroscopy. The sample was mounted on a liquid-He-flow-type 5-axis goniometer (i-GONIO LT, R-DEC Co.). The sample temperature was set at 13 and 150 K. The pressure of the main chamber was lower than  $2 \times 10^{-10}$  Torr. The angle between the lens axis of the detector and incident synchrotron radiation was  $45^\circ$ . The polarization vector of the undulator radiation was parallel to the  $[\bar{1}\bar{1}0]$  direction (p-polarized geometry).

Figure 2 shows FS images for Au(110) taken at incident photon energies of  $h\nu = 40.5$ - $59.9$  eV at the sample temperature of 13 K. We could observe half of the elliptic FS centered at the  $\bar{Y}$  point of SBZ. Since the FS at the  $\bar{\Gamma}$  and  $\bar{Y}$  points are not identical, the surface of the present sample was not reconstructed. Since the size and shape of the FS does not depend on the incident photon energy, we can confirm that the Au(110) SS forming FS are indeed localized at surface.

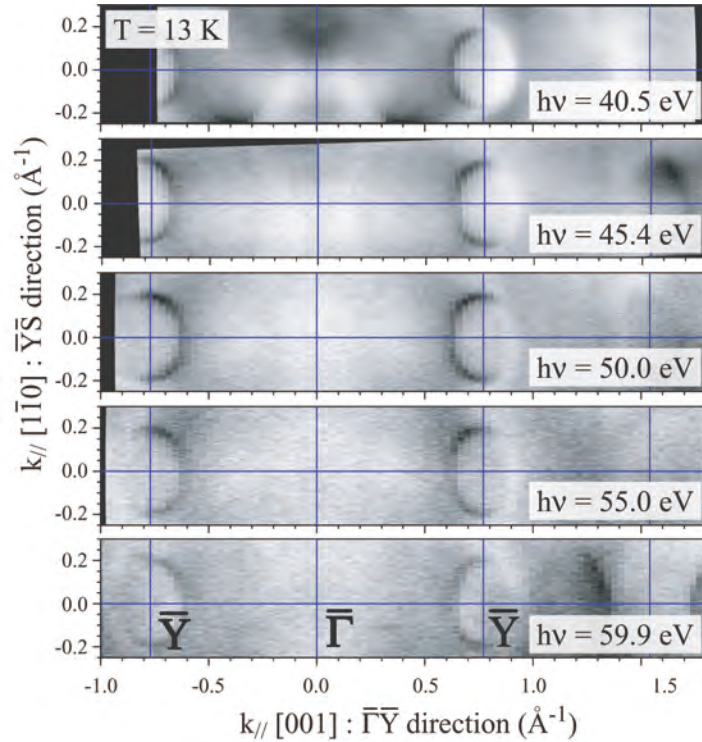


Figure 2. The photon energy dependence FS image for Au(110) taken at  $h\nu=40.5$ - $59.9$  eV.

Figures 3(a) and (b) show intensity plots of the FS of the Au(110) SS around the  $\bar{Y}$  point at 13K and 150K, respectively. In order to evaluate the shape and size of FS, we fitted the momentum distribution curves (MDCs) with Lorentzians at the Fermi level. The evaluated peak positions are indicated by circles in Figs. 3(a) and (b). The contour of FS is well reproduced by the elliptic fit. The size and shape of FS are almost the same at 13K and 150K. The area of the Fermi surface was determined to be  $S_{\text{EF}} = 0.088 \text{ \AA}^2$ , which corresponds to the carrier density of  $2.2 \times 10^{13} \text{ cm}^{-3}$ .

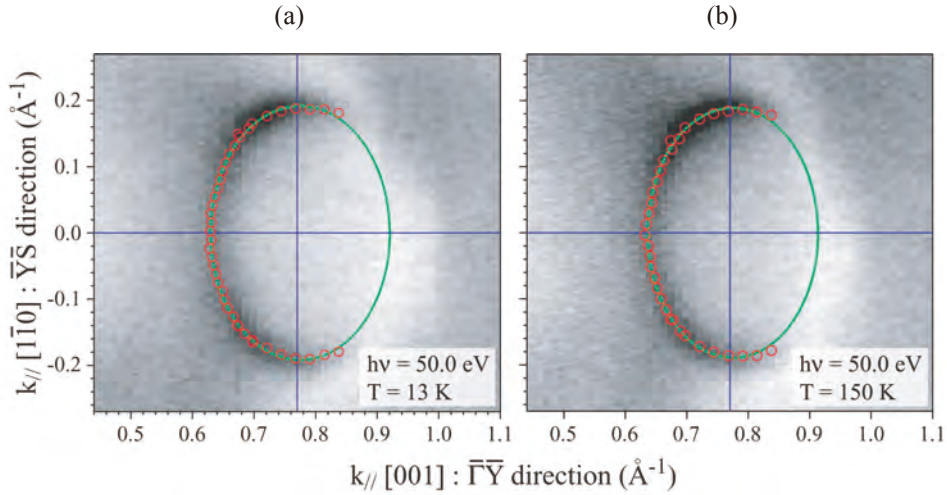


Figure 3. The intensity plots of the FS of the Au(110) Shockley state at 13K (a) and 150K (b).

Figures 4 and 5 exhibit the intensity plots of the band dispersion and energy distribution curves (EDCs) along the  $\bar{Y}\bar{S}$  and  $\bar{\Gamma}\bar{Y}$  directions, respectively. One can see almost free-electron-like band dispersion. By the fitting of EDCs with a Lorentzian, we evaluated peak positions (circles in Figs. 4(a) and 5(a)). The observed energy band dispersions are explained well by a parabolic function (solid lines in Fig. 4(a) and 5(a)). Along the  $\bar{\Gamma}\bar{Y}$  direction, half of the spectral intensity was suppressed. We assume that the suppression of the spectral intensity is derived from the matrix element effect. The Fermi energy was evaluated as  $\varepsilon_0^{\bar{Y}\bar{S}} = 590 \pm 5 \text{ meV}$  along the  $\bar{Y}\bar{S}$  direction. The Fermi wave number along the  $\bar{Y}\bar{S}$  direction,  $k_F^{\bar{Y}\bar{S}} = 0.195 \text{ \AA}^{-1}$ , is larger than that along the  $\bar{\Gamma}\bar{Y}$  direction,  $k_F^{\bar{\Gamma}\bar{Y}} = 0.167 \text{ \AA}^{-1}$ . Accordingly, the effective mass with respect to the free electron mass ( $m_e$ ) along the  $\bar{Y}\bar{S}$  direction,  $m^* = 0.25 m_e$ , is heavier than that along the  $\bar{\Gamma}\bar{Y}$  direction,  $m^* = 0.13 m_e$ .

In conclusion, we have performed a high-resolution ARPES of Au(110) SS using tunable photons. We observed elliptic FS centered at the  $\bar{Y}$  point of SBZ. We found that half of the spectral intensity of FS was suppressed. We estimated the shape and size of FS, as well as

band parameters such as  $k_F$  and  $m^*$ . These parameters did not depend on the photon energy, confirming highly two dimensional nature of Au(110) SS.

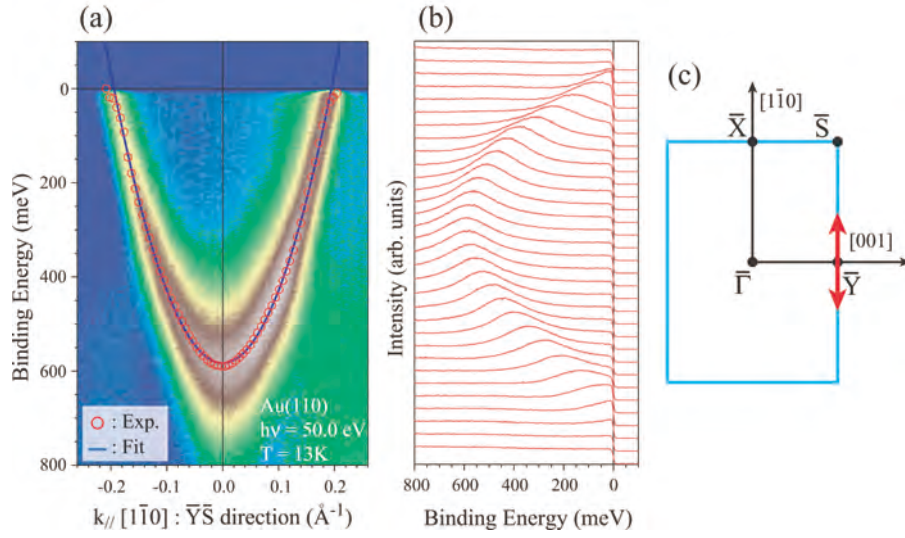


Figure 4. The intensity plot of the band dispersion (a), EDC spectra (b) along the  $\bar{Y}\bar{S}$  direction. (c) SBZ of Au(110) and measured direction (red arrows).

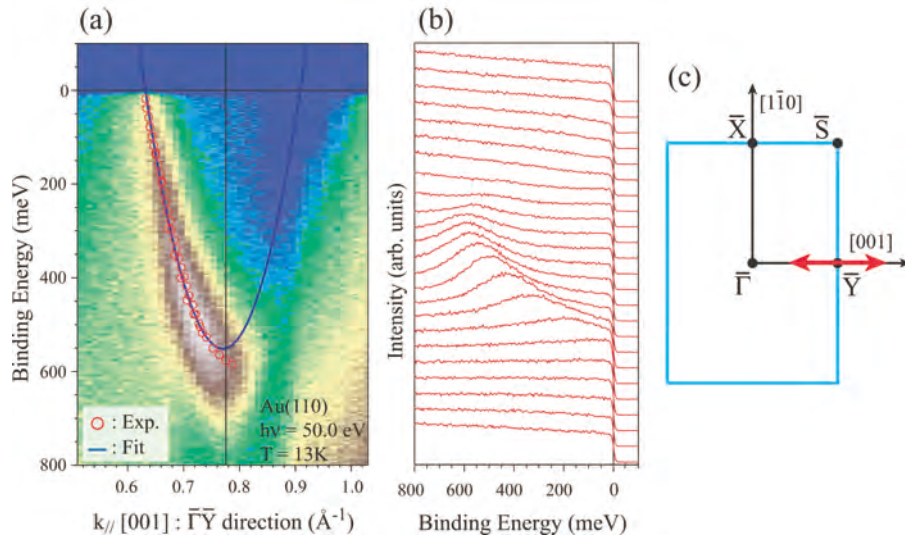


Figure 5. The intensity plot of the band dispersion (a), EDC spectra (b) along the  $\bar{\Gamma}\bar{Y}$  direction. (c) SBZ of Au(110) and measured direction (red arrows).

## References

- [1] K. -M. Ho, K. P. Bohnen, Phys. Rev. Lett. **19**, 1833 (1987).
- [2] Y. Uehara, F. Fujita, S. Ushioda, Phys. Rev. Lett. **83**, 2445 (1999).
- [3] Y. Uehara, S. Ushioda, Phys. Rev. B **66**, 165420 (2002).

## Angle-resolved photoemission study of Pt (111)

N. Tobita<sup>1</sup>, S. Fukuda<sup>1</sup>, N. Nakajima<sup>1</sup>, N. Ishimatsu<sup>1</sup>, H. Maruyama<sup>1</sup>,  
H. Hayashi<sup>2</sup>, K. Tanaka<sup>1</sup>, J. Jyan<sup>1</sup>, M. Higashiguchi<sup>1</sup>, K. Shimada<sup>3</sup>,  
H. Namatame<sup>3</sup> and M. Taniguchi<sup>1,3</sup>

<sup>1</sup>*Grad. Sch. of Sci., Hiroshima Univ.*, <sup>2</sup>*Fac. of Sci. Hiroshima. Univ.*,

<sup>3</sup>*Hiroshima Synchrotron Radiation Center, Hiroshima. Univ.*

Platinum is known as one of the most important catalytic materials for long. Its catalytic effect is thought to be caused by a relativistic effect which is also related to surface reconstruction of clean surfaces. In noble metals with an fcc structure such as Cu, Ag and Au, a bit wider band-gaps exist at the Fermi level around an L point and also Shockley surface-states derived from an *sp*-like bulk bands are observed in between the gaps. Among them, a splitting of the surface-state bands caused by strong spin-orbit interaction was observed in Au. Recently, it is observed that the intensity of the splitting depends on crystal orientation [1]. Pt also shows strong spin-orbit interaction and is therefore expected to be a basic material for spintronics devices or a good testground for spin Hall effect in metals.

The lowered dimensionality of intrinsic electron states favors the production of screening singularities and phonon anomalies, and is thus responsible for the surface reconstruction [2]. Therefore, it is important to clarify the surface state of Pt. In this study, we have performed an angle-resolved photoemission study (ARPES) of a Pt (111) clean surface.

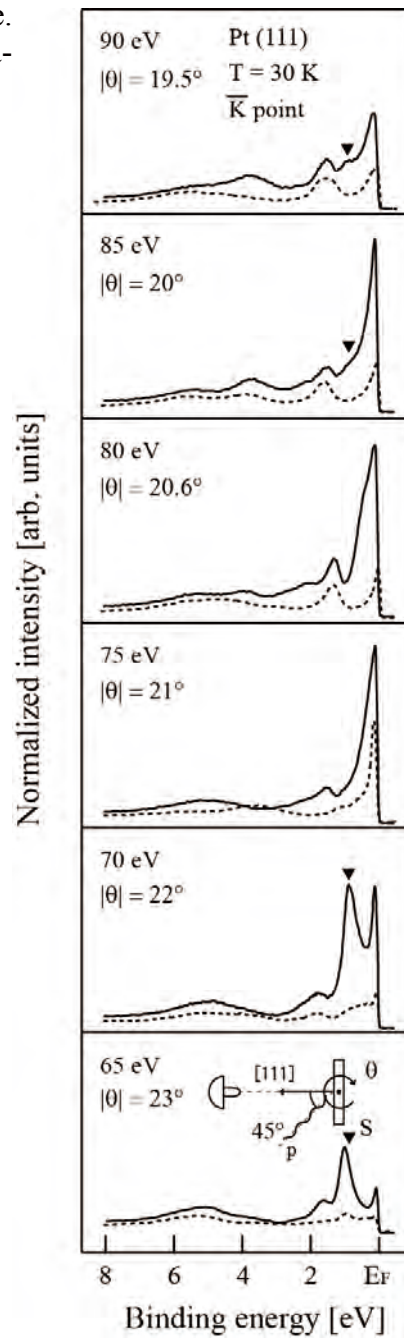
The ARPES spectra were measured on the undulator beamline BL1 at HiSOR. All the experiments were performed at low temperature ( $\sim 30\text{K}$ ). The base pressure of the chamber was an order of  $10^{-10}$  Torr. A clean (111) surface was simply prepared by  $\text{Ar}^+$  ion sputtering and annealing. Once a clean surface was obtained, the sample surface was almost free from contaminations.

Figure 1 shows photoemission spectra of a Pt (111) surface at several  $\bar{K}$  points. Solid (dashed) lines are the spectra for positive (negative) polar angle ( $\theta$ ) which origin ( $\theta = 0^\circ$ ) is set to a normal emission configuration. At each photon energy, the spectra show strong dependence on the polarity of  $\theta$ , which is directly due to the difference in the components of polarization and may be influenced by an *sp*-like nature of the corresponding bands. The binding energies ( $E_B$ ) of several peaks for  $E_B$  below 3.8 eV strongly depend on the polarity of  $\theta$ , however, those of the peaks for  $0 \text{ eV} < E_B < 2 \text{ eV}$  remain the same except the peak S labeled by solid triangles ( $\blacktriangledown$ ). Compared to a theoretical prediction of the band structure [3], all the peaks except the peak S locate in the projection of bulk bands at the  $\bar{K}$  point. The peak S shows strong dependence on the polarity of  $\theta$ . Besides, the binding energy for positive  $\theta$  is almost constant. It is therefore safely concluded that the peak S is a surface state derived from the *sp*-like bulk bands.

Fig. 1: ARPES spectra of a Pt (111) clean surface. Solid (dashed) lines are the spectra for positive (negative) polar angles ( $\theta$ ).

At BL-1, new energy analyzer (Scienta R4000) will be installed on a brand-new chamber which enables the polarization dependence measurement without breaking the vacuum. A complete understanding of the spectra will be achieved soon.

- [1] M. Higashiguchi, Doctoral thesis, Hiroshima Univ. (2008).
- [2] H. H. Ernst *et al.*, Phys. Rev. Lett. **58**, 1941 (1987); W. Kohn, *ibid.* **2**, 393 (1959).
- [3] D. A. Papaconstantopoulos, Handbook of the Band Structure of Elemental Solids (Plenum, New York, 1986); W. Di *et al.*, Phys. Rev. B **45**, 3652 (1992).



## Angle-resolved photoemission study of Cr (110)

S. Fukuda<sup>1</sup>, N. Tobita<sup>1</sup>, N. Nakajima<sup>1</sup>, N. Ishimatsu<sup>1</sup>, H. Maruyama<sup>1</sup>,  
H. Hayashi<sup>2</sup>, K. Tanaka<sup>1</sup>, J. Jyan<sup>1</sup>, M. Higashiguchi<sup>1</sup>, K. Shimada<sup>3</sup>,  
H. Namatame<sup>3</sup> and M. Taniguchi<sup>1,3</sup>

<sup>1</sup>*Grad. Sch. of Sci., Hiroshima Univ.*, <sup>2</sup>*Fac. of Sci. Hiroshima Univ.*,

<sup>3</sup>*Hiroshima Synchrotron Radiation Center, Hiroshima Univ.*

Chromium (Cr) is one of the key elements for the recent study on the spintronics mainly because its antiferromagnetic nature can be utilized to manipulate the spin state of materials. Among the wide variety of 3d transition metals, antiferromagnetism of Cr is the most challenging problem to tackle with. Especially, a spin-density wave (SDW) and a charge-density wave which result in modulation of electronic states are still under debates together with surface ferromagnetism caused by lattice expansion. These fascinating features are still difficult to examine partly due to difficulties in preparing a clean (contamination-free) surface. The recent progress of evaporation techniques for preparing ultrathin films has made it possible to easily obtain clean Cr surfaces and intensive studies such as photoemission and scanning tunneling spectroscopy are performed using these films. However, the above-mentioned nature of Cr is very delicate and faint to see depending on the film conditions such as lattice parameters and/or surface morphology.

In order to eliminate the uncertainty arising from the film condition, we have used a bulk sample with an (110) surface. A clean surface was carefully prepared by repeated cycles of Ar<sup>+</sup> ion sputtering (< 3 kV) and annealing (< 800 K) followed by a thermal flash at 1100 K. Special care was paid to the initial cleaning process in order not to create an oxidized surface which is hard to remove in a vacuum. The angle-resolved photoemission spectra were measured on the undulator beamline BL1 at HiSOR. Throughout the course of experiments, the base pressure of the chamber was an order of 10<sup>-10</sup> Torr.

Figure 1 shows a Fermi surface mapping of Cr (110) in a  $\Gamma$ HPN plane of a bcc Brillouin zone taken at 77K with photon energy of 139 eV. Two pantographs around  $\Gamma$  and H points correspond to electron and hole pockets, respectively. A momentum distribution curve along a white dashed line reveals a back-folding band caused by an antiferromagnetic order. Details of multifolding bands due to the SDW will be examined in a forthcoming experiment.

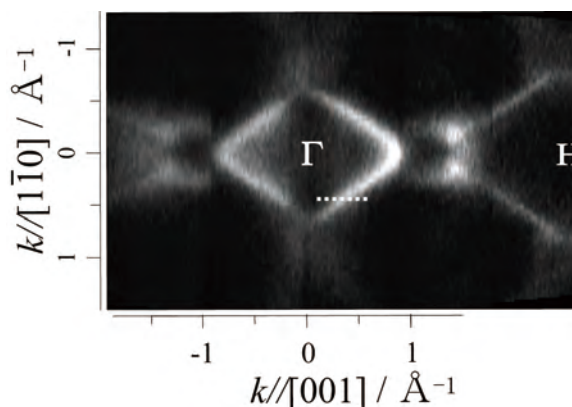


Fig. 1: A Fermi surface mapping of a Cr (110) clean surface taken at 77K with photon energy of 139 eV.

## High-resolution angle-resolved photoemission study of the surface-derived state in Al(100) single crystal

J. Jiang<sup>a</sup>, K. Shimada<sup>b</sup>, M. Higashiguchi<sup>a</sup>, N. Tobida<sup>a</sup>, K. Tanaka<sup>a</sup>,  
S. Fukuda<sup>a</sup>, H. Hayashi<sup>a</sup>, Y. Aiura<sup>c</sup>, H. Namatame<sup>b</sup>, M. Taniguchi<sup>a,b</sup>

<sup>a</sup>*Grad. Sch. of Sci., Hiroshima Univ.,*

<sup>b</sup>*HSRC, Hiroshima Univ.,*

<sup>c</sup>*AIST*

Recently, energy and momentum resolutions of angle-resolved photoemission spectroscopy (ARPES) have been improved drastically. Now one can examine fine electronic structures of solids that are directly related to the physical properties of solids. Using photon energies in the vacuum ultraviolet and soft X-ray region, ARPES spectra are sensitive to the electronic states at surface. Based on the quantitative analyses of photoemission spectral features, one can evaluate the magnitudes of the electron-phonon and electron-electron interactions at a specific point on the Fermi surface.

Aluminum is the textbook example of a trivalent nearly-free electron metal and a weak coupling superconductor. It has been well known that there exists a free-electron-like surface-derived state around the  $\bar{\Gamma}$  point of the surface Brillouin zone in the (100) surface [1-4]. So far, there has been no report on the quasi-particle properties near Fermi level ( $E_F$ ) of aluminum by means of ARPES. In this study, we have done high-resolution ARPES of Al(100) to evaluate the many-body interactions on the quasi-particles near  $E_F$  in the surface-derived state. A kink structure has been clearly observed in the energy band dispersion of the surface-derived state. The magnitudes of the electron-phonon and electron-electron coupling parameters at low temperature have been successfully evaluated. The obtained electron-phonon coupling parameter showed reasonable agreement with the calculated one [4].

ARPES experiments were performed on the linear undulator beamline (BL-1) of a compact electron-storage ring (HiSOR) at Hiroshima University [5]. High-resolution ARPES measurements were carried out using an angular mode of hemispherical electron-energy analyzer (ESCA200, GAMMADATA-SCIENTA at BL-1). Linearly polarized undulator radiation ( $h\nu=43$  eV) was used. We set the total energy resolution at  $\Delta E=15$  meV and  $\Delta\theta=0.3^\circ$ . The clean surface of Al(100) single crystal (purity 99.9999%) was obtained by repeated cycles of  $\text{Ar}^+$  sputtering (5 keV) over 10 hours and annealing at 400°C for 30 minutes to minimize surface roughness introduced by  $\text{Ar}^+$  sputtering. The amount of impurities such as C, O, and S on the surface was evaluated below the detection limit of Auger electron spectroscopy. The sample was mounted on the liquid-He-flow-type 5-axis

goniometer (i-GONIO LT, R-DEC Co.). The sample temperature was set at 30 K. The pressure of the main chamber was  $1 \times 10^{-8}$  Pa.

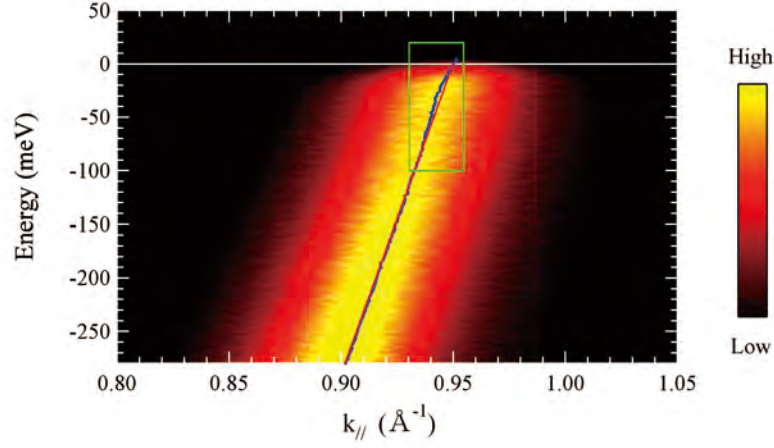


Fig. 1. The ARPES results of Al(100) surface-derived state at  $h\nu = 43$  eV and at 30 K.

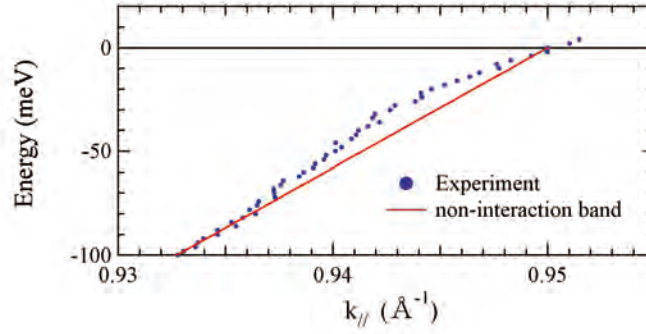


Fig. 2. Experimentally determined band points near  $E_F$ . A kink structure exists at -37 meV.

Figure 1 shows the energy-band dispersion of the surface-derived state centered at the  $\bar{\Gamma}$  point. It has a sharp spectral feature and a parabolic dispersion, which is suitable for the detailed line shape analyses to elucidate many-body interactions. In order to quantitatively analyze the spectral shape, we used Lorentzian on a linear background to fit the momentum distribution curves (MDCs). The blue points and red lines in Fig. 1 indicate evaluated peak positions, and assumed non-interaction band. Figure 2 shows the area surrounded by the green square in Fig. 1. One can recognize a clear kink structure at -37 meV below  $E_F$ . Since the magnitude of the energy of the kink coincides well with the energy scale of the Debye temperature of Al ( $\Theta_D=426$  K,  $k_B\Theta_D=37$  meV), it is reasonable to assume that the structure is derived from the electron-phonon interaction [6,7].

Next we examine the strength of many-body interactions on the quasi-particles near  $E_F$ , by evaluating the self-energy,  $\Sigma(k, \omega)$ . The ARPES spectral features are given by the single-particle spectral function  $A(k, \omega)$ , which is related to the imaginary part of the

single-particle Green's function,  $G(k, \omega)$  :

$$A(k, \omega) = -\frac{1}{\pi} G(k, \omega) = -\frac{1}{\pi} \frac{\text{Im}\Sigma(k, \omega)}{[\omega - \varepsilon_k^0 - \text{Re}\Sigma(k, \omega)]^2 + [\text{Im}\Sigma(k, \omega)]^2} \quad (1)$$

where  $\varepsilon_k^0$  represents the energy of non-interacting band. In the present analyses, we have assumed that  $\varepsilon_k^0$  is linear near  $E_F$  as shown by a solid line in Fig. 2.  $\text{Re}\Sigma(k, \omega)$  gives an energy shift from the energy of non-interaction band. The  $\text{Im}\Sigma(k, \omega)$  is related to the spectral width,  $\Gamma = |2\text{Im}\Sigma(k, \omega)|$  [6,7]. In the present analyses, we used the MDC width,  $\delta k$ , to estimate the  $\text{Im}\Sigma(k, \omega)$ , namely,  $|2\text{Im}\Sigma(k, \omega)| = \delta E = (dE/dk)\delta k$ , where  $dE/dk$  is the gradient of the energy band.

In the case that electron-scattering processes such as the electron-phonon, electron-electron, and electron-impurity interactions can be regarded as independent, the lifetime broadening ( $\Gamma = |2\text{Im}\Sigma(k, \omega)|$ ) of the quasi-particles is expressed by the sum of each contribution:  $\Gamma = \Gamma_{el-ph} + \Gamma_{el-el} + \Gamma_0$ .

Figure 3(a) and 3(b) respectively show obtained  $\Gamma = |2\text{Im}\Sigma(k, \omega)|$  and  $\text{Re}\Sigma(k, \omega)$ . Solid and dashed lines in Fig. 3(a) exhibit theoretical  $\Gamma_{el-ph}$  and  $\Gamma_{el-el}$ , respectively. One can see observed  $\Gamma = |2\text{Im}\Sigma(k, \omega)|$  is explained well by the theoretical curve  $\Gamma_{el-ph} + \Gamma_{el-el}$ . Solid line in Fig. 3(b) indicates the theoretical  $\text{Re}\Sigma_{el-ph}$ , which agrees well with the experimental one. These results confirm that the kink structure originates from electron-phonon interaction.

One can evaluate the dimensionless coupling parameter of the electron-phonon interaction as follows.

$$\lambda_{el-ph} = - \left. \frac{\partial \text{Re}\Sigma_{el-ph}}{\partial \omega} \right|_{\omega=0} \quad (2)$$

Using the observed gradient of  $\text{Re}\Sigma_{el-ph}$  at  $E_F$  (dashed line in Fig. 3(b)), we have obtained  $\lambda_{el-ph} = 0.67$ . Recently, Sklyadneva et al. have reported an *ab initio* study of the electron-phonon interaction in the surface electronic states of Al(100), on the basis of the density-functional theory using a linear response approach in the plane-wave pseudopotential representation [4]. The calculated electron-phonon coupling parameter is  $\lambda_{el-ph} = 0.51$  at the  $\bar{\Gamma}$  point. However, the coupling parameter increases with energy [4]. Although the coupling parameter at  $E_F$  was not provided, calculated  $\text{Re}\Sigma_{el-ph}$  (solid line in Fig. 3(b)) using theoretical  $\alpha^2 F$  coincides well with the experimental one near  $E_F$ . It clearly indicates experimental coupling parameter is in good agreement with the theoretical value.

In order to evaluate the magnitude of the electron-electron interaction, on the other hand, we fit the observed  $|2\text{Im}\Sigma|$  assuming  $2\beta\omega^2 [1/4 + \ln 2 - 1/2 \ln|\omega/\omega_0|] + C$  for the energy region of  $-800 \text{ meV} \leq \omega \leq -50 \text{ meV}$ . Here  $C$  is a constant, and the Fermi energy was set at  $\omega_0 = 2.63 \text{ eV}$ . We have obtained  $2\beta = 0.03 \text{ eV}^{-1}$ . Using the Kramers-Kronig relation, one can evaluate the coupling parameter of the electron-electron interaction as

$$\lambda_{el-el} = 4\beta\omega_0\zeta/\pi = 0.060 \quad [8].$$

In summary, we have performed a high-resolution ARPES study of the surface-derived state centered at the  $\bar{\Gamma}$  point in Al(100). We have observed a clear kink structure in the energy-band dispersion at  $\omega = -37$  meV, which corresponds well to the energy scale of the Debye temperature. We have evaluated the electron-phonon and electron-electron coupling parameters as  $\lambda_{el-ph} = 0.67$  and  $\lambda_{el-el} = 0.060$ , respectively. We have found that  $\lambda_{el-el}$  is much smaller than  $\lambda_{el-ph}$ .

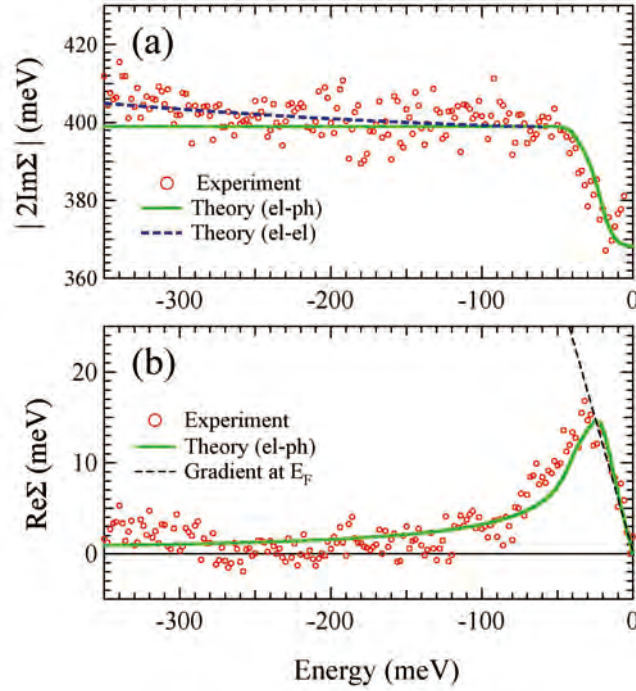


Fig. 3 Imaginary part (a) and real part (b) of self-energy of the surface-derived state in Al(100).

We thank the N-BARD, Hiroshima University for supplying liquid helium.

## References

- [1] H. J. Levinson, F. Greuter and E. W. Plummer, *Phys. Rev. B* **27**, 727 (1983).
- [2] Ph. Hofmann, S. V. Hoffmann et al., *Phys. Rev. B* **66**, 245422 (2002).
- [3] E. E. Krasovskii and W. Schattke, *Phys. Rev. Lett.* **93**, 027601 (2004).
- [4] I. Y. Sklyadneva, E. V. Chulkov and P. M. Echenique, *J. Phys.: Condens. Matter* **20**, 165203 (2008).
- [5] K. Shimada, M. Arita, Y. Takeda, H. Fujino, K. Kobayashi, T. Narimura, H. Namatame, M. Taniguchi, *Surf. Rev. Lett.* **9**, 529 (2002).
- [6] T. Valla, A. V. Fedorov, P. D. Johnson, S. L. Hulbert, *Phys. Rev. Lett.* **83**, 2085 (1999).
- [7] M. Higashiguchi, K. Shimada, K. Nishiura, X. Y. Cui, H. Namatame, M. Taniguchi, *Phys.*

Rev. B **72**, 214438 (2005).

[8] In the present analyses, we have assumed the imaginary part of the self-energy as

$$\text{Im}\Sigma_{el-el}(\omega) = -\beta\omega^2 \left[ \frac{1}{4} + \ln 2 - \frac{1}{2} \ln \left| \frac{\omega}{\omega_0} \right| \right] \quad \text{for } |\omega| \leq \omega_0, \quad \text{and} \quad \text{Im}\Sigma_{el-el} = -\beta\omega_0^2 \left[ \frac{1}{4} + \ln 2 \right]$$

for  $|\omega| > \omega_0$ . Here  $\omega_0$  is the Fermi energy. On the basis of the Kramers-Kronig relation, one can calculate the real part of the self-energy as follows.

$$\text{Re}\Sigma_{el-el}(\omega) = \frac{1}{\pi} P \int_{-\omega_0}^{+\omega_0} \frac{\text{Im}\Sigma_{el-el}(\omega')}{\omega' - \omega} d\omega' \quad (|\omega| \leq \omega_0)$$

Then, the coupling parameter can be calculated as follows.

$$\lambda_{el-el} = - \left. \frac{\partial \text{Re}\Sigma_{el-el}(\omega)}{\partial \omega} \right|_{\omega=0} = - \frac{1}{\pi} P \int_{-\infty}^{+\infty} \frac{\text{Im}\Sigma_{el-el}(\omega')}{\omega'^2} d\omega'$$

$$\therefore \lambda_{el-el} = \frac{4\beta\omega_0}{\pi} \left[ \frac{1}{2} + \ln 2 \right] = \frac{4\beta\omega_0}{\pi} \zeta, \quad \zeta \equiv \left[ \frac{1}{2} + \ln 2 \right] \sim 1.193$$

## High-resolution angle-resolved photoemission spectroscopy of Rh(100)

Hirokazu Hayashi<sup>a</sup>, Kenya Shimada<sup>b</sup>, Katsunori Tanaka<sup>c</sup>, Mitsuharu Higasiguchi<sup>c</sup>, Naohisa Tobita<sup>c</sup>, Jan Jing<sup>c</sup>, Shugo Fukuda<sup>c</sup>, Hirofumi Namatame<sup>b</sup>, Masaki Taniguchi<sup>a,b</sup>

<sup>a</sup>*Fac. of Sci. Hiroshima Univ.,*

<sup>b</sup>*HSRC, Hiroshima Univ.,*

<sup>c</sup>*Grad. Sci. of Sci. Hiroshima Univ.*

Rhodium is one of the most important and widely used metals as a catalyst cleaning exhaust gas from automobiles. So far, the electronic band structures of Rh clean surface together with molecule adsorbed surface have been studied by means of angle-resolved photoemission spectroscopy (ARPES). However, the detail of the electronic band structures and the Fermi surface of Rh clean surface have not been elucidated yet. In this study, by means of high-resolution ARPES with tunable synchrotron radiation, we have examined three-dimensional Fermi surface of Rh. In the vacuum ultraviolet region, one can observe both surface- and bulk-derived electronic structures. It is noted that the surface electronic state is closely related to catalysis. We also elucidate quasi-particles in the bulk-derived electronic states.

Experiments were done on the linear undulator beamline (HiSOR BL-1) of Hiroshima Synchrotron Radiation Center. By repeated Ar<sup>+</sup> sputtering and high temperature anneal at 1200 K, we obtained clean surface of Rh(100). Cleanliness of the sample surface was checked by Auger spectroscopy. The sample was mounted on the 5-axes low-temperature goniometer (iGONIO) for the Fermi surface mapping. A high-resolution hemispherical electron-energy analyzer (ESCA200) was used for the ARPES measurements. The overall energy and momentum resolutions were respectively set at  $\Delta E = 13.4 - 89.7$  meV and  $\Delta k = 0.011 - 0.027 \text{ \AA}^{-1}$ , depending on the incident photon energy range  $h\nu = 63.5 - 155.7$  eV.

Figure 1 shows an image plot of the observed Fermi surface in the  $\Gamma$ KWX plane of the Brillouin zone (Fig. 2) taken at photon energy of  $h\nu=155.7$  eV and at sample temperature of

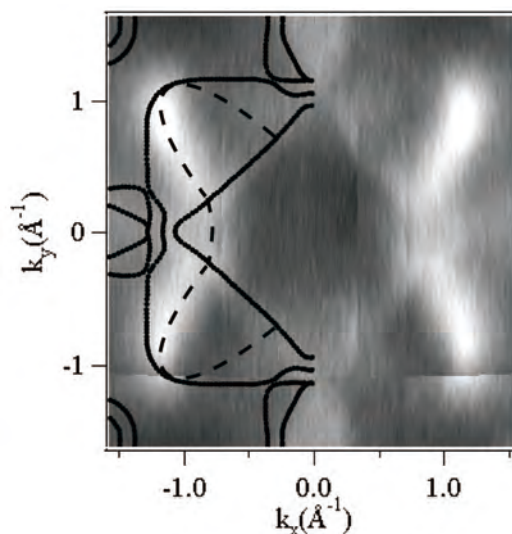


Figure 1. Fermi surface mapping of Rh (100) taken at  $h\nu = 155.7$  eV, at 150 K. White portion corresponds to the highest spectral intensity. Solid lines show Fermi surfaces calculated by the band-structure calculation [1]. Broken lines trace structures that cannot be explained by the bulk-derived Fermi surfaces.

150 K. White portion corresponds to the highest spectral intensity. Solid lines exhibit theoretical Fermi surfaces given by the band-structure calculation [1]. One can see good agreements between experiment and theory. However, Broken lines trace structures that cannot be explained by the bulk-derived Fermi surfaces.

We also measured energy-band dispersions along the  $\Gamma$ X and XW high symmetry lines. The energy band positions at the high symmetry points were found to coincide well with those given by the calculation [1]. We could identify the bulk-derived electronic states unambiguously. Near the  $\bar{M}$  point of the surface Brillouin zone (Fig. 2), on the other hand, we found structures S, S<sub>1</sub> and S<sub>2</sub> which were not predicted by the bulk band-structure calculation (Fig. 3). In order to confirm the origin of the structure, we measured ARPES at  $h\nu=63.9$  eV, 115.2 eV and 135.9 eV. The spectral feature at the  $\bar{M}$  point showed no  $h\nu$  dependence. It clearly indicates that the structure is derived from the surface electronic states.

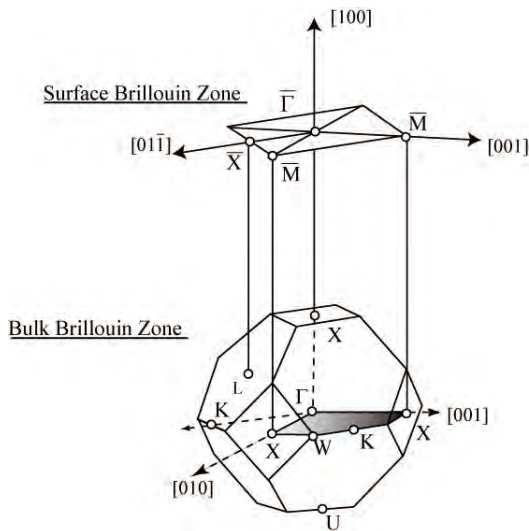


Figure 2. Surface Brillouin zone and bulk Brillouin zone.

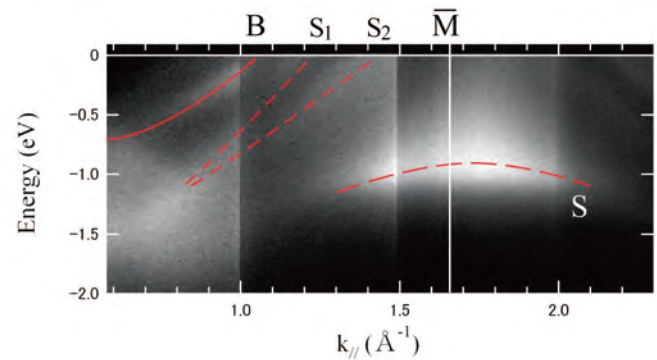


Figure 3. Band dispersion of Rh (100) taken at  $h\nu = 63.9$  eV and at 31K. White portion corresponds to the highest spectral intensity. Solid line (B) shows the bulk-derived band. Broken lines (S, S<sub>1</sub>, S<sub>2</sub>) show the structures that are derived from the surface electronic states.

## Reference

- [1] G.S. Tripathi *et al.*, Phys. Rev. B **38** (1988) 10454.

## High-resolution angle-resolved photoemission spectroscopy of Rh(111)

K. Tanaka<sup>a</sup>, K. Shimada<sup>b</sup>, N. Tobita<sup>a</sup>, S. Fukuda<sup>a</sup>, H. Hayashi<sup>a</sup>,  
J. Jiang<sup>a</sup>, Y. Aiura<sup>c</sup>, H. Namatame<sup>b</sup>, M. Taniguchi<sup>a,b</sup>

<sup>a</sup>*Grad. of Sci. Hiroshima Univ.*

<sup>b</sup>*HSRC, Hiroshima Univ.*

<sup>c</sup>*AIST*

Rhodium is one of the most important and widely used metals as a catalyst cleaning exhaust gas from automobiles. In this study, by means of high-resolution angle-resolved photoemission spectroscopy (ARPES) with tunable synchrotron radiation, we have clarified the Fermi surfaces and the bulk-derived electronic states of Rh(111). By means of quantitative analyses of the ARPES spectra, we have evaluated the coupling parameter of the electron-phonon interaction.

Experiments have been performed on the linear undulator beamline BL-1. By repeated Ar<sup>+</sup> sputtering and high temperature annealing at 1200 K, we obtained clean surface of Rh(111) single crystal. We used a high-resolution hemispherical electron energy analyzer (SCIENZA SES200). The overall energy and momentum resolutions were respectively set at  $\Delta E = 11\text{-}170$  meV and  $\Delta k = 0.011\text{-}0.027$  Å<sup>-1</sup>, depending on the incident photon energy  $h\nu = 21.2\text{-}172.5$  eV.

Figure 1 shows an image plot of the observed Fermi surface located around the L point in the  $\Gamma K X$  plane at the photon energy of  $h\nu = 35.4$  eV and sample temperature of  $T = 20$  K. The black portion indicates strong spectral intensity at  $E_F$ . We examined the energy band along the red line in Fig. 1.

In order to evaluate peak position of the energy band, we fit momentum distribution curves with a Lorentzian. If the electron-phonon coupling

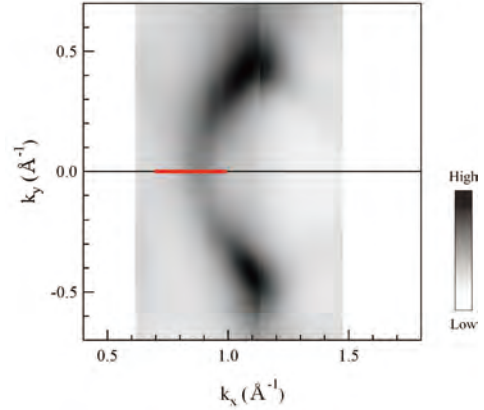


Figure 1. Fermi surface mapping of Rh(111) taken at  $h\nu = 35.4$  eV and  $T = 20$  K.

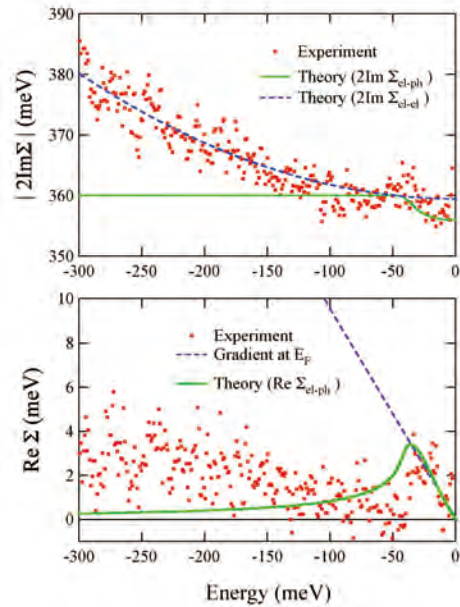


Figure 2. Experimental and theoretical imaginary and real parts of the self-energy.

is strong enough, one can see a kink structure at the energy scale of the Debye temperature ( $k_B\Theta_D$ ) [1]. In the case of Rh, the energy scale is expected to be  $k_B\Theta_D = 41$  meV ( $\Theta_D = 480$  K) [2]. Although the kink structure in the observed energy-band dispersion was very weak, we could discern a kink structure at energy of  $-30 \sim -40$  meV.

Figure 2 shows evaluated real and imaginary parts of the self-energy ( $\Sigma$ ) deduced from the lineshape analyses [2]. We have evaluated a dimensionless coupling parameter of the electron-phonon interaction as  $\lambda = 0.10$ , based on the gradient of  $\text{Re } \Sigma$  at  $E_F$ . On the other hand, by the fit of the lower energy part of  $|2\text{Im } \Sigma|$  with a function  $2\beta\omega^2$ , we obtained  $2\beta = 0.25$  eV<sup>-1</sup> which gives a measure of the electron-electron interaction. The  $2\beta$  value is comparable with that for the Cu  $\Sigma_1$  band ( $2\beta = 0.2$  eV<sup>-1</sup>)[3], but smaller than that for the Ni  $\Sigma_1$  band ( $2\beta = 0.6-1.4$  eV<sup>-1</sup>) [1]. Present results indicate that the effective mass enhancement is negligible for the energy band we examined, confirming that electrons in Rh have itinerant nature.

## References

- [1] M. Higashiguchi, K. Shimada, K. Nishiura, X. Y. Cui, H. Namatame, M. Taniguchi, Phys. Rev. B **72**, 214438 (2005), and references therein.
- [2] C. Kittel, *Introduction to Solid State Physics 8th ed.* (John Wiley & Sons Inc. New York, 2005).
- [3] M. Higashiguchi, Ph.D. thesis, Hiroshima University (March 2008).

## Angle resolved photoemission spectroscopy measurements of VO<sub>2</sub> thin films

K. Saeki<sup>1</sup>, Y. Muraoka<sup>1, 4</sup>, T. Wakita<sup>2</sup>, M. Hirai<sup>1</sup>, T. Yokoya<sup>1, 4</sup>, R. Eguchi<sup>3</sup>,  
S. Shin<sup>3</sup>, K. Shimada<sup>5</sup>

<sup>1</sup>*Graduate School of Nature Science and Technology, Okayama University,*  
<sup>2</sup>*Faculty of Science, Okayama University,* <sup>3</sup>*RIKEN/SPring-8,* <sup>4</sup>*JST-CREST,*  
<sup>5</sup>*Hiroshima Synchrotron Radiation Center, Hiroshima University*

Vanadium dioxide, VO<sub>2</sub>, exhibits a sharp metal-insulator transition (MIT) at 341K, which is a first-order phase transition accompanied by a structural change from a high-temperature rutile-type tetragonal form to a low-temperature monoclinic form. Even though many scientists have tried to clarify the MIT mechanism, it is under debate that this MIT is caused by whether electronic correlation (Mott-Hubberd-type) or electron-lattice interaction (Peierls-type). Angle-resolved photoemission spectroscopy (ARPES) study is important to elucidate the electronic structure of VO<sub>2</sub> which helps to understand the underlying physics of the MIT. However, few ARPES measurements of VO<sub>2</sub> have been carried out because VO<sub>2</sub> single crystals do not have chemically stable cleaved surface and crack easily due to the change of unit cell volume when they undergo the MIT. Recent our work reveals that by using the thin films of VO<sub>2</sub> we have obtained the PES spectra without any difficulties as seen in the case of single crystals. In this work, we perform the ARPES measurements using VO<sub>2</sub> thin films and demonstrate for the first time the energy dispersion of V3*d* band in VO<sub>2</sub>.

We fabricated epitaxial thin films of VO<sub>2</sub> grown on TiO<sub>2</sub> (001) single crystal substrates using a pulsed laser deposition technique. The prepared thin films were found to exhibit a MIT at 300K from resistivity measurements. The ARPES measurements with various photon energy for VO<sub>2</sub> (001) surface was carried out on the beamline BL-1 at Hiroshima synchrotron radiation center (HiSOR) in Hiroshima University.

Fig.1 (a) shows the photon energy dependence of ARPES spectra near  $E_F$  for the VO<sub>2</sub> (001) surface at 350K. Broad peak around binding energy of 0.2eV is attributed to the V3*d* state. We can see that this broad peak moves with photon energy, indicating that the V3*d* band shows the energy dispersion along a  $\Gamma$ -Z direction in the rutile-type tetragonal Brillouin zone. Fig. 1 (b) shows intensity at  $E_F$  plotted against the  $k_{\perp}$  which represents the wave number along the  $\Gamma$ -Z direction. Two sets of peaks labeled A - A' and B - B' are observed, and each set of peaks is symmetrical to  $k_{\perp} = 6.6 \text{ \AA}^{-1}$  ( $\Gamma$ - points. inner potential of 16 meV). This means that these two kinds of V3*d* bands are crossing the Fermi level and form electron pockets in the band structure of the metallic VO<sub>2</sub> thin films.

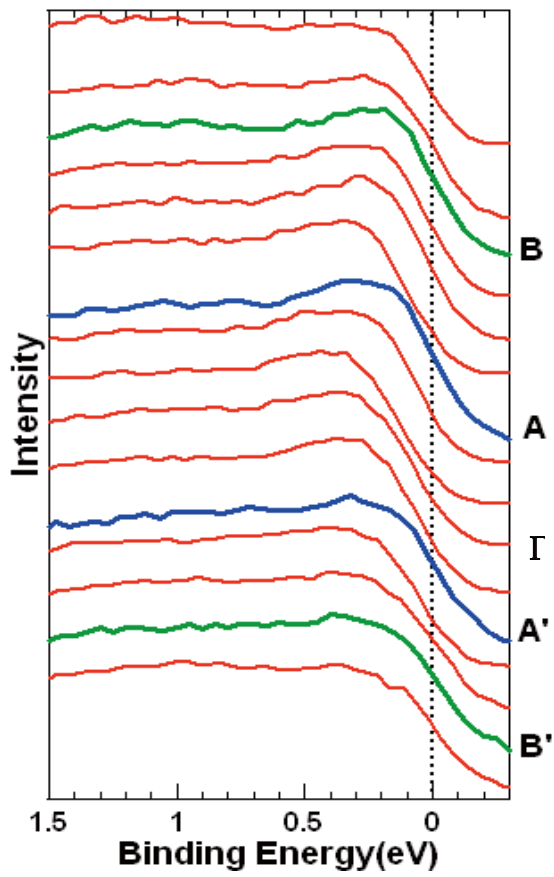
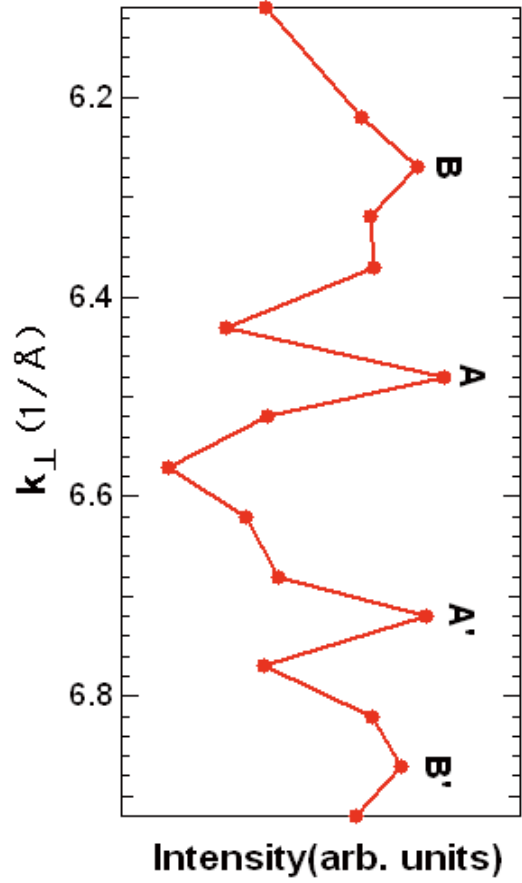


Fig. 1 (a) ARPES spectra near  $E_F$  of (001) surface of  $\text{VO}_2$  thin films measured at 350K. Photon energy of the spectra labeled A,A', B,B' corresponds nearly to the Fermi wave number (see Fig. 1(b)).



(b) Intensity at  $E_F$  as a function of the wave number  $k_{\perp}$  along the  $\Gamma$ -Z direction.

**Carrier-doping effects on Cr-doped perovskite-type titanates  
 $\text{Sr}_{1-(x+y)}\text{La}_{x+y}\text{Ti}_{1-x}\text{Cr}_x\text{O}_3$  studied by photoemission spectroscopy**

H. Iwasawa<sup>a,b</sup>, S. Kaneyoshi<sup>a</sup>, K. Kurahashi<sup>a</sup>, T. Saitoh<sup>a</sup>, T. Katsufuji<sup>c</sup>, Y. Miura<sup>d</sup>, M. Higashiguchi<sup>d</sup>, and K. Shimada<sup>e</sup>, H. Namatame<sup>e</sup>, and M. Taniguchi<sup>d,e</sup>

<sup>a</sup>*Department of Applied Physics, Tokyo University of Science, Shinjuku-ku, Tokyo 162-8601, Japan*

<sup>b</sup>*National Institute of Advanced Industrial Science and Technology, Tsukuba, Ibaraki 305-8568, Japan*

<sup>c</sup>*Department of Physics, Waseda University, Tokyo 169-8555, Japan*

<sup>d</sup>*Graduate School of Science, Hiroshima University, Higashi-Hiroshima 739-8526, Japan*

<sup>e</sup>*Hiroshima Synchrotron Radiation Center, Hiroshima University, Higashi-Hiroshima 739-0046, Japan*

Recent developments on semiconductor devices are directed towards two or more functionalities by utilizing the charge and spin degrees of freedom of electrons. Magnetic semiconductors are one of such devices, called spintronics devices, many of the recent studies on which have been done on oxide semiconductors doped with magnetic ions with very high ferromagnetic transition temperatures ( $T_C$ ), such as  $\text{Ti}_{1-x}\text{Co}_x\text{O}_2$  ( $T_C \sim 400$  K).[1-3] However, it is still unknown why and how the room temperature ferromagnetism appears in spite of the very small amount of transition-metal (TM) doping. In this context, it is necessary to perform a systematic as well as detailed investigation on the electronic structure of a system including local-spins coupled by (itinerant) conduction electrons.

A Cr-doped perovskite-type titanate  $\text{Sr}_{1-(x+y)}\text{La}_{x+y}\text{Ti}_{1-x}\text{Cr}_x\text{O}_3$  is suitable to perform such a systematic study. Starting from the  $d^0$  band insulator  $\text{SrTiO}_3$ , we can control the electric and magnetic properties independently by two TM elements Ti and Cr. Carrier doping can be realized by  $\text{La}^{3+}$  substitution for  $\text{Sr}^{2+}$ , which introduces electrons ( $y$ ) into Ti  $3d$  conduction band. A further manipulation of the resulting  $\text{Sr}_{1-y}\text{La}_y\text{TiO}_3$  is to introduce  $\text{Cr}^{3+}$  by replacing  $\text{SrTiO}_3$  with  $\text{LaCrO}_3$  by the amount of  $x$ . Because  $\text{Cr}^{3+}$  ( $3d^3$ ) ions are usually magnetic in oxides, the above substitution of  $\text{Cr}^{3+}$  for  $\text{Ti}^{4+}$  would realize a “spin doping” of  $S=3/2$  local moment at the Ti sites. According to the previous magnetic and transport measurements,  $x$  and  $y$  actually represent the spin and carrier concentration, respectively.[4] Our recent photoemission study also found that the spectral weight of the Cr  $3d$  state is completely proportional to  $x$  irrespective of  $y$ . However, the near Fermi-level ( $E_F$ ) spectral weight due to the Ti  $3d$  states can not be controlled solely by  $y$ . [5] In this report, we investigate the  $y$ -dependence of the electronic structure of this system in detail using high-resolution photoemission spectroscopy, to examine how independently we can control the charge and spin degrees of freedom.

Polycrystalline samples of  $\text{Sr}_{1-(x+y)}\text{La}_{x+y}\text{Ti}_{1-x}\text{Cr}_x\text{O}_3$  were prepared by solid-state reaction. To identify the  $y$ -dependence of this system, we fixed the spin concentration at  $x=0.2$ , and varied  $y$  from 0.05 to 0.2. Photoemission measurements were done at BL-1 of Hiroshima Synchrotron Radiation Center (HSRC). The beamline is equipped with a high-resolution, hemispherical electron analyzer (SCIENIA ESCA200). The clean surface of the samples was obtained by fracturing *in situ* in ultrahigh vacuum (better than  $1 \times 10^{-10}$  Torr) at 50 K. All the spectra were taken with the photon energy of 150 eV at 50 K, being the overall experimental

energy resolution better than 40 meV, which was confirmed by Fermi edge spectra of evaporated Au. The backgrounds due to the unscattered electrons were removed from all the spectra.

Figure 1 (a) shows the valence-band photoemission spectra of  $\text{Sr}_{0.8-y}\text{La}_{0.2+y}\text{Ti}_{0.8}\text{Cr}_{0.2}\text{O}_3$  for several carrier concentrations. The four spectral features can be clearly observed as denoted  $A$  to  $D$ , consistent with our previous study.[5] From the Ti  $3p-3d$  and Cr  $3p-3d$  resonant photoemission measurements, the leading feature  $A$  (-0.7 eV) and the subsequent feature  $B$  (-2.7 eV) can be assigned to the Ti  $3d$  and Cr  $3d$  states, respectively.[5] The following features  $C$  (-5.1 eV) and  $D$  (-6.9 eV) are the O  $2p$  non-bonding band and Ti and Cr  $3d-O$   $2p$  bonding bands, respectively.

Figures 1 (b) and (c) demonstrate the carrier-dependence ( $y$ -dependence) of the features  $B$  and  $A$ , where an integrated intensity of the features  $B$  and  $A$  are plotted as functions of  $y$ . The integration windows are from -3.5 to -2.0 eV ( $B$ ) and from -0.4 to 0.1 eV ( $A$ ). As is seen in Fig. 1 (b) and (c), the Cr  $3d$  states have an almost constant intensity for all  $y$ , whereas the coherent spectral weight of the Ti  $3d$  states shows a proportional relationship to  $y$ . It is, therefore, the carrier density can be controlled by  $y$  when  $x$  is fixed, which is in perfect agreement with the electrical resistivity data.

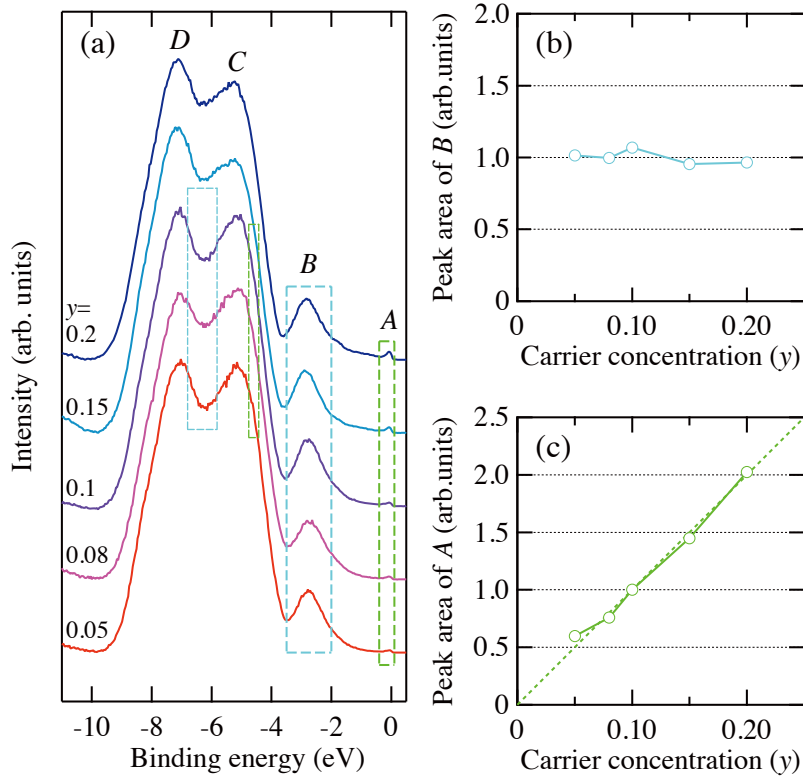


FIG. 1 (a)  $y$ -dependence of valence-band photoemission spectra of  $\text{Sr}_{0.8-y}\text{La}_{0.2+y}\text{Ti}_{0.8}\text{Cr}_{0.2}\text{O}_3$  taken with 150 eV at 50 K. (b) and (c) Integrated intensity of the features  $B$  and  $A$  as functions of  $y$ , respectively. The intensity is normalized by the averaged intensity of  $B$  [Fig. 1 (b)] and the intensity at (0.2, 0.1) [Fig. 1 (c)]. Each integration window is shown by dotted rectangles.

In conclusion, we have investigated the detailed  $y$ -dependence of the electronic structure of  $\text{Sr}_{1-(x+y)}\text{La}_{x+y}\text{Ti}_{1-x}\text{Cr}_x\text{O}_3$  by high-resolution photoemission spectroscopy. We found that the Cr  $3d$  peak intensity were not affected by changing  $y$ , and the near- $E_F$  intensity composed of the

Ti  $3d$  states showed a very proportional relationship with  $y$  at a fixed  $x$ , demonstrating that the carrier-density control is realized on the condition that  $x$  is fixed.

This work was partly supported by a Grant-in-Aid for COE Research (13CE2002) by MExT of Japan, and also was performed under the Cooperative Research Program of HiSOR, Hiroshima Synchrotron Radiation Center, Hiroshima University. (Accept No. 06-A-39 and 07-A-18).

## References

- [1] S. A. Wolf *et al.*, *Science* **294**, 1488 (2001).
- [2] J. W. Quilty *et al.*, *Phys. Rev. Lett.* **96**, 027202 (2006).
- [3] K. Mamiya *et al.*, *Appl. Phys. Lett.* **89**, 062506 (2006).
- [4] J. Inaba and T. Katsufuji, *Phys. Rev. B* **72**, 052408 (2005).
- [5] H. Iwasawa *et al.*, *Phys. Rev. Lett.* **96**, 067203 (2006).

## ARPES study of Fermi surface of T\*-phase high- $T_c$ cuprate $\text{SmLa}_{0.8}\text{Sr}_{0.2}\text{CuO}_4$

Y. Nakashima<sup>a</sup>, H. Anzai<sup>a</sup>, T. Fujita<sup>a</sup>, A. Ino<sup>a</sup>, M. Higashiguchi<sup>a</sup>, N. Tobita<sup>a</sup>, J. Jiang<sup>a</sup>,  
K. Tanaka<sup>a</sup>, S. Fukuda<sup>a</sup>, K. Shimada<sup>b</sup>, M. Arita<sup>b</sup>, H. Namatame<sup>b</sup>, M. Taniguchi<sup>a,b</sup>,  
T. Kakeshita<sup>c</sup>, S. Adachi<sup>d</sup>, S. Tajima<sup>d,e</sup>

<sup>a</sup>Graduate School of Science, Hiroshima University

<sup>b</sup>Hiroshima Synchrotron Radiation Center, Hiroshima University

<sup>c</sup>National Institute for Materials Science

<sup>d</sup>Superconductivity Research Laboratory of the International Superconductivity Technology Center

<sup>e</sup>Department of Physics, Osaka University

Two-dimensional  $\text{CuO}_2$  planes are widely considered as the stage of high- $T_c$  superconductivity in cuprates. However, the effect of apical oxygens adjacent to the  $\text{CuO}_2$  plane has also been discussed for long. Here,  $\text{SmLa}_{1-x}\text{Sr}_x\text{CuO}_4$  crystallizes in a unique structure called T\*-phase, where the apical oxygen is located only on one side of the single  $\text{CuO}_2$  plane, but the low-energy electronic structure of  $\text{SmLa}_{1-x}\text{Sr}_x\text{CuO}_4$  has still been unclear. In order to clarify the effect of the apical oxygens, we performed an high-resolution angle-resolved photoemission spectroscopy and determined the Fermi surface and pseudogap structure of T\*-phase  $\text{SmLa}_{1-x}\text{Sr}_x\text{CuO}_4$  system.

Figure 1 shows the result of Fermi-surface mapping for the sample of relatively high Sr-substitution  $x = 0.20$  and of  $T_c = 20$  K. The momentum-space distribution has been obtained by integrating the photoemission spectral intensity in an energy range of  $0 > \omega > -20$  meV. In the nodal direction along  $(0,0)$ - $(\pi,\pi)$  line, the band dispersion crossing Fermi level has clearly been observed. In the antinodal region around  $(\pi,0)$ , the spectral peak is appreciably broadened and shifted in energy away from Fermi level, and the leading-edge midpoint of the spectral feature is lower than  $-30$  meV. These observations indicate the formation of a pseudogap in the antinodal region, and thus that Fermi surface is not closed as so-called ‘‘Fermi arc’’ even at the high Sr-substitution level of  $x = 0.20$ . The result of  $\text{SmLa}_{0.8}\text{Sr}_{0.2}\text{CuO}_4$  is in sharp contrast to that of overdoped  $\text{La}_{1.8}\text{Sr}_{0.2}\text{CuO}_4$ , suggesting that the pseudogap formation is affected by the apical site.

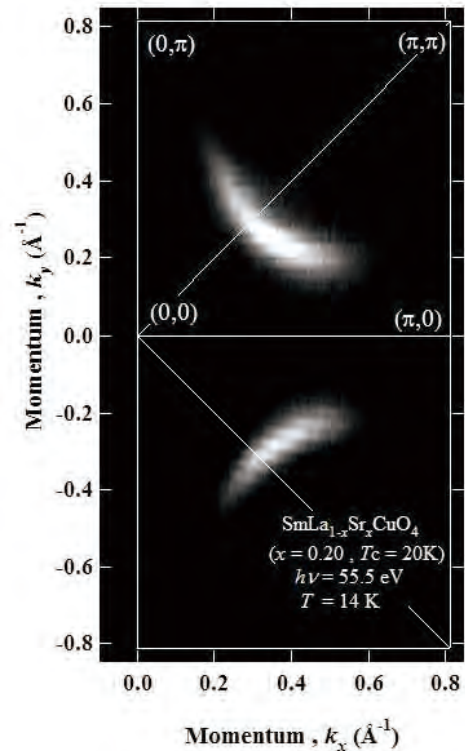


Fig. 1 Fermi-surface mapping of  $\text{SmLa}_{0.8}\text{Sr}_{0.2}\text{CuO}_4$  ( $T_c = 20$  K).

## Annealing effect on the chemical structure of diamondlike carbon (DLC) by C 1s photoelectron spectroscopy

Susumu Takabayashi<sup>a</sup>, Kenya Shimada<sup>b</sup>, Keishi Okamoto<sup>a,c</sup>, Tatsuyuki Nakatani<sup>c</sup>,  
Hiroyuki Sakaue<sup>a</sup>, and Takayuki Takahagi<sup>a</sup>

<sup>a</sup>*Graduate School of Advanced Sciences of Matter (AdSM), Hiroshima University*

<sup>b</sup>*Hiroshima Synchrotron Radiation Center (HSRC), Hiroshima University*

<sup>c</sup>*Toyo Advanced Technologies Co., Ltd., 5-3-38 Ujina-Higashi, Minami-ku,  
Hiroshima 734-8501, Japan*

Diamond-like carbon (DLC) is an amorphous carbonaceous material, which is composed of  $sp^2$  carbon,  $sp^3$  carbon, and hydrogen.<sup>1</sup> So far, the analysis varies by authors. Recently, we have analyzed a DLC film prepared by the ionized deposition method with benzene gas by angle-resolved C 1s XPS with the Doniach-Šunjić function.<sup>2</sup> Sequentially we analyzed other DLC films with different electrical resistivities prepared by the unbalanced magnetron sputtering (UBMS) method with using the same procedures<sup>3</sup>, and concluded that the C 1s spectrum for DLC is divided into four curves for, in the order of the binding energy,  $sp^3$  carbon in the carbon-carbon bonds (C-C  $sp^3$ , 283.8 eV),  $sp^2$  carbon in the carbon-carbon bonds (C-C  $sp^2$ , 284.3 eV),  $sp^2$  carbon in the hydrogen-carbon bonds (H-C  $sp^2$ , 284.8 eV), and  $sp^3$  carbon in the hydrogen-carbon bonds (H-C  $sp^3$ , 285.3 eV).

The characteristics of DLC are subject to vary by heat treatment. In this report, we analyzed the influence of heat on the characteristics of DLC by C 1s photoelectron spectroscopy.

All experiments were performed at BL-1. The DLC films were prepared by the ionized deposition method with benzene gas. Before the photoelectron measurements, the films were annealed in UHV at fixed temperatures for 30 min. The photoelectron measurements were conducted with the incident energy of 408 eV, and the total resolution of 0.22 eV. The binding energy was calibrated by the Au  $4f_{7/2}$  spectrum of a clean Au (110) single crystal.

Figure 1 shows the C 1s spectra of the DLC films after annealing. The spectrum of a clean kish graphite was also shown. The C 1s spectrum of the DLC film shifted a little positively in binding energy with increasing the

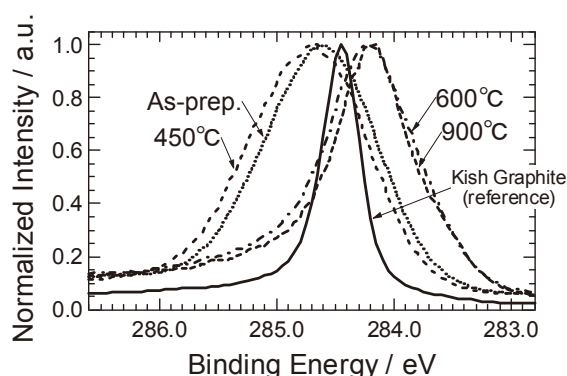


Fig. 1 C 1s photoelectron spectra of the DLC films after annealing in UHV at different temperatures.

annealing temperature until 450°C. However, at 600°C, the spectrum drastically negative-shifted and showed a different lineshape. Over 600°C, the spectrum was almost no shifted, but the FWHM decreased.

Figure 2 shows the C 1s spectra with the fitting-curves analyzed by the Doniach-Šunjić function according to the procedures in our previous report.<sup>2,3</sup> Figure 3 shows the fraction intensities of the components as a function of temperature. These results demonstrate that the H-C components are decreased suddenly during 450-600°C. Thus in this region, hydrogen (or CH<sub>x</sub> species) in the DLC film are emitted to the outside. Over 600°C, the C-C *sp*<sup>2</sup> component is enhanced gradually. thus in this region, the graphitization proceeds.

We concluded that the variation of DLC by heat treatment in UHV is analyzed by its C 1s photoelectron analysis with considering the difference between H-C and C-C bonds.

The authors gratefully acknowledge Mr. Yuichi Miura, Dr. Mitsuharu Higashiguchi, and Dr. Naohisa Tobita, Graduate School of Science, Hiroshima University for kindly support.

## References

- <sup>1</sup> J. Robertson, Mater. Sci. Eng., R **37**, 129 (2002).
- <sup>2</sup> S. Takabayashi, K. Motomitsu, T. Takahagi, A. Terayama, K. Okamoto, and T. Nakatani, J. Appl. Phys. **101**, 103542 (2007).
- <sup>3</sup> S. Takabayashi, K. Okamoto, K. Shimada, K. Motomitsu, H. Motoyama, T. Nakatani, H. Sakaue, H. Suzuki, and T. Takahagi, Jpn. J. Appl. Phys. **47**, 3376 (2008).

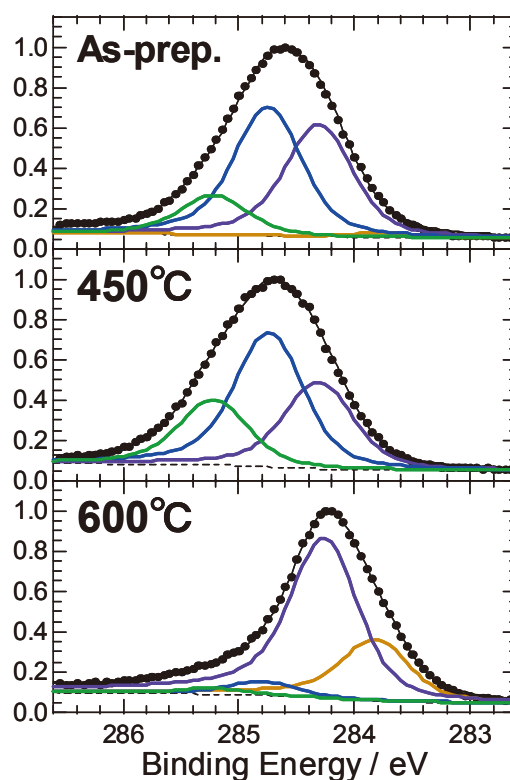


Fig. 2 C 1s photoelectron spectra of the DLC films with fitting-curves for the components after the UHV-annealing at different temperatures.

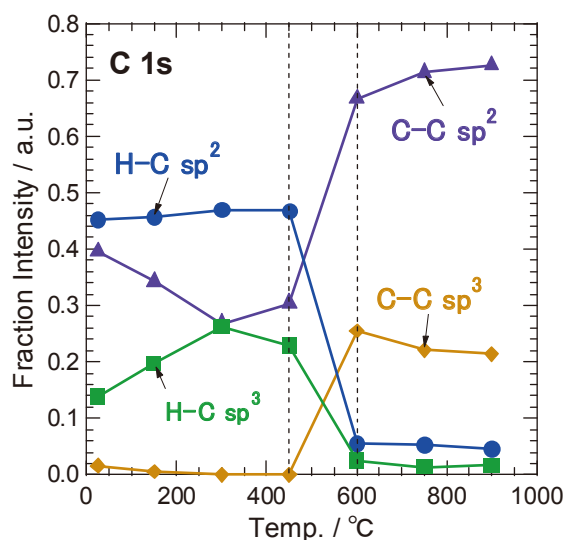


Fig. 3 Correlation between the fraction intensities of the components of the C 1s spectra of the DLC films and the annealed temperature.

## NEXAFS, XPS and AFM studies of Rh deposited on Al<sub>2</sub>O<sub>3</sub> thin film/NiAl(100)

T. Nomoto<sup>a</sup>, S. Yagi<sup>a</sup>, K. Soda<sup>a</sup>, H. Namatame<sup>b</sup> and M. Taniguchi<sup>b</sup>

<sup>a</sup>*Department of Quantum Engineering, School of Engineering, Nagoya University; Chikusa-ku, Nagoya, 464-8603 Japan*

<sup>b</sup>*Synchrotron Radiation Center, Hiroshima University; 2-313 Kagamiyama, Higashi-Hiroshima, 739-8526 Japan*

### 1. Introduction

In the field of automotive catalyst, the nano-particles of platinum group metals are supported on Al<sub>2</sub>O<sub>3</sub>. These catalysts play an important role in the reduction of NO<sub>x</sub> and the oxidation of CO. Those performances are frequently degraded by some deactivation factors because of the use in the severe environment. The high temperature causes a diffuse of catalyst metals and it leads to an aggregation of metals or dissolution into support materials [1, 2]. Therefore, it is important to understand the thermal change in the chemical state and the morphology of the catalyst surface.

The aim of this work is to investigate the structural and chemical changes of Rh on Al<sub>2</sub>O<sub>3</sub>/NiAl(100) depending upon heat treatment by means of Near Edge X-ray Absorption Fine Structure (NEXAFS), X-ray Photoelectron Spectroscopy (XPS) and Atomic Force Microscopy (AFM) techniques.

### 2. Experimental

A well-ordered ultrathin Al<sub>2</sub>O<sub>3</sub> layer was grown on exposing the cleaned NiAl(100) to O<sub>2</sub> (~1000 L) at 500 K and subsequently annealing at 1000 K for 5 min [3]. 1.0 ML of rhodium was deposited on the Al<sub>2</sub>O<sub>3</sub> thin layer at room temperature. After deposition, the sample was heated at 600 K or 1000 K for 5 min. Four types of samples were prepared in this work, which were Al<sub>2</sub>O<sub>3</sub>/NiAl(100), Rh/Al<sub>2</sub>O<sub>3</sub>/NiAl(100) as Rh deposited, Rh/Al<sub>2</sub>O<sub>3</sub>/NiAl(100) heated at 600 K or 1000 K. The AFM images of each surface were measured by NanoScope III-a (Veeco Instruments). The XPS measurements were recorded by use of the concentric hemispherical electron energy analyzer (PHOIBOS 100-5ch, SPECS) with MgK $\alpha$  X-ray (1253.6 eV). The NEXAFS spectra were recorded at the soft X-ray double crystal monochromator beamline BL-3.

### 3. Results and Discussion

#### 3. 1. Surface morphology

Figures 1(a)-(d) show the obtained AFM images. A lot of stripe structures are observed on the Al<sub>2</sub>O<sub>3</sub>/NiAl(100) surface in Figure 1-(a). These structures are thought to grow preferentially

along the crystal directions. The stripes disappear when the surface covered with Rh layer. The deposited Rh on  $\text{Al}_2\text{O}_3/\text{NiAl}(100)$  forms a protruded structures with the height of 0.3-0.7 nm. Thereby, it can be speculated that nanoclusters with 1-3 Rh layers formed on the  $\text{Al}_2\text{O}_3/\text{NiAl}(100)$  surface. These structures become higher and spherical shape after the heat-treatment at 600 K. This means the aggregation of Rh atoms on the  $\text{Al}_2\text{O}_3$  layer caused by the thermal migration. After heating at 1000 K, the surface morphology drastically changes into the surface with a lot of nano-hole structures as shown in Figure 1-(d). With NEXAFS and XPS results, this outmost surface seems to be composed with the  $\text{Al}_2\text{O}_3$  layer

## 2. 2. Chemical change in Rh/ $\text{Al}_2\text{O}_3/\text{NiAl}(100)$

Figure 2 shows the Rh  $3d_{5/2}$  peaks (with deconvolution results) for the Rh/ $\text{Al}_2\text{O}_3/\text{NiAl}(100)$  systems. Rh on  $\text{Al}_2\text{O}_3/\text{NiAl}(100)$  has two chemical states after the deposition at room temperature. The lower binding energy peak (307.2 eV) is assigned to the Rh atom in second layer or more, because the peak position corresponds to that of the metallic Rh such as Rh(111) bulk [4]. The second peak locating at 307.7 eV shifts from the metallic Rh state to the higher energy side, indicating the first layer Rh atoms on the  $\text{Al}_2\text{O}_3$  layer which interact with each other. In contrast, the peak shape of the Rh/ $\text{Al}_2\text{O}_3/\text{NiAl}(100)$  heated at 1000 K can be described with a single state at 307.4 eV. The state extremely stabilizes against various treatments, such as the DMS adsorption, the heating and the  $\text{O}_2$  exposure. These integral intensities decay in comparison with that of the Rh as-deposited sample. Therefore, we can speculate the dissolution of Rh atom into the substrate.

Figure 3 shows the Rh 3d XPS spectra for the Rh/ $\text{Al}_2\text{O}_3/\text{NiAl}(100)$  systems after different thermal treatments. In order to compare these peak shapes, the main peak positions are matched each other. The area colored with green signifies the difference between each spectrum and that of bulk Rh. One can find that the peak width of as-deposited surface becomes broader than that of bulk Rh. Therefore, Rh atoms seem to form clusters with at least two layers on  $\text{Al}_2\text{O}_3/\text{NiAl}(100)$  surface. The peak width becomes narrower when the sample is heated at 600 K. Then the spectral shape is considerably corresponding to that of bulk Rh. This change indicates the aggregation of Rh atoms on the  $\text{Al}_2\text{O}_3$  layer. In contrast to the former two spectra, the spectrum of the Rh/ $\text{Al}_2\text{O}_3/\text{NiAl}(100)$  heated at 1000 K can be seen with a sharper and symmetric peak shape. Furthermore, the peak undergoes a higher shift in comparison with bulk Rh, and the satellite structure locating at higher binding energy side disappears. Similar change in a XPS spectral shape was observed on nickel aluminides [5]. They have reported that the positive shifts of Ni  $2p_{3/2}$  energy level increases, the satellite structure disappears, and further, the peak shape of Ni  $2p_{3/2}$  becomes symmetric with the decrease of nickel concentration in the alloys. Such changes can be well understood with the charge-transfer satellite. Therefore, the Rh atoms are likely to form the alloy like state at 1000 K. Then, we can confirm that the Rh atoms dissolve into the  $\text{NiAl}(100)$  substrate through the  $\text{Al}_2\text{O}_3$  layer, occurred by the heat-treatment at 1000 K.

Rh L<sub>3</sub>-edge NEXAFS are shown in Figure 4. The spectral shape, such as the peak height and the width, is quite similar between the bulk Rh and the Rh/Al<sub>2</sub>O<sub>3</sub>/NiAl(100) heat-treated at 1000 K. Thus, one can also verify the aggregation of Rh atoms at 600 K by Rh L<sub>3</sub>-edge NEXAFS analysis. When the sample is heated at 1000 K, the peak intensity of the main peak at 3007.0 eV decrease, and another structure appears at the higher energy side. We can speculate that the new structure shows the bonds between Rh-Al or Rh-Ni. These Rh atoms are assumed to exist as single atom and/or small cluster, because the spectrum has two peaks assigned to alloy and metallic states. The schematic model for the Rh state on Al<sub>2</sub>O<sub>3</sub>/NiAl(100) with elevated temperatures is shown in Figure 5.

## References

- [1] K. Dohmae Y. Hirose, M. Kimura, *TOYOTA Central Laboratory R&D review*. **32**, 75 (1997).  
 [2] T. Nomoto, S. Yagi, K. Soda, H. Namatame, M. Taniguchi, submitted to *e-J. Surf. Sci. Nanotech*.  
 [3] M. Ozawa, M. Kimura, H. Sobukawa, K. Yokota, *TOYOTA Central Laboratory R&D review*. **27**, 43 (1992).  
 [3] M. S. Zei, C. S. Lin, W. H. Wen, C. I. Chiang, M. F. Luo, *Surf. Sci.* **600**, 1942 (2006).  
 [4] T. L. Barr, *J. Phys. Chem.* **82**, 1801 (1978).  
 [5] N. Ohtsu, M. Oku, T. Shishido, K. Wagatsuma, *Appl. Surf. Sci.* **253**, 8713 (2007).

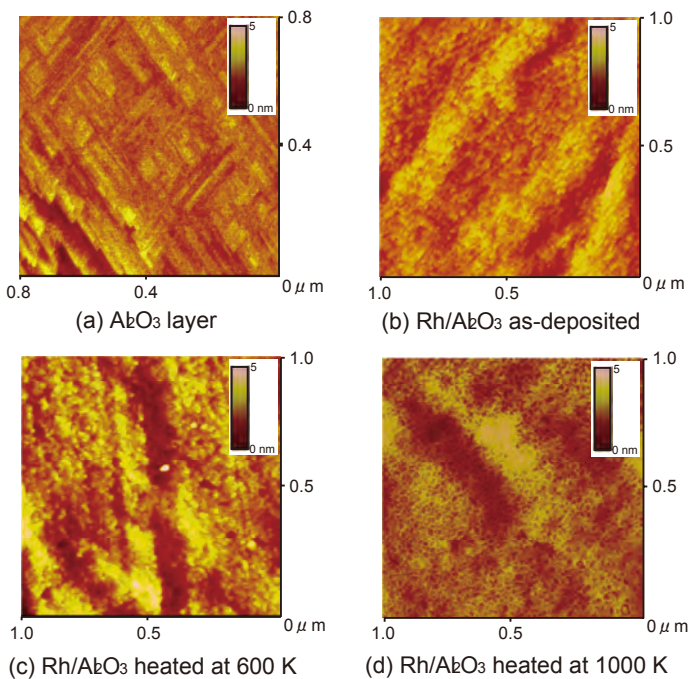


Figure 1. AFM images for the surfaces of (a) Al<sub>2</sub>O<sub>3</sub>/NiAl(100), (b) Rh/Al<sub>2</sub>O<sub>3</sub>/NiAl(100) as-deposited, (c) Rh/Al<sub>2</sub>O<sub>3</sub>/NiAl(100) heated at 600 K, and (d) Rh/Al<sub>2</sub>O<sub>3</sub>/NiAl(100) heated at 1000 K.

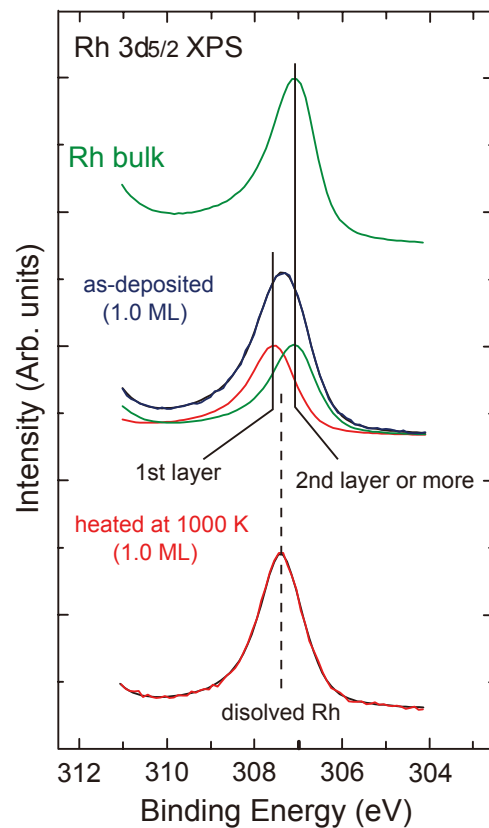


Figure 2. Thermal dependence of Rh 3d<sub>5/2</sub> XPS spectra for Rh/Al<sub>2</sub>O<sub>3</sub>/NiAl(100) as-deposited, and Rh/Al<sub>2</sub>O<sub>3</sub>/NiAl(100) heated at 1000 K surfaces.

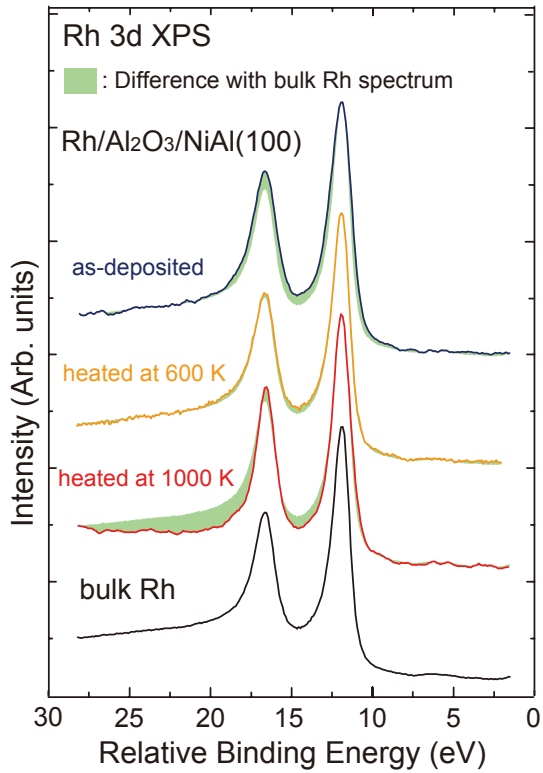


Figure 3. Rh 3d XPS spectra for the Rh/Al<sub>2</sub>O<sub>3</sub>/NiAl(100) systems after different thermal treatments. The main peak positions are matched each other, and the area colored with green signifies the difference between each spectrum and that of bulk Rh.

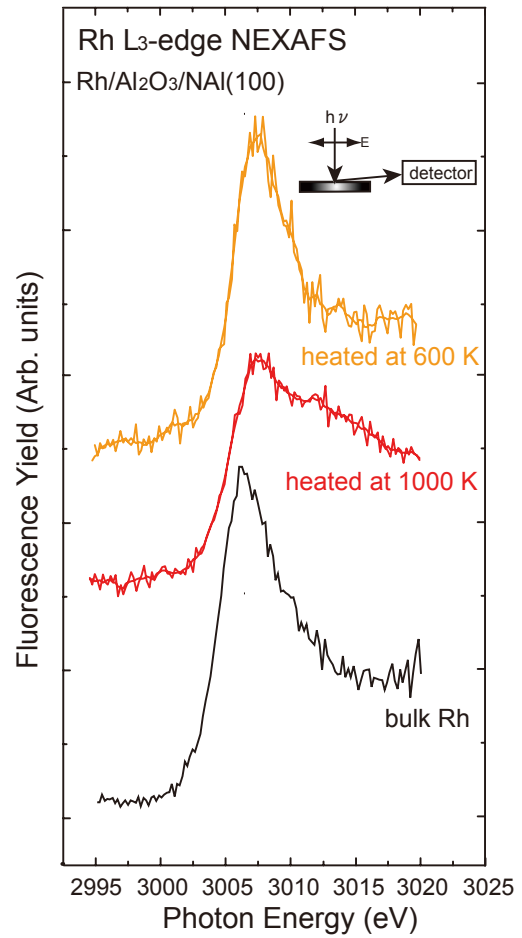


Figure 4. Rh L<sub>3</sub>-edge NEXAFS spectra for the bulk Rh and the Rh/Al<sub>2</sub>O<sub>3</sub>/NiAl(100) systems after heat-treatment at 600 K or 1000 K.

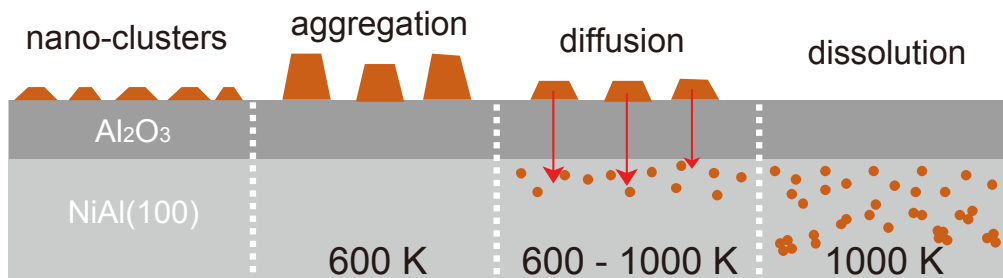


Figure 5. Schematic model for the Rh chemical states on Al<sub>2</sub>O<sub>3</sub>/NiAl(100) with elevated temperatures.

## Adsorption and oxidation reaction of sulfur on Rh/Al<sub>2</sub>O<sub>3</sub>/NiAl(100) studied by XPS and NEXAFS

T. Nomoto<sup>a</sup>, S. Yagi<sup>a</sup>, K. Soda<sup>a</sup>, H. Namatame<sup>b</sup> and M. Taniguchi<sup>b</sup>

<sup>a</sup>*Department of Quantum Engineering, School of Engineering, Nagoya University; Chikusa-ku, Nagoya, 464-8603 Japan*

<sup>b</sup>*Synchrotron Radiation Center, Hiroshima University; 2-313 Kagamiyama, Higashi-Hiroshima, 739-8526 Japan*

### 1. Introduction

Platinum group metals supported on oxides, such as Al<sub>2</sub>O<sub>3</sub>, CeO<sub>2</sub> and ZrO<sub>2</sub>, are widely used as the typical catalysts in the purification process of the automobile exhaust gas. For example, Rh/Al<sub>2</sub>O<sub>3</sub> catalyst is noticeable in the reduction of NO<sub>x</sub>. Those performances are frequently degraded by some deactivation factors because of the use in the severe environment. Especially, the poisoning of catalyst surface is regarded as the main problems [1]. The residual sulfur in fuel causes a sulfur adsorption on the catalyst surface, so-called “Sulfur-Poisoning” [2]. In order to remove such sulfur contaminations, the oxidation reaction of sulfur on the catalyst surface is of great interest in the field of an automotive catalyst.

The aim of this work is to reveal the oxidation reaction of atomic sulfur on Rh/Al<sub>2</sub>O<sub>3</sub>/NiAl(100) surface by means of Near Edge X-ray Absorption Fine Structure (NEXAFS), X-ray Photoelectron Spectroscopy (XPS) and Atomic Force Microscopy (AFM) techniques.

### 2. Experimental

A well-ordered ultrathin Al<sub>2</sub>O<sub>3</sub> layer was grown on exposing the cleaned NiAl(100) to O<sub>2</sub> (~1000 L) at 500 K and subsequently annealing at 1000 K for 5 min [3]. 1.0 ML of rhodium was deposited on the Al<sub>2</sub>O<sub>3</sub> thin layer at room temperature. After deposition, the sample was heated at 1000 K for 5 min. Three types of samples were prepared in this work, which were Al<sub>2</sub>O<sub>3</sub>/NiAl(100), Rh/Al<sub>2</sub>O<sub>3</sub>/NiAl(100) as Rh deposited, Rh/Al<sub>2</sub>O<sub>3</sub>/NiAl(100) heated at 1000 K. (CH<sub>3</sub>)<sub>2</sub>S : DMS gas was admitted via the variable leak valve into the UHV chamber as the sample was cooled down to 90 K. The atomic sulfur was obtained by the adsorption of DMS, and subsequently the thermal dissociation with annealing up to 300 K. The sulfur oxidation reaction was promoted under O<sub>2</sub> environment (2.7×10<sup>-5</sup> Pa for 1h) at 523 K or in air (for 3 days, at 300 K). The XPS measurements were recorded by use of the concentric hemispherical electron energy analyzer (PHOIBOS 100-5ch, SPECS) with MgK $\alpha$  X-ray (1253.6 eV). The NEXAFS spectra were recorded at the soft X-ray double crystal monochromator beamline BL-3.

### 3. Results and Discussion

#### 3. 1. Adsorption reaction of DMS on Rh/Al<sub>2</sub>O<sub>3</sub>/NiAl(100)

Figure 1 shows the temperature dependent S 2p XPS spectra for DMS on Rh(1.0 ML)/Al<sub>2</sub>O<sub>3</sub>/NiAl(100) as-deposited, Rh(1.0 ML)/Al<sub>2</sub>O<sub>3</sub>/NiAl(100) heated at 1000 K, and Al<sub>2</sub>O<sub>3</sub>/NiAl(100) surfaces. On the Al<sub>2</sub>O<sub>3</sub>/NiAl(100) surface, most of DMS adsorb on Al<sub>2</sub>O<sub>3</sub> layer without dissociation into CH<sub>3</sub>S- and atomic S at 90 K. It is found that the sulfur in DMS has an interaction with the substrate and is picked some electrons up by the Al<sub>2</sub>O<sub>3</sub> layer, because the main peak position located at 164.3 eV undergoes a higher energy shift from that of the multilayer DMS at 163.8 eV [4]. Almost all of the adsorbates desorb from the Al<sub>2</sub>O<sub>3</sub>/NiAl(100) surface at 200 K, indicating no catalytic performance for DMS dissociative reaction. Dissociation of DMS also hardly occurs on the Rh/Al<sub>2</sub>O<sub>3</sub>/NiAl(100) as-deposited surface at 90 K. More than half the molecules (0.18 ML) remain on the surface at 200 K without desorption. Some of those molecules undergo the scission in the S-C bonds. The dissociation is promoted as the temperature rises, and most of the S-C bonds are cleaved at 300 K. Thus the Rh over-layer possesses a catalytic performance for the dissociative reaction of DMS. In the case of the Rh/Al<sub>2</sub>O<sub>3</sub>/NiAl(100) heated at 1000 K, the dissociative reaction and the desorption behavior are quite equivalent to that on the Al<sub>2</sub>O<sub>3</sub>/NiAl(100) surface, meaning inert against the dissociation process of DMS.

The sulfur-poisoned Rh/Al<sub>2</sub>O<sub>3</sub>/NiAl(100) as-deposited surface was heated under O<sub>2</sub> environment to remove the sulfur atoms. The main peak is located at 162.0 eV showing the adsorption of the atomic sulfur. One can find the broad peak at 166 eV to 169 eV, when the sample is annealed at 423 K and 473 K. This chemical state is assigned to SO<sub>x</sub> species [1]. The broad peak disappears at 523 K, and simultaneously the total coverage of sulfur decreases. Those changes indicate the oxidation of sulfur and the desorption of SO<sub>x</sub> from the Rh/Al<sub>2</sub>O<sub>3</sub>/NiAl(100) as-deposited surface. The desorption onset temperature is higher than that reported with polycrystalline Rh and Rh(100) surfaces, on which the sulfur atoms desorb at 423 K [1, 5]. Therefore, the performance of Rh in the sulfur removal reaction is weakened on the Al<sub>2</sub>O<sub>3</sub> layer.

#### 3. 3. Oxidation of sulfur on Rh/Al<sub>2</sub>O<sub>3</sub>/NiAl(100)

Figure 2 shows the S 2p XPS spectra for atomic sulfur on Rh/Al<sub>2</sub>O<sub>3</sub>/NiAl(100) as-deposited surface, which were measured after O<sub>2</sub> treatment at 523 K and after exposing to air. The initial coverage of atomic sulfur is estimated to be about 0.1 ML. The S 2p XPS feature of S/Rh(100) shows a single state of atomic sulfur. In previous study [6], we have revealed the desorption of atomic sulfur from the Rh/Al<sub>2</sub>O<sub>3</sub>/NiAl(100) surface caused by oxidation ( $2.7 \times 10^{-5}$  Pa of O<sub>2</sub> at 523 K). However, most of the atomic sulfur is not oxidized and remains on the surface. Therefore, a similar feature to S/Rh(100) is obtained for the sulfur on

Rh/Al<sub>2</sub>O<sub>3</sub>/NiAl(100) after O<sub>2</sub> treatment. After the exposure to air, the intensity of the main peak at 162 eV decreases and a broad peak appears from 165 eV to 171 eV. These chemical states are assigned to atomic S and SO<sub>x</sub> species (x = 1-4) [1]. The Sulfur K-edge NEXAFS spectrum for this sample, shown in Figure 3, also has both peaks for the atomic sulfur at 2470.7 eV and the oxidized sulfur state at 2479.1 eV. The chemical state of the oxidized sulfur atom on the Rh/Al<sub>2</sub>O<sub>3</sub>/NiAl(100) can be assigned to SO<sub>2</sub> or SO<sub>3</sub>, because the peak lies at the middle position between SO and SO<sub>4</sub> states. Noticeable oxidation of the atomic sulfur occurs under atmospheric environment even at 300 K. From these results, it is found that not only the reaction temperature but also the degree of the O<sub>2</sub> partial pressure significantly affects the oxidation reaction of the atomic sulfur on the Rh/Al<sub>2</sub>O<sub>3</sub>/NiAl(100) surface. This oxidation reaction is important in the removal reaction of sulfur from catalyst surfaces, because it is known that such sulfur contaminations desorb from catalyst surfaces as SO<sub>2</sub>.

## References

- [1] K. Dohmae, *TOYOTA Central Laboratory R&D review*. **35**, 43 (2000).
- [2] M. Ozawa, M. Kimura, H. Sobukawa, K. Yokota, *TOYOTA Central Laboratory R&D review*. **27**, 43 (1992).
- [3] M. S. Zei, C. S. Lin, W. H. Wen, C. I. Chiang, M. F. Luo, *Surf. Sci.* **600**, 1942 (2006).
- [4] T. Nomoto, S. Yagi, G. Kutluk, K. Soda, E. Hashimoto, M. Taniguchi, *J. Surf. Anal.* **12**, 238 (2005).
- [5] T. Nomoto, K. Miura, S. Yagi, G. Kutluk, H. Sumida, K. Soda, E. Hashimoto, H. Namatame, M. Taniguchi. *Surf. Sci.* **601**, 3784 (2007).
- [6] T. Nomoto, S. Yagi, K. Soda, H. Namatame, M. Taniguchi, submitted to *e-J. Surf. Sci. Nanotech.*

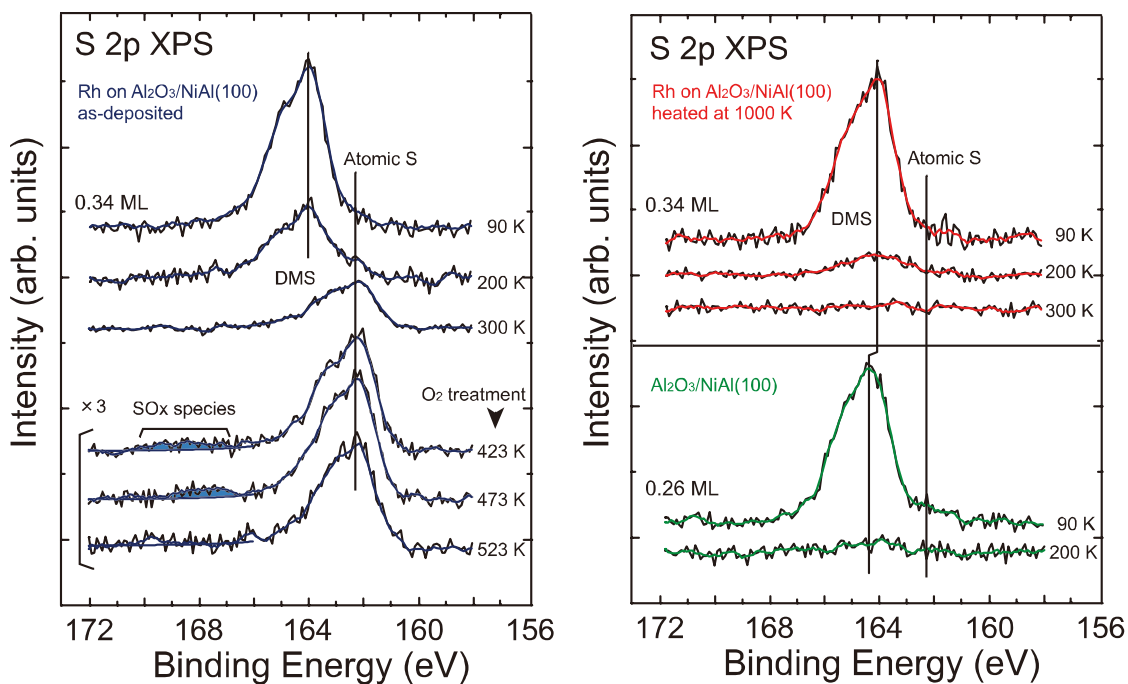


Figure 1. Thermal dependence of S 2p XPS spectra for DMS on Rh/Al<sub>2</sub>O<sub>3</sub>/NiAl(100) as-deposited, Rh/Al<sub>2</sub>O<sub>3</sub>/NiAl(100) heated at 1000 K, and Al<sub>2</sub>O<sub>3</sub>/NiAl(100). Rh coverage is 1.0 ML. The samples were treated with O<sub>2</sub> gas above 423 K.

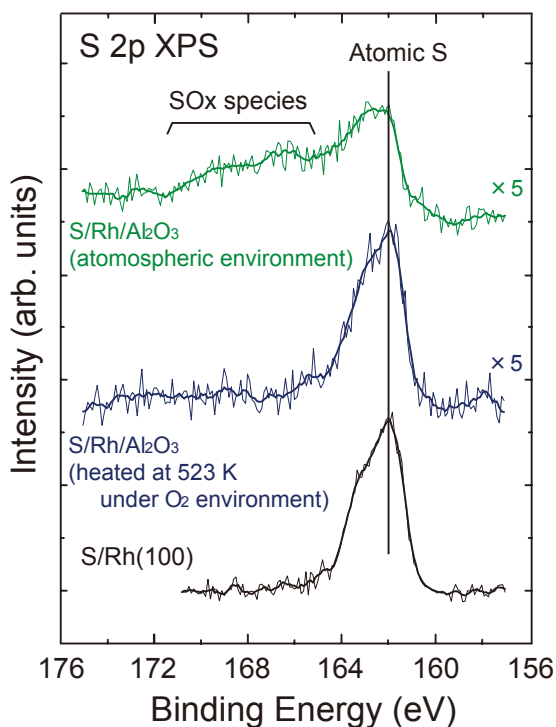


Figure 2. S 2p XPS spectra for atomic sulfur on Rh/Al<sub>2</sub>O<sub>3</sub>/NiAl(100) as-deposited surface, which were measured after O<sub>2</sub> treatment at 523 K and after exposing to air.

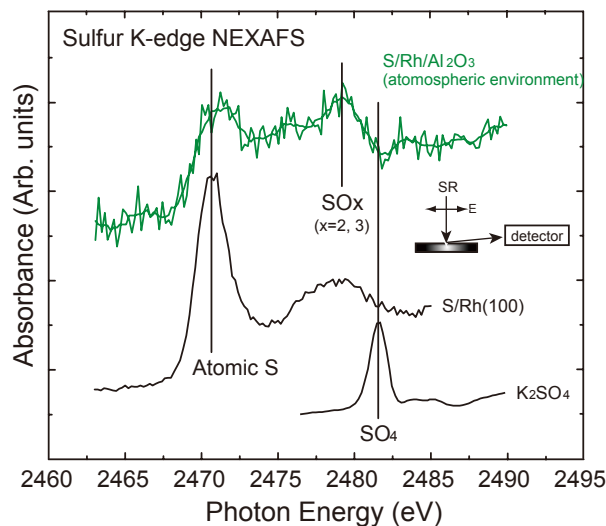


Figure 3. S K-edge NEXAFS spectra for atomic sulfur on Rh/Al<sub>2</sub>O<sub>3</sub>/NiAl(100) under atmospheric environment, S/Rh(100), and K<sub>2</sub>SO<sub>4</sub>.

## Cl K-edge NEXAFS and AFM study of Pd(PVP) nanoparticle by means of He path system

S. Yagi<sup>a</sup>, T. Kodera<sup>a</sup>, T. Nomoto<sup>a</sup>, G. Kutluk<sup>b</sup>, H. Namatame<sup>b</sup>, M. Taniguchi<sup>b</sup>

<sup>a</sup>*Department of Quantum Engineering, Graduate School of Engineering, Nagoya University; Chikusa-ku, Nagoya, 464-8603 Japan*

<sup>b</sup>*Synchrotron Radiation Center, Hiroshima University; 2-313 Kagamiyama, Higashi-Hiroshima, 739-8526 Japan*

Metal nanoparticles have a good property for the purification effects. In these years, the regulation value for the emission gas has become severe. Moreover the reduction of the amount of precious metals has been demanded in the world. Therefore, the catalyst with nanoparticle having a large effect for the purification is much desired. Especially, Pd and Pt nanoparticles have been used as a DPF (diesel particulate filter) and are much in demand in recent years. Thus there are many reports about the applications of the nanoparticle focused on the DPF [1-3]. We have revealed that the changes of the particle size and the chemical state about the Rh(PVP) nanoparticles, which are fabricated by means of the reflux-flow method at 353 K [4,5]. In those studies, we have used the AFM and NEXAFS measurements. Because both measurements are nondestructive, the same sample can be used for other experiments. It suggests that both two measurements are suitable for doing the combined measurement to the same sample. In this study, our purposes are to fabricate the Pd nanoparticle by means of similar method of our previous way for Rh(PVP), and to characterize the nanoparticle by the combined measurements of both AFM and NEXAFS techniques.

We have fabricated the Pd(PVP) nanoparticles with one kind of PVP (K-15, molecular weight of 10000) received by KISHIDA CHEMICAL CO., Ltd. The  $5.0 \times 10^{-2}$  mmol palladium chloride received from Mitsuwa Chemicals Co., Ltd and 0.5 mmol PVP were dissolved into a mixture solvent of ethanol and distilled water (total volume: 70 ml). The Pd(PVP) nanoparticle colloidal solution was fabricated by the reflux-flow system at 353 K for 2 hours. We have prepared the nanoparticle thin film by the spin-coating method for the Pd(PVP) nanoparticles on the Ni (for NEXAFS) and Si (for AFM) substrates ( $10 \times 10$  mm<sup>2</sup>, 0.5 mm thickness) at 4000 rpm and heated at several temperatures in the air. The AFM images for each Pd(PVP)/Si specimens were measured by NanoScope IIIa (Veeco Instruments) with non-contact tapping mode at Innovation Plaza Hiroshima JST. The Near-edge XAFS (NEXAFS) spectra were carried out by yielding fluorescence X-rays with the atmospheric XAFS measurement system using He gas at the soft X-ray double crystal monochromator beamline BL-3.

### AFM Results

We have used AMF for the estimation of the particle size of Pd(PVP) nanoparticles. In general, a vertical value of AFM image has a little error bar in comparison with a horizontal one. Therefore, the particle size can be evaluated by the height value of the AFM analysis. Figures 1(a)-(d) show the AFM images with inset of the size distribution of the Pd(PVP) nanoparticles, which are as-prepared, heating up to 723 K, 873 K and 1073 K. As reported about the Rh(PVP) nanoparticle by Ashida and Yagi *et al.*, since the nanoparticles with using PVP polymer are covered with the capping molecule, we can not obtain an exact particle size [4,5]. Because the PVP polymer decomposes at temperature higher than 673 K, reported by Ashida *et al.* [4], we have prepared the samples by heating at temperatures higher than 723 K.

Judging from each AFM measurements, the average particle sizes with standard deviation are estimated to be (a)  $0.8\pm 0.2$ , (b)  $2.0\pm 0.6$ , (c)  $2.4\pm 1.1$  and (d)  $3.3\pm 1.1$  nm, respectively. The estimated particle size about the as-prepared sample is very small, it suggests that the average particle size is underestimated. It is found that the average particle size is gradually growing along with the rise of annealing temperature. It is necessary to note that there are some nanoparticles, which have a large particle size of 5-6 nm, as annealing temperature of the substrate rises. This result is not obtained by our previous study about Rh(PVP) nanoparticles. It might depend upon the element kind, whether the nanoparticles grew up largely or not by heating the specimens.

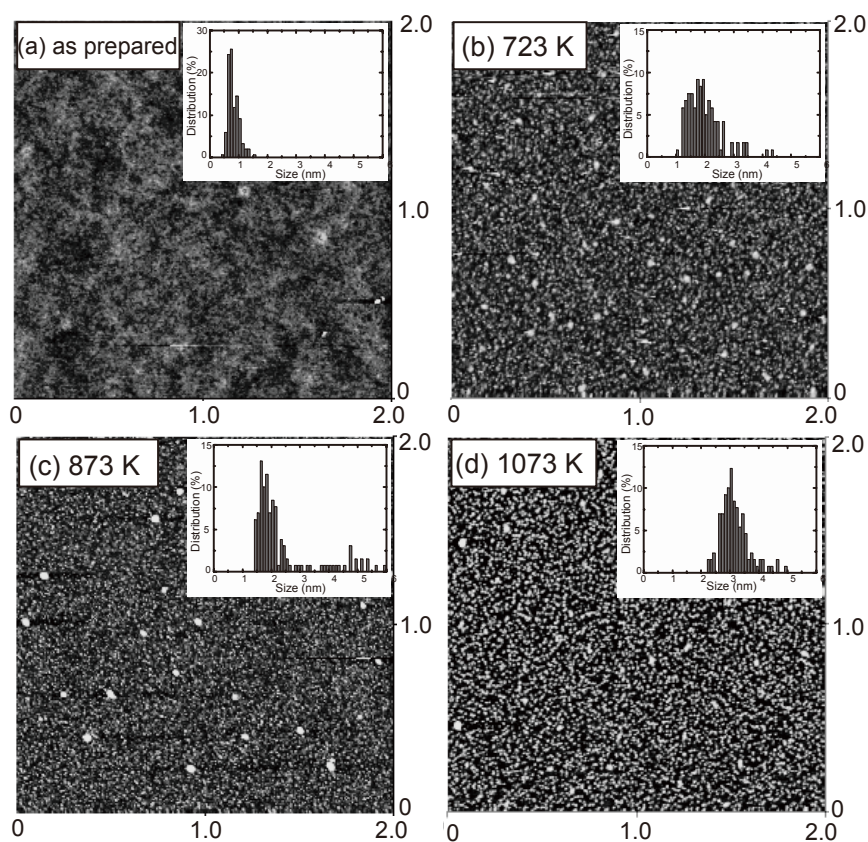
### Cl K-edge NEXAFS Results

Figure 2 shows the Cl K-edge NEXAFS spectra of (a) PdCl<sub>2</sub> powder, (b) PdCl<sub>2</sub> aqueous solution, and (c)-(f) Pd(PVP) with annealing at several temperatures. All spectra were normalized to the edge-jump. There are four peaks (A), (B), (C) and (D), which are shown in Figure 2. The peak (A) can observe in spectra (a), (b) and (c) and is associated with the transition from the Cl 1s level to the lowest antibonding molecular orbital  $a_g(\sigma^*)$  of the [PdCl<sub>4</sub>]<sup>2-</sup> state [6,7]. The peak at 2822.1 eV in the spectrum (b) is observed accurately at different peak position of (A). Because the chemical state of Cl in (b) is ionic state in the aqueous solution, this peak shows the Cl<sup>-</sup> state. It is found that the chemical state of Cl in (c) is almost same as (a), since the peak positions are almost correspond to (a). Therefore, the Pd atoms of the nanoparticle have a chemical bonding with the Cl atom before annealing. Peak (A) disappears after annealing Pd(PVP) nanoparticles. This result suggests that there is no Cl<sup>-</sup> state in the annealed samples of (d)-(f). On the other hand, peaks (C) and (D) can be seen in all NEXAFS spectra though there is a difference of the peak intensity. Sugiura *et al.* has reported that the origin of those peaks are the square-planar complex ions of [MCl<sub>4</sub>]<sup>2-</sup> [6]. Here, M is the palladium. Hence, it is found that there are same structures of [MCl<sub>4</sub>]<sup>2-</sup> about Pd-Cl bonding in the Pd(PVP) nanoparticles. After annealing up to 1073 K, two peaks of (C) and (D) are still observed. It seems that the structure of [MCl<sub>4</sub>]<sup>2-</sup> is a very stable structure. Peak B can be seen only in the spectrum of (f), annealed up to 1073 K. The origin of this peak is unknown. However, we think that peak (B) appears, if the chlorine atom receives one electron or less. A more detailed experiment is necessary in the future.

Figure 3 shows the Cl K-edge NEXAFS spectra for Pd(PVP) specimens which are (c) RT, and annealed at (d) 723 K, (e) 823 K and (f) 1073 K. All NEXAFS spectra are plotted by the agreement with each base line. The difference value between the post-edge at 2845 eV and the pre-edge at 2810 eV is the edge-jump value and means a total amount of Cl atoms. Therefore we can estimate the Cl amount of decrease in comparison with the edge-jump values. The edge-jump values decrease with raising the annealing temperature. Those results indicate that some of chlorine atoms desorb from the sample. But the chlorine atom for 1073 K specimen remains about 25 %, (edge-jump value (1073 K)/edge-jump value (RT) %), in comparison with the start specimen of RT. In our previous study for Rh(PVP) nanoparticle, the residual chlorine atoms have decreased to less than 10 % [5]. There is a big difference about the amount of the residual chlorine atoms between Pd(PVP) and Rh(PVP). It is thought that this difference depends upon a stability of chlorine atom in the nanoparticles. Actually, the NEXAFS spectrum for Rh(PVP) has no peak such as (C) and (D) shown in Figure 2. This result seems to show the chlorine atom has no structure of [RhCl<sub>4</sub>]<sup>2-</sup> state in Rh(PVP) nanoparticle

## References

- [1] A. Güthenke et al., Chem. Eng. Sci. **62**, 5357 (2007).
- [2] Ulrich G. Alkemade et al., Solid State Ionics **177**, 2291 (2006).
- [3] S. Yagi et al., to be submitted.
- [4] T. Ashida et al., Surf. Sci. **601**, 3898 (2007).
- [5] S. Yagi et al., submitted to Surf. Interface Anal.
- [6] CHIKARA SUGIURA and SHINJI MURAMATSU, J. Phys. Chem. Solids **46**, 1215 (1985).
- [7] P. BEHRENS et al., Synthetic Metals **34**, 199 (1989).



Figures 1(a)-(d). The AFM images with inset of the size distribution of the Pd(PVP) nanoparticles, which are (a) as-prepared, heating up to (b) 723 K, (c) 873 K and (d) 1073 K. Each scan size is  $2 \times 2 \mu\text{m}^2$ .

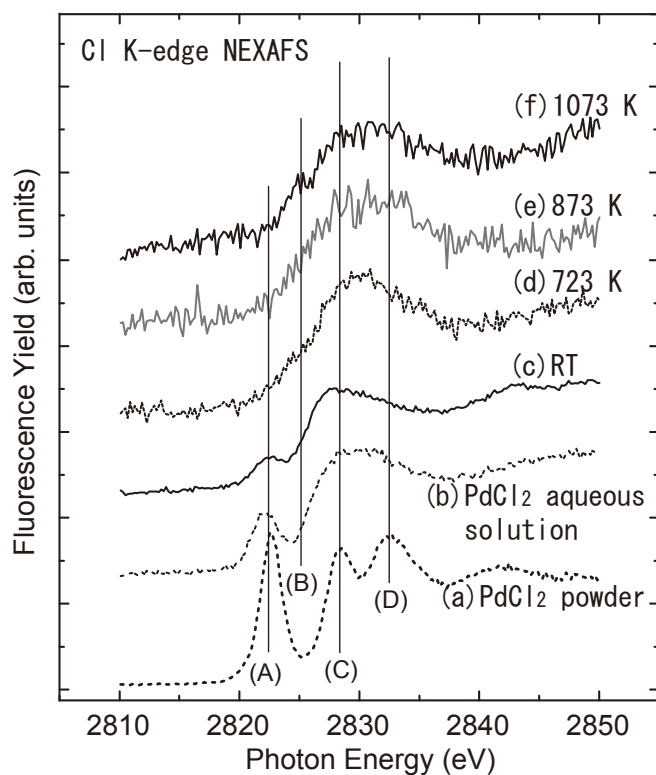


Figure 2. The Cl K-edge NEXAFS spectra of (a) PdCl<sub>2</sub> powder, (b) PdCl<sub>2</sub> aqueous solution, and (c)-(f) Pd(PVP) with annealing at several temperatures.

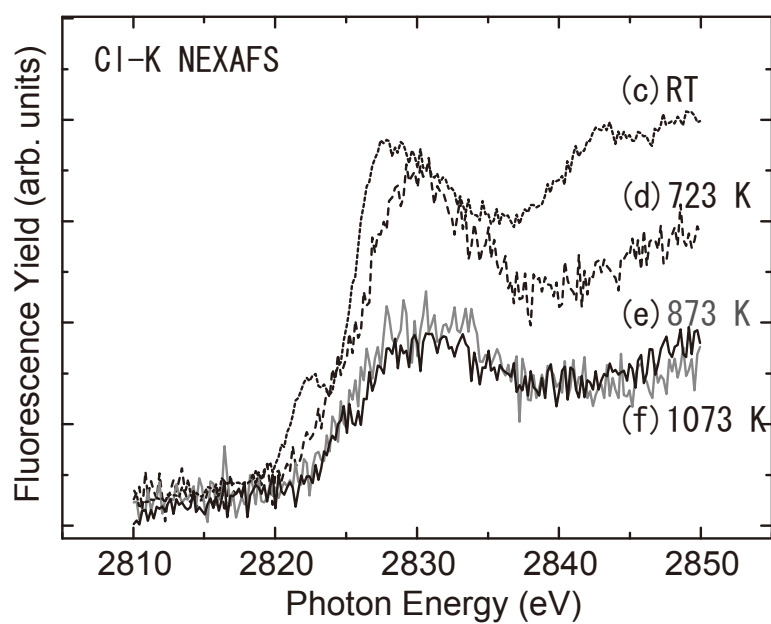


Figure 3. The Cl K-edge NEXAFS spectra for Pd(PVP) specimens which are (c) RT, and annealed at (d) 723 K, (e) 823 K and (f) 1073 K.

Pd L<sub>3</sub>-edge NEXAFS study of Pd(PVP) nanoparticle  
by means of He path system

S. Yagi<sup>a</sup>, T. Kodera<sup>a</sup>, T. Nomoto<sup>a</sup>, G. Kutluk<sup>b</sup>, H. Namatame<sup>b</sup>, M. Taniguchi<sup>b</sup>

<sup>a</sup>*Department of Quantum Engineering, Graduate School of Engineering, Nagoya University;  
Chikusa-ku, Nagoya, 464-8603 Japan*

<sup>b</sup>*Synchrotron Radiation Center, Hiroshima University; 2-313 Kagamiyama,  
Higashi-Hiroshima, 739-8526 Japan*

Metal nanoparticles have a good property for the purification effects. In these years, the regulation value for the emission gas has become severe. Moreover the reduction of the amount of precious metals has been demanded in the world. Therefore, the catalyst with nanoparticle having a large effect for the purification is much desired. Especially, Pd and Pt nanoparticles have been used as a DPF (diesel particulate filter) and are much in demand in recent years. Thus there are many reports about the applications of the nanoparticle focused on the DPF [1-3]. We have revealed that the changes of the particle size and the chemical state about the Rh(PVP) nanoparticles, which are fabricated by means of the reflux-flow method at 353 K [4,5]. In those studies, we have used the AFM and NEXAFS measurements. Because both measurements are nondestructive, the same sample can be used for other experiments. It suggests that both two measurements are suitable for doing the combined measurement to the same sample. In this study, our purposes are to fabricate the Pd nanoparticle by means of similar method of our previous way for Rh(PVP), and to characterize the chemical state of the nanoparticle by Pd L<sub>3</sub>-edge NEXAFS technique.

We have fabricated the Pd(PVP) nanoparticles with one kind of PVP (K-15, molecular weight of 10000) received by KISHIDA CHEMICAL CO., Ltd. The  $5.0 \times 10^{-2}$  mmol palladium chloride received from Mitsuwa Chemicals Co., Ltd and 0.5 mmol PVP were dissolved into a mixture solvent of ethanol and distilled water (total volume: 70 ml). The Pd(PVP) nanoparticle colloidal solution was fabricated by the reflux-flow system at 353 K for 2 hours. We have prepared the nanoparticle thin film by the spin-coating method for the Pd(PVP) nanoparticles on the Ni (for NEXAFS) substrate ( $10 \times 10$  mm<sup>2</sup>, 0.5 mm thickness) at 4000 rpm and heated at several temperatures in the air. The Near-edge XAFS (NEXAFS) spectra were carried out by yielding fluorescence X-rays with the atmospheric XAFS measurement system using He gas at the soft X-ray double crystal monochromator beamline BL-3.

Figure 1 shows the Pd L<sub>3</sub>-edge NEXAFS spectra of (a) PdCl<sub>2</sub> powder, (b) Pd bulk, (c) Pd nanoparticle on Ni substrate (by dry process), (d) PdCl<sub>2</sub> aqueous solution, and (e)-(h)

Pd(PVP) annealed at several temperatures. All spectra were normalized to the edge-jump. There are two peaks (A) and (B), which are shown in Figure 1. Since the peak (A) is corresponding to (b)Pd bulk peak, the peak (A) can be assigned to the metal Pd<sup>(0)</sup> state. On the other hand, the peak (B) is same as the peak position of (c) Pd nanoparticle, which is fabricated by the gas evaporation method with He gas [6]. Yagi *et al.* [6] and Miura *et al.* [7] have reported that the surface of the Pd nanoparticle is easily oxidized by the exposure to the air at room temperature. Therefore, the peak (B) shows that there is the oxidized state in Pd(PVP) nanoparticle. However, the peak of (d) Pd aqueous solution has a same position of (B). In the aqueous solution, the Pd atom can exist in the state of the Pd<sup>2+</sup>. In other words, the Pd<sup>2+</sup> state is equal to the same state of the oxidized state. Thus, it is found that most of Pd atoms in Pd(PVP) nanoparticle take the Pd<sup>2+</sup> state, regardless of the substrate temperature. Such results was not seen for Rh(PVP) nanoparticle [4,5]. The Rh L<sub>3</sub>-edge NEXAFS spectra show that the peak position shifts to the lower energy side with annealing in the air. When Pd(PVP) nanoparticle is compared with the result of Rh(PVP), it has been understood that Pd can not easily reduce with annealing in the air.

## References

- [1] A. Güthenke *et al.*, Chem. Eng. Sci. **62**, 5357 (2007).
- [2] Ulrich G. Alkemade *et al.*, Solid State Ionics **177**, 2291 (2006).
- [3] S. Yagi *et al.*, to be submitted.
- [4] T. Ashida *et al.*, Surf. Sci. **601**, 3898 (2007).
- [5] S. Yagi *et al.*, submitted to Surf. Interface Anal.
- [6] S. Yagi *et al.*, e-J. Surf. Sci. Nanotech. **4**, 258 (2006).
- [7] K. Miura *et al.*, submitted to J. Surf. Anal.

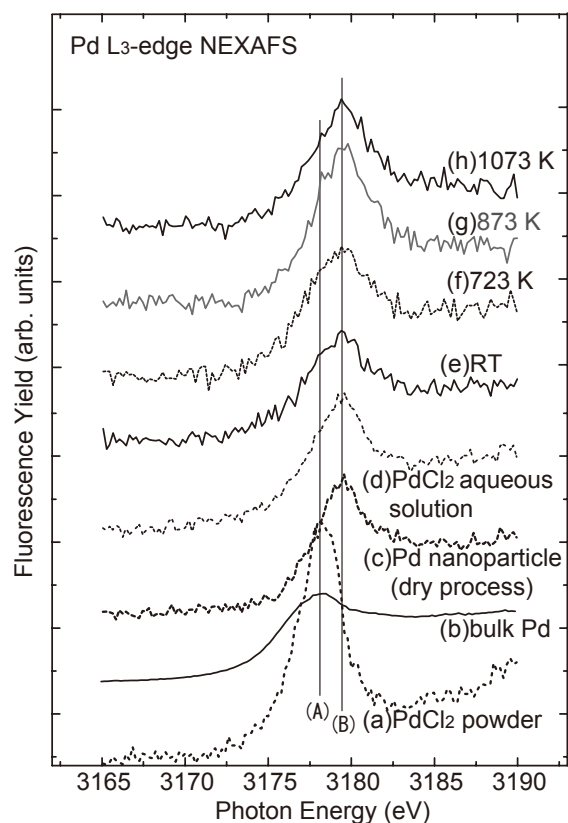


Figure 1. The Pd L<sub>3</sub>-edge NEXAFS spectra of (a) PdCl<sub>2</sub> powder, (b) Pd bulk, (c) Pd nanoparticle on Ni substrate (by dry process), (d) PdCl<sub>2</sub> aqueous solution, and (e)-(h) Pd(PVP) at several temperatures.

## Reaction study of L-cysteine on Rh(PVP) nanoparticle surface in the aqueous solution environment

S. Gohda<sup>a</sup>, T. Ashida<sup>a</sup>, S. Yagi<sup>a</sup>, H. Namatame<sup>b</sup> and M. Taniguchi<sup>b</sup>

<sup>a</sup> *Department of Quantum Engineering, School of Engineering, Nagoya University; Japan*

<sup>b</sup> *Synchrotron Radiation Center, Hiroshima University; Japan*

The platinum group elements show a high reactivity for halogen and chalcogen. Especially, the nanoparticle made of the platinum group metal is expected to remove the halogen and chalcogen efficiently because the ratio of the surface atom to internal atom increases on a nanoparticle phase. Therefore, this nanoparticle has been used in the cosmetic and medical products in these years.

In our previous study, we have investigated the reaction of L-cysteine on Rh(PVP) nanoparticle surface in the nanocolloidal solution [1]. It indicates that L-cysteine molecule decomposes to cysteine thiolate, the thiolate adsorbs on Rh nanoparticle surface through the sulfur and cystine molecule is produced by making the S-S bond from two cysteine thiolates. However, existence state of the cystine in the aqueous solution environment has not been cleared yet. Besides, chlorine ions which remain in the nanocolloidal solution may influence the reaction between L-cysteine and Rh(PVP) nanoparticle. In this work we have clarified the reaction of L-cysteine on Rh(PVP) nanoparticle surface under the aqueous solution environment by near edge X-ray absorption fine structure (NEXAFS) of S-K and Cl-K edges.

Rh(PVP) nanocolloidal solution were prepared by the liquid reduction method [2]. The rhodium chloride tri-hydrate ( $\text{RhCl}_3(3\text{H}_2\text{O})$ ) and PVP were dissolved into a mixed solvent of distilled water and ethanol, and refluxed at 353 K. The sample was prepared by dissolving L-cysteine powder into Rh(PVP) nanocolloidal solution and keeping reaction for the appropriate time at room temperature. The S-K and Cl-K edges NEXAFS measurements of the liquid samples were surveyed by the yielding fluorescence X-ray using the atmospheric pressure XAFS measurement system with He gas at the beamline BL-3 [3].

Figure 1 shows S K-edge NEXAFS spectra for L-cysteine aqueous solution, L-cystine aqueous solution and the mixed samples that passed each time after dissolving L-cysteine powder (5 hours, 1, 30, 180 days). The spectra after 30 and 180 days have the shoulder structure at 2473.9 eV and this position is assigned to the peak position of  $\sigma^*(\text{S-C})$  for L-cystine. Figure 2 shows the relation between the reaction time and the relative peak intensity at 2473.9 eV. As seen in this figure, the amount of the cystine increases in proportion to the reaction time. The amount of the produced cystine gradually increases and keeps constant after 30 days. It is suggested that L-cysteine dissolved into the nanocolloidal solution

is used by cystine synthesis reaction and the reaction is finished for saturation of cystine after 30 days.

Figures 3 and 4 show Cl K-edge NEXAFS spectra for Rh(PVP) nanocolloidal solution and the mixed samples. In Figure 3, two peaks of Rh(PVP) nanocolloidal solution are located at 2822.4 eV and 2828.8 eV. These peaks are attributed to chlorine ion state and the bonding between chlorine and rhodium, respectively [2]. The main peak at 2828.8 eV shifts to 2827.4 eV after dissolving L-cysteine into Rh(PVP) nanocolloidal solution and the peak intensity at 2827.4 eV increases with the reaction time. The previous researches have reported that the peak at around 2827.4 eV can be observed in the Cl K-edge NEXAFS spectra for the specimen of ammonium hexachlororhodate(III)  $[(\text{NH}_4)_3[\text{RhCl}_6]]$  [4, 5]. In Figure 4, it is observed that the peak intensity at 2827.4 eV increases for the reaction time within 2 hours. In addition, the peak intensity of chlorine ion state observed at 2822.4 eV decreases with the reaction time. Therefore, this indicates that the similar structure to  $(\text{NH}_4)_3[\text{RhCl}_6]$  is made from the surface Rh atom of Rh(PVP) nanoparticle, chlorine ion and amino group of cysteine (cystine). Moreover, it is supposed that chlorine ions contribute to form the complex structure on Rh(PVP) nanoparticle surface.

- [1] S. Gohda, T. Ashida, S. Yagi, H. Namatame, M. Taniguchi, *J. Surf. Anal.* in press.
- [2] T. Ashida, T. Miura, T. Nomoto, S. Yagi, H. Sumida, G. Kutluk, K. Soda, H. Namatame, M. Taniguchi, *Surf. Sci.* **601**, 3898 (2007).
- [3] S. Yagi, Y. Matsumura, K. Soda, E. Hashimoto, M. Taniguchi, *Surf. Interface Anal.* **36**, 1064 (2004).
- [4] H. Rumpf, H. Modrow, J. Hormes, P. Amann, A. Möller, G. Meyer, *J. Synchrotron Rad.* **8**, 707 (2001).
- [5] C. Sugiura, M. Kitamura, S. Muramatsu, *J. Chem. Phys.* **84**, 4824 (1986).

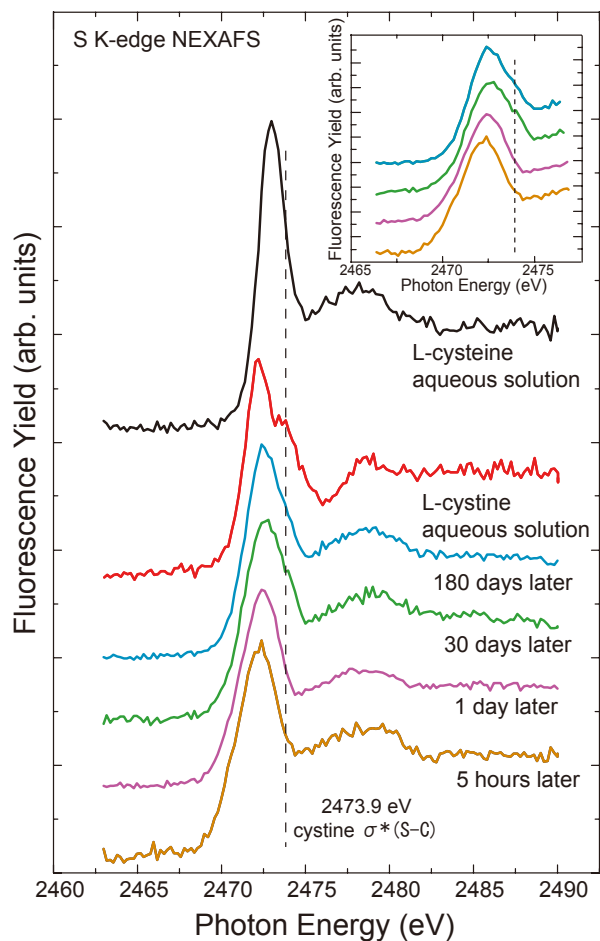


Figure 1. S K-edge NEXAFS spectra for L-cysteine aqueous solution, L-cystine aqueous solution and the mixed samples that have left for arbitrary time. The inset shows the detailed NEXAFS spectra of the mixed samples.

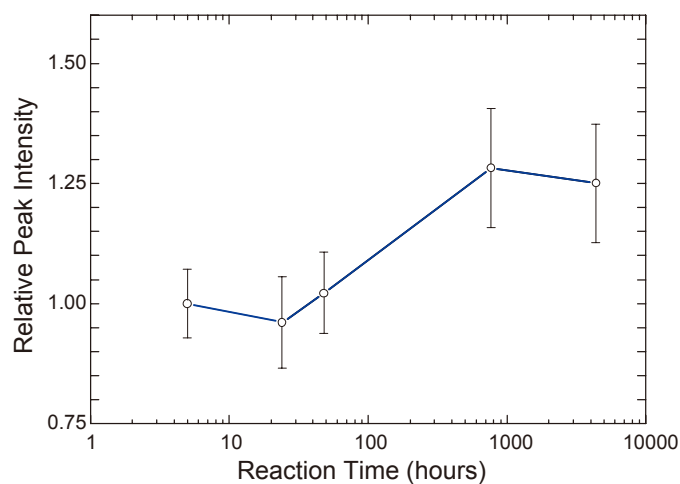


Figure 2. Relation between the reaction time and the relative peak intensity of  $\sigma^*(S-C)$  for L-cystine.

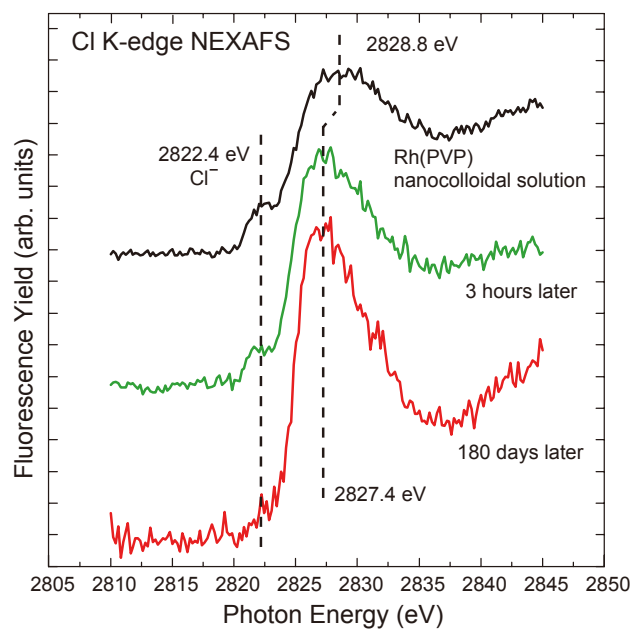


Figure 3. Cl K-edge NEXAFS spectra for Rh(PVP) nanocolloidal solution and the mixed samples after 3 hours and 180 days.

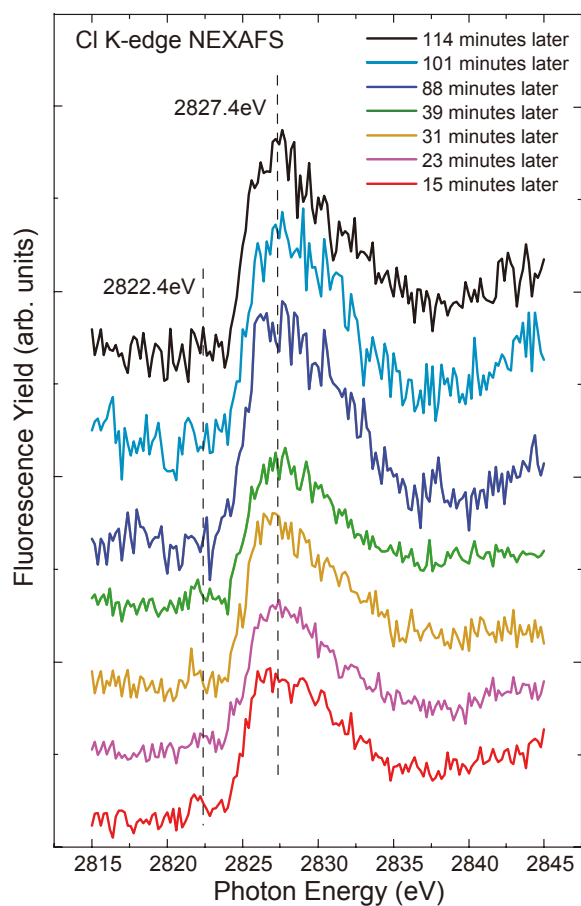


Figure 4. Cl K-edge NEXAFS spectra for the mixed samples that have left for arbitrary time.

## **Dissociation reaction of (CH<sub>3</sub>)<sub>2</sub>S adsorbed on Pd nanoparticles fabricated by gas evaporation method using NEXAFS and in-situ XPS**

M. Morihara<sup>a</sup>, K. Miura<sup>a</sup>, T. Nomoto<sup>a</sup> and S. Yagi<sup>a</sup>  
G. Kutluk<sup>b</sup>, H. Namatame<sup>b</sup> and M. Taniguchi<sup>b</sup>

<sup>a</sup>*Department of Quantum Engineering, School of Engineering, Nagoya University, Japan*

<sup>b</sup>*Synchrotron Radiation Center, Hiroshima University, Japan*

Automobile catalyst is composed of the platinum group metals (Pd, Rh and Pt) since these metals indicate the superior property of the purification of the automobile exhaust gas [1-3]. The platinum-group metals are used as nanoparticle since it is effective to enhance its catalytic performance. However, there are two problems of decreasing the catalytic property: (1) surfactant molecules remain on the active sites of nanoparticle surface, which are fabricated by chemical reduction method [1] and (2) the performance of automobile catalyst is decreased by sulfur-containing molecules in gasoline fuel, known as “Sulfur Poisoning” [2]. In previous study, we have fabricated the Pd nanoparticles (Pd NPs) with clean surface by the gas evaporation method, and we expose dimethyl sulfide (DMS: (CH<sub>3</sub>)<sub>2</sub>S) to the Pd NPs surface [3]. This result shows that the activity of Pd NP surface is higher than that of bulk Pd surface. However, it is not found the relation between dissociation reaction of DMS and the amount of deposited Pd NPs. Thus, we have investigated the dissociation reaction of DMS depending on amount of deposited Pd NPs using Near Edge X-ray Absorption Fine Structure (NEXAFS) and in-situ X-ray Photoelectron Spectroscopy (XPS).

Pd NPs with clean surface were fabricated by the gas evaporation method using He gas and deposited on Ni(111) substrate. The amount of Pd NPs on Ni(111) was controlled as an aggregated phase or a dispersed one. Pd substrate sample was prepared as a reference. The samples were transferred to the ultra high vacuum chamber without breaking the vacuum condition. After cooling these substrates down to 90 K, they were exposed to DMS. XPS measurement was carried out by using Mg K $\alpha$  X-ray. NEXAFS measurements (ex-situ condition) were carried out by the fluorescence yielding method under the atmospheric condition of He gas at BL-3.

Figure 1 shows a summary of S 2p XPS spectra for multilayer, DMS adsorbed on Ni(111), bulk Pd and different amount of deposited Pd NPs (0.26, 0.40, 0.58 and 0.90 layer of Pd NPs). DMS adsorbed on Ni(111) and bulk Pd does not decompose. However, DMS dissociates into methanethiolate (MT: CH<sub>3</sub>S<sup>-</sup>) and atomic S on Pd NPs/Ni(111). Therefore, it indicates that the activity of Pd NPs surface is higher than that of the bulk Pd surface. This result is corresponding to previous our study [3]. In addition, it is found that the dissociation

reactions of DMS adsorbed on different amount of deposited Pd NPs are different. When the amount of deposited Pd NPs increases, the area of Pd NP surface becomes large and the existence ratio of MT increases. Thus, DMS dissociates into MT on Pd NPs surface. On the other hand, the area of Pd-Ni interface becomes large on dispersed phase and decreases on aggregated phase. This behavior is similar to that of atomic S as shown in Figure 2. Therefore, it is supposed that DMS dissociates into atomic S at Pd-Ni interface. Figure 3 shows the results of Pd L<sub>3</sub>-edge NEXAFS spectra of bulk Pd and Pd NPs (ex-situ). The chemical states of Pd NPs (ex-situ) have three phases, such as metal Pd, Pd<sub>oxidized 1</sub> and Pd<sub>oxidized 2</sub>. To reveal the interaction of Pd NPs surface and DMS, we have a plan to measure in-situ NEXAFS.

## References

- [1] T. Ashida, K. Miura, T. Nomoto, S. Yagi, H. Sumida, G. Kutluk, K. Soda, H. Namatame and M. Taniguchi, *Surf. Sci.* **601**, 3898 (2007).  
 [2] T. Nomoto, S. Yagi, K. Soda, G. Kutluk, H. Sumida, E. Hashimoto and M. Taniguchi, *e-J. Surf. Sci. Nanotech.* **4**, 39 (2006).  
 [3] M. Morihara, K. Miura, T. Nomoto, S. Yagi in press.

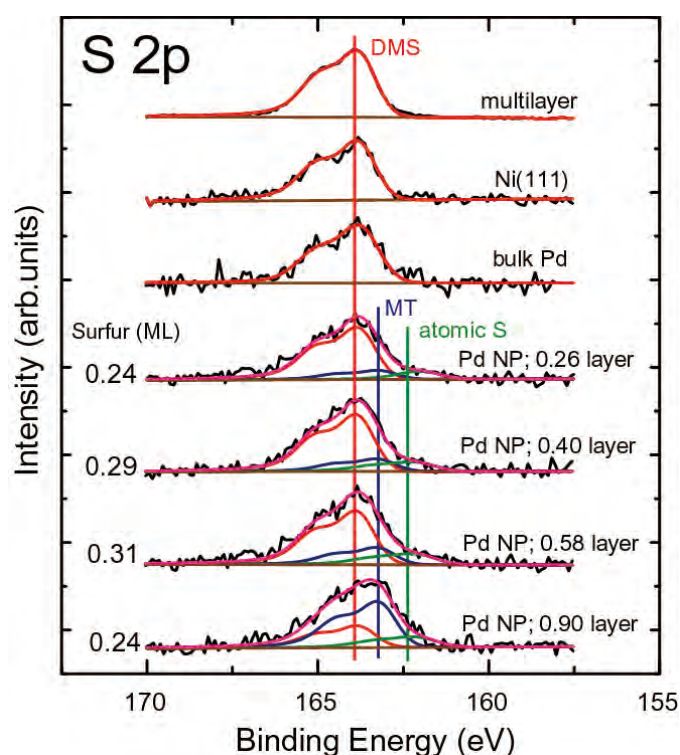


Figure 1. S 2p in-situ XPS spectra for multilayer, DMS/Ni(111), DMS/Pd and DMS/Pd NPs/Ni(111).

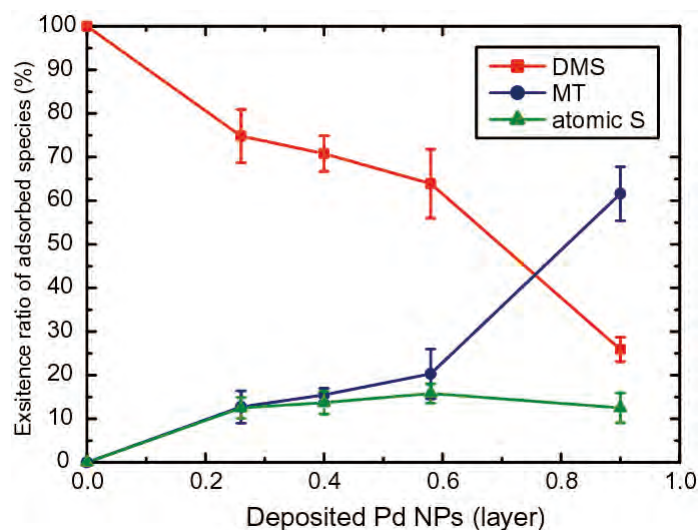


Figure 2. The existence ratio of adsorbed species depending on the amount of deposited Pd NPs.

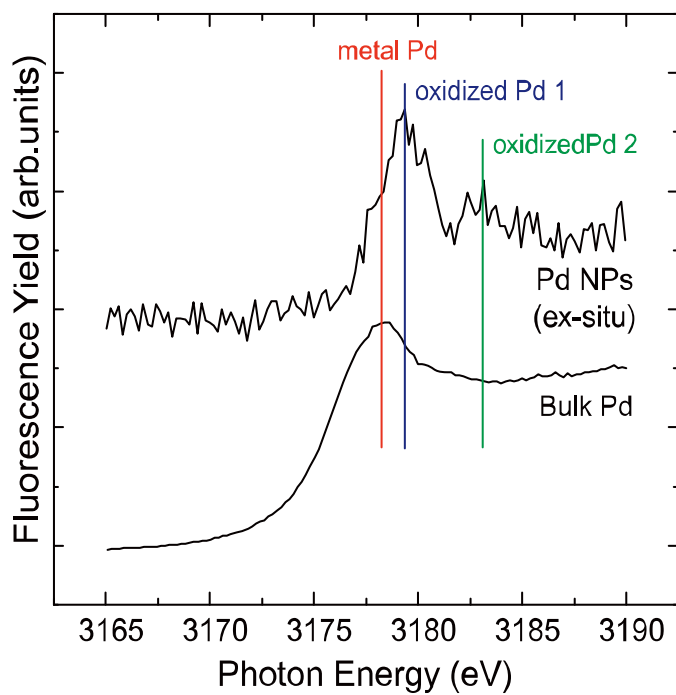


Figure 3. The Pd L<sub>3</sub>-edge NEXAFS spectra for bulk Pd and Pd NPs (ex-situ).

## Site- and state-selective dissociation of core-excited organic molecules: Deuterium-labeled methyl acetate

R. Kawasaki<sup>a</sup>, T. Yamanaka<sup>a</sup>, H. Yoshida<sup>b,c</sup>, and K. Tabayashi<sup>a,c</sup>

<sup>a</sup>Department of Chemistry, Graduate School of Science, Hiroshima University

<sup>b</sup>Department of Physical Science, Graduate School of Science, Hiroshima University

<sup>c</sup>Hiroshima Synchrotron Radiation Center (HSRC), Hiroshima University

Core-electrons are localized closely to a nucleus and their binding energies are sensitive to electronic and structural properties of the local surroundings of the absorbing atom. If the same element atoms in a molecule have nonequivalent structural environments, the differences in their core-electron binding energies are generally significant so that selective core-electron excitation of the atoms can be made. For example, acetone molecule ((CH<sub>3</sub>)<sub>2</sub>CO) has two types of nonequivalent C atoms available for different C1s core-electron excitation, and simple esters (RC(O)OR') have two different O atoms for O1s site-selective excitation, *etc.* Using tunable soft X-rays from synchrotron radiation sources, the excitation site- and state-selective photoreactions following core-electron excitation have so far been examined as fundamental subjects, in the last two decades, for isolated molecules in the gas phase and condensed molecules on the surfaces.

The excitation site-specific fragmentation was firstly reported by Eberhardt *et al.* [1] from the observation of partial ion-yields (PIYs) of gaseous acetone at the C1s electron transitions to antibonding  $\pi^*_{CO}$  and Rydberg orbitals. Tinone *et al.* [2] observed photon-stimulated ion desorption (PSID) of poly-(methyl-methacrylate) (PMMA,  $-\text{[CH}_2\text{C(CH}_3\text{)C(O)-OCH}_3\text{]}_n-$ ) thin film in the oxygen K-edge region and found efficient desorption of excitation state-specific cations (CH<sub>3</sub><sup>+</sup>, CHO<sup>+</sup>) that strongly depended on the antibonding character of resonant core-excited states. In order to elucidate the changes in fragmentation mechanisms between the isolated molecules and macromolecules on the surfaces upon O1s excitation, the state-selective fragmentation of methyl-isobutyrate (MIB, (CH<sub>3</sub>)<sub>2</sub>CHC(O)OCH<sub>3</sub>), *i.e.* a monomer methyl-ester unit of PMMA, has been lately examined in the isolated condition [3]. In the PIY measurement of MIB, enhancement of CHO<sup>+</sup> production was observed at the 1s(O-CH<sub>3</sub>) →  $\sigma^*(\text{C-OCH}_3)$  band, however, the state-selective CH<sub>3</sub><sup>+</sup> production at the 1s(O-CH<sub>3</sub>) →  $\sigma^*(\text{O-CH}_3)$  could not be identified, as opposed to the efficient production of CH<sub>n</sub><sup>+</sup> cations found in PMMA. For the absence of the state-selectivity, possible interfering production of the CH<sub>n</sub><sup>+</sup> cations from the isopropyl site of MIB has been proposed on the ground of large excess-energy transfer within the isolated molecules. In order to eliminate such CH<sub>n</sub><sup>+</sup> contamination and determine the level of site- and state-selective dissociation for the isolated esters, it is of particular importance to distinguish either C<sub>p</sub>H<sub>q</sub> functional group by labeling hydrogen with deuterium atoms.

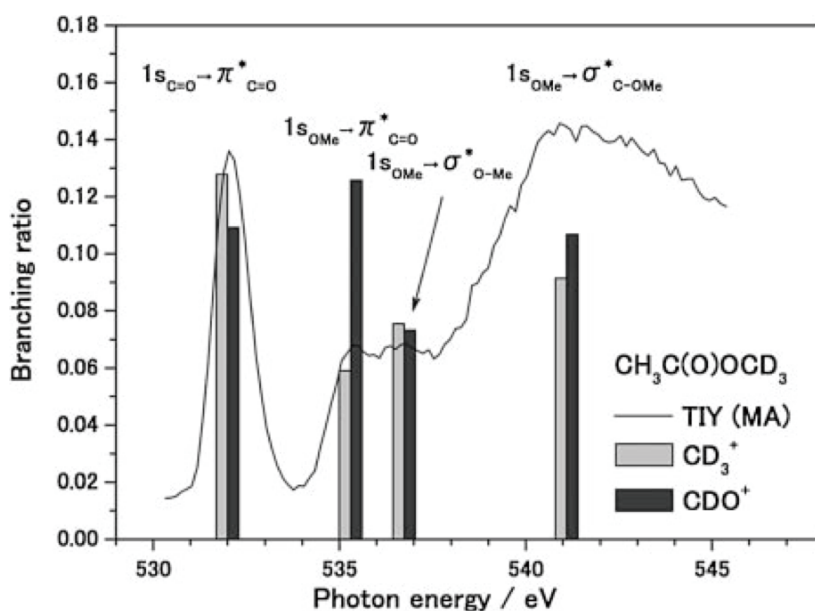


Fig. 1 Comparison of the branching ratios between  $\text{CD}_3^+$  and  $\text{CDO}^+$  production at the core-to-valence excitation bands.

Here, we studied inner-shell excitation and fragmentation of methyl acetate molecule (MA,  $\text{CH}_3\text{C}(\text{O})\text{OCH}_3$ ), *i.e.* a prototype of methyl-ester, in the gas phase using time-of-flight (TOF) fragment-mass spectroscopy. Total-ion-yield (TIY) spectrum of MA was measured in the oxygen K-edge region, and O1s core-to-valence excitation bands were properly assigned. In the PIY measurements for the site- and state-selective dissociation analysis, specifically labeled methyl-d3 acetate (Md3A,  $\text{CH}_3\text{C}(\text{O})\text{OCD}_3$ ) was used in place of normal MA to examine the influence of different methyl sites on the photo-induced processes. Deuterium labeled experiments showed that the site-selective bond scission takes place between the ( $\text{O}1\text{s}_{\text{CO}}^{-1}\pi^*_{\text{CO}}$ ) and ( $\text{O}1\text{s}_{\text{OMe}}^{-1}\pi^*_{\text{CO}}$ ) transitions, whereas the state-selective excitation at the ( $\text{O}1\text{s}_{\text{OMe}}^{-1}\sigma^*_{\text{O-Me}}$ ) does not lead to predominant  $\text{CD}_3^+$  production. The lack of the state-selectivity for both MA and MIB observed was interpreted as being due to the small core-to-valence cross sections buried into the congestion of Rydberg transitions.

## References

- [1] W. Eberhardt, T. K. Sham, R. Carr *et al.*, *Phys. Rev. Lett.*, **50**, 1038 (1983).
- [2] M. C. K. Tinone, K. Tanaka, J. Maruyama *et al.*, *J. Chem. Phys.*, **100**, 5988 (1994).
- [3] K. Tanaka ed., *Report of the Grant-in-Aid on Research for Future 'Photoscience'* (JSPS-RFTF-98P01202), (2003), p. 53

# Hydrogen-bond interactions of small ammonia clusters observed with inner-shell excitation spectroscopy at the nitrogen *K*-edge

T. Yamanaka<sup>a</sup>, T. Maruyama<sup>a</sup>, H. Yoshida<sup>b,c</sup>, and K. Tabayashi<sup>a,c</sup>

<sup>a</sup>Department of Chemistry, Graduate School of Science, Hiroshima University

<sup>b</sup>Department of Physical Science, Graduate School of Science, Hiroshima University

<sup>c</sup>Hiroshima Synchrotron Radiation Center (HSRC), Hiroshima University

In order to obtain new spectroscopic insight into the local hydrogen bond (HB) interaction within molecular clusters, we previously observed inner-shell excitation spectra of small formic acid clusters [1], where constituent acid molecules interact strongly through the HBs (C=O $\cdots$ H-O). By monitoring partial-ion-yields (PIYs) of cluster-origin products, cluster-specific core-excitation spectra with no contribution from molecular excitation could be studied. Comparison of the cluster bands with those of molecular formic acid showed that the first and second core-to-valence bands shift in energy by ca. +0.2 and ca. -0.6 eV upon clusterization. The band shifts of the resonance transitions have been interpreted as being due to the changes in core electron binding energy (CEBE) of the oxygen atoms upon HB formation. Here, we studied inner-shell excitation spectroscopy of small ammonia (AM) clusters at the nitrogen *K*-edge and examined the contribution of (N $\cdots$ H-N) HB interaction on the core-excited AM clusters.

The experiments were carried out using a cluster beam-photoreactive scattering apparatus (CBPRSA) [2] where AM cluster beam was generated by supersonic expansion of 9.9% AM/He mixture at  $P_0 = 0.15$  MPa through a  $\phi 50$   $\mu\text{m}$  nozzle. Time-of-flight (TOF) spectra of the clusters were compared with those of isolated molecules recorded under the effusive beam condition. Besides the molecular cation, we found a single series of protonated clusters, (AM) $_n \cdot \text{H}^+$  in the TOF spectra.

**Fig. 1** shows the PIY spectra at the first/second resonances (N1s $^{-1}$ 3s $_1/3p_e$ ) obtained in the cluster beam. Although free AM molecules are still involved in the cluster beam, “cluster-origin” excitation spectra can be recorded without contribution of free molecules by monitoring PIYs of the fragments originating from AM clusters [1]. Comparison of the “cluster-origin” bands with the “monomer-origin” bands showed that both cluster resonance bands are considerably broadened and that the second N1s $^{-1}$ 3p $_e$  band clearly shifts to a lower energy. The changes in the band structures can be understood by the non-equivalent N sites generated upon clusterization through the HBs. The core-to-valence band behavior of AM clusters will be discussed on the basis of density functional theory calculations.

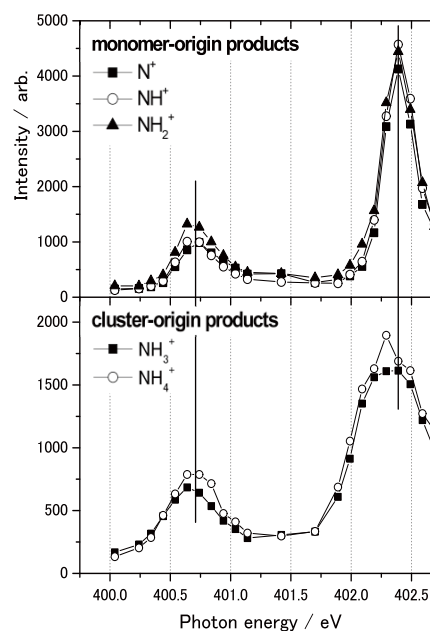


**Fig.1** PIY spectra of AM clusters

## References

- [1] K. Tabayashi *et al.*, *J. Chem. Phys.* **125**, 194307 (2006).  
 [2] K. Tabayashi *et al.*, *AIP Conf. Proceedings*, **879**, 1788 (2007).

## Dissociation dynamics of multiply-charged $\text{CF}_4$ and $\text{CHF}_3$ by momentum imaging spectroscopy

Y. Kimura<sup>1</sup>, I. Miyagami<sup>1</sup>, Y. Kawakami<sup>1</sup>, H. Kawabata<sup>1</sup>, H. Yoshida<sup>1,2</sup>, A. Hiraya<sup>1,2</sup>

<sup>1</sup> *Department of Physical Science, Hiroshima University*

<sup>2</sup> *Hiroshima Synchrotron Radiation Center, Hiroshima University*

Multiply-charged ion is often produced by inner-shell ionization through Auger decay, and it generally dissociates into some fragment ions by Coulomb explosion. We have investigated the dissociation processes of inner-shell ionized  $\text{CHF}_3$  and  $\text{CF}_4$  with a time-of-flight mass spectrometer and a two-dimensional position-sensitive detector at the BL6 of HiSOR. Angular distributions of ejected ions are obtained by measuring the three-dimensional initial momenta derived from the detected position (X, Y) and flight time (T) of fragment ions.

In Fig.1, we show the obtained distributions of correlation angles for  $\theta_1(\text{F}^+_{\text{(First hit)}}$ ,  $\text{F}^+_{\text{(Second hit)}}$ ),  $\theta_2(\text{F}^+_{\text{(First hit)}}$ ,  $\text{CF}^+)$ , and  $\theta_3(\text{F}^+_{\text{(Second hit)}}$ ,  $\text{CF}^+)$  in the  $(\text{F}^+, \text{F}^+, \text{CF}^+)$  formation process after C1s ionization of  $\text{CF}_4$ . Both  $\theta_2$  and  $\theta_3$  distribute  $\sim 120^\circ$ . The F-C-F angle in the stable structure of the neutral ground state is  $109.5^\circ$  with  $T_d$  symmetry. The experimental values of  $\sim 120^\circ$  are larger than it. On the other hand,  $\theta_1$  distributes  $\sim 113^\circ$ , which is relatively close to  $109.5^\circ$ . We consider the 4-body dissociation process as



The calculated correlation angles for  $(\text{F}, \text{F}^+)$  and  $(\text{F}, \text{CF}^+)$  using the experimental results are  $100^\circ$  and  $97^\circ$ , respectively. Dissociation dynamics to produce  $(\text{F}^+, \text{F}^+, \text{CF}^+)$  ion trio are summarized in Fig.2.

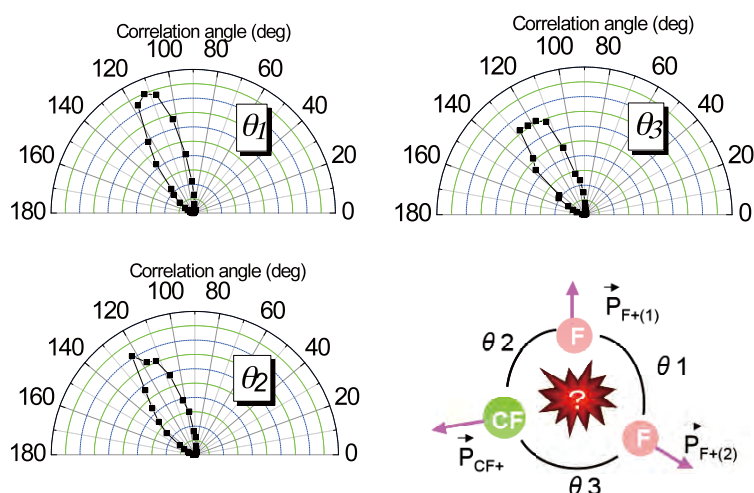


Fig.1 Correlation angles in the  $(\text{F}^+, \text{F}^+, \text{CF}^+)$  formation after C1s ionization of  $\text{CF}_4$ .

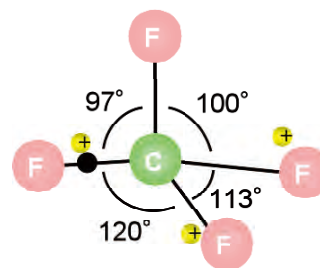


Fig.2 Dissociation dynamics to produce  $(\text{F}^+, \text{F}^+, \text{CF}^+)$  ion trio.

## Study on symmetries of core-excited states in CF<sub>4</sub> and CHF<sub>3</sub>

I. Miyagami<sup>1</sup>, Y. Kimura<sup>1</sup>, Y. Kawakami<sup>1</sup>, H. Kawabata<sup>1</sup>, H. Yoshida<sup>1,2</sup>, A. Hiraya<sup>1,2</sup>

<sup>1</sup> Department of Physical Science, Hiroshima University

<sup>2</sup> Hiroshima Synchrotron Radiation Center, Hiroshima University

We have investigated dissociation processes of CF<sub>4</sub> and CHF<sub>3</sub> in the F1s excitation region with a time-of-flight mass spectrometer (TOF-mass) and a two-dimensional position-sensitive detector at the BL-6 of HiSOR. Total-ion yield spectrum of CHF<sub>3</sub> at the F1s excitation region is shown in Fig.1. The peak at 690.8 eV was already assigned to F1s→σ\* excitation. However, there are two possible symmetries of electronic state, σ\*a<sub>1</sub> and σ\*e, since CHF<sub>3</sub> molecule belongs to C<sub>3v</sub> point group. In the present study, we measured the ejected angle of F<sup>+</sup> against the electric vector (ε) of synchrotron radiation at 688.9 eV (σ\*-low) and 693.6 eV (σ\*-high), which are lower and higher energies of the σ\* peak, respectively. The three-dimensional initial momenta of fragment ions arise from core-excited CHF<sub>3</sub> were obtained by analyzing the detected position (X, Y) and the flight-time (T) of them. The detection axis of the TOF-mass coincides with the direction of ε.

In order to remove the contribution of isotropic F<sup>+</sup> distribution by successive dissociation, we selected F<sup>+</sup> measured in coincidence with CF<sup>+</sup>. Ion-pair dissociation is considered to occur immediately by Coulomb explosion after Auger decay of core-excited molecules. Therefore, the ejected angle of F<sup>+</sup> in (F<sup>+</sup>, CF<sup>+</sup>) would reflect the initial configuration of CHF<sub>3</sub> in space. The obtained angular distributions at σ\*-low and σ\*-high are shown in Fig.2. The upper spectrum shows a peak ~30°, while the lower one shows almost constant. As shown in Figs. 3(a) and 3(b), the C-H bond of CHF<sub>3</sub> is perpendicular to ε in σ\*e excitation, while that is parallel in σ\*a<sub>1</sub> excitation. F<sup>+</sup> should be ejected ~20° in σ\*e, while ~70° in σ\*a<sub>1</sub> if the ion-pair dissociation is much faster than molecular rotation and deformation. At the σ\*-low spectrum, the observed peak of ~30° is in good agreement with ~20° in σ\*e. Thus, we concluded that σ\*e state exists at around “σ\*-low” position. On the other hand, the almost isotropic distribution at “σ\*-high” indicates that some of Rydberg states with both e and a<sub>1</sub> symmetries would overlap complexly.

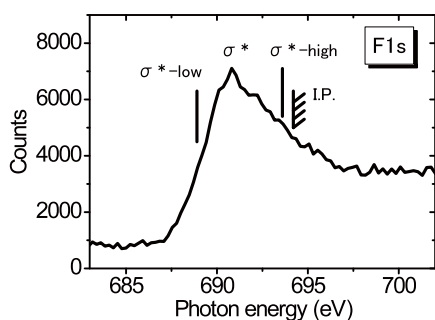


Fig.1 Total ion yield spectra

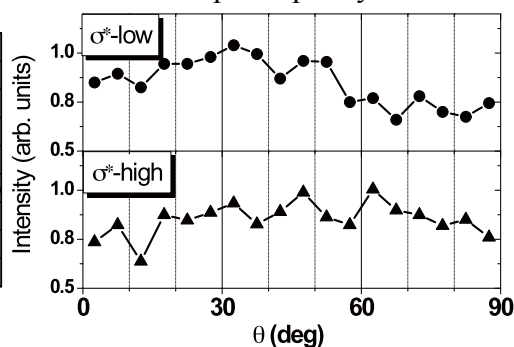


Fig.2 Angular distribution of F<sup>+</sup>

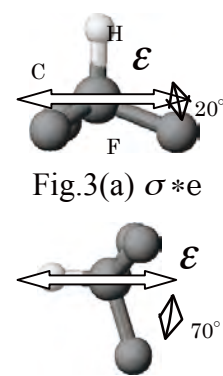


Fig.3(a) σ\*e

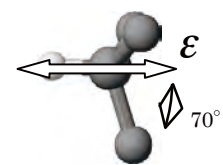


Fig.3(b) σ\*a<sub>1</sub>

## Dissociation dynamics of multiply-charged $\text{CH}_2\text{F}_2$ by momentum imaging spectroscopy

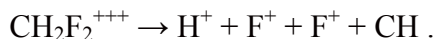
Y. Kawakami<sup>1</sup>, Y. Kimura<sup>1</sup>, I. Miyagami<sup>1</sup>, H. Kawabata<sup>1</sup>, H. Yoshida<sup>1,2</sup>, A. Hiraya<sup>1,2</sup>

<sup>1</sup> *Department of Physical Science, Hiroshima University*

<sup>2</sup> *Hiroshima Synchrotron Radiation Center, Hiroshima University*

Multiply-charged ion is often produced by inner-shell ionization through Auger decay, and it generally dissociates into some fragment ions by Coulomb explosion. We have investigated the dissociation processes of inner-shell ionized  $\text{CHF}_3$  and  $\text{CF}_4$  with a time-of-flight mass spectrometer and a two-dimensional position-sensitive detector at the BL6 of HiSOR. In the present study, we discuss on dissociation dynamics of  $\text{CH}_2\text{F}_2$ . Angular distributions of ejected ions are obtained by measuring the three-dimensional initial momenta derived from the detected position ( $X$ ,  $Y$ ) and flight time ( $T$ ) of fragment ions.

In Fig.1, we show the obtained distributions of correlation angles for  $(\text{H}^+, \text{F}^+_{(\text{First hit})})$ ,  $(\text{H}^+, \text{F}^+_{(\text{Second hit})})$ , and  $(\text{F}^+, \text{F}^+)$  in the  $(\text{H}^+, \text{F}^+, \text{F}^+)$  formation process after F1s ionization of  $\text{CH}_2\text{F}_2$ . Both  $(\text{H}^+, \text{F}^+)$  and  $(\text{F}^+, \text{F}^+)$  distribute  $\sim 110^\circ$ . The H-C-F and F-C-F angles in the stable structure of the neutral ground state are  $108.9^\circ$  and  $108.5^\circ$ , respectively. The experimental values of  $\sim 110^\circ$  are in good agreement with them. Supposing that all the simultaneous dissociation occur along the direction of the respective bond axis, the momentum of undetected particle can be estimated by synthesizing the all momenta of detected particles. Now, we consider the 4-body dissociation process as



The calculated correlation angles for  $(\text{H}^+, \text{CH})$  and  $(\text{F}^+, \text{CH})$  are  $72^\circ$  and  $124^\circ$ , respectively. Dissociation dynamics to produce  $(\text{H}^+, \text{F}^+, \text{F}^+)$  ion trio is summarized in Fig.2.

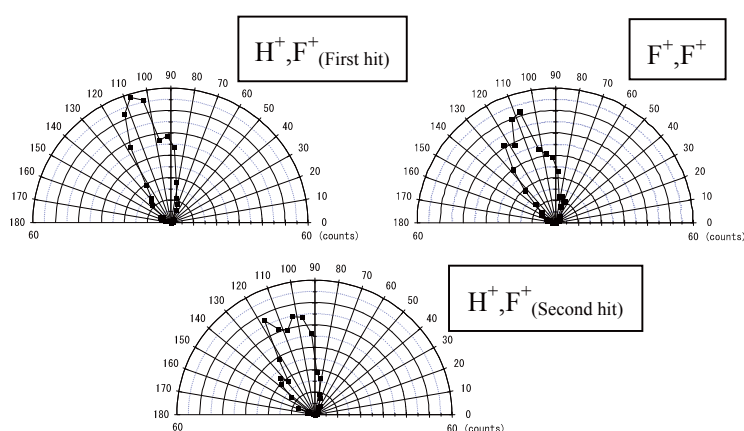


Fig.1 Correlation angles (deg) in the  $(\text{H}^+, \text{F}^+, \text{F}^+)$  formation after F1s ionization of  $\text{CH}_2\text{F}_2$ .

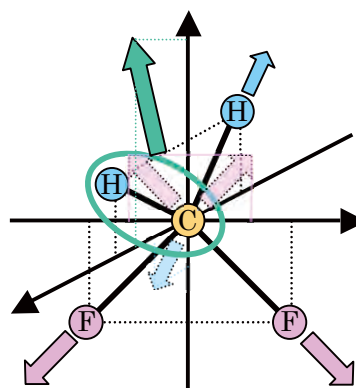


Fig.2 Dissociation dynamics to produce  $(\text{H}^+, \text{F}^+, \text{F}^+)$  ion trio.

## Dissociation dynamics of multiply-charged SF<sub>6</sub> by momentum imaging spectroscopy

H. Kawabata<sup>1</sup>, Y. Kimura<sup>1</sup>, I. Miyagami<sup>1</sup>, Y. Kawakami<sup>1</sup>, H. Yoshida<sup>1,2</sup>, A. Hiraya<sup>1,2</sup>

<sup>1</sup> Department of Physical Science, Hiroshima University

<sup>2</sup> Hiroshima Synchrotron Radiation Center, Hiroshima University

Multiply-charged ion is often produced by inner-shell ionization through Auger decay, and it generally dissociates into some fragment ions by Coulomb explosion. We have investigated the dissociation processes of inner-shell ionized SF<sub>6</sub> with a time-of-flight mass spectrometer and a two-dimensional position-sensitive detector at the BL6 of HiSOR. Angular distributions of ejected ions are obtained by measuring the three-dimensional initial momenta derived from the detected position (X, Y) and flight time (T) of fragment ions.

In Fig.1, we show the obtained distributions of correlation angles for  $\theta_1$  (F<sup>+</sup><sub>(First hit)</sub>, F<sup>+</sup><sub>(Second hit)</sub>),  $\theta_2$  (F<sup>+</sup><sub>(Second hit)</sub>, F<sup>+</sup><sub>(Third hit)</sub>), and  $\theta_3$  (F<sup>+</sup><sub>(First hit)</sub>, F<sup>+</sup><sub>(Third hit)</sub>) in the (F<sup>+</sup>, F<sup>+</sup>, F<sup>+</sup>) formation process after F1s ionization of SF<sub>6</sub>. Both  $\theta_1$  and  $\theta_2$  distribute  $\sim 100^\circ$ . The F-S-F angle in the stable structure of the neutral ground state is  $90^\circ$  with O<sub>h</sub> symmetry. The experimental values of  $\sim 100^\circ$  are larger than it. On the other hand,  $\theta_3$  has two peaks at  $\sim 100^\circ$  and  $\sim 165^\circ$ . This is ascribed to the difference of spatial distributions of three F<sup>+</sup> ions and will be discussed in detail.

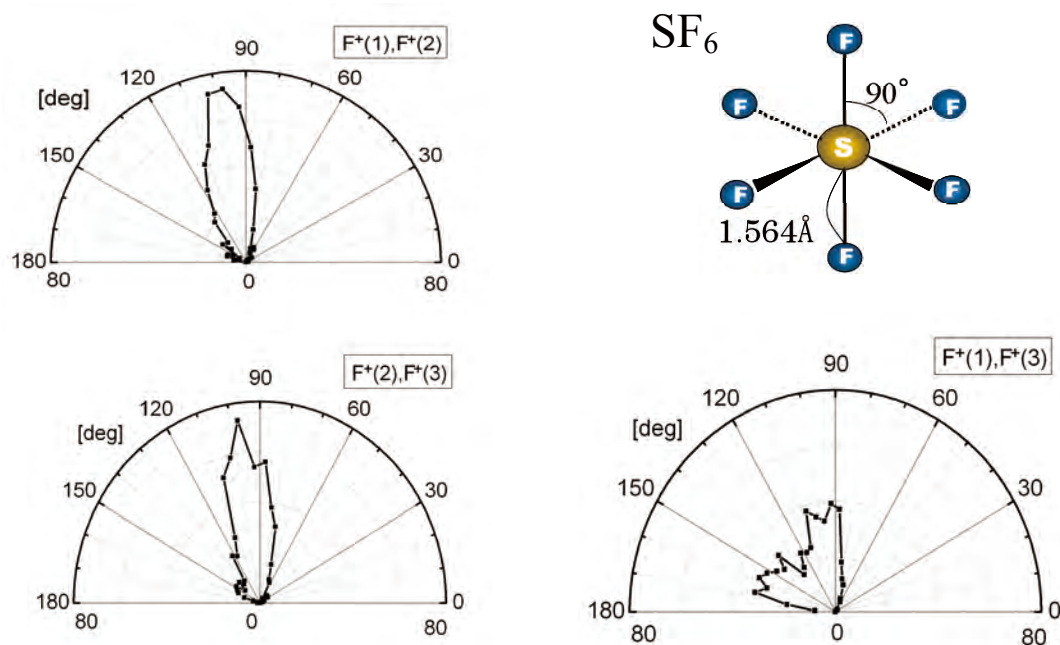


Fig.1 Correlation angles in the (F<sup>+</sup>, F<sup>+</sup>, F<sup>+</sup>) formation after F1s ionization of SF<sub>6</sub>.

# Photoemission study of fluorescein isothiocyanate isomer 1 (FITC) monolayer on platinum

Toshiki Maeda<sup>a,b</sup>, Masashi Nakatake<sup>c</sup>, Hirofumi Namatame<sup>c</sup>, Masaki Taniguchi<sup>c,d</sup>,  
Taka-aki Ishibashi<sup>a,b</sup>

<sup>a</sup>*Department of Chemistry, Graduate School of Science,  
Hiroshima University*

<sup>b</sup>*Center for Quantum Life Sciences*

<sup>c</sup>*Hiroshima Synchrotron Radiation Centre, Hiroshima University*

<sup>d</sup>*Graduate School of Science,  
Hiroshima University*

## 1. Introduction

Photoemission spectroscopy (PES) of fluorescein isothiocyanate isomer 1 (FITC, Fig.1) monolayer on platinum was carried out to investigate how FITC chemisorb to platinum. We found that FITC molecules take two distinct adsorption forms on platinum by sum-frequency generation spectroscopy and fluorescence spectroscopy [1]. However, the detailed adsorption states have not been clear yet. In this study, we elucidated them using PES.

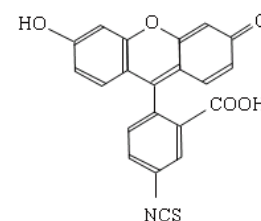


Figure 1. Chemical structure of FITC.

## 2. Experimental

The FITC monolayers were prepared on platinum substrates (10 mm x 15 mm, Koshin Kogaku) by immersing the substrate in a 1 mM ethanolic solution of FITC (Dojin Kagaku) for about 24 hours. After the treatment, the samples were thoroughly rinsed with copious ethanol and dried by the blow with pure nitrogen. The spin-coating method was used to form the multilayer of FITC on platinum. PES experiments were conducted at the beamline BL-7 on HiSOR.

## 3. Results

Figure 2 (a) and (b) show PES spectra of FITC monolayer and spin-coated film on platinum in S2p region. To estimate for the contribution of inelastic scattering of photoelectrons, integrated backgrounds of Shirley type were subtracted from raw spectra. A convolution of Lorentzian and Gaussian line shapes was used to fit the individual peaks of the spectra. In the fitting, a fixed intensity ratio of 1:2 ( $S2p_{1/2} : S2p_{3/2}$ ), a spin-orbit splitting of 1.1 eV, [2] and constant full width at half maximum for each peak were assumed. Five and three  $2p_{3/2}/p_{1/2}$  spin-orbit split doubles were seen in the spectrum of monolayer and multilayer, respectively. This observation suggests that there are five distinct kinds of sulfur atoms on the monolayer, while three on the multilayer. Thus, the interaction of sulfur to the platinum

of the monolayer differs from that of the multilayer.

To examine the bonding states of FITC monolayer on platinum, the PES spectrum in the S2p region was measured for the FITC monolayer on platinum treated with an alkaline solution. The alkaline treatment of FITC monolayer was conducted by immersing the substrate in NaOH solution for about 90 seconds and by blow drying with nitrogen gas. The solution was made by mixing 3-M NaOH aqueous solution with ethanol in the volume ratio of 1:200.

The spectral change for the S2p spectrum of the monolayer occurred after the alkaline treatment. This result implies that the change in the spectrum with the treatment was due to the shifting of the chemical equilibrium of different forms of FITC on the substrate; FITC may have changed from protonated form to deprotonated one with the treatment, inducing the spectral change. The assignments of the each peak to specific adsorption states of FITC molecules to platinum are now under study.

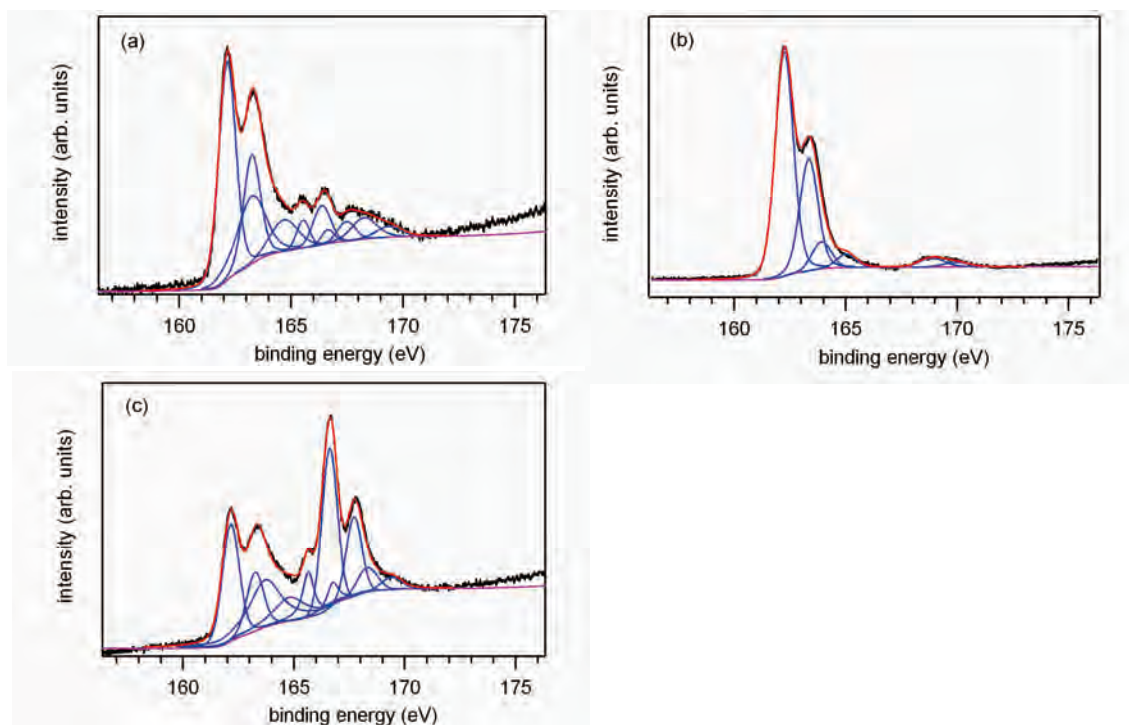


Figure 2. PES spectra of a monolayer before alkaline treatment (a), a multilayer (b), and a monolayer after alkaline treatment (c) of FITC monolayer.

[1] T. maeda et al. manuscript in preparation.

[2] M. Cardona, L. Ley (ed). *Photoemission in Solids I: General Principles*, Springer, 1978

## Core-level photoemission spectra and glass-forming ability in $\text{Pd}_{42.5}\text{Ni}_{7.5}\text{Cu}_{30}\text{P}_{20}$ bulk metallic glass

S. Hosokawa,<sup>a</sup> M. Nakatake,<sup>b</sup> H. Sato,<sup>b</sup> N. Happo,<sup>c</sup> T. Ichitsubo,<sup>d</sup> E. Matsubara,<sup>d</sup> and N. Nishiyama<sup>e</sup>

<sup>a</sup>*Center for Materials Research Using Third-Generation Synchrotron Radiation Facilities, Hiroshima Institute of Technology, Hiroshima 731-5193, Japan*

<sup>b</sup>*Hiroshima Synchrotron Radiation Center, Hiroshima University, Higashi-Hiroshima 739-0046, Japan*

<sup>c</sup>*Graduate School of Information Sciences, Hiroshima City University, Hiroshima 731-3194, Japan*

<sup>d</sup>*Department of Materials Science and Engineering, Graduate School of Engineering, Kyoto University, Kyoto 606-8501, Japan*

<sup>e</sup>*R&D Institute of Metals and Composites for Future Industries, Sendai 980-8577, Japan*

Bulk metallic glasses of Pd-Ni-Cu-P alloys, discovered by Nishiyama and Inoue [1], have intensively been investigated due to their good glass-forming abilities (GFA). They have optimized the concentration dependence of the critical-cooling-rate, and found that  $\text{Pd}_{42.5}\text{Ni}_{7.5}\text{Cu}_{30}\text{P}_{20}$  has at present the slowest critical-cooling-rate (CCR) of 0.067 K/s and can form a massive bulk glass with a diameter of more than 40 mm by simple water-quenching [2]. Although several thermodynamic and mechanical properties have been investigated for the Pd-Ni-Cu-P glassy alloys in detail [2], only a few fundamental attempts have been made from the viewpoints of its structural and electronic properties to understand why it has such an excellent GFA. Electrical conductivity,  $\sigma$ , measurements for the  $\text{Pd}_{42.5}\text{Ni}_{7.5}\text{Cu}_{30}\text{P}_{20}$  metallic glass [3] showed that  $\sigma$  decreases by exchanging the Ni with Cu atoms from the reference  $\text{Pd}_{40}\text{Ni}_{40}\text{P}_{20}$  glass [4], which has a bad CCR of 1.6 K/s [5], suggesting a decrease of electronic density of states (DOS) at the Fermi energy,  $N(E_F)$ . With the further replace of Ni by Cu, the  $\text{Pd}_{40}\text{Cu}_{40}\text{P}_{20}$  glass has a worse CCR of more than  $10^3$  K/s, and a smaller  $\sigma$  value [6].

In order to clarify the role of the electronic structure in this excellent glass-former  $\text{Pd}_{42.5}\text{Ni}_{7.5}\text{Cu}_{30}\text{P}_{20}$  by comparing to the  $\text{Pd}_{40}\text{Ni}_{40}\text{P}_{20}$  reference glass, a series of electronic spectroscopic measurements were recently performed [7], such as in-house photoemission spectroscopy (PES) and inverse-photoemission spectroscopy (IPES), incident photon energy dependence of PES using synchrotron radiation. Since the knowledge of the partial DOS is essential for the detailed study of the electronic DOS, we have also measured the Ni and Cu 3d partial DOS in the valence band using soft X-ray emission spectroscopy (SXES), and the Pd 4d, Ni and Cu 3d partial DOS in the conduction band using X-ray absorption spectroscopy (XAS). From these data, partial DOS of Pd 4d, Ni 3d, and Cu 3d electrons were estimated, and it was found that the Pd 4d partial DOS largely decreases near the  $E_F$ , and its feature seems to become localized by replacing the Ni atoms with the Cu atoms, while the Ni partial DOS remains almost unchanged. Therefore, these electronic data demonstrate that these results are closely related to the excellent GFA of the  $\text{Pd}_{42.5}\text{Ni}_{7.5}\text{Cu}_{30}\text{P}_{20}$  bulk metallic glass through a selective formation of Pd-P covalent bonds. This was also supported by a recent study of local atomic structure around the Pd atoms using an anomalous X-ray scattering [8].

Due to an extremely small value of the photoionization crosssection of the P element [9], information on the electronic structure of the P atoms has been completely lack. Subsequently to the above works, we have recently measured Pd 3d, Ni 3p, Cu 3p, and P 2p core-level spectra of the  $\text{Pd}_{42.5}\text{Ni}_{7.5}\text{Cu}_{30}\text{P}_{20}$  glass, and compared them to those of the  $\text{Pd}_{40}\text{Ni}_{40}\text{P}_{20}$  and  $\text{Pd}_{40}\text{Cu}_{40}\text{P}_{20}$  reference glasses. In this report, we present the obtained data, and

discuss changes of the chemical nature of the whole elements by replacing the Ni atoms with the Cu atoms, and the relation to the excellent GFA of the  $\text{Pd}_{42.5}\text{Ni}_{7.5}\text{Cu}_{30}\text{P}_{20}$  glass.

The procedure of the sample preparation was given elsewhere [2]. The absence of crystallinity in the samples was confirmed by X-ray diffraction and calorimetry. The composition of the samples was examined to be within 1 % by an electron-probe micro-analysis method before and after the experiments. The core spectra were measured using a PES spectrometer at the beamline BL7 of Hiroshima Synchrotron Radiation Center. Ultraviolet photons generated from the storage ring HiSOR with the ring energy of 700 MeV and the ring current of 160-300 mA were monochromatized with a Dragon-type monochromator, covering the incident photon-energy  $h\nu$  from 20 to 600 eV. A PES spectrometer with a hemispherical photoelectron energy-analyzer (GAMMA-DATA SCIENTA SES100) attached to the analyzer chamber at the end-station of BL7, was used for the PES experiment. The overall energy resolution of the PES spectrometer was about 0.1 eV at  $h\nu = 220$  eV for the Ni 3p, Cu 3p, and P 2p spectra, and about 0.5 eV at  $h\nu = 450$  eV for the Pd 3d spectra. All the core spectra were collected at room temperature. Clean surfaces were in situ obtained by Ar ion sputtering in a sample preparation chamber attached with the analyzer ones, which were kept under ultrahigh vacuum with a basic pressure below  $1 \times 10^{-10}$  mbar. Any core spectra due to oxygen or carbon contamination were not visible within 24 h after the sample cleaning, and the measurements were performed within 12 h. The energy of all spectra was defined with respect to the  $E_F$  determined from the spectra of a freshly evaporated Au film.

Figure 1 shows the P 2p core spectra of  $\text{Pd}_{42.5}\text{Ni}_{7.5}\text{Cu}_{30}\text{P}_{20}$ ,  $\text{Pd}_{40}\text{Ni}_{40}\text{P}_{20}$  and  $\text{Pd}_{40}\text{Cu}_{40}\text{P}_{20}$  glasses measured at  $h\nu = 220$  eV observed at a binding energy of about  $-130$  eV, the intensities of which are reduced to be unity at the peak position with respect to the background at the higher energies. By replacing the Ni atoms by the Cu atoms, the P  $2p_{3/2}$  core spectrum shows a slight shift towards a *smaller* binding-energy by 0.04 eV in  $\text{Pd}_{42.5}\text{Ni}_{7.5}\text{Cu}_{30}\text{P}_{20}$ , and much larger shift in  $\text{Pd}_{40}\text{Cu}_{40}\text{P}_{20}$  towards a *smaller* binding-energy by 0.29 eV. It should be noted that the spectral shapes change with adding the Cu atoms, and the new P  $2p_{3/2}$  core level appears at about  $-129.8$  eV in  $\text{Pd}_{42.5}\text{Ni}_{7.5}\text{Cu}_{30}\text{P}_{20}$  glass. Thus, the center of gravity of the P  $2p_{3/2}$  core level shifts towards the larger binding-energy in  $\text{Pd}_{42.5}\text{Ni}_{7.5}\text{Cu}_{30}\text{P}_{20}$  glass.

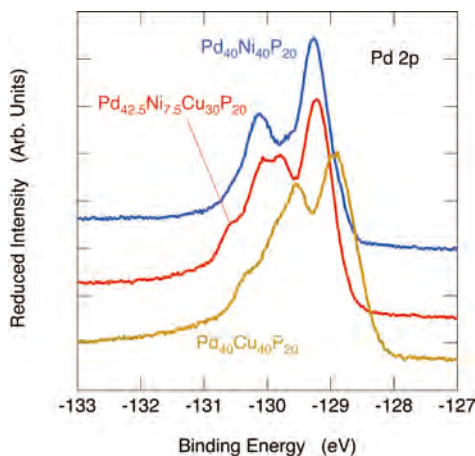


Fig. 1. The P 2p core spectra of  $\text{Pd}_{42.5}\text{Ni}_{7.5}\text{Cu}_{30}\text{P}_{20}$  and  $\text{Pd}_{40}\text{Ni}_{40}\text{P}_{20}$  glasses measured at  $h\nu = 220$  eV.

Figure 2 shows the reduced Pd  $3d_{5/2}$  core spectra of  $\text{Pd}_{42.5}\text{Ni}_{7.5}\text{Cu}_{30}\text{P}_{20}$ ,  $\text{Pd}_{40}\text{Ni}_{40}\text{P}_{20}$  and  $\text{Pd}_{40}\text{Cu}_{40}\text{P}_{20}$  glasses measured at  $h\nu = 400$  eV observed at a binding energy of about  $-336$  eV.

By replacing the Ni atoms by the Cu atoms, the P  $3d_{5/2}$  spectrum shows a large shift in  $\text{Pd}_{42.5}\text{Ni}_{7.5}\text{Cu}_{30}\text{P}_{20}$  towards a *larger* binding-energy from by  $-0.38$  eV. With the further replace by the Cu atoms, however, the P  $3d_{5/2}$  spectrum shows a large shift towards *smaller* binding-energy from by  $-0.28$  eV. The same shifts are also observed in the Pd  $3d_{3/2}$  core spectra.

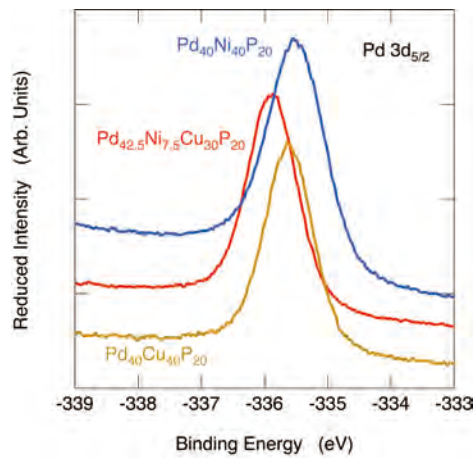


Fig. 2. The Pd  $3d_{5/2}$  core spectra of  $\text{Pd}_{42.5}\text{Ni}_{7.5}\text{Cu}_{30}\text{P}_{20}$  and  $\text{Pd}_{40}\text{Ni}_{40}\text{P}_{20}$  glasses measured at  $h\nu = 400$  eV.

Figure 3 shows the reduced Ni  $3p$  core spectra of  $\text{Pd}_{42.5}\text{Ni}_{7.5}\text{Cu}_{30}\text{P}_{20}$  and  $\text{Pd}_{40}\text{Ni}_{40}\text{P}_{20}$  glasses measured at  $h\nu = 220$  eV observed at a binding energy of about  $-67$  eV. Although the Ni  $3p$  spectrum is rather scattered due to the small concentration of the Ni element, a shift towards a larger binding-energy is observed by  $0.28$  eV in the Ni  $3p_{3/2}$  spectra by replacing the Ni atoms by the Cu atoms. Although the Ni  $3d$  partial valence-band DOS measured by SXES seems not to be changed [7], the core level shifts can be seen.

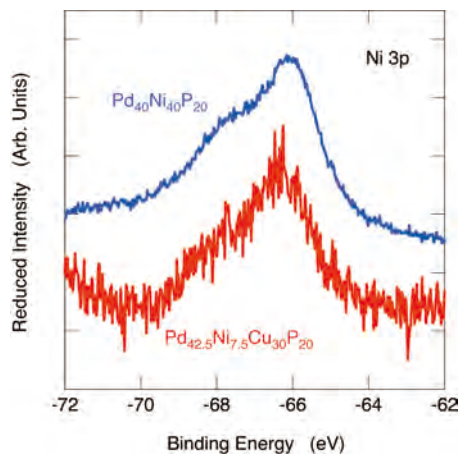


Fig. 3. The Ni  $3p$  core spectra of  $\text{Pd}_{42.5}\text{Ni}_{7.5}\text{Cu}_{30}\text{P}_{20}$  and  $\text{Pd}_{40}\text{Ni}_{40}\text{P}_{20}$  glasses measured at  $h\nu = 220$  eV.

Figure 4 shows the reduced Cu  $3p$  core spectra of  $\text{Pd}_{42.5}\text{Ni}_{7.5}\text{Cu}_{30}\text{P}_{20}$  and  $\text{Pd}_{40}\text{Cu}_{40}\text{P}_{20}$  glasses measured at  $h\nu = 220$  eV observed at a binding energy of about  $-75$  eV. A slight shift towards a smaller binding-energy is observed by  $0.11$  eV in the Cu  $3p_{3/2}$  spectra by replacing the Ni atoms by the Cu atoms.

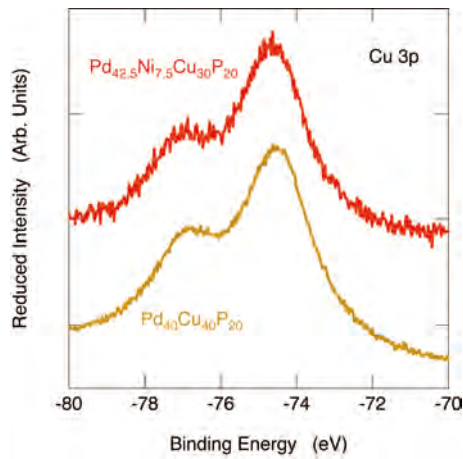


Fig. 4. The Cu 3p core spectra of  $\text{Pd}_{42.5}\text{Ni}_{7.5}\text{Cu}_{30}\text{P}_{20}$  and  $\text{Pd}_{40}\text{Cu}_{40}\text{P}_{20}$  glasses measured at  $h\nu = 220$  eV.

It should be noted that the core spectra in all the elements, Pd 3d<sub>5/2</sub>, Ni 3p<sub>3/2</sub>, Cu 3p<sub>3/2</sub>, and P 2p<sub>3/2</sub> always show the larger values in  $\text{Pd}_{42.5}\text{Ni}_{7.5}\text{Cu}_{30}\text{P}_{20}$  glass compared to the reference  $\text{Pd}_{40}\text{Ni}_{40}\text{P}_{20}$  and  $\text{Pd}_{40}\text{Cu}_{40}\text{P}_{20}$  glasses. The shifts of the binding energies in every core-level are observed, indicating changes of the chemical nature of these elements by replacing the Ni atoms with the Cu atoms. A similar change in the core spectra was already discussed by Alamgir et al. [10] for  $\text{Pd}_{40}\text{Ni}_{40}\text{P}_{20}$  alloys from crystal and glassy states, and such shifts indicate a charge transfer. The present finding of the shifts in the core levels revealed that all the elements in the  $\text{Pd}_{42.5}\text{Ni}_{7.5}\text{Cu}_{30}\text{P}_{20}$  have the smallest electron charges among three metallic glasses, which may closely related to the excellent GFA in the  $\text{Pd}_{42.5}\text{Ni}_{7.5}\text{Cu}_{30}\text{P}_{20}$  glass.

In conclusion, the Pd 3d, Ni 3p, Cu 3p, and P 2p core-level spectra of the  $\text{Pd}_{42.5}\text{Ni}_{7.5}\text{Cu}_{30}\text{P}_{20}$  were measured by PES together with those of the reference  $\text{Pd}_{40}\text{Ni}_{40}\text{P}_{20}$  and  $\text{Pd}_{40}\text{Cu}_{40}\text{P}_{20}$  glasses. By replacing the Ni atoms with the Cu atoms, a shift towards a larger binding-energy is observed in the core spectra of all the elements, Pd 3d<sub>5/2</sub>, Ni 3p<sub>3/2</sub>, Cu 3p<sub>3/2</sub>, and P 2p<sub>3/2</sub>, by which it can be concluded that all the elements in the  $\text{Pd}_{42.5}\text{Ni}_{7.5}\text{Cu}_{30}\text{P}_{20}$  have the smallest electron charges among three metallic glasses, which may closely related to the excellent GFA in the  $\text{Pd}_{42.5}\text{Ni}_{7.5}\text{Cu}_{30}\text{P}_{20}$  glass.

- [1] N. Nishiyama and A. Inoue, *Mater. Trans. JIM* 37 (1996) 1531.
- [2] N. Nishiyama and A. Inoue, *Appl. Phys. Lett.* 80 (2002) 568.
- [3] O. Haruyama et al., *J. Non-Cryst. Solids* 312-314 (2002) 552.
- [4] O. Haruyama et al., *Mater. Sci. Eng. A* 375-377 (2004) 288.
- [5] N. Nishiyama and A. Inoue, *Mater. Trans. JIM* 38 (1997) 464.
- [6] G. L. Tangonan, *Phys. Lett.* 54A, 307 (1975).
- [7] S. Hosokawa et al., *Acta Mater.* 55 (2007) 3413.
- [8] S. Hosokawa et al., *Mater. Trans.* 48, 2358 (2007).
- [9] J. J. Yeh and I. Lindau, *At. Data Nucl. Data Table* 4s 32 (1985) 1.
- [10] F. M. Alamgir FM et al., in ed. by T. B. Massalski and P. E. A. Turchi, *The Science of Complex Alloy Phases*, Warrendale (PA), The Minerals, Metals and Materials Society, 2005.

## Electronic States in $Zr_{70}Ni_{20}Al_{10}$ Bulk Metallic Glass

T.Nasu<sup>a</sup>, S.Hosokawa<sup>b</sup>, M.Nakatake<sup>c</sup>, H.Sato<sup>c</sup>, W.Zhang<sup>d</sup> and A.Inoue<sup>d</sup>

<sup>a</sup>*Faculty of Education, Art and Science, Yamagata University, Yamagata 990-8560 Japan*

<sup>b</sup>*Hiroshima Institute of Technology, Hiroshima 731-5193 Japan*

<sup>c</sup>*Hiroshima Synchrotron Radiation Research Center, Hiroshima University, Higashi-Hiroshima 739-0046 Japan*

<sup>d</sup>*Institute of Materials Research, Tohoku University, Sendai 980-8577 Japan*

**Abstract.** A Zr-based bulk metallic glass of  $Zr_{70}Ni_{20}Al_{10}$  has an excellent glass-forming ability (GFA), and can form a massive bulk glass by simple water-quenching. In order to clarify the role of electronic structure in this excellent GFA of  $Zr_{70}Ni_{20}Al_{10}$  glass by comparing to the  $Zr_{70}Ni_{30}$  reference, having a worse GFA, valence-band photoemission spectra were measured with changing the incident photon energy using synchrotron radiation at BL7 of HiSOR. We have also measured Ni 3P, Zr 3d and Zr 4p core-level photoemission spectra of the  $Zr_{70}Ni_{20}Al_{10}$  glass, and compared them to those of the  $Zr_{70}Ni_{30}$  reference glass. The shifts of the binding energies in every core-level are observed, indicating changes of the chemical nature by replacing the Ni atoms with Al atoms.

### 1. Introduction

Bulk metallic glass of Zr-Ni-Al alloys was discovered by Inoue et al [1]. It is well known that the glass forming ability (GFA) in the Zr-Ni-based binary metallic glass can be improved by the addition of Al [1]. Nagel and Tauc suggested that good GFA is closely related to the decrease of  $N(E_F)$ , or Mott's pseudogap, under a free-electron model [2]. Electronic structural studies on GFA of bulk metallic glass were done by Suzuki et al.[3] and Hosokawa et al.[4]. These results showed good agreements with the prediction of correlation of GFA with electronic structure. Short range structure change of Zr-Ni-based metallic glass induced by addition of Al was studied by Sato et al by means of X-ray diffraction and EXAFS [5]. The main purpose of this research is to investigate electronic structural change of Ni-Zr alloy by Al addition in terms of GFA.

### 2. Experimental procedure

The samples were prepared as follows [1]. The master ingots were prepared by arc-melting mixtures of pure Zr, Ni and Al in an argon atmosphere. Rapid quenching was done by using single-roller technique for obtaining metallic glass sample from the master ingot pieces. The  $h$  dependent photoemission spectra (PES) experiments were carried out at beamline BL7 of the Hiroshima Synchrotron Radiation Centre. Ultraviolet photons generated from the storage ring HiSOR with a ring energy of 700 MeV and a ring current of 160-300 mA were monochromatized with a Dragon-type monochromater, ranging  $h\nu$  values from 20 to 380 eV. A PES spectrometer with a hemispherical photoelectron energy analyzer (SCIENTA SES100) equipped with the analyzer chamber at the end-station of BL7, was used for the PES experiment. The overall energy resolution of the PES spectrometer was set to be 0.1 eV at  $h\nu=100$  eV. All the PES spectra were collected at room temperature. Clean surfaces were in situ obtained by Ar sputtering in a sample preparation chamber attached to the analyzer chambers, which were kept under ultrahigh vacuum below  $1 \times 10^{-10}$  mbar. Any changes in the spectral features due to oxygen or carbon contamination were not observed within 12 h after the sample cleaning and the measurements were performed within 6 h. The energy of each of the spectra was defined with respect to the  $E_F$  determined from the spectra of a freshly evaporated Au film.

### 3. Results

Figure 1 shows the PES spectra from  $h\nu=30-150$  eV of  $Zr_{70}Ni_{20}Al_{10}$  as a function of the binding energy,  $E_B$ . Figure 2 shows the PES spectra from  $h\nu=30-150$  eV of  $Zr_{70}Ni_{30}$  glasses as a function of  $E_B$ .

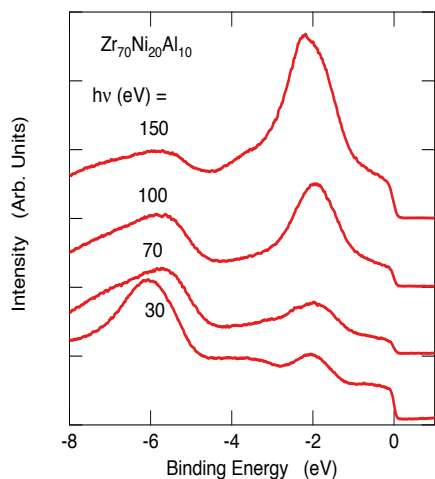


Fig.1. The  $h\nu$  dependent PES spectra between  $h\nu=30$  and 150 eV of  $Zr_{70}Ni_{20}Al_{10}$  metallic glass.

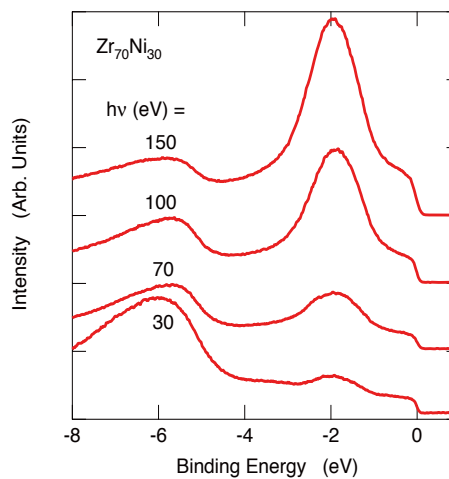


Fig.2. The  $h\nu$  dependent PES spectra between  $h\nu=30$  and 150 eV of  $Zr_{70}Ni_{30}$  metallic glass.

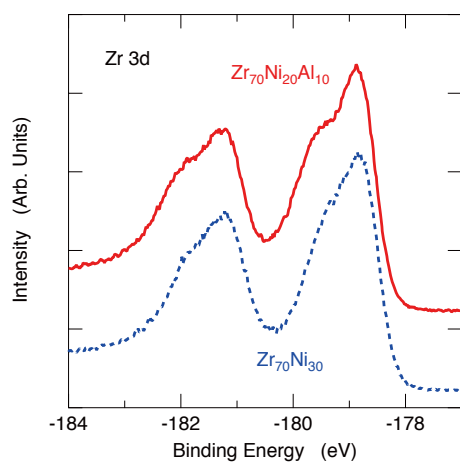


Fig.3. Zr 3d core-level PES spectra with  $h\nu=320$  eV of  $Zr_{70}Ni_{20}Al_{10}$  metallic glass (solid line) and  $Zr_{70}Ni_{30}$  metallic glass (dashed line)..

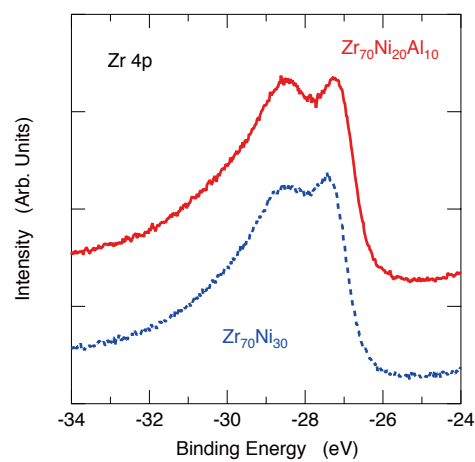


Fig.4. Zr 4p valence-band PES spectra with  $h\nu=240$  eV of  $Zr_{70}Ni_{20}Al_{10}$  metallic glass (solid line) and  $Zr_{70}Ni_{30}$  metallic glass (dashed line).

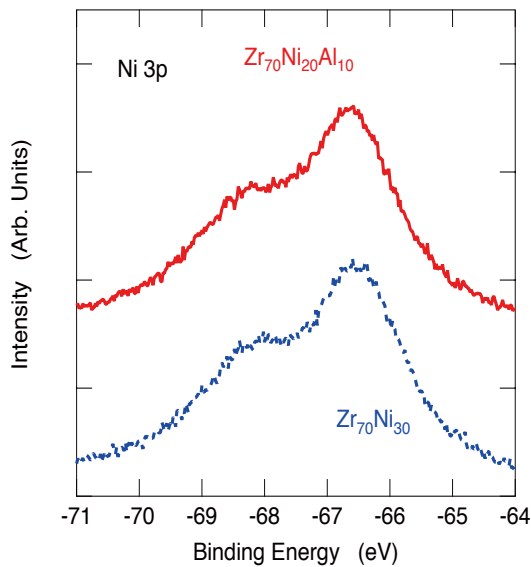


Fig.5 Ni 3p core-band PES spectra with  $h\nu=240$  eV of  $Zr_{70}Ni_{20}Al_{10}$  metallic glass (solid line) and  $Zr_{70}Ni_{30}$  metallic glass (dotted line).

Figure 3 shows Zr 3d core-level PES spectra of  $Zr_{70}Ni_{20}Al_{10}$  metallic glass (solid line) and  $Zr_{70}Ni_{30}$  metallic glass (dotted line). The peak position does not seem to shift by replacing Ni atom to Al atom as shown in Fig.3. Figure 4 shows Zr 4p valence-band PES spectra of  $Zr_{70}Ni_{20}Al_{10}$  metallic glass (solid line) and  $Zr_{70}Ni_{30}$  metallic glass (dotted line). In this case, the peak position of Zr 4p shifts 0.15 eV to smaller binding energy side by replacing Ni atom to Al atom as shown in Fig.4. Figure 5 shows Ni 3p core-level PES spectra of  $Zr_{70}Ni_{20}Al_{10}$  metallic glass (solid line) and  $Zr_{70}Ni_{30}$  metallic glass (dotted line). The peak position of Ni 3p shifts 0.1 eV to larger binding energy side by replacing Ni atom to Al atom.

#### 4. Discussion

Nagel and Tauc suggested that good GFA is closely related to the decrease of  $N(E_F)$ , or Mott's pseudogap, under a free-electron model. Electronic structural studies on GFA of bulk metallic glass were done by Suzuki et al. [3] and Hosokawa et al. [4]. Their results showed good agreements with the prediction of correlation of GFA with electronic structure by Nagel and Tauc. From the results of measurements on the  $h\nu$  dependent PES spectra of  $Zr_{70}Ni_{20}Al_{10}$  and  $Zr_{70}Ni_{20}$  metallic glasses as shown in Fig.1 and Fig.2, it was not so clear that if the density of state near the Fermi energy decreases or not by replacing Ni atoms to Al atoms. In Fig.1, the peak at around 6 eV corresponds to Zr, the peak at 2 eV corresponds to Ni, and the weak shoulder beside the peak at 2 eV corresponds to Al atom. Comparing Fig.1 with Fig.2, it is clear that the peak around 2 eV shifts to larger binding energy side and makes a shoulder by replacing Ni atoms to Al atoms. As shown in Fig.5, the peak position of Ni 3p shifts 0.1 eV to larger binding energy side, and the peak position of Zr 4p shifts 0.15 eV to smaller binding energy side by replacing Ni atom to Al atom as shown in Fig.4. This means that electrons transferred from Ni atoms to Zr atoms. By the way, the short range structure change of Zr-Ni-based metallic glass induced by addition of Al was studied by Sato et al. by means of X-ray diffraction and EXAFS [5]. According to Sato's structural research, the Al-induced disordered local environment accompanying with the formation of novel local structure of Zr-Al and decomposition of that of Zr-Ni would improve effectively thermal stability of the Zr-Ni-Al metallic glass [5]. The formation of novel local structure of Zr-Al made a shift of Zr 4p level as shown in Fig.4. The decomposition of local structure of Zr-Ni made a shift of Ni 3p as shown in Fig.5. Totally, electron transfer occurs from Ni atom to Zr atom by replacing the

Ni atoms to Al atoms. The electrons, which transferred to Zr atoms from Ni atoms, presumably play an important role for the formation of novel local structure of Zr-Al.

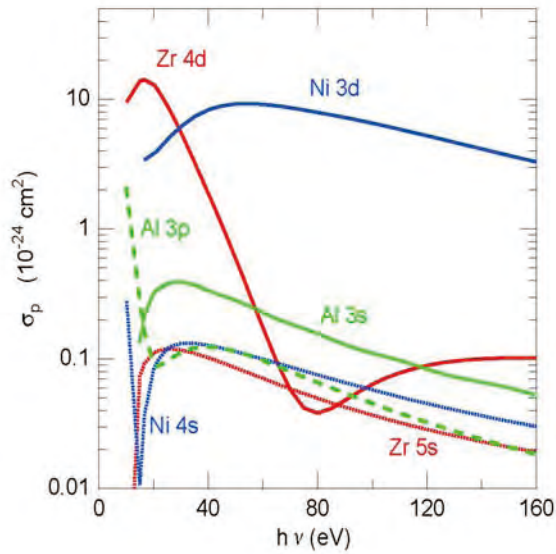


Fig.6 The photo ionization crosssection  $\sigma_p$  values of Zr 4d and 5s, Ni 3d and 4s and Al 3s, 3p electrons as a function of  $h\nu$ .

## 5. Summary

The PES spectra of  $Zr_{70}Ni_{20}Al_{10}$  metallic glass were measured to examine the excellent glass forming ability (GFA) compared with those of  $Zr_{70}Ni_{30}$  glass. By replacing Ni atoms to Al atoms, the peak position of Ni 3p shifts 0.1 eV to larger binding energy side and the peak position of Zr 4p shifts 0.15 eV to smaller binding energy side. This means the electrons transfer occur from Ni atoms to Zr atoms. It suggests that Zr-Al strong correlation formed by this electron transfer which occurs by addition of Al atoms to Zr-Ni glass, and increases GFA.

## References

- [1] Inoue A, Zhang T and Masumoto T 1990 *Mater. Trans. JIM* 31 177
- [2] Nagel SR and Tauc J 1975 *Phys. Rev.Lett.* 35 380
- [3] Suzuki K, Miyazaki K, Soda K, Takeuchi K, Hasegawa T, Sato Y and Mizutani U 2006 *J. Jpn. Soc. Powder and Powder Metallurgy* 53 107
- [4] Hosokawa S, Sato H, Happo N, Mimura K, Tezuka Y, Ichitubo T, Matsubara E and Nishiyama N 2007 *Acta Mater.* 55 3413
- [5] Sato S, Sanada T, Saida J, Imafuku M, Matsubara E and Inoue A 2005 *Mater. Trans.* 46 2893

## Angle-resolved photoemission spectroscopy of SrSi<sub>2</sub>/Si(111)

H. Maso<sup>a</sup>, H. Kurihara<sup>a</sup>, Y. Tatsukawa<sup>a</sup>, H. Sato<sup>b</sup>, M. Nakatake<sup>b</sup>, H. Namatame<sup>b</sup> and M. Taniguchi<sup>a,b</sup>

<sup>a</sup>Graduate School of Science, Hiroshima University, <sup>b</sup>HiSOR, Hiroshima University

In recent years, epitaxial silicides on silicon have been a subject to intense investigations as well as increasing technological application. Evaporation of the alkali earth metal or the rare earth metal such as M=Ca, Sr, Ce and so on, on the Si substrate forms MSi<sub>2</sub> epitaxial film with a various Si network. Recently, we have grown tr6-type CaSi<sub>2</sub> epitaxial film by Ca evaporation on the Si (111) substrate and have successfully derived the experimental band dispersion for the grown CaSi<sub>2</sub> films by means of angle-resolved photoemission spectroscopy (ARPES) [1]. The results exhibit that the CaSi<sub>2</sub> epitaxial film shows the metallic behavior and a band crosses the Fermi level (E<sub>F</sub>) near the  $\Gamma$  point forming “hole pocket” with the Fermi wavenumber of  $k_F=0.22 \text{ \AA}^{-1}$ . The whole feature of band structures of CaSi<sub>2</sub> epitaxial film is in good agreement with the calculated result [2]. We have also observed the Fermi surface with a six-fold symmetry, which reflects the ty6-type CaSi<sub>2</sub>(111) surface symmetry and is similar to that of YSi<sub>2</sub> [3].

In this study, we have tried to grow SrSi<sub>2</sub> epitaxial film on the Si(111) substrate by evaporating the Sr element and have carried out ARPES for the grown films. Recently, Yamanaka *et al.* have been revealed that the Sr evaporation onto the Si(111) substrate leads to the EuGe<sub>2</sub>-type (h1-type) SrSi<sub>2</sub>(111) epitaxial films, which is very similar to tr6-type one, with a low lattice mismatch with the Si(111) substrate [4]. It is noted that the EuGe<sub>2</sub>-type (h1-type) SrSi<sub>2</sub> is not naturally grown. The electronic structure of SrSi<sub>2</sub> is not known at present.

The SrSi<sub>2</sub> epitaxial film was prepared by evaporating the Sr element with a purity of 99.9 % onto the Si(111) substrate at 800 °C with 0.05 Å/sec. After the evaporation, the substrate temperature is kept at 800 °C for 1 hour to proceed the reaction between Sr and Si. For the grown films, the 2×2 RHEED (reflection high energy electron diffraction) pattern was successfully obtained, which was also observed for CaSi<sub>2</sub> [1], and AES (Auger electron spectroscopy) analysis showed no contamination just after the growth. For the grown samples, we have *in situ* measured the ARPES spectra o beamline BL7 of HiSOR.

Figure 1 shows the intensity plot of the ARPES spectra of SrSi<sub>2</sub> ( $\theta_{Sr}=100 \text{ \AA}$ ) taken at  $h\nu=27 \text{ K}$  along  $\Gamma$ - $\Sigma$ -M direction. Since it is somewhat difficult to direct see the band dispersion from the plot, we indicate those by dashed lines for guide. The upper right panel

exhibits the expanded intensity plot around  $E_F$  with the second-order derivative of the ARPES spectra. We find characteristic three bands A, B and C. Of these bands, the A and B bands originate from Si(111). The C band newly appears by evaporating Sr and crosses  $E_F$  near the  $\Gamma$  point forming “hole pocket”. An existence of the C band indicates that SrSi<sub>2</sub> epitaxial film shows the metallic behavior, though the density of states is extremely low at  $E_F$ .

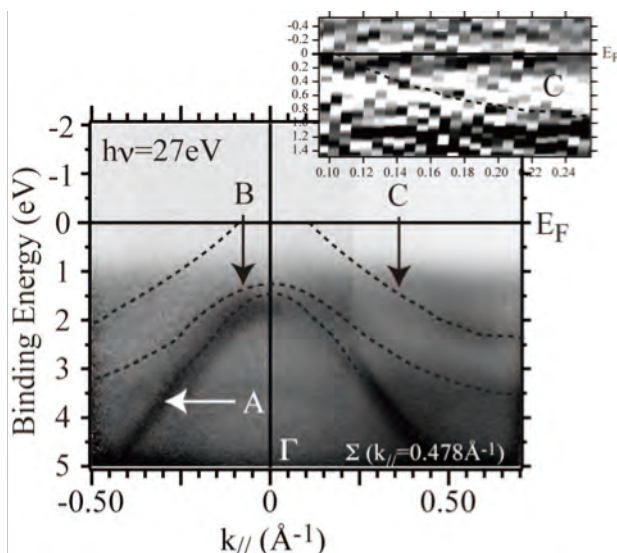


**Fig. 1.** Experimentally derived band dispersion of SrSi<sub>2</sub>/Si(111) epitaxial film.

The whole feature of the band structure of SrSi<sub>2</sub> is very similar to that of CaSi<sub>2</sub>,

reflecting their similar crystal structure (h1-type for SrSi<sub>2</sub> and tr6-type for CaSi<sub>2</sub>). In case of CaSi<sub>2</sub>, its C band is derived from the hybridization between the Ca 3d and Si 3p orbitals normal to (111) layers, in comparison with the results of the band-structure calculation [2]. Accordingly, also for SrSi<sub>2</sub>, the C band is derived from the Sr 4d – Si 3p hybridization bands.

Although h1-type SrSi<sub>2</sub> and tr6-type CaSi<sub>2</sub> show the similar band dispersion, we find slight differences in the C band; its binding energy of SrSi<sub>2</sub> is deeper than that of CaSi<sub>2</sub> and  $k_F=0.10 \text{ \AA}^{-1}$  for SrSi<sub>2</sub> is also smaller than  $k_F=0.22 \text{ \AA}^{-1}$ . These differences are qualitatively explained by the band-structure calculations for h1-type CaSi<sub>2</sub> and tr6-type CaSi<sub>2</sub> [1]. The Sr 4d states more strongly hybridize with the Si 3p states compared with the Ca 3d and Si 3p states and the energy gap between Sr 4d – Si 3p bonding and anti-bonding bands becomes larger, leading to the deeper binding-energy and the small  $k_F$  of SrSi<sub>2</sub>.

The difference of the h1-type and tr6-type crystal structure is also reflected in the Si 2p spectra as the difference of the number of the Si site; the Si 2p spectrum of h1-type SrSi<sub>2</sub> with one Si site is composed of one component, while that of tr6-type CaSi<sub>2</sub> with two Si sites is composed of two components.

## References

- [1] S. Nishimoto, Master Thesis, Graduate School of Science, Hiroshima University 2006; S. Nishimoto *et al.*, the 10th Hiroshima International Symposium on Synchrotron Radiation, P-28, 2006.
- [2] S. Fahy and D. R. Hamann, Phys. Rev. B **41**, 7587 (1990).
- [3] C. Rogero *et al.*, Phys. Rev. B **69**, 045312 (2004).
- [4] Y. Tokinaga, Master Thesis, Graduate School of Engineering, Hiroshima University 2001.

## The Constant Volume Dilution Effect of Eu Site in $\text{EuPd}_2\text{Si}_2$ : Eu 4*d*-4*f* Resonant Photoemission Study

K. Mimura, D. Okumura, T. Ishizu, M. Nakatake<sup>A</sup>, T. Kuwai<sup>B</sup>,  
H. Namatame<sup>A</sup>, M. Taniguchi<sup>A</sup>, Y. Taguchi, and K. Ichikawa

*Graduate School of Engineering, Osaka Prefecture University, Sakai 599-8531, Japan*

<sup>A</sup>*HSRC, Hiroshima University, Higashi-Hiroshima 739-0046, Japan*

<sup>B</sup>*Faculty of Science, Toyama University, Toyama 930-8555, Japan*

$\text{EuPd}_2\text{Si}_2$  undergoes an abrupt but continuous valence transition at around 160 K: the Eu mean valence changes from 2.8 below 130 K to 2.3 above 180 K [1-3]. Recently, in the Eu-diluted system substituted by nonmagnetic ( $\text{La}_{0.67}\text{Y}_{0.33}$ ) with constant lattice volume, electrical and magnetic anomalies at dilution concentration ( $x$ ) higher than 0.25 have been discussed from the standpoint of the Kondo effect [4]. In this study we have investigated the  $x$  dependence of Eu 4*f* states in  $(\text{Eu}_{1-x}(\text{La}_{0.67}\text{Y}_{0.33})_x)\text{Pd}_2\text{Si}_2$  by means of Eu 4*d*-4*f* resonant photoemission spectroscopy (RPES)

We used polycrystalline  $(\text{Eu}_{1-x}(\text{La}_{0.67}\text{Y}_{0.33})_x)\text{Pd}_2\text{Si}_2$  samples ( $x = 0, 0.12, 0.85$ ) grown by arc melting and by annealing at 900 °C for one week. Eu 4*d*-4*f* RPES measurements at the temperature lower than 20 K were performed at BL-7 with the excitation photon energies ( $h\nu$ 's) between 120 and 170 eV. The sample was *in situ* fractured under the base pressure of  $4 \times 10^{-8}$  Pa. The overall energy resolution around the Eu 4*d*-4*f* threshold was set at 150 meV.

Figure 1 shows Eu 4*f* spectra of  $(\text{Eu}_{1-x}(\text{La}_{0.67}\text{Y}_{0.33})_x)\text{Pd}_2\text{Si}_2$  ( $x = 0, 0.12$  and  $0.85$ ). The Eu 4*f* spectrum has been evaluated by subtracting the spectrum measured at the resonance minimum ( $h\nu = 136$  eV) from that at the  $\text{Eu}^{3+}$  4*f* resonance maximum ( $h\nu = 150.5$  eV). In each spectrum, multiplet structures from  $\sim E_F$  to 3 eV and from 5.5 to 11 eV ascribed to the  $\text{Eu}^{2+}$  and  $\text{Eu}^{3+}$  4*f* states, respectively. Furthermore, the component around 0.7 eV is ascribed to the bulk  $\text{Eu}^{2+}$  4*f* states, while that around 2 eV to the surface  $\text{Eu}^{2+}$  4*f* states, respectively. A noteworthy point is that the  $\text{Eu}^{3+}$  4*f* component is observed even in the spectrum of  $x = 0.85$ , even though the suppression of Eu intersite interaction has been suggested at the diluted concentration higher than  $x = 0.25$  [4]. Then, we extracted bulk  $\text{Eu}^{2+}$  and  $\text{Eu}^{3+}$  components from the spectrum of  $x = 0.85$  and found that its integrated intensity ratio ( $I^{3+}/I^{2+}$ ) is nearly the same as that of  $x = 0.12$ . This probably suggests that the valence fluctuation of Eu in  $(\text{Eu}_{1-x}(\text{La}_{0.67}\text{Y}_{0.33})_x)\text{Pd}_2\text{Si}_2$  occurs across the

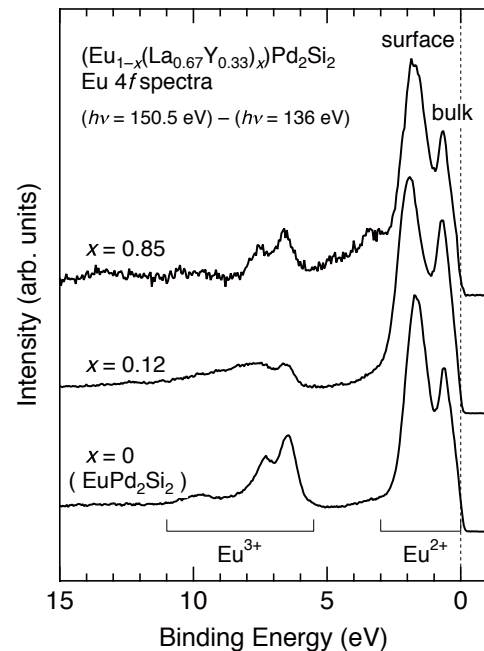


Fig. 1. The Eu site dilution dependence of Eu 4*f* spectra of  $(\text{Eu}_{1-x}(\text{La}_{0.67}\text{Y}_{0.33})_x)\text{Pd}_2\text{Si}_2$ . All the spectra were normalized by peak intensity of the  $\text{Eu}^{2+}$  4*f* state at around 2 eV.

extremely long range.

Figure 2 shows the  $\text{Eu}^{2+}$   $4f$  spectra of  $(\text{Eu}_{1-x}(\text{La}_{0.67}\text{Y}_{0.33})_x)\text{Pd}_2\text{Si}_2$  measured in detail. The detailed  $\text{Eu}$   $4f$  spectrum has been evaluated by subtracting the resonance minimum spectrum ( $h\nu = 136$  eV) from the  $\text{Eu}^{2+}$   $4f$  resonance maximum spectrum ( $h\nu = 141$  eV). We can find that a weak shoulder structure is observed at 0.15 eV in the spectrum of  $x = 0.85$ . The feature of its shoulder may be a quasi-particle peak due to the Kondo effect that in  $\text{Eu}$  compounds has not been discussed so far except for a few examples [5, 6]. We cannot, however, declare whether the shoulder is a quasi-particle peak or not at this moment, because of the difficulties of the accuracy for the  $\text{Eu}$   $4f$  spectral subtraction (The spectral intensity of conduction electrons for  $x = 0.85$  is much larger than those for  $x = 0$  and 0.12) and the energy resolution. We are planning to measure the spectra by  $\text{Eu}$   $3d$ - $4f$  RPES and hard X-ray photoemission spectroscopy with highly bulk sensitivity and discuss the Kondo effect for the sample with low concentration of  $\text{Eu}$ .

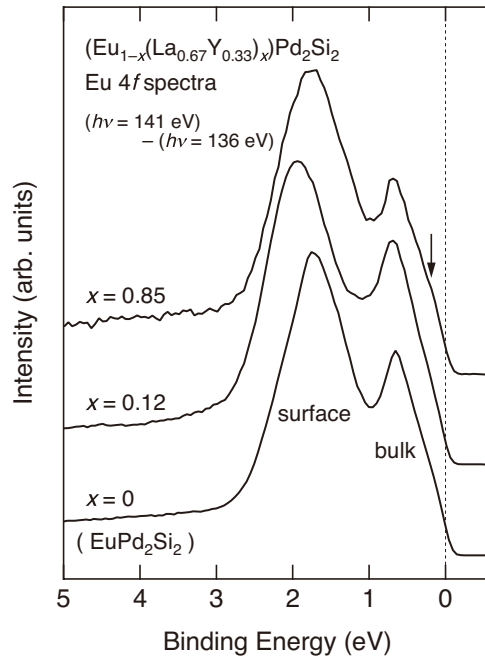


Fig. 2. The detailed  $\text{Eu}^{2+}$   $4f$  spectra of  $(\text{Eu}_{1-x}(\text{La}_{0.67}\text{Y}_{0.33})_x)\text{Pd}_2\text{Si}_2$ .

- [1] E.V. Sampathkumaran *et al.*, J. Phys. C: Solid State Phys. **14**, L237 (1981).
- [2] E. Kemly *et al.*, J. Magn. Magn. Mater. **47&48**, 403 (1985).
- [3] G. Wortmann *et al.*, J. Magn. Mang. Mater. **49**, 325 (1985).
- [4] T. Kuwai, *et al.*, J. Magn. Magn. Mater. **310**, e68 (2007).
- [5] S. Fukuda, *et al.*, J. Phys. Soc. Jpn. **72**, 3189 (2003).
- [6] Z. Hossain, *et al.*, Phys. Rev. B **69**, 014422 (2004).

## Temperature-Dependent Angle-Resolved Photoemission Spectra of TlInSe<sub>2</sub>: Specification of Incommensurate and Commensurate Phases

K. Mimura, T. Nogami, K. Abe, K. Wakita<sup>A</sup>, M. Arita<sup>B</sup>, N. Mamedov<sup>C</sup>, G. Orudzhev<sup>C</sup>, J. Takasu, Y. Yonehira, H. Namatame<sup>B</sup>, M. Taniguchi<sup>B</sup>, Y. Taguchi, and K. Ichikawa  
*Graduate School of Engineering, Osaka Prefecture University, Sakai 599-8531, Japan*  
<sup>A</sup> *Faculty of Engineering, Chiba Institute of Technology, Narashino, Chiba 275-0016, Japan*  
<sup>B</sup> *HSRC, Hiroshima University, Higashi-Hiroshima 739-0046, Japan*  
<sup>C</sup> *Azerbaijan National Academy of Science, Baku, AZ-1143, Azerbaijan*

TlInSe<sub>2</sub> has attracted much interest because of the structural low-dimensionality, and the interesting electric and thermoelectric properties [1, 2]. TlInSe<sub>2</sub> crystallizes in a quasi one-dimensional chain structure with a body-centered tetragonal unit cell of  $D_{4h}^{18}$  space group [3]. The structure is built-up of the edge-sharing InSe<sub>4</sub> tetrahedron along the crystallographic  $c$  axis, and of the Tl atoms positioned between the chains. Recently, the Seebeck coefficient of TlInSe<sub>2</sub> has then been found to be positive only below 473 K, reaching very high values of more than  $10^6$   $\mu\text{V/K}$  below 413 K [2]. The record-breaking thermoelectric power of TlInSe<sub>2</sub> has then been ascribed to the inhomogeneous charge distribution inherent in modulated structures, particularly, incommensurate phases.

Normal–incommensurate–commensurate (N–I–C) phase transition with decreasing temperature was observed in many materials of the TlMeX<sub>2</sub> (Me = Ga, In; X = S, Se, Te) family. In particular, temperature-dependent X-ray diffraction studies [4] disclosed the N–I–C transition in TlGaTe<sub>2</sub> [4]. In a similar way, the I phase might have taken place in TlInSe<sub>2</sub>. However, neither extended X-ray nor neutron scattering examination has been undertaken so far to come to unambiguous conclusions in this regard.

Very recently, our temperature-dependent angle-resolved photoemission spectroscopy (ARPES) studies at low temperature on TlInSe<sub>2</sub> have revealed splitting of some bands, related to the phase transition of this material [5]. In this study, we focus on the temperature-dependent experimental bands including the valence-band maximum (VBM) at the  $T$  point of the Brillouin zone (BZ), and discuss the observed peculiar temperature changes in terms of the N–I–C phase transition of TlInSe<sub>2</sub>.

The sample used was single crystalline TlInSe<sub>2</sub>. The ARPES spectra at 50 and 280 K were measured at the circular undulator beam line BL-9A. Clean (110) surfaces were obtained by *in situ* cleaving of the sample under the pressure lower than  $8 \times 10^{-11}$  Torr. We selected the excitation photon energy ( $h\nu$ ) of 11.4 eV to observe the ARPES spectra along the  $\Gamma$ - $H$ - $T$  ( $N$ - $P$ - $N$ ) direction of BZ of TlInSe<sub>2</sub>. This direction is parallel to the chains. The overall energy resolution was set at 5 meV and angular resolution was better than  $0.3^\circ$ .

Figure 1 shows the experimental bands that form VBM in the  $\Gamma$ - $H$ - $T$  ( $N$ - $P$ - $N$ ) direction parallel to the chains. The plots for 280 and 50 K correspond to Figs. 1(a) and 1(b), respectively. The blue solid circles in Fig. 1 indicate the peak positions determined from the ARPES spectrum at each wave number. According to the theoretical results [5], the observed band of this area originates from Se  $4p$  states. Interesting enough, VBM includes not only Se  $4p$  states but also some admixture of Tl  $6s$  states, as calculated partial density-of-states [5] and LCAO (linear combination of atomic orbitals) analyses [6] show.

One can see from Fig. 1 that the largest energy shift of 423 meV is observed for the band that forms VBM at the  $T$  point after lowering the temperature. A strong downward shift of the Fermi level ( $E_F$ ), which is known to depend very much on temperature especially in the I

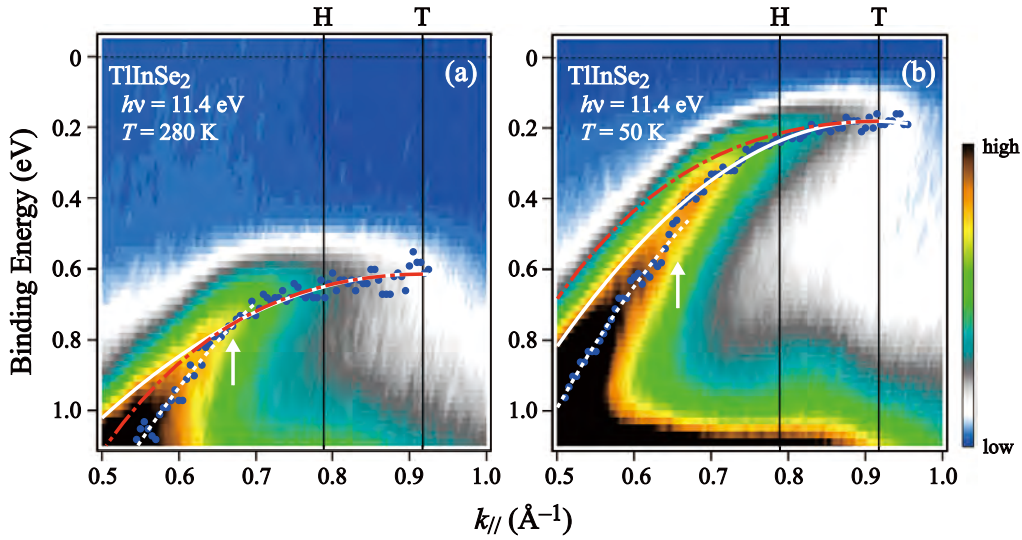


Fig. 1. The experimental band structure (ARPES intensity plot) near the valence band maximum along the  $\Gamma$ - $H$ - $T$  ( $N$ - $P$ - $N$ ) direction of  $\text{TlInSe}_2$  at 280 K (a) and 50 K (b). White solid and broken lines represent the results of the fit. Vertical arrows indicate the position of the kink or gap structure. Red dot-dashed lines are the LAPW-based results for  $\text{TlInSe}_2$  [5]. The details are given in the text.

phases due to formation of the new electronic levels inside the band gap [7], is considered to be responsible for the observed ARPES spectral shift with temperature.

As it has already been mentioned, the I phase of  $\text{TlInSe}_2$  is very likely to occupy some temperature region below 473 K [2]. The splitting with further formation of the multi-gap structure in the energy bands at 50 K is an unambiguous evidence of a phase transition in  $\text{TlInSe}_2$  [5]. Note, however, that the temperature region of the I phase is a very peculiar region where phase transition occurs continuously throughout the phase until the modulation vector is locked in some (commensurate) point of the BZ. The temperature at which this happens is the temperature of the I-C transition. Therefore, the question regarding whether the observed energy band transformations reflect the evolution of the I phase or the terminal I-C transition remains open. In fact, the temperature-dependent photoluminescence measurements on  $\text{TlInSe}_2$  have disclosed a very unusual temperature behavior of the 0.97-eV peak intensity, related to a phase transition at 55 K [8]. All these make us believe that the I-C transition occurs above 50 K and below this temperature  $\text{TlInSe}_2$  is already in the C phase.

From the above reasoning, the following picture of the N-I-C transition in  $\text{TlInSe}_2$  comes in sight. The phase transition from the N to the I phase that causes unusual behavior of the thermoelectric power of  $\text{TlInSe}_2$  occurs between 413 K and 473 K [2]. The terminal I-C transition takes place at around 55 K [8]. Then, the temperature 280 K at which the ARPES spectra were taken is well below (by at least 133 K) the N-I transition point, remaining well above (by 225 K) the I-C transition point. In other words, the accessed temperature is close to the middle of the I phase.

Then, in order to check the ARPES spectral shape between 280 and 50 K, all experimental data were fitted by a parabolic arch with the maximum at the  $T$  point. The results of the fit are shown in Fig. 1 by a white solid curve. One can see that the data points for the wave numbers smaller than approximately  $0.65 \text{ \AA}^{-1}$  are not reproduced well by this fit. Fitting (white broken curve in Fig. 1) performed in this region with the aid of other polynomials has revealed a kink structure at  $0.67 \text{ \AA}^{-1}$  in the plot for 280 K and a gap-like structure at practically the same point ( $0.66 \text{ \AA}^{-1}$ ) in the plot for 50 K. Furthermore, by superimposing the calculated results for

relevant bands of normal phase onto the corresponding experimental bands, we have found the following. The experimental band at 280 K corresponds well to the calculated band (Fig. 1(a), red dash-dotted curve) from the kink to the  $T$  point, while at 50 K, the correspondence between the experimental and calculated data becomes much worse (Fig. 1(b), red dash-dotted curve).

Thus, the above detailed analysis has definitely given a valuable insight into the structure of the topmost valence band of  $\text{TlInSe}_2$  and the revealed kink structure is definitely a room temperature manifestation of the I phase of this material. If we add here that the wave vector position of the kink structure in the BZ coincides not only with the position of the gap structure but also with the position of the wave vector at which intersection between the acoustic and low-frequency optical modes occurs [9], the self-consistence of the drawn picture of the phase transition in  $\text{TlInSe}_2$  causes no doubts. What still remains unclear is whether this picture is complete. The point is that the I phase may also appear due to the softening of the low-frequency optical mode along the  $\Delta$  direction of the BZ [9]. The  $\Delta$  direction is perpendicular to the chains whereas the above-mentioned the  $A$  direction is parallel. Since low-temperature gap structures in the valence bands have been observed by ARPES for both directions, the incommensurability linked to two independent wave vectors in the BZ might also be considered as plausible. But, by any account, further studies are necessary for drawing a more precise and complete picture of the N–I–C phase transition in  $\text{TlInSe}_2$ .

### Acknowledgement

This work was partly supported by the grants from the Japan Society for the Promotion of Science (Grant-in-Aid for Scientific Research (C), No. 18560014).

### References

- [1] M. Haniyas, A. N. Anagnostopoulos, K. Kambas, and J. Spyridelis, *Phys. Rev. B* **43** (1991) 4135.
- [2] N. Mamedov, K. Wakita, A. Ashida, T. Matsui, and K. Morii, *Thin Solid Films* **499** (2006) 275.
- [3] D. Müller, G. Eulenberger, and H. Hahn, *Z. Anorg. Allg. Chem.* **398** (1973) 207.
- [4] V. A. Aliev, M. A. Aldzhanov, and S. N. Aliev, *JETP Lett.* **45** (1987) 534.
- [5] K. Mimura, K. Wakita, M. Arita, N. Mamedov, G. Orudzhev, Y. Taguchi, K. Ichikawa, H. Namatame, and M. Taniguchi, *J. Electron Spectrosc. Relat. Phenom.* **156-158** (2007) 379.
- [6] N. Mamedov, K. Wakita, S. Akita, and Y. Nakayama, *Jpn. J. Appl. Phys.* **44** (2005) 709.
- [7] J. B. Sokoloff: *Phys. Rev. B* **25** (1982) 5901.
- [8] K. Abe, K. Wakita, Y. Shim, and N. Mamedov, *Ext. Abstr. 15th Int. Conf. Ternary and Multinary Compounds*, Kyoto, 2006, Tue-P-35B.
- [9] G. Orudzhev, V. Jafarova, S. Schorr, K. Mimura, K. Wakita, Y. Shim, N. Mamedov, F. Hashimzade, *Jpn. J. Appl. Phys.*, *in press*.

## Fermi surface and CDW gap of 2H-TaS<sub>2</sub> studied by angle resolved photoemission spectroscopy

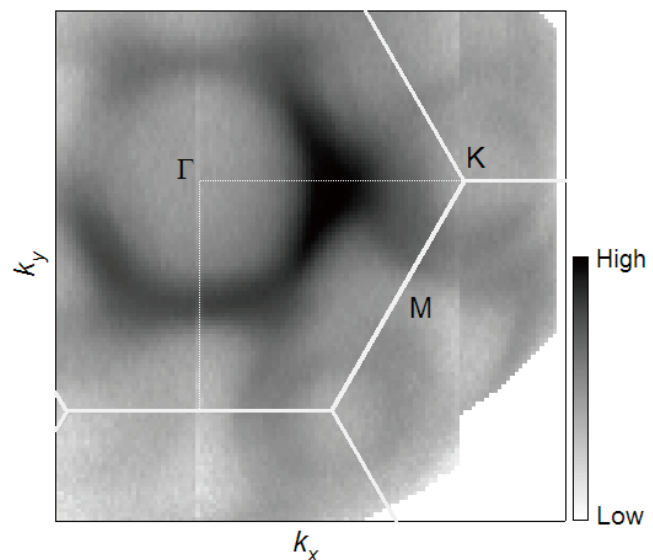
M. Arita<sup>a</sup>, H. Sato<sup>a</sup>, Y. Utsumi<sup>a</sup>, H. Namatame<sup>a</sup>, M. Taniguchi<sup>a,b</sup>, M. Sasaki<sup>c</sup>  
<sup>a</sup>Hiroshima Synchrotron Radiation Center, <sup>b</sup>Graduate School of Science,  
 Hiroshima University, Kagamiyama, Higashi-Hiroshima 739-8526, Japan  
<sup>c</sup>Department of Physics, Faculty of Science, Yamagata University, Kojirakawa, Yamagata  
 990-8560, Japan

Layered transition-metal dichalcogenides have various charge density wave (CDW) phases. Especially, 2H-polytype materials are very interesting, because some of them becomes superconductor at low temperature. Thus the competition and/or coexistence of CDW and superconductivity take place in the system. In the stoichiometric 2H-TaS<sub>2</sub>, incommensurate CDW order is observed below  $T_{CDW} \sim 75$  K and the system is not into the commensurate CDW at low temperature. Upon the intercalation of Na into one, the CDW transition is suppressed and the transition temperature decreases. On the other hand, the superconducting phase appears and  $T_c$  increases up to 4.4 K. There are a few reports about the Fermi surface (FS) and CDW gap of 2H-TaS<sub>2</sub> with the angle resolve photoemission spectroscopy [1]. As the clear FS and gap structures have not observed yet, the CDW mechanism of the system is not clear.

In this report, we performed ARPES in non-intercalated 2H-TaS<sub>2</sub>,  $T_{CDW}$ s of which are  $\sim 75$  K, to clarify the FS structures and the CDW gaps. ARPES measurements were performed at undulator beam line BL-9A.

Figure shows the image of the photoemission intensity around Fermi energy ( $E_F$ ) with  $h\nu = 19.2$  eV at 100 K, that is, in the normal phase. The solid lines indicate the hexagonal Brillouin Zone. A hole-type hexagonal FS is found around  $\Gamma$  point and there are two nearly circular FS around K points. The obtained FS's are similar to the FS of 2H-TaSe<sub>2</sub> and 2H-NbSe<sub>2</sub> in ARPES[1,2]. In respect of the FS's around K, the FS's near the K and M are called "inner FS" and "outer FS", respectively.

In order to find the FS nesting parts, the temperature dependences of the spectra are measured at some momentums where the CDW gap is expected to opens. As a result, in the spectrum along the KM line, the clear gap structure is observed in inner FS below 50 K. In other loci of the inner and outer FS's, the spectral intensities around  $E_F$  decrease with decreasing temperature. On the other hand, the gap is not found in the FS around  $\Gamma$ . Therefore it is considered that FS nesting occurs around K. That is similar to the case of 2H-TaSe<sub>2</sub> [3].



Map of ARPES spectral intensity around  $E_F$  in 2H-TaS<sub>2</sub> at 100 K with  $h\nu = 19.2$  eV. The solid lines indicate the hexagonal Brillouin Zone.

[1]W. C. Tonjes, *et al.*, Phys. Rev. B **63**, 235101 (2001).

[2]R. Liu, *et al.*, Phys. Rev. B **61**, 5212 (2000).

[3]K. Rossnagel, *et al.*, Phys. Rev. B **72**, 121103 (2005).

## Primary role of the barely occupied states in the charge density wave formation of NbSe<sub>2</sub>

D. W. Shen<sup>a</sup>, Y. Zhang<sup>a</sup>, L. X. Yang<sup>a</sup>, J. Wei<sup>a</sup>, H. W. Ou<sup>a</sup>, J. K. Dong<sup>a</sup>, B. P. Xie<sup>a</sup>, C. He<sup>a</sup>, J. F. Zhao<sup>a</sup>, B. Zhou<sup>a</sup>, M. Arita<sup>b</sup>, K. Shimada<sup>b</sup>, H. Namatame<sup>b</sup>, M. Taniguchi<sup>b</sup>, J. Shi<sup>c</sup> and D. L. Feng<sup>a</sup>

<sup>a</sup>*Department of Physics, Surface Physics Laboratory(National Key Laboratory) and Advanced Materials Laboratory, Fudan University, Shanghai 200433, P. R. China*

<sup>b</sup>*Hiroshima Synchrotron Radiation Center and Graduate School of Science, Hiroshima University, Hiroshima 739-8526, Japan*

<sup>c</sup>*School of Physics, Wuhan University, Wuhan, 430072, P. R. China*

2H-NbSe<sub>2</sub> is one of the most studied materials for its prototypical superconductivity (SC) and two dimensional charge density wave (CDW). Based on experiments conducted on NbSe<sub>2</sub>, understanding on some of the most basic properties of SC and CDW was reached. Nevertheless, the very mechanism of the CDW in NbSe<sub>2</sub> itself has been mysterious and controversial for over three decades. In the typical picture of CDW, the scattering of electrons between the parallel Fermi surface (FS) sections would give the so called nesting condition for CDW. Similarly, saddle band points, where the singularities of density of states (DOS) are located, were proposed to cause CDW as well [1]. Recently, the authors discussed another Fermi-patch CDW mechanism for some polaronic systems, where large DOS at E<sub>F</sub> hovers over an extended area of the Brillouin zone (BZ) and work collectively to favor certain CDW order [2]. However, the CDW in NbSe<sub>2</sub> cannot be explained by any of these scenarios.

We have performed the high resolution ARPES experiment at BL-9 on NbSe<sub>2</sub>, where the CDW related weight-suppressed momenta were precisely revealed for the first time and thus the aforementioned long-standing controversies are naturally solved [3]. In this experiment, the used photo energy was 21.2eV and the total energy resolution was tuned to be better than 10meV.

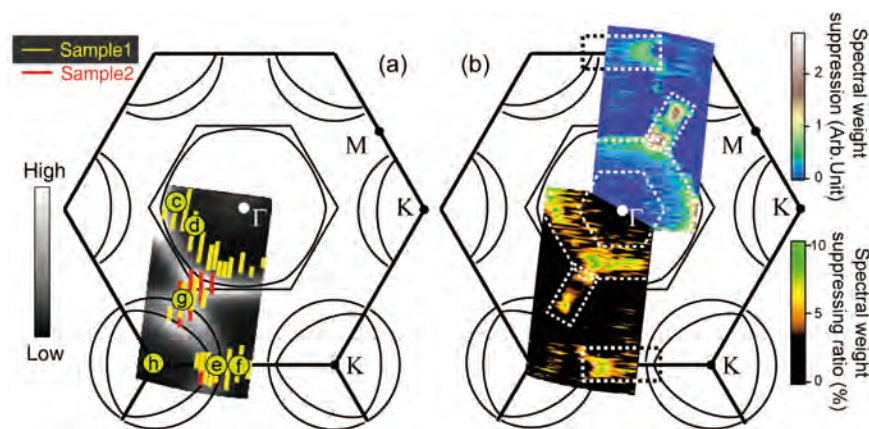


**Figure 1.** (a) The illustration of the CDW induced weight-suppressed regions (b) The spectral weight suppression map and its corresponding ratio map are false color plotted, where the dashed lines contour the obviously suppressed regions.

Through careful examination, the delicate spectral weight suppression upon CDW is observed. Therefore, the weight-suppressed regions in the BZ can be determined accurately, as marked in Fig. 1(a) by bars. Moreover, both the maps of the spectral weight suppression and its corresponding suppressing ratio confirm the result as well (Fig.1(b)). This distribution makes a broken-honeycomb-shaped structure in the BZ, as shown in Fig. 2(a). Obviously, these regions can be well connected by the CDW wavevector  $Q_i$ 's (represented by the double-headed arrows). In this way, the long-lost nesting condition is naturally satisfied.

In addition, we note that the distribution includes some regions where the DOS at  $E_F$  is very weak. However, the spectral weight suppression over these regions accounts for around 60% of the total one. In other words, although the DOS is low, the barely occupied states indeed play the primary role in the CDW formation due to their relatively extensive momentum space. This result will be more clearly illustrated through the so-called weighted joint DOS analysis, which can effectively estimate the contribution of the states to the final CDW instability. It is found that the saddle band points (high DOS) only contribute about 17% of the total weighted joint DOS computed over the entire broken-honeycomb region, as shown in Fig.2(b). Therefore, the nesting of states with low DOS at  $E_F$  indeed dominates the charge instability at  $Q_i$ 's here.

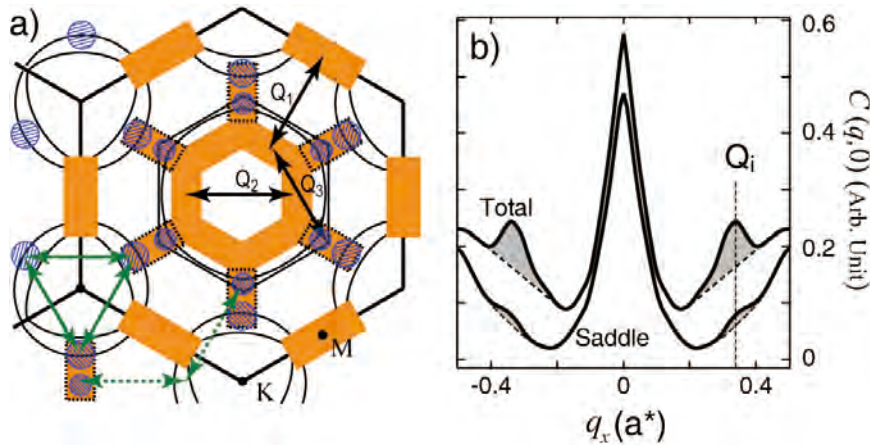


**Figure 2.** (a) The distribution of CDW related weight suppression over the entire BZ sketched from the spectral weight suppression map, which are marked by the orange broken-honeycomb-shaped structure. (b) Comparison of the corresponding joint DOS results along  $\Gamma$ -M.

Our findings not only recover the long-lost nesting condition for this classic CDW material, but also show that collective contribution of the weakly occupied states can play the primary role in CDW formation in some cases, which may amend the conventional wisdom of CDW.

## References

- 1 T. M. Rice and G. K. Scott, Phys. Rev. Lett. **35**, 120 (1975).
- 2 D. W. Shen *et al*, Phys. Rev. Lett. **99**, 216404 (2007).
- 3 D. W. Shen *et al*, Phys. Rev. Lett. (in press).

**Superconducting coherence peak in the electronic excitations of a  
single layer cuprate superconductor  $\text{Bi}_2\text{Sr}_{1.6}\text{La}_{0.4}\text{CuO}_{6+\delta}$**

J. Wei<sup>1</sup>, Y. Zhang<sup>1</sup>, H. W. Ou<sup>1</sup>, B. P. Xie<sup>1</sup>, D. W. Shen<sup>1</sup>, J. F. Zhao<sup>1</sup>, L. X. Yang<sup>1</sup>, M. Arita<sup>2</sup>,  
K. Shimada<sup>2</sup>, H. Namatame<sup>2</sup>, M. Taniguchi<sup>2</sup>, Y. Yoshida<sup>3</sup>, H. Eisaki<sup>3</sup>, and D. L. Feng<sup>1\*</sup>

<sup>1</sup>*Department of Physics, Surface Physics Laboratory (National Key Laboratory) and  
Advanced Materials Laboratory, Fudan University, Shanghai 200433, P. R. China*

<sup>2</sup>*Hiroshima Synchrotron Radiation Center and Graduate School of Science, Hiroshima  
University, Hiroshima 739-8526, Japan*

<sup>3</sup>*National Institute of Advanced Industrial Science and Technology (AIST), Tsukuba, Ibaraki,  
3058568, Japan*

For investigation of the mechanism of high temperature superconductivity, one central issue is whether there are certain bosons that play the critical mediating role of phonons in a conventional BCS superconductor. So far, signatures of electron-boson interactions have been identified in single particle excitations measured by angle resolved photoemission spectroscopy (ARPES).

We have performed ARPES on optimally doped  $\text{Bi}_2\text{Sr}_{1.6}\text{La}_{0.4}\text{CuO}_{6+\delta}$  (La-Bi2201) ( $T_C=34\text{K}$ ) using BL 9 [1]. The photon energy was 22.5eV, and energy resolution was 7 meV. The samples were cleaved in ultra-high vacuum ( $5\times 10^{-11}$  mbar).

Figure.1 shows photoemission data in the superconducting state of La-Bi2201. The data were taken in the  $\Gamma$ -Y quadrant of the Brillouin zone. In the vicinity of  $(\pi, 0)$ , a feature near the Fermi energy ( $E_F$ ) gradually becomes quite prominent as indicated by the diamonds in Figs.1a(5-8), b(5-8). Though weak, the appearance of such two-component structure over a broad momentum area clearly proves its robustness against the experimental uncertainties. It is the first time to observe the superconducting coherence peak (SCP) or two-component spectrum in the antinodal region of single layer compounds. We attribute it to the minimized disorder effects in the current sample. As comparison, for another optimally doped La-Bi2201 sample ( $T_C = 32\text{K}$ ) with finite residual resistivity (Fig.1c), its spectrum in the antinodal region is much broader than that of the current sample (Fig.1d).

Figure.2 shows the temperature dependences and compares the spectra below and above  $T_C$  after removing the temperature broadening effects in Fig.2b. The data evidence that the sharp peak in the antinodal region is the SCP as observed in multi-layered cuprates before. Fig.2c shows the associated “peak-dip-hump” (PDH) structures for three momenta near  $(\pi, 0)$ . Through a phenomenological fitting, one could precisely determine the peak position and the separation between the peak and dip, which is about 19 meV at all three momenta. Follow the same analyses as in many previous ARPES studies that the peak-dip separation corresponds to the energy of a bosonic mode. We consider this low energy mode could have an intriguing correlation with the energy scale of spin excitations near  $(\pi, \pi)$ . The weaker dip structure, in Bi2201 is consistent with the weaker intensity of the spin excitations observed in low- $T_C$  systems.

In summary, we have discovered the PDH in the antinodal region of the single layer La-Bi2201, found the peak-dip distance to be about 19 meV, suggesting the possibility of a bosonic mode in Bi2201 with a much lower energy than that in Bi2212 [2]. It will face serious challenges to consistently explain the PDH's in different systems [3, 4]. The temperature dependence of the PDH in the antinodal region and the 19 meV peak-dip separation of La-Bi2201 intriguingly correlate with the behaviors of spin fluctuations. Our data provides a critical piece to the global picture, which would help to eventually resolve controversial issues and uncover the glue of high- $T_c$  superconductivity.

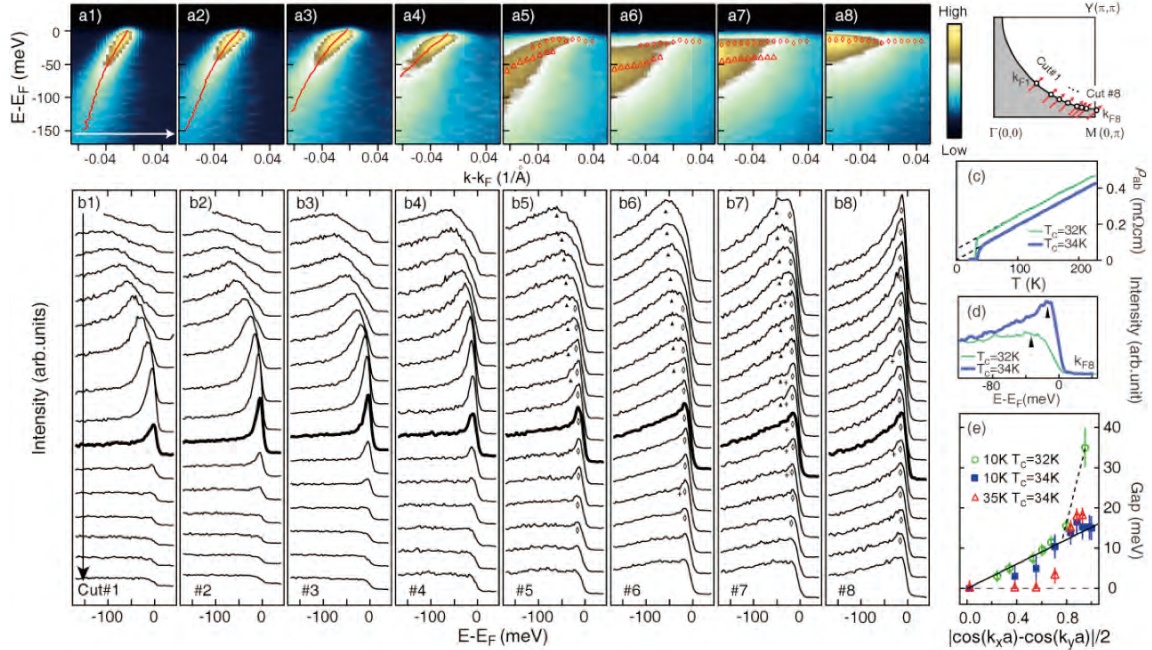


Fig. 1: Photoemission data of La-Bi2201. (a1-a8) Photoemission intensity map along cuts 1–8 across the Fermi surface in the superconducting state. Thick lines in a1-a4 are the dispersions fitted from momentum distribute curves. (b1-b8) display the corresponding spectra in panel a1-a8. (c) The resistivity of two La-Bi2201 samples, (d) their corresponding spectrum at  $k_{F8}$ , and (e) the momentum dependence of their gaps.

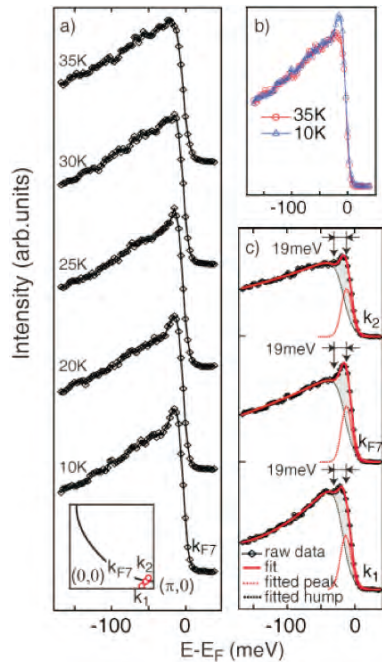


Fig. 2: (a) Detailed temperature dependence of photoemission data at  $k_{F7}$ , as indicated in the inset, (b) compare the spectra below and above  $T_c$  at  $k_{F7}$  after removing the temperature broadening effects, (c) the SCP in the vicinity of  $(\pi, 0)$ , Peak and dip positions are illustrated by the arrows.

[1] J. Wei et al., Phys. Rev. Lett. 101, 097005 (2008).  
[2] D. L. Feng et al., Science 289, 277 (2000)  
[3] Z. X. Shen and J. R. Schrieffer, Phys. Rev. Lett. 78, 1771(1997)  
[4] A. A. Kordyuk et al., Phys. Rev. Lett. 89, 077003 (2002).

## Novel electronic structure induced by a highly strained oxide interface with incommensurate crystal fields

H. W. Ou<sup>a,b</sup>, J. F. Zhao<sup>a,b</sup>, Y. Zhang<sup>a,b</sup>, B. P. Xie<sup>a,b</sup>, D. W. Shen<sup>a,b</sup>, Y. Zhu<sup>a</sup>, Z. Q. Yang<sup>a</sup>, J. G. Che<sup>a</sup>, X. G. Luo<sup>c</sup>, X. H. Chen<sup>c</sup>, M. Arita<sup>d</sup>, K. Shimada<sup>d</sup>, H. Namatame<sup>d</sup>, M. Taniguchi<sup>d</sup>, C. M. Cheng<sup>e</sup>, K. D. Tsuei<sup>e</sup>, and D. L. Feng<sup>a,b\*</sup>

<sup>a</sup> *Surface Physics Laboratory (National key laboratory) and Physics Department, Fudan University, Shanghai 200433, P. R. China*

<sup>b</sup> *Advanced Materials Laboratory, Fudan University, Shanghai 200433, P. R. China*

<sup>c</sup> *Hefei National Laboratory for Physical Sciences at Microscale and Department of Physics, University of Science and Technology of China, Hefei, Anhui 230026, P. R. China*

<sup>d</sup> *Hiroshima Synchrotron Radiation Center and Graduate School of Science, Hiroshima University, Hiroshima 739-8526, Japan*

<sup>e</sup> *National Synchrotron Radiation Research Center, and Department of Physics, National Tsing-Hua University, Hsinchu 30077, Taiwan, Republic of China*

Novel phenomena emerging from the oxide interfaces have attracted enormous attention, which provide opportunities for promising applications: one may be able to make oxide heterostructure devices with desired physical properties. A thorough understanding of the microscopic processes at the oxide interface is the first step toward designing functional heterostructures. Particularly, it is crucial to find out the electronic behavior at oxide interfaces, *e.g.*, how the electron bands behave on both sides of the interface; and how they react to strain and peculiar phonon structures at the interface. The answers to these questions would lead to the understanding of the charge transfer process, the insulator-metal transitions, and anomalous transport behavior of the interfaces.

Angle-Resolved Photoemission Spectroscopy (ARPES) is proven to be a powerful tool to investigate the electronic structure of solids and thin films. However, due to the short mean free path of photoelectrons, photoemission signals from the interface of pulsed-laser deposited oxides are very weak, which forbids high resolution and momentum resolved measurements. The misfit oxide single crystal, which is made of alternating rocksalt-structured [MO] layers (M=Ca, Bi, Ba, Sr) and CdI<sub>2</sub>-type hexagonal CoO<sub>2</sub> layers, provides an alternative solution. It resembles a very clean artificial oxide heterostructure and is suitable for photoemission experiments.

Misfit Cobaltate Bi<sub>2</sub>Ba<sub>1.3</sub>K<sub>0.6</sub>Co<sub>2.13</sub>O<sub>7.94</sub> (BBKCO) was studied by ARPES at HiSOR BL-9A beam line. Detailed electronic structure of such a highly strained oxide interface is revealed for the first time. As illustrated in Fig.1, we found that under the two incommensurate crystal fields, electrons are confined within individual sides of the interface, and scattered by umklapp scattering of the crystal field from the other side. In addition, the high strain on the rocksalt layer raises its chemical potential and induces large charge transfer to the CoO<sub>2</sub> layer.

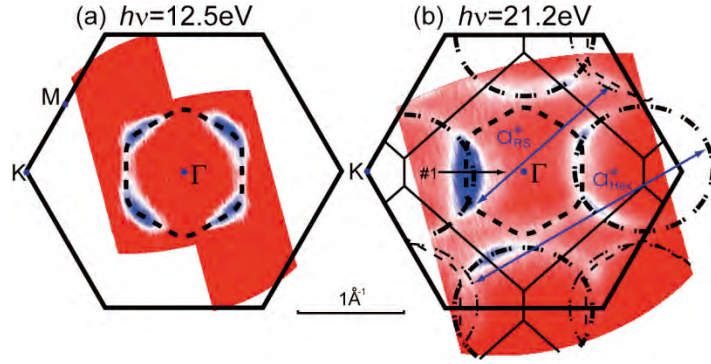


Fig. 1 Fermi surfaces (FS) measured at 20K with (a) 12.5 eV and (b) 21.2 eV photons respectively, which are obtained by integration of the spectral weight in a 20meV window around  $E_F$ . The dash-dotted and dashed thick curves are  $[\text{CoO}_2]$ -derived and  $[\text{BiO}/\text{BaO}]$ -derived Fermi pockets respectively. Their umklapp FS's are indicated by thinner curves.

Furthermore, a novel interface effect, the interfacial enhancement of electron-phonon interactions, is discovered. As shown in Fig.2, the  $\text{Na}_{0.7}\text{CoO}_2$  dispersion is a smooth curve [Fig.2 (c)], however there are strong kinks on the dispersions of the BBKCO bands [Fig.2 (a-b)]. These kinks are suggesting an intrinsic effect due to interactions with some bosonic modes, most likely phonons induced by the interface here. This strong coupling is also reflected in its scattering rate [Fig. 2(d)], where a clear turning point around 60meV appears for both the bands of BBKCO.

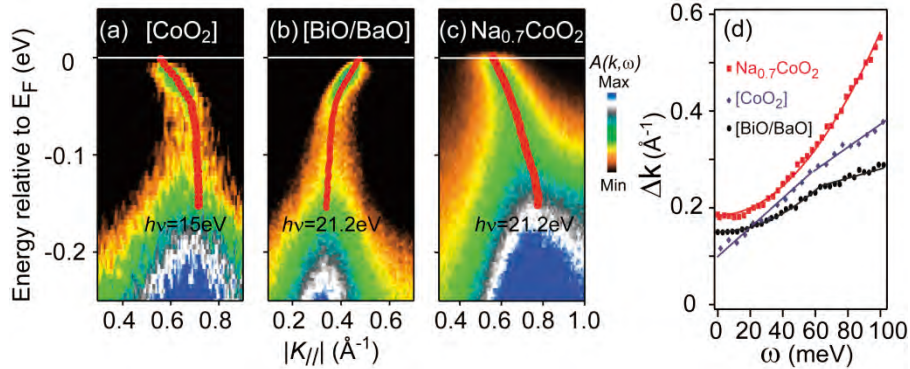


Fig. 2 Photoemission intensity along  $\Gamma$ -K (cut #1 in Fig. 1) taken at 20K, for (a) BBKCO's  $\text{CoO}_2$  layer ( $h\nu=15\text{eV}$ ), (b) BBKCO's  $[\text{BiO}/\text{BaO}]$  layers ( $h\nu=21.2\text{eV}$ ), and (c)  $\text{Na}_{0.7}\text{CoO}_2$  ( $h\nu=21.2\text{eV}$ ). The red thick curves are fitted dispersions. (d) The width of the momentum distribution curve vs. binding energy for data presented in panel a-c, which is an estimate of the quasiparticle scattering rate.

In conclusion, we have studied various interfacial electronic properties by ARPES, and the relation between strain and charge transfer across oxide interface is illustrated from a microscopic level. Our results suggest that interfacial strain might cause large charge transfer without severely changing the properties of participating layers. The enhancement of electron phonon coupling and interfacial umklapp scattering are discovered, which affect the low energy electronic behavior. Our findings provide an electronic structure foundation for understanding oxide interfaces, and some important guidelines for designing oxide devices.

Note: the manuscript on this work has been submitted to *Phys. Rev. Lett.*

**Observation of the multibands and superconducting gaps in the trilayer high- $T_c$  cuprate superconductor  $\text{Bi}_2\text{Sr}_2\text{Ca}_2\text{Cu}_3\text{O}_{10+\delta}$**

S. Ideta<sup>1</sup>, K. Takashima<sup>1</sup>, M. Hashimoto<sup>1</sup>, T. Yoshida<sup>1</sup>, A. Fujimori<sup>1</sup>, A. Ino<sup>2</sup>, H. Anzai<sup>2</sup>,  
T. Fujita<sup>2</sup>, Y. Nakashima<sup>2</sup>, M. Arita<sup>3</sup>, H. Namatame<sup>3</sup>, M. Taniguchi<sup>2,3</sup>,  
K. M. Kojima<sup>1</sup> & S. Uchida<sup>1</sup>

<sup>1</sup>*Department of Physics, University of Tokyo, Bunkyo-ku, Tokyo 113-0033, Japan.*

<sup>2</sup>*Graduate School of Science, Hiroshima University, Higashi-Hiroshima 739-8526, Japan.*

<sup>3</sup>*Hiroshima Synchrotron Center, Hiroshima University, Higashi-Hiroshima 739-0046, Japan*

It has been empirically known that the superconducting transition temperature ( $T_c$ ) of optimally doped high- $T_c$  cuprate superconductors (HTSCs) increases with the number of adjacent  $\text{CuO}_2$  planes ( $n$ ) from single-layer ( $n = 1$ ) to trilayer ( $n = 3$ ) and then decreases with more layer number ( $n > 3$ ). In the case of Bi-based HTSCs, the optimum  $T_c$  increases from single-layer  $\text{Bi}_2\text{Sr}_2\text{CuO}_{6+\delta}$  (Bi2201,  $T_{c \text{ max}} = 35$  K), bilayer  $\text{Bi}_2\text{Sr}_2\text{CaCu}_2\text{O}_{8+\delta}$  (Bi2212,  $T_{c \text{ max}} = 95$  K) to trilayer  $\text{Bi}_2\text{Sr}_2\text{Ca}_2\text{Cu}_3\text{O}_{10+\delta}$  (Bi2223,  $T_{c \text{ max}} = 110$  K). According to a theory with tunneling of Cooper pairs between the  $\text{CuO}_2$  planes,  $T_c$  continues to increase with increasing  $n$ <sup>1</sup>. However, when the charge imbalance and a competing order parameter are taken into account,  $T_c$  becomes maximum at  $n = 3$ <sup>2</sup>.  $T_c$  tends to be large when the value of next nearest-neighbor hopping parameter  $t'/t$  is large<sup>3</sup> and the  $\text{CuO}_2$  plane is the ideally flat<sup>4</sup>. However, the microscopic origin of the correlation between the  $n$  and  $T_c$  has been unclear so far because of the lack of detailed knowledge about the multi-layer effects in the electronic structure. Angle-resolved photoemission spectroscopy (ARPES) is one of the most powerful tools to investigate the electronic structure of HTSCs. In previous ARPES results on the double-layer Bi2212 and the four-layer  $\text{Ba}_2\text{Ca}_3\text{Cu}_4\text{O}_8\text{F}_2$  (F0234), splitting of the band dispersions and two Fermi surfaces (FSs) have been observed. In the case of Bi2212, hybridization between orbitals on the two  $\text{CuO}_2$  planes causes band splitting into the anti-bonding and bonding bands<sup>5</sup>. Recently, band splitting in the nodal direction has also been observed in high resolution experiment<sup>9</sup>. F0234 has indicated band splitting due to the differences in the hole concentrations for the inner  $\text{CuO}_2$  planes (IPs) and outer  $\text{CuO}_2$  planes (OPs), and two FS sheets corresponding to IPs and OPs have been observed<sup>10</sup>. The gap magnitude of the IP band is approximately twice as large as that of the OP. However, previous ARPES results on Bi2223, which has three  $\text{CuO}_2$  planes, have not shown band splitting corresponding to the IP and OP bands<sup>6-8</sup>. In the present work, we have observed the band splitting for Bi2223 and shown that the electronic structures of the IP and OP have different doping levels and the gap magnitudes. Single crystals of optimally doped Bi2223 ( $T_c = 110$  K) were grown by the travelling solvent floating zone (TSFZ) method<sup>11</sup>. ARPES experiments were carried out using

at BL-9A ( $h\nu = 6.6\text{-}12.9$  eV, circularly polarized light) at Hiroshima Synchrotron Radiation Center, and the total energy resolution ( $\Delta E$ ) was set at 5 meV. The samples were cleaved *in situ* under an ultrahigh vacuum of  $\sim 1 \times 10^{-11}$  Torr and all experiments were measured at  $T = 10$  K.

In Fig. 1(a), we show spectral weight mapping around 40 meV below the Fermi level ( $E_F$ ) integrated with a window 10 meV. Two FS sheets corresponding to the IP and OP are clearly observed. Particularly, as shown in Fig. 1(b), the intensity of IP is enhanced for  $h\nu = 11.95$  eV. In the NMR study of trilayer HTSCs, the hole concentration of OPs and IP are found to be in the overdoped and underdoped regions, respectively<sup>12</sup>. Thus, we assign the FS sheets close to the  $\Gamma$  point is the OPs, and the other FS to IP. The dispersions in the nodal direction corresponding to Fig. 1(a) and (b) are shown in Fig. 1(d) and (e), respectively. Since there are three neighbouring  $\text{CuO}_2$  planes, one would expect to observe three bands which come from one IP and two OP bands. Although theoretical calculation shows the three bands clearly<sup>13</sup>, we have observed only two bands, implying that the two OP bands, i.e., the bonding and anti-bonding OP bands, are degenerate. In fact, the full width at half maximum (FWHM) of the momentum distribution curve (MDC) for the OP band at  $E_F$ ,  $\sim 0.011 \text{ \AA}^{-1}$ , is significantly larger than that of the IP band  $\sim 0.0074 \text{ \AA}^{-1}$ , indicating the presence of two unresolved bands. The FWHM of IP's is almost the same as that of Bi2212,  $0.0065 \text{ \AA}^{-1}$ <sup>9</sup>. The  $k_F$  positions of the FSs for OP and IP have been determined by the minimum-gap-locus. The result of tight-binding (TB) fit is shown in Fig. 1(c). The hole concentrations for IP and OP deduced from the FS areas are  $6 \pm 3$  and  $25 \pm 2$  %, respectively, indicating that IP and OP are underdoped and overdoped region, respectively. The values of the TB parameter  $-t'/t$  are  $\sim 0.29$  (IP) and  $\sim 0.26$  (OP) similar to the theoretically predicted values for multi-layer materials such as  $\text{HgBa}_2\text{Ca}_2\text{Cu}_3\text{O}_{1+\delta}$ ,  $\text{Tl}_2\text{Ba}_2\text{Ca}_2\text{Cu}_3\text{O}_{10}$  ( $n = 3$ )<sup>3</sup>.

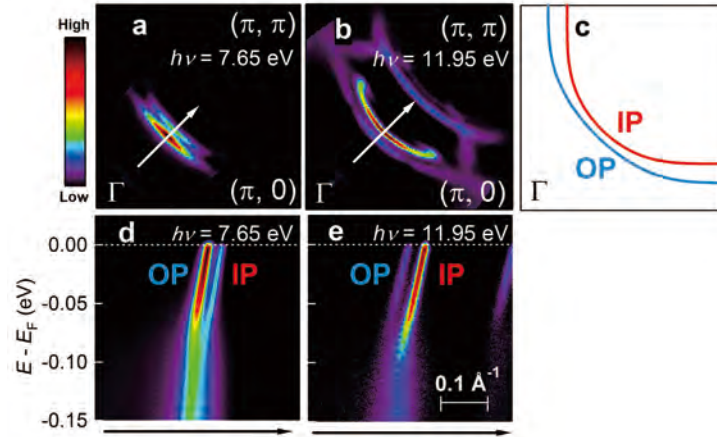


**Figure 1** Intensity plots of ARPES spectra integrated within  $E = -40 \pm 5$  meV (a, b). Two-FSs have been observed, and correspond to the inner  $\text{CuO}_2$  plane (IP) and outer  $\text{CuO}_2$  planes (OPs). The hole concentration of the OP is higher than that of IP, therefore the FS for OP locate near the  $\Gamma$  point (c). (d) and (e) show the band dispersion taken by  $h\nu = 7.65$  and  $11.95$  eV. In using excitation energy of  $7.65$  eV, OP band-spectra are enhanced mainly, while in  $11.95$  eV, IP band is enhanced.

In Fig.2 (a) and (b), we show band dispersions in the superconducting state for OP and IP, respectively, from the nodal to off-nodal regions. Due to matrix-element effects, the intensities of the OP and IP bands' are enhanced at photon energies  $h\nu = 9$  and  $11.95$  eV, respectively.

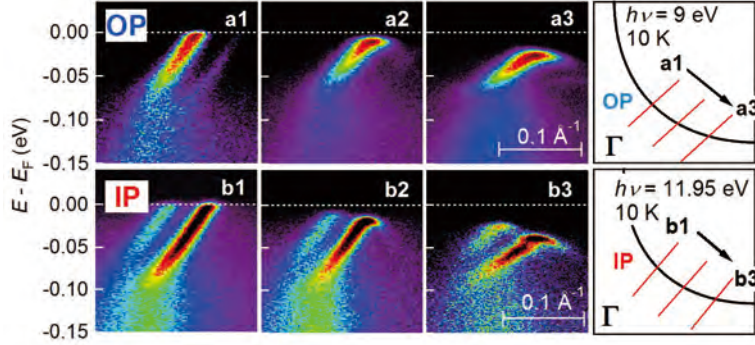


**Figure 3:** Intensity plots for OP band from the nodal to the off-nodal region (a1 - a3) and for IP band (b1 - b3) observed in the superconducting state ( $T = 10$  K) corresponding to the cuts (red lines) for the right panels. The photon energies,  $h\nu = 9$  eV and  $11.95$  eV, enhance the OP and IP bands, respectively. We can clearly see the difference of the gap amplitudes for the IP and OP bands in the off-nodal region.

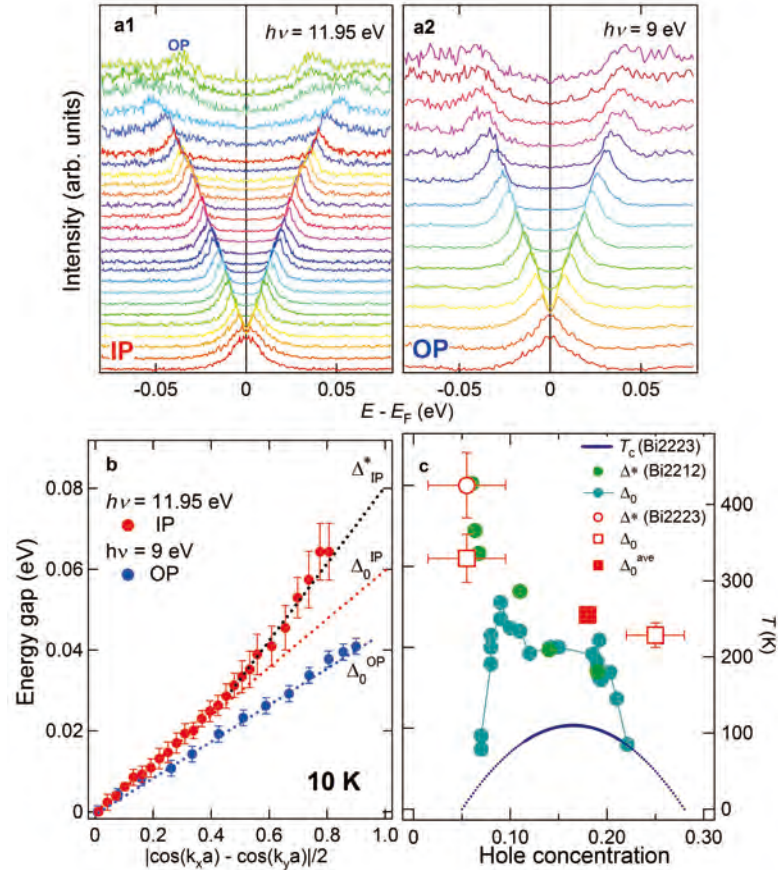


**Figure 2:** The Energy distribution curve (EDC) spectra for OP and IP bands' are shown in panels (a1) and (a2), respectively. (b) The gap anisotropies for the IP and OP bands have different characters. The OP's SC gap shows the simple  $d$ -wave, while the IP's deviates from the  $d$ -wave (c). The gap size of Bi2223 is compared with that of Bi2212 and one can see the gap sizes between Bi2212 and Bi2223 have a large difference (c). Red filled square indicates the average of  $\Delta_0$  for IP and OP bands.

respectively. The gap energies for both bands are very different, as in the case of the other

multi-layer cuprate F0234 ( $n = 4$ ). In Fig. 3(a1) and (a2), the symmetrised EDCs at  $k_F$  are shown. The momentum dependence of the gap anisotropy for OP is almost simple  $d$ -wave like  $\Delta_0^{\text{OP}}|\cos(k_x a) - \cos(k_y a)|/2$  with  $\Delta_0^{\text{OP}} \sim 40$  meV as shown in Fig. 3(b). On the other hand, the SC gap for IP band deviates from the simple  $d$ -wave, and the gap size is  $\Delta_0^{\text{IP}} \sim 60$  meV and  $\Delta_{\text{IP}}^* \sim 80$  meV, where  $\Delta_0$  and  $\Delta^*$  are defined by the extrapolation of nodal and anti-nodal gaps to  $|\cos(k_x a) - \cos(k_y a)|/2 = 1$ , respectively, as shown in Fig. 3(b)<sup>14, 15</sup>. Since the deviation from the simple  $d$ -wave is prominent in the underdoped region, the observed gap and anisotropy is consistent with the doping levels estimated from the FS area. Judging from the present result of the OP gap  $\Delta_0 \sim 40$  meV, one can conclude that the previous ARPES result  $\Delta_0 \sim 40$  meV for Bi2223 represents the OP band<sup>6, 7</sup>. In Fig.3 (c), compared with Bi2212, Fig. 3(c), the gap size of OP band is almost the same as that of optimally doped Bi2212 in spite of heavily overdoping<sup>14-17</sup>. Now, let us discuss the origin of the large  $\Delta_0$  in Bi2223 compared with the other cuprates. In Bi2223, there are three possible factors for large  $\Delta_0$ : (1) the value of hopping parameter,  $t'/t$ , which has a correlation with  $T_c$ , is larger than those of single and bilayer cuprates<sup>3</sup>, (2) disorder effect is small because the inner  $\text{CuO}_2$  plane is ideally flat among various cuprates<sup>4</sup>, (3) the interlayer tunneling of Cooper pairs between  $\text{CuO}_2$  planes enhances superconducting order parameter<sup>1, 2</sup>.

In conclusion, we have measured the band splitting of Bi2223 by ARPES using low photon energy. The Fermi surfaces corresponding to the IP and OP bands have been observed and the superconducting gaps of OP and IP's show the different values between them.

## References

1. J. M. Wheatley *et al.*, *Nature* **333**, 121 (1988).
2. S. Chakravarty *et al.*, *Nature* **428**, 53 (2004).
3. E. Pavarini *et al.*, *Phys. Rev. Lett.* **87**, 047003 (2001).
4. H. Eisaki *et al.*, *Phys. Rev. B* **69**, 064512 (2004).
5. D. L. Feng *et al.*, *Phys. Rev. Lett.* **86**, 5550 (2001).
6. T. Sato *et al.*, *Phys. Rev. Lett.* **91**, 157003 (2003).
7. H. Matsui *et al.*, *Phys. Rev. B* **67**, 060501 (2003).
8. D. L. Feng *et al.*, *Phys. Rev. Lett.* **88**, 107001 (2002).
9. K. Yamasak *et al.*, *Phys. Rev. B* **75**, 140513(R) (2007).
10. Y. Chen *et al.*, *Phys. Rev. Lett.* **97**, 236401 (2006).
11. T. Fujita *et al.*, *J. Phys. Chem. Solids* **62**, 171 (2001).
12. K. Kotegawa *et al.*, *J. Phys. Chem. Solids* **62**, 171 (2001).
13. M. Mori *et al.*, *Phys. Rev. B* **66**, 064502 (2002).
14. K. Tanaka *et al.*, *Science* **314** (2006).
15. W. S. Lee *et al.*, *Nature* **450**, 81 (2007).
16. J. Mesot *et al.*, *Phys. Rev. Lett.* **83**, 840 (1999).
17. H. Ding *et al.*, *Phys. Rev. Lett.* **87**, 227001 (2001).

## Impurity effect of nodal fine quasiparticle structure of $\text{Bi}_2\text{Sr}_{1.6}(\text{La,Gd})_{0.4}\text{CuO}_{6+\delta}$ studied by low-energy synchrotron-radiation ARPES

T. Fujita<sup>a</sup>, T. Kamo<sup>a</sup>, H. Anzai<sup>a</sup>, A. Ino<sup>a</sup>, M. Arita<sup>b</sup>, H. Namatame<sup>b</sup>, M. Taniguchi<sup>a,b</sup>,  
A. Fujimori<sup>c</sup>, Z.-X. Shen<sup>d</sup>, K. Fujita<sup>c</sup>, S. Uchida<sup>c</sup>

<sup>a</sup>*Graduate School of Science, Hiroshima University*

<sup>b</sup>*Hiroshima Synchrotron Radiation Center, Hiroshima University*

<sup>c</sup>*Department of Physics, University of Tokyo*

<sup>d</sup>*Department of Physics and Stanford Synchrotron Radiation Laboratory, Stanford University*

The structural unit common to all the high- $T_c$  cuprate superconductors is the  $\text{CuO}_2$  planes, which is considered as the main stage of the superconductivity. However, in order to understand the diversity of the cuprates such as the difference in superconducting critical temperatures  $T_c$ , we have to clarify the effect of the part outside  $\text{CuO}_2$  plane. For  $\text{Bi}_2\text{Sr}_{1.6}\text{Ln}_{0.4}\text{CuO}_{6+\delta}$  ( $\text{Ln} = \text{La}, \text{Gd}$ ), the degree of out-of-plane disorder may be systematically controlled with Ln site, and  $T_c$  decreases with increasing the out-of-plane disorder. So far, angle-resolved photoemission (ARPES) studies are concentrated on the antinodal region, while it is required for extremely high resolution to observe the small gap near a node.

In the present study, we performed an ARPES experiment with high energy and momentum resolution by using low-energy synchrotron radiation ( $h\nu = 7.8$  eV), and determined the directional-dependence of the gap magnitude around the nodal direction. Figure 1 shows the ARPES spectra of  $\text{Bi}_2\text{Sr}_{1.6}\text{La}_{0.4}\text{CuO}_{6+\delta}$  ( $T_c = 33$  K) collected along the Fermi surface. The near-nodal gap is well consistent to the directional dependence of  $d$ -wave symmetry,  $2\Delta / k_B T_c = 9.1 k_B T_c$ . Substituting 50% of La with Gd, the out-of-plane disorder increases and thus  $T_c$  reduces to 27 K. However, while the quasiparticle peak is appreciably broadened, the decrease in the gap magnitude is smaller than that in  $T_c$ , suggesting that the out-of-plane disorder mainly affects the quasiparticle coherence.

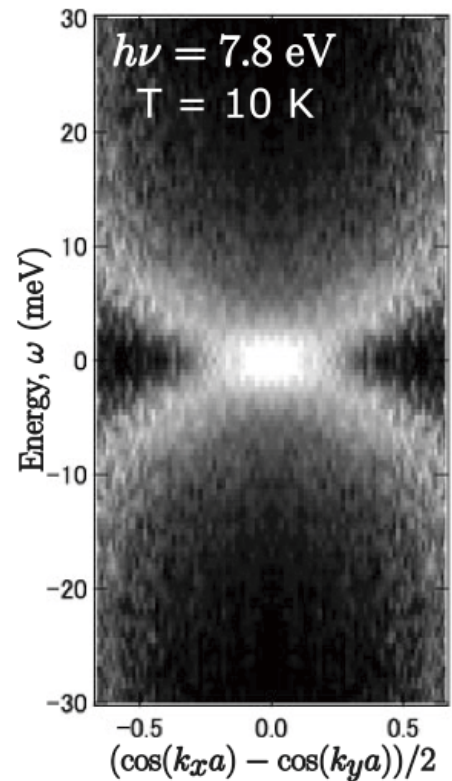


Fig. 1 ARPES spectra of  $\text{Bi}_2\text{Sr}_{1.6}\text{La}_{0.4}\text{CuO}_{6+\delta}$  ( $T_c = 33$  K) collected along the Fermi surface, indicating that the near-nodal gap is consistent to  $d$ -wave symmetry.

## Doping dependence of gap anisotropy of $\text{Bi}_2\text{Sr}_2\text{CaCu}_2\text{O}_{8+\delta}$ studied by low-energy ARPES

H. Anzai <sup>a</sup>, T. Kamo <sup>a</sup>, T. Fujita <sup>a</sup>, A. Ino <sup>a</sup>, M. Arita <sup>b</sup>, H. Namatame <sup>b</sup>, M. Taniguchi <sup>a,b</sup>,  
M. Ishikado <sup>c</sup>, A. Fujimori <sup>c</sup>, S. Uchida <sup>c</sup>, and Z.-X. Shen <sup>d</sup>

<sup>a</sup>Graduate School of Science, Hiroshima University, Higashi-Hiroshima 739-8526, Japan

<sup>b</sup>Hiroshima Synchrotron Radiation Center, Hiroshima University, Higashi-Hiroshima 739-0046, Japan

<sup>c</sup>Department of Physics, University of Tokyo, Tokyo 113-0033, Japan

<sup>d</sup>Department of Applied Physics and SSRL, Stanford University, Stanford, CA94305, USA

High- $T_c$  cuprates show diverse phases depending on the concentration of doped holes. Hence, the doping evolution of electronic structure may be the key to the understanding of the mechanism of the high- $T_c$  superconductivity. It has been established that the superconducting gap of the cuprates has nodes like in  $d$ -wave superconductors, but the detail of the directional dependence of the gap magnitude is still unclear. Here, we have systematically studied the hole-concentration dependence of the superconducting gap of bilayer cuprate  $\text{Bi}_2\text{Sr}_2\text{CaCu}_2\text{O}_{8+\delta}$  ( $\text{Bi}2212$ ) by angle-resolved photoemission spectroscopy (ARPES). Experiments were performed at BL-9 of HiSOR.

With the photon-energy tunability and the high momentum and energy resolution, we have determined the shape of two Fermi surfaces split due to intra-bilayer interaction for all over the Brillouin zone, and revealed the fine detail of the directional dependence of gap magnitude for each of the bonding and antibonding bands. Figure 1 (a) shows the ARPES spectra of underdoped  $\text{Bi}2212$ , taken along the Fermi surface of the bonding band. The open circles

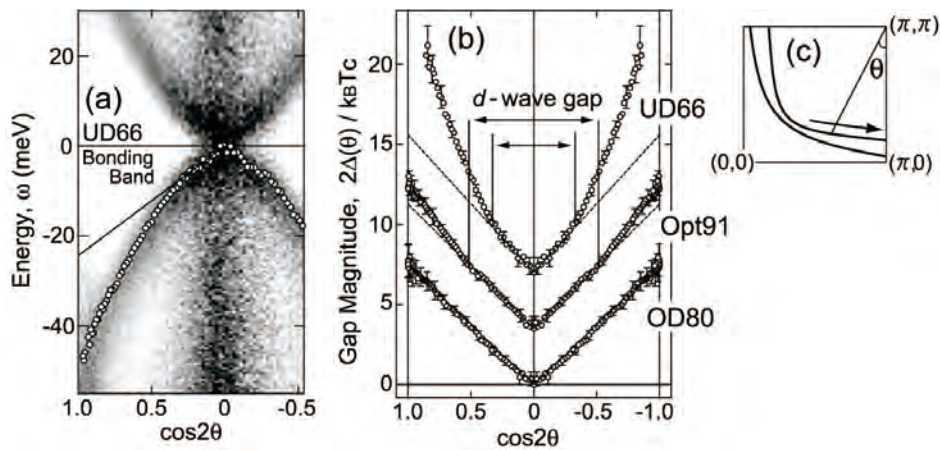


Fig.1 (a) The ARPES spectra of underdoped  $\text{Bi}2212$  ( $T_c = 66$  K), taken along the Fermi surface of the bonding band. (b) Directional dependence of the gap magnitude for underdoped (UD66), optimally-doped (Opt91) and overdoped (OD80) samples. (c) Schematic diagram of momentum space. The spectra are cut along Fermi surface.

denote the energy of the spectral peak, indicating the directional dependence of the gap magnitude as a function of  $d_{x^2-y^2}$  wave-gap magnitude,  $\cos 2\theta$ . Near the node, the result is consistent with  $d_{x^2-y^2}$ -symmetry, whereas in the antinodal region it is appreciably deviated from the  $d_{x^2-y^2}$ -symmetry. Figure 1 (b) shows the directional dependence of the gap magnitude for various hole concentration. The magnitude of antinodal gap rapidly increases as hole concentration decreases, suggesting that the antinodal gap is related to antiferromagnetic fluctuation. We have found that the near-nodal  $d$ -gap region rapidly shrinks as hole concentration decreases, and that  $2\Delta(\theta)/k_B T_c \cos 2\theta \sim 8$  in the near-nodal region for all the doping levels. This value is larger than the value  $\sim 4.12$ , which is predicted by BCS weak-coupling model for  $d$ -wave gap within mean-field approximation. It has also been observed for underdoped samples that the quasiparticle group velocity gradually decelerates in going from  $|\omega| \sim -20$  meV to Fermi level in  $(0,0) - (\pi,\pi)$  direction. The Fermi velocity of the underdoped samples is suppressed to 75% of that of the optimally-doped samples, indicating that the renormalization effect increases with decreasing hole concentration. These observations imply that excessively strong interaction may lead to the shrinkage of the near-nodal  $d$ -gap region.

## ARPES study of the quantum size effects in atomically uniform Pb films on Si(111)-7x7

Shaolong He <sup>1</sup>, Zhenhua Zeng <sup>2</sup>, Masashi Arita<sup>1</sup>, Masahiro Sawada <sup>1</sup>,  
Kenya Shimada <sup>1</sup>, Shan Qiao <sup>3</sup>, Guoling Li <sup>2</sup>, Xin Liu <sup>2</sup>, Wei-Xue Li <sup>2</sup>, Yan-feng  
Zhang<sup>4</sup>, Jinfeng Jia<sup>5</sup>, Qi-kun Xue<sup>5</sup>, Hirofumi Namatame <sup>1</sup>, and Masaki Taniguchi <sup>1</sup>

<sup>1</sup> *Hiroshima Synchrotron Radiation Center, and Graduate School of Science,  
Hiroshima University, Higashi-Hiroshima 739-8526, Japan*

<sup>2</sup> *State Key Laboratory of Catalysis, Dalian Institute of Chemical Physics,  
Chinese Academy of Sciences, Dalian 116023, China*

<sup>3</sup> *Advanced Materials Laboratory, Fudan University, Shanghai 200433, China*

<sup>4</sup> *Institute of Multidisciplinary Research for Advanced Materials, Tohoku University, Japan and*

<sup>5</sup> *Department of Physics, Tsinghua University, Beijing 100084, China*

(Dated: October 8, 2008)

The electronic structures and the Fermi surface (FS) topology of atomically uniform Pb(111) films are investigated by high resolution angle resolved photoemission spectroscopy (ARPES). Our results reveal a well-defined FS topology of the atomically uniform Pb films on Si(111) surface. First principle calculations can reproduce the main FS features and further clarify that FS features centered at the  $\Gamma$  point are composed of a well-shaped hexagonal hole pocket and a snowflake-shaped hole pocket. In addition, we clearly demonstrate that the quantum well states induced oscillations in density of state near  $E_F$  are directly related to the numbers of the subbands which survive to enclose hole pockets at the Fermi level.

The electronic structures of thin metallic films are of great research interests due to that these quasi two-dimensional electron systems exhibit novel properties quite different from their bulk counterparts. Many important properties such as the superconductivity,<sup>1-5</sup> electron-phonon coupling,<sup>6</sup> and surface chemical reactivities,<sup>7</sup> can be modulated by the quantum well states (QWS)<sup>8</sup> formed in these metallic films. Such modulation in physical transport properties and chemical reactivity by quantum size effects (QSE) has been convincingly demonstrated to relate closely with the oscillations in density of states (DOS) near  $E_F$  induced by the formation of the QWS in the films.<sup>9</sup> However, the interesting issue about how QWS modulate the DOS near  $E_F$  has remained elusive. The recent advances in manufacturing atomical-layer-resolved Pb films on Si(111)<sup>9</sup> provide us an unique opportunity to explore this fundamental issue by using high resolution angle resolved photoemission spectroscopy (ARPES).

In addition, the convincingly demonstrations of  $T_c$  oscillations in Pb films<sup>1</sup> is of particular interests. While  $T_c$  is strongly influenced by zone-averaged electronic structure especially by the Fermi-level DOS, the Fermi surface (FS) topology also play a significant role. On the other hand, the FS topology may be also shaped or distorted by dimensional confinement in thin films and therefore affect  $T_c$ . Hence investigations on the electronic structures and the FS topology of atomically-layer-resolved Pb films are of fundamental interests and importance.

In this letter, we present a systematic electronic structures study of the atomically uniform Pb(111) films over a wide range of thickness. It is found that Pb(111) films have a well-defined FS which differs significantly from that of bulk Pb(111) crystals. The FS topology features of Pb films are further clarified by density functional the-

ory (DFT) calculations. Detailed theoretical and experimental studies show that the QWS induced oscillations in DOS near  $E_F$  are directly related to the numbers of the subbands which survive to enclose hole pockets at  $E_F$ .

The experiment was performed at Hiroshima Synchrotron Radiation Center (HSRC), Hiroshima University. The clean and defect free Si(111) - (7 × 7) reconstructed surfaces were prepared and checked by STM and LEED. The Pb(111) films were then prepared by evaporating lead from a Mo crucible on Si(111) - (7 × 7) surfaces. The evaporating rate was carefully adjusted to favor the layer-by-layer growth mode at 100 K, which were verified by STM and reflection high energy electron diffraction pattern. The prepared films were gradually annealing to room temperature and then transferred to the analysis chamber with base pressure of  $1 \times 10^{-11}$  Torr for *in situ* ARPES measurements. The ARPES spectra were taken by a Scienta-R4000 electron analyzer at beamline BL-9A<sup>10</sup> with resolution of about 12 meV at photon energy around 21 eV.

The Vienna ab initio simulation package (VASP)<sup>11</sup> was used to solve the Kohn-Sham equations with projector augmented wave (PAW) potentials<sup>12</sup> and GGA-PBE functional for exchange-correlation interaction.<sup>13</sup> Pb 6s and 6p electrons were treated as valence electrons, and plane wave cutoff (100 eV) for PAW potentials were used. The spin-orbit coupling were found to be important to describe band structure properly, and included in all our calculations. Calculated lattice constant (5.03 Å) was used to build the supercell separated by 20 Å vacuum. The Brillouin zone was sampled by Monkhorst-Pack (12 × 12 × 1) grid, and Methfessel-Paxton approach with parameter of 0.20 for accelerating the electronic relaxation.<sup>14</sup> The top five metal layers on both

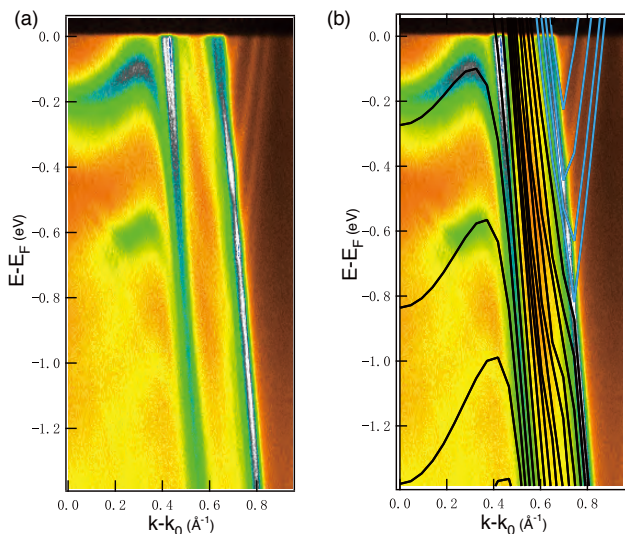


FIG. 1: (a) ARPES intensity image of a 21 ML Pb(111) film taken, at a temperature of 12 K, along  $\Gamma M$  direction with a photon energy of 21 eV. (b) The calculated band structures on the 21 ML Pb(111) slabs. The black and blue lines represent the two different group subbands. The ARPES intensity image in (a) is also included for comparison.

sides of the slab were relaxed until the forces less than  $0.0X \text{ eV/\AA}$ .

Fig. 1 shows ARPES intensity images along  $\Gamma M$  obtained on a Pb(111) film with thickness of 21 monolayers (ML). For a 21 ML Pb(111) film, the bulk bands are split into 21 two-dimensional subbands as indicated by the results from DFT calculations (solid lines) in Fig. 1(b), where the same ARPES intensity image in Fig. 1(a) is also included for comparison. The dispersions of the QWS in the 21 ML Pb(111) film is very similar to a previous ARPES study on thin Pb(111) films.<sup>15</sup> Near the zone center, a sharp QWS peak, which located above binding energy of 0.2 eV, can be resolved indicating the high quality of the Pb films. However, around  $k_{\parallel} \sim 0.7 \text{ \AA}^{-1}$ , there are four subbands crossing  $E_F$  and enclosed hole pockets around the M point which can be reproduced by the calculations presented in Fig. 1(b) and Fig. 2(d) (blue lines). These band features have not been reported in previous ARPES results on Pb(111) films<sup>15-17</sup> since it needs high quality films and high resolution ARPES.

The FS evolution in the Pb(111) films over a wide range of thickness is summarized in Fig. 2. For comparison, we also include calculated FS of the Pb(111) crystal in (a) (dotted red line, only the FS feature near zone center is shown) and that of the 21 ML Pb(111) slabs in (d). The experimental FS mapping was obtained from high-resolution ARPES data and integrated over the energy window  $E_F \pm 5 \text{ meV}$  with photon energy of 21 eV. The main features of the experimental FS can be reproduced by this calculation. While the bulk FS fea-

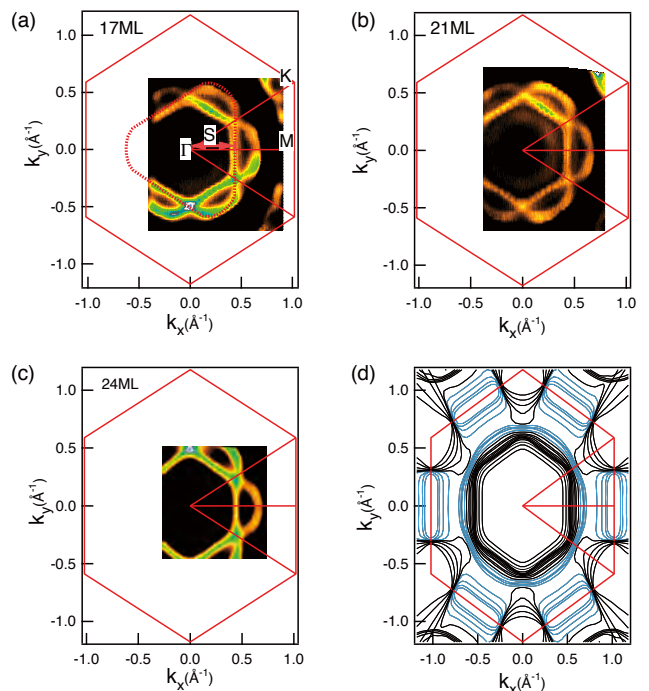


FIG. 2: ARPES intensity mapping integrated over the energy window  $E_F \pm 5 \text{ meV}$  taken on Pb(111) films over a wide range of thickness at a temperature of 10 K with a photon energy of 21 eV. Bright regions correspond to bands crossing  $E_F$ , and thus to sections of the FS. (a) FS mapping of a 17 ML Pb(111) film. The surface Brillouin zone (SBZ) of a Pb(111) surface is indicated by solid red line. Also included is the calculated bulk FS contour center at the  $\Gamma$  point (dotted red line) obtained on the (111) surface of Pb(111) crystal. (b) FS mapping of 21 and (c) 24 ML Pb films. (d) The calculated FS of the 21 ML Pb(111) slabs.

ture has three-fold symmetry, the film FS are clearly six fold symmetric indicating a two-dimensional origination. Near the zone center, the film FS is composed of two crossing triangular bulk FS, which are both center at  $\Gamma$  and are rotated  $60^\circ$  apart from each other. To further clarify the two-dimensional character of the film FS, we measured the ARPES spectra on the films by varying the incident photon energy from 15 to 35 eV, which can cover  $\sim 60\%$  of the Brillouin zone. The band dispersions associated with the inner hexagonal FS features indeed remain the same regardless of the incident photon energies. Hence, the Pb(111) film FS shown in Fig. 2 is of true two-dimensional nature.

Here we are interested in FS features around the zone center. As can be seen in Fig. 2, at the crossing points of the two isotropic triangular features, there are non-crossing gaps open. Their details are further examined in Fig. 3 showing the band dispersions close to a crossing point. Fig. 3(a) is a band mapping close to one of the crossing point along the red line drew in the FS sketch in Fig. 3(c), where the dotted red and green lines represent the Pb bulk FS after rotated  $60^\circ$  apart from each

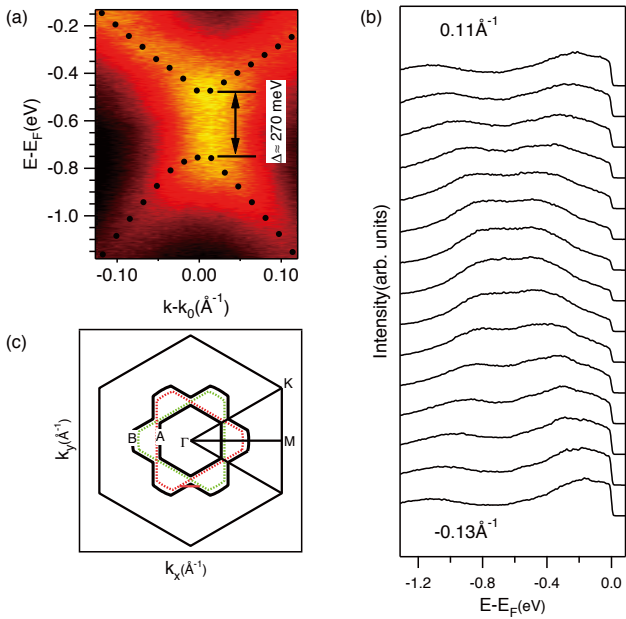


FIG. 3: (a) The band mapping close to the crossing point along the red line drawn in the FS sketch in (c). The filled black circles are band positions extracted from the same data but displayed as EDCs in (b). (c) A sketch of the film FS features centered at the  $\Gamma$  point. The dotted red and green lines represent the Pb bulk FS after rotated  $60^\circ$  from each other. The FS feature contains a hexagonal hole pocket (solid black line A) and a snowflake-shaped hole pocket (solid black line B).

other. The gap can be directly resolved in Fig. 3(a) and further determined in Fig. 3(b), where the energy distribution curves (EDCs) clearly exhibit two well separated peaks indicating a noncrossing gap opens when the two bands, which are associated with the right and left triangular bulk FS respectively, intersect. To determine the gap size, we fit the EDCs in Fig. 3(b) after subtracted a suitable background and obtained the band position depicted as solid circles in Fig. 3(a). The determined gap size is about 270 meV. The origination of this gap is due to strong spin-orbit interaction since the calculated band structures without spin-orbit coupling show no gap opens. As a result of the interaction between the right and left triangular FS features, the film FS (near zone center) contains two closed contours, namely, a hexagonal hole pocket (A) and a snowflake-shaped hole pocket (B) both centered at the  $\Gamma$  point. The snowflake-shaped hole pocket and the hexagonal pocket are derived, respectively, from two different group of subbands indicated as black and blue lines in Fig. 2(d) and 4(a). These two group of subbands separated from each other in energy due to strong spin-orbit interaction, which also plays a dominant role in forming the noncrossing band gap discussed in Fig. 3. It is interesting to clarify the origination of the observed six-fold symmetric film FS. The first possibility is that we may have observed the bulk-derived

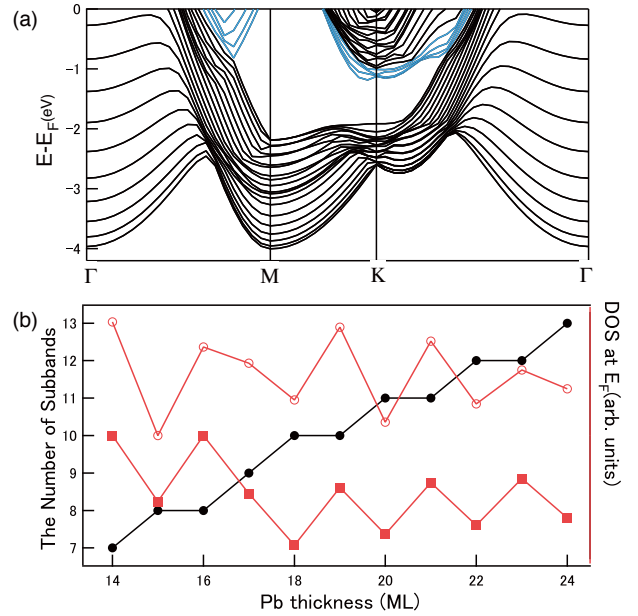


FIG. 4: First principle calculated results on the 21 ML free-standing Pb(111) slabs. (a) The calculated band structures of the Pb(111) slabs. (b) The calculated DOS at  $E_F$  as a function of Pb(111) films thickness (open circles). Also plotted vs the thickness is the number of the subbands which cross  $E_F$  and enclose hole pockets at  $E_F$  (filled black circles) and the electron density determined by the volume of hole pockets associated with the FS feature A (filled red squares). The lines between markers are to guide the eyes.

FS features, which are averaged along the  $k_z$  direction due to the ambiguity along the  $k_z$  direction. However, for a 21 ML Pb films, the estimated  $k_z$  uncertainty is about  $\Delta k_z \sim 1\%$  of the Brillouin zone. On the other hand, features originating from lack of  $k_z$ -resolution are usually more broad and accompanied by a diffuse background. Therefore, our observations do not favor the above explanation. Noting that the surface plane might be approximately six-fold symmetric then it is possible we are seeing the electronic states localized at surface. This is indeed consistent with the photon energy dependent measurements results which reveal that the film FS is of two-dimensional nature.

To examine the FS topology transition induced by film thickness, we will compare the sizes of the FS feature for different thickness since the FS shape in Fig. 2 are almost identical regardless of their thickness. Here, for example, we compare the sizes of the FS feature A for different thickness. Since the FS feature A has a good hexagonal shape with parallel FS edges, the size of the FS feature A can be characterized by a vector  $\vec{S}$  as shown in Fig. 2(a). The magnitude of  $\vec{S}$  is estimated to be  $\sim 0.44, 0.43, 0.44,$  and  $0.43 \text{ \AA}^{-1} (\pm 0.01 \text{ \AA}^{-1})$  for thickness of 17, 21, 24, and 25 ML (data not shown in Fig. 2) and can be considered to be the same within the error level. The fact of no or weak thickness dependence on the shape and

size of the films FS comes from the weak QSE of FS edge, which is far from  $\Gamma$  point. Our DFT calculations show that QSE is not only size but also wavevector dependent: being maximum at  $\Gamma$  due to strong interlayer coupling between  $p_z$  orbitals, but could be vanishingly small at other symmetry points due to weak interlayer coupling between  $p_{x,y}$  orbitals.<sup>18</sup>

As was already discussed in Fig. 1, for a given film with thickness of  $t$  ML, the bulk bands of Pb are split into  $t$  two-dimensional subbands. Some of the subbands, which are associated with the FS feature A, sink below  $E_F$  due to the formation of the QWS in the film normal direction. In order to determine the number of the subbands that are survived to crossing  $E_F$ , we check the calculated results for thickness of 21 ML as presented in Fig. 2 (d) and Fig. 4(a). For the hexagonal FS feature A, 10 of 21 subbands sink below  $E_F$  due to QWS and thus only 11 subbands survive to enclose hole pockets at  $E_F$ . With increasing the thickness of Pb layers, one subband moves down to cross  $E_F$  and becomes occupied for every two added layer. This produces a 2-ML step increase in the number of the survived subbands crossing  $E_F$  as shown in Fig. 4(b) as filled black circles.

So far we have clarified that the film FS features A and B are two-dimensional hole pockets and determined the number of subbands which enclosed hole pockets associated with the FS features A. It is therefore straightforward to determine the carrier density by calculating the volume of these pockets for a given thickness. For simplicity, we only calculate the Luttinger volume of FS features A and the consequent results should represent the true oscillatory trend induced by QSE effects, since the QWS are totally derived from the subbands associated with the FS feature A. The thus determined electron density is plotted as a function of the films' thick-

ness in Fig. 4(b) as filled red squares. Also displayed in Fig. 4(b)(open circles) is the calculated DOS at  $E_F$ . Interestingly, the calculated electron density according to the Luttinger volume of the FS feature A also exhibits a 2-ML oscillations with a beating node showing at 17 ML and can exactly match the oscillatory trend of the DOS at  $E_F$ . Our results, therefore, indicate convincingly that the formation of QWS in the Pb(111) films determines the number of the subbands, which survive to cross the Fermi level and enclose hole pockets at  $E_F$ , and thus determine the oscillatory behavior of electron density of the Pb(111) films. For the first time, we are able to explain quantitatively how the QWS formed in the film normal direction modulates the DOS at  $E_F$ .

In conclusion, the high-resolution ARPES data presented in this paper clearly revealed a well-defined FS with sixfold symmetry for the atomical-layer-resolved Pb(111) films. By varying the incident photon energy, we established convincingly that the film Fermi surface features centered at the  $\Gamma$  point are of true two-dimensional nature. The details of film FS features centered at the  $\Gamma$  point are further clarified to be composed of a well-shaped hexagonal hole pocket and a snowflake-shaped hole pocket. In addition, we, for the first time, reveal that the QWS modulate the DOS at the Fermi level by affecting the number of the subbands enclosed the hexagonal hole pockets at  $E_F$ .

## Acknowledgments

The synchrotron radiation experiments were performed under the approval of HSRC (Proposal No. 07-A-66).

- 
- <sup>1</sup> Y. Guo, Y.-F. Zhang, X.-Y. Bao, T.-Z. Han, Z. Tang, L.-X. Zhang, W.-G. Zhu, E. G. Wang, Q. Niu, Z. Q. Qiu, J.-F. Jia, Z.-X. Zhao, and Q.-K. Xue, *Science* **306**, 1915 (2004).  
<sup>2</sup> X.-Y. Bao, Y.-F. Zhang, Y. peng Wang, Jin-Feng Jia, Qi-Kun Xue, X. C. Xie, and Zhong-Xian Zhao, *Phys. Rev. Lett.* **95**, 247005 (2005).  
<sup>3</sup> D Eom, S Qin, M.Y. Chou, and C.K. Shih, *Phys. Rev. Lett.* **96**, 027005 (2006).  
<sup>4</sup> M.M. Özer, J.R. Thompson, and H.H. Weitering, *Nature Physics* **2**, 173 (2006).  
<sup>5</sup> M.M. Özer, Y. Jia, Z.Y. Zhang, J.R. Thompson, and H.H. Weitering, *Science* **316**, 1594 (2007).  
<sup>6</sup> Y.F. Zhang, J.F. Jia, T.Z. Han, Z. Tang, Q.T. Shen, Y. Guo, Z.Q. Qiu, and Q.K. Xue, *Phys. Rev. Lett.* **95**, 096802 (2005).  
<sup>7</sup> X. Ma, P. Jiang, Y. Qi, J. Jia, Y. Yang, W. Duan, W.-X. Li, X. Bao, S. B. Zhang, and Q.-K. Xue, *Proc. Natl. Acad. Sci. U.S.A.* **104**, 9204 (2007).  
<sup>8</sup> For a review, see T.-C. Chiang, *Surf. Sci. Rep.* **39**, 181 (2000).  
<sup>9</sup> J.F. Jia, S.C. Li, Y.F. Zhang, and Q.K. Xue, *J. Phys. Soc. Jpn.* **76**, 082001 (2007).  
<sup>10</sup> M. Arita, K. Shimada, H. Namatame, and M. Taniguchi, *Surf. Rev. Lett.* **9**, 535 (2002).  
<sup>11</sup> G. Kresse and J.Furthmüller, *Phys. Rev. B* **54**, 11169(1996).  
<sup>12</sup> G. Kresse and D. Joubert, *Phys. Rev. B* **59**, 1758 (1999).  
<sup>13</sup> J. Perdew, K. Burke, and M. Ernzerhof, *Phys. Rev. Lett.* **77**, 3865 (1996)  
<sup>14</sup> H. J. Monkhorst and J. D. Pack, *Phys. Rev. B* **13**, 5188 (1976).  
<sup>15</sup> M.H. Upton, T. Miller, and T.-C. Chiang, *Phys. Rev. B* **71**, 033403 (2005).  
<sup>16</sup> J.H. Dil, T.U. Kampen, B. Hülßen, T. Seyller, and K. Horn, *Phys. Rev. B* **75**, 161401 (R) (2007).  
<sup>17</sup> P. S. Kirchmann, M. Wolf, J. H. Dil, K. Horn, and U. Bovensiepen, *Phys. Rev. B* **76**, 075406 (2007).  
<sup>18</sup> X. Liu, S. B. Zhang, X. C. Ma, J. F. Jia, Q. K. Xue, X. H. Bao and W. X Li, *Appl. Phys. Lett.* **93**, 093105 (2008).

## Optimization of fluorescence XAFS spectroscopy for L edge measurements of Pd nano particles supported onto ZrO<sub>x</sub>

Shinjiro Hayakawa<sup>a</sup>, Hiroyuki Koga<sup>a</sup>, Hirosuke Sumida<sup>b</sup>, Hirofumi Namatame<sup>c</sup> and Takeshi Hirokawa<sup>a</sup>

<sup>a</sup>Department of Applied Chemistry, Hiroshima University, Hiroshima, Japan

<sup>b</sup>Technical Research Center, Mazda Motor Co., Hiroshima, Japan

<sup>c</sup>Hiroshima Synchrotron Radiation Center, Hiroshima University, Hiroshima, Japan

X-ray absorption fine structure (XAFS) measurements are widely utilized for characterization of noble metal catalysis. However, characterization of modern Pd catalysis for vehicle exhausts requires trace sensitivity because the size and the amount of the Pd particles are getting smaller while maintaining their functions.

We have investigated the reduction of the detection limit (DL) with the fluorescence yield method. The improvements in the signal to background ration (S/B) can be achieved with the use of a Si detector compared to the conventional gas counter. However, the advantage of the intense SR beam may be lost when the upper counting rate is determined by the signals from supporting materials. We have investigated the use of a poly-ethylene (PE) filter to realize higher S/B for Pd catalysis supported onto ZrO<sub>x</sub>.

Fig.1 shows x-ray fluorescence spectra of Pd catalysis supported onto ZrO<sub>x</sub> with and without a PE filter. Without the PE filter Pd L<sub>α</sub> peak could be rarely recognized owing to the higher energy tail of the strong Zr peak. The DL is inversely proportional to the square root of S<sup>2</sup>/B, and the DL for Pd was reduced from 86 ppm to 13 ppm (wt) with the filter of 120 μm. Fig.2 shows a comparison of Pd L<sub>3</sub> XAFS spectra, and the reduction of the background successfully improved signal to noise ratio of XAFS spectra.

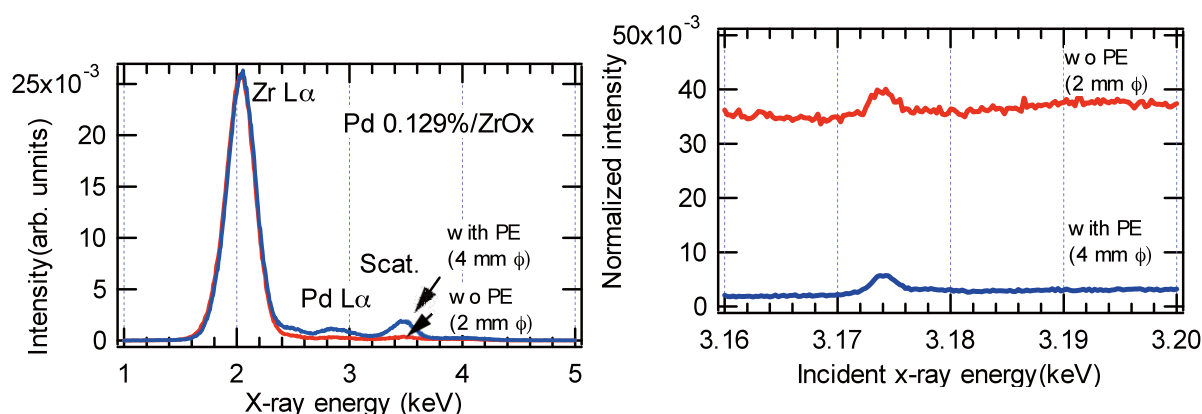


Fig. 1 (left) XRF spectra from Pd/ZrO<sub>x</sub> (0.129%) with and without a PE filter (120 μm).

Fig. 2 (right) Pd L<sub>3</sub> XAFS spectra of Pd/ZrO<sub>x</sub> with and without the PE filter.

[1] S. Hayakawa et al., *Anal. Sci.* 24, 835(2008).

## Molecular chain effect in photon stimulated ion desorption of self-assembled monolayers induced by carbon core excitation

A. Hirano<sup>a</sup>, I. Ohyama<sup>a</sup>, Y. Tanikawa<sup>a</sup>, S. Wada<sup>a,b</sup>, and K. Tanaka<sup>a,b</sup>

<sup>a</sup>*Department of Physical Science, Hiroshima University,  
Higashi-Hiroshima 739-8526, Japan*

<sup>b</sup>*Hiroshima Synchrotron Radiation Center, Hiroshima University,  
Higashi-Hiroshima 739-0046, Japan*

### Introduction

Possibility of site-selective ionic dissociation induced by core excitation has been focused on research in soft X-ray induced chemical reaction. Recently, remarkable site-selective ion desorption was observed in methyl ester terminated self-assembled monolayer (MHDA SAM: Au-S(CH<sub>2</sub>)<sub>15</sub>COOCH<sub>3</sub>) [1]. This finding revealed the more selective reaction in MHDA-DSAM than that of PMMA (-[CH<sub>2</sub>C(CH<sub>3</sub>)COOCH<sub>3</sub>]<sub>n</sub>-) thin film due to its higher orientation. In the following study, the ion desorption yield of MHDA SAM was compared with that of methyl mercaptoacetate (MA SAM: Ag-SCH<sub>2</sub>OCOCH<sub>3</sub>), because it can be considered that such selectivity in ion desorption depends on molecular environment, especially interaction between reaction moiety (methyl-ester group) and metal surface. In fact, site-selective ion desorption is different between MA and MHDA, namely less desorption yield in MA [2]. From these previous studies, thus, photon simulated ion desorption (PSID) reaction depends on molecular environment. In this study, PSID of methyl mercaptopropionate (MP SAM: Ag-S(CH<sub>2</sub>)<sub>2</sub>OCOCH<sub>3</sub>), 4-methoxy benzyl mercaptan (MeOPh SAM: Au-SCH<sub>2</sub>(C<sub>6</sub>H<sub>4</sub>)OCH<sub>3</sub>), and 4-methylbenzyl mercaptan (MePh SAM: Au-SCH<sub>2</sub>(C<sub>6</sub>H<sub>4</sub>)CH<sub>3</sub>) were investigated in order to clarify molecular chain effect in PSID (Fig. 1).

### Experiment

Experiments were performed at the beamline BL-13 of HiSOR. The experimental chamber was equipped with a conventional ion detector and its pressure was  $5 \times 10^{-10}$  torr at room temperature. Total ion yield (TIY) was obtained by the ion detector. Near edge X-ray absorption fine structure (NEXAFS) was recorded in total electron yield (TEY) mode by measuring a sample drain current. All spectra measured were normalized to the incident photon flux monitored with a gold-coated W mesh.

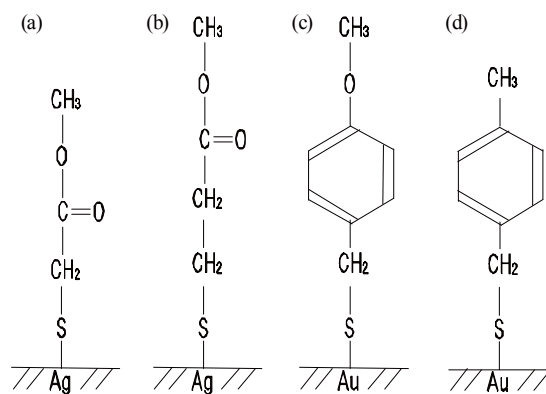


**Fig. 1** Molecular structures of (a) MA, (b) MP, (c) MeOPh, and (d) MePh SAMs.

MePh and MeOPh SAMs were prepared by immersing Au coated Si substrates into 1.0 mM ethanol (Kanto Chemical) solutions during 24 h. Similarly, MA and MP monolayers were also prepared by the same manner for Ag coated Si substrates. SAMs were rinsed in ethanol immediately after removal from solutions and quickly inserted into the UHV chamber for analysis. Chemicals used in this study are illustrated in Fig. 1.

## Results and Discussion

Fig. 2 shows relative TIY spectra in the C K-edge region, where ion yields in the pre-edge are subtracted. Comparing MP with MA SAMs, the desorbing ion yield of MP become higher than that of MA. Difference between MP and MA is the length of methylene chain, namely MA has one methylene group, while MP has two. In previous study, ion yield of MHDA

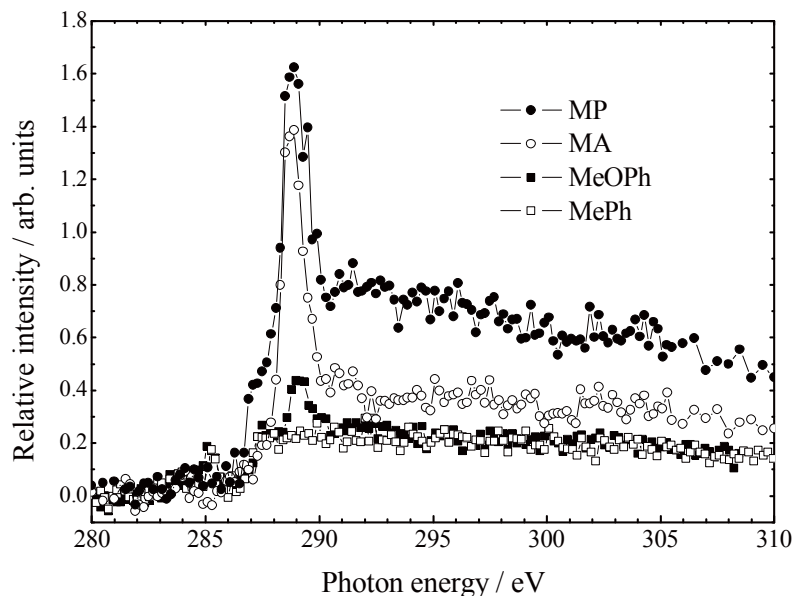


**Fig. 2** TIY spectra for MP, MA, MeOPh, and MePh SAMs in the C K-edge region.

SAM was compared with that of MA SAM, and it was concluded that ion desorption from the core-excited MA is strongly suppressed due to its thinness and therefore occurrence of reneutralization [2]. Methyl ester group where ionic dissociation induced core excitation occurs abundantly exists apart from the metal surface by a methylene group in the MP monolayer compared with that of MA. Based on the result, it can be considered that variation of desorbing ion yield is attributed to different strength of interaction between ionic moieties and the metal surface in desorbing.

On the other hand, TIY spectra of MeOPh and MePh SAMs indicate less desorption compared with those of MP and MA SAMs. This result contradicts the above result because molecular lengths of MeOPh ( $\sim 8$  Å) and MePh ( $\sim 7$  Å) are longer than those of MP ( $\sim 4$  Å) and MA ( $\sim 3$  Å). This result is very interesting. MP and MA SAMs are composed of methylene group, while MeOPh and MePh SAMs are composed of phenyl group. As PSID is strongly inhibited by rapid delocalization of excess energy including a charge,  $\pi$  conjugated systems of MeOPh and MePh SAMs would induce delocalization of excess energy. In conclusion, it can be considered that chemical property of main chain which compose SAM greatly influence PSID.

**References** [1] S. Wada et al., *J. Phys.: Condens. Matter* **18** (2006) S1629. [2] H.Kizaki et al., *Surf.Sci.* **601** (2007) 3956.

## Adsorption of $\text{HS}(\text{CH}_2)_2\text{COOCH}_3$ on Cu(111) surface studied by XPS and NEXAFS spectroscopy

Kei Yufu<sup>a</sup>, Katsumi Watanabe<sup>a</sup>, Kazuhiro Matsushita<sup>a</sup>,  
Shin-ichi Wada<sup>a,b</sup> and Kenichiro Tanaka<sup>a,b</sup>

<sup>a</sup> *Department of Physical Science, Hiroshima University,  
Higashi-Hiroshima 739-8526, Japan*

<sup>b</sup> *Hiroshima Synchrotron Radiation Center, Hiroshima University,  
Higashi-Hiroshima 739-0046, Japan*

### Introduction

It is well-known that thiol molecules chemisorb on metal surfaces by strong S-metal bonding via experiencing deprotonation of thiol groups (thiolate formation). Such detailed investigation about bonding with metal surfaces can be applied to technological application of molecular electronics. Therefore, the understanding of the adsorption structure and the interaction of organic thiol molecules with metal surfaces are very useful to clarify chemical and physical surface processes.

In the previous study, we revealed the adsorption structure of methyl mercaptoacetate ( $\text{HSCH}_2\text{COOCH}_3$  : MA) on the clean Cu(111) surface at room temperature, which has two reactive functional groups, thiol and carbonyl groups [1]. MA adsorbs on the surface via thiolate formation and weak interaction of the carbonyl group with the surface. Moreover, two different adsorption states were confirmed besides atomic sulfur. It is interesting how the adsorption structure and the interaction with metal surfaces vary by an elongation of methylene chain. In this study, we investigated the adsorption structure of methyl mercaptopropionate ( $\text{HS}(\text{CH}_2)_2\text{COOCH}_3$  : MP) on the Cu(111) surface at room temperature using synchrotron radiation (SR) spectroscopy.

### Experiment

Experiments were carried out in a surface photochemistry chamber equipped with a concentric hemispherical electron analyzer (CHA) and a low energy electron diffraction (LEED) apparatus at the soft X-ray beamline BL13 in HiSOR. The clean surface was obtained by repetitive cycles of annealing at 800K and argon ion irradiation. The cleanliness of the surface was checked by LEED and X-ray photoelectron spectroscopy (XPS) using Mg-K $\alpha$  source. Multilayer of MP was obtained by dosing with a few tens of Langmuirs at low temperature with liquid N<sub>2</sub>. And monolayer of MP was obtained by annealing the multilayer up to room temperature. Polarization-dependent near edge X-ray absorption fine structure (NEXAFS) spectra and XPS spectra were measured to estimate adsorption structure and surface-functional group interaction. The NEXAFS spectra, which were obtained by drain

current of the sample as total electron yield (TEY), were measured by changing an incidence light angle to the surface between 20° and 90°. XPS spectra were measured by changing an exposure of MP.

## Results and Discussion

Carbon and oxygen 1s, and sulfur 2p XPS spectra indicate the discriminative peak shifts by different adsorption conditions from the multilayer to the monolayer, in other words, from the physisorbed to chemisorbed states. Typical example measured for C1s is shown in Fig. 1. The XPS analysis reveals that MP is chemisorbed on the Cu(111) surface with the strong Cu-S bonding, and has week interaction between the C=O group and the Cu surface. Moreover, results of S2p XPS spectra reveal that the atomic sulfide coexists on the Cu(111) surface.

C1s and O1s NEXAFS spectra depicted in Fig. 2 show the presence of sharp and polarization-dependent resonances. The C, O1s(C=O)  $\rightarrow$   $\pi^*(\text{C=O})$  resonances located at the photon energy of 288.5eV and 531.8eV, respectively, indicate clear polarization dependence. From the E-vector polarization analysis of C and O 1s NEXAFS spectra,  $\pi^*(\text{C=O})$  transition dipole moment is tilted by  $64\pm 8^\circ$  from the surface normal. In the same way, orientations of the other transition dipole moments ( $\sigma^*(\text{O-CH}_3)$ ,  $\sigma^*(\text{C=O})$  etc.) were also determined.

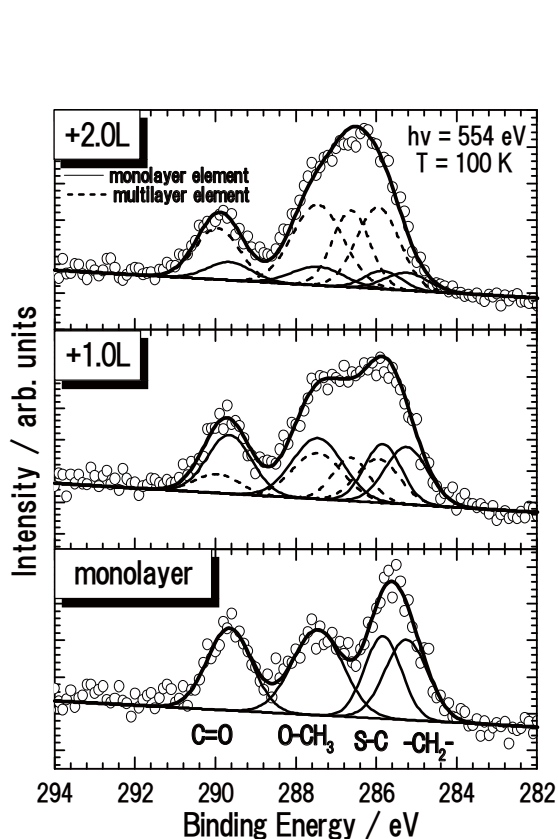


Fig. 1. C1s XPS spectra of MP in different exposure conditions.

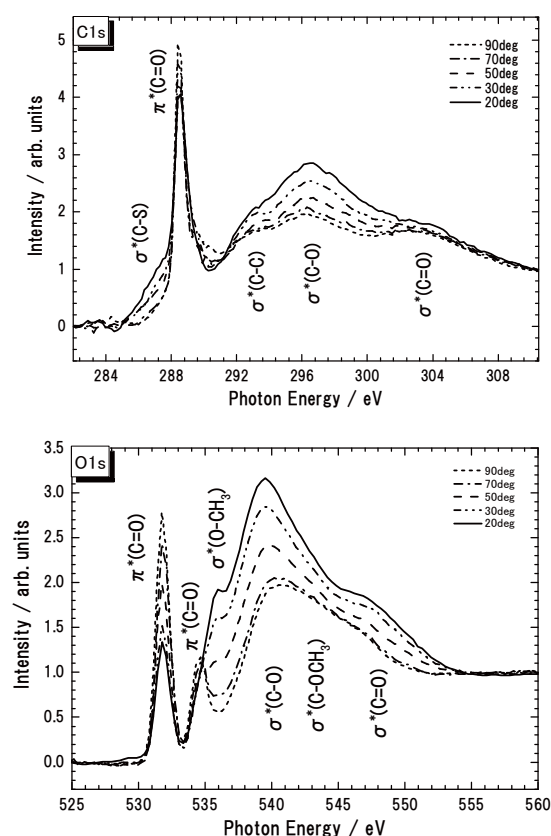


Fig. 2. C1s and O1s NEXAFS spectra of MP measured for various SR incident angles.

From the results of NEXAFS and XPS measurements, the carbonyl oxygen faces the substrate side and  $-C-(C=O)-O$  plane skeleton tilts by  $26\pm 8^\circ$  from the surface normal. Such adsorption structure of MP resembles that of MA in the  $-C-(C=O)-O$  plane skeleton, even though the methylene chain of MP is elongated. The proposed adsorption structure of MP on Cu(111) is illustrated in Fig. 3.

#### References

- [1] S. Wada et. al., Surf. Sci. 601, 3833 (2007).

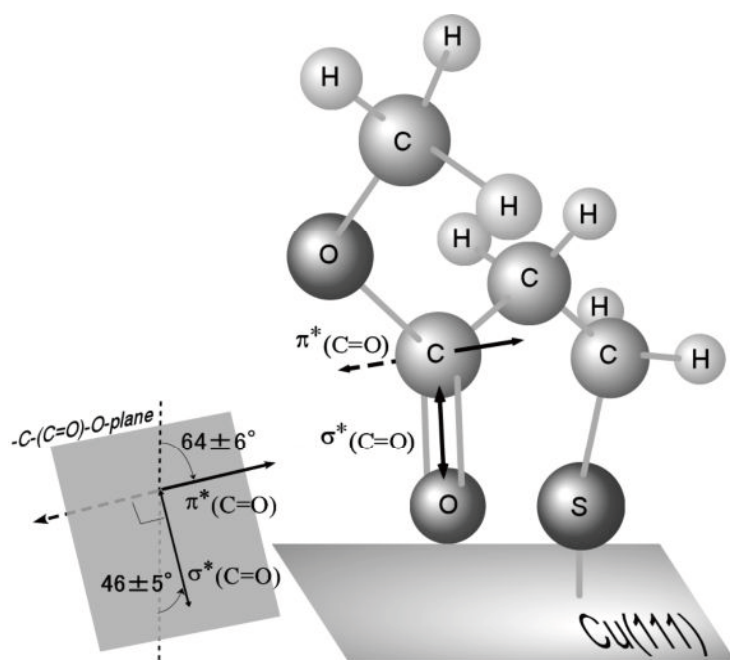


Fig. 3. Schematic structure proposed for MP adsorbed on Cu(111).

## Site-selective ion desorption of fluorine substituted self-assembled monolayers by core electron excitations

Shin-ichi Wada<sup>1,2</sup>, Noriyuki Kushima<sup>1</sup>, Takahiro Yamamoto<sup>1</sup>, and Kenichiro Tanaka<sup>1,2</sup>

<sup>1</sup> Department of Physical Science, Hiroshima University,  
Higashi-Hiroshima 739-8526, Japan

<sup>2</sup> Hiroshima Synchrotron Radiation Center, Hiroshima University,  
Higashi-Hiroshima 739-0046, Japan

### Introduction

Core-electron excitations have quite unique nature differently from valence excitations because of special localization of core electrons. So, ionic dissociation induced by resonant core excitations also reveals characteristic phenomena. In particular, site-selective ionic dissociation is one of noteworthy characteristics. So far, we have found that such selective bond breaking can occur on organic surfaces, especially for ester compounds like poly-methylmethacrylate (PMMA) thin films and ester-terminated self-assembled monolayers (SAMs) [1].

In this study, near-edge X-ray absorption fine structure (NEXAFS) and the following ionic dissociation were spectroscopically investigated for fluorine substituted SAMs, alkane type SAM ( $\text{CF}_3(\text{CF}_2)_7(\text{CH}_2)_2\text{S}/\text{Au}$ ; FD SAM) and benzyl type one ( $p\text{-FC}_6\text{H}_4\text{CH}_2\text{S}/\text{Au}$ ; pFPh SAM), in which strong C-F bond scission is expected under the equivalent core model ( $Z+1$  approximation).

### Experiment

Experiments were carried out on the soft X-ray beamline BL13. NEXAFS spectra in the C 1s and F 1s edges were recorded in total electron yield (PEY) and total ion yield (TIY) modes. In polarization-dependent TEY measurements, incident angle of X-ray was changed by

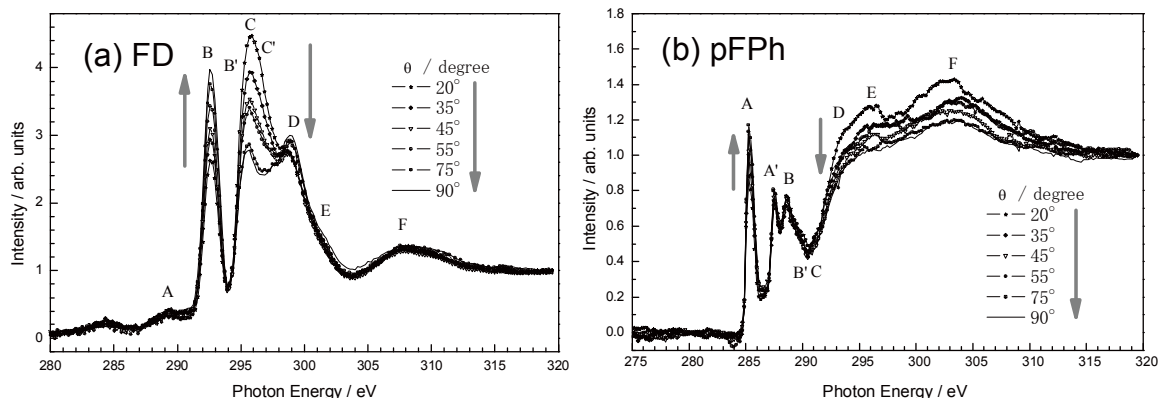


Fig. 1. TEY spectra of core-excited (a) FD and (b) pFPh SAMs in the C1s regions measured at the SR incident angle of 20° (grazing incidence) - 90° (normal incidence).

rotating a sample holder. During measurements, the experimental chamber was kept at  $2 \times 10^{-10}$  Torr. Photon energy was calibrated by PMMA thin film for the C 1s edge and gaseous SF<sub>6</sub> for the F 1s. Monolayer films were prepared by immersing Au coated Si substrates into 1.0 mM ethanol solutions during 24 hours.

## Results and Discussion

Fig. 1 shows the incident-angle dependent TEY spectra measured for (a) FD and (b) pFPh SAMs in the C 1s region. The spectra were measured at 20° - 90° incident angles ( $\theta$ ) from sample surfaces. Assignment of each peak labeled in the figure is listed in Table 1 based on refs. 2-5. Clear dependence are seen in the spectra for peaks mainly attributed to the  $\sigma^*(\text{C-F})$  (peak B) and  $\sigma^*(\text{C-C})$  (peak C) excitations for FD, and  $1\pi^*(\text{C-H})$  (peak A) excitation for pFPh. Net intensities for the resonances derived from curve fitting procedure are plotted as a function of incident angle of SR as shown in Fig. 2. From the polarization (incident) angle dependence, angles of transition dipole moments from surface normal for the excitations can be derived. It should be noted here that the angle  $\alpha$  of the transition moment of the  $\sigma^*(\text{C-C})$  excitation for FD SAM corresponds to the average tilting angle of C-C skeleton and the angle of the  $\sigma^*(\text{C-F})$  corresponds to the angle perpendicular to the C-C skeleton ( $90 - \alpha$ ). The derived angle  $\beta$  of the transition moment of  $1\pi^*(\text{C-H})$  for pFPh SAM also corresponds to the angle perpendicular to the tilting phenyl ring from the surface normal. From the dependence, tilting angles of FD and pFPh SAMs were derived to be  $\sim 44^\circ$  and  $\sim 33^\circ$  using the formula between the angles of the electric field vector (incident angle of SR,  $\theta$ ) and the transition dipole moment [6].

TIY spectra measured for both SAMs in the C and F 1s regions are shown in Fig. 2 together with the corresponding TEY. All of TIY spectra indicate different spectral features, indicating specific ionic dissociation promoted by resonant core excitations. Moreover, it is noted that such specific ion desorption makes obscure peaks buried in the TEY spectra visible in the TIY, like peaks B' and C' in the C 1s of FD, and peak C in the C1s and peak A in the F 1s of pFPh. Especially in the F 1s edge, it is noteworthy that the  $\sigma^*(\text{C-F})$  excitations of both SAMs cause strong ion desorption as expected by the equivalent core model (Z+1 approximation).

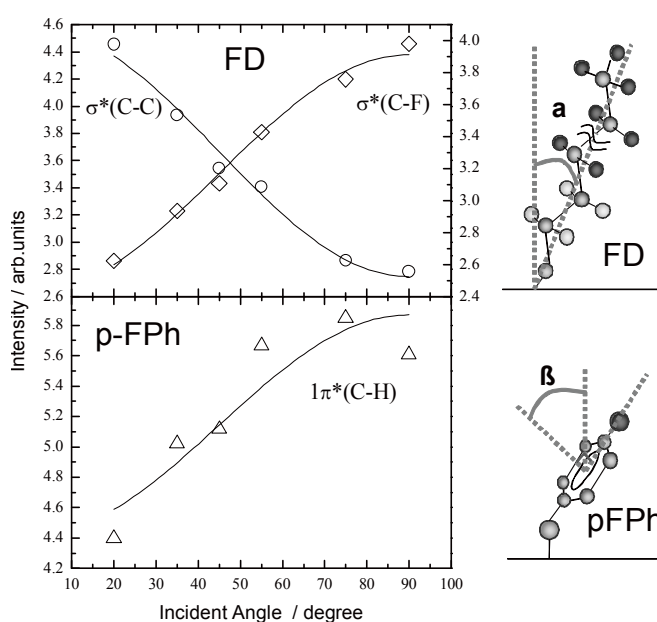


Fig. 2. Incident angle dependence of integrated intensities of the net  $\sigma^*(\text{C-C})$  and  $\sigma^*(\text{C-F})$  excitations for FD and the  $1\pi^*(\text{C-H})$  for pFPh.

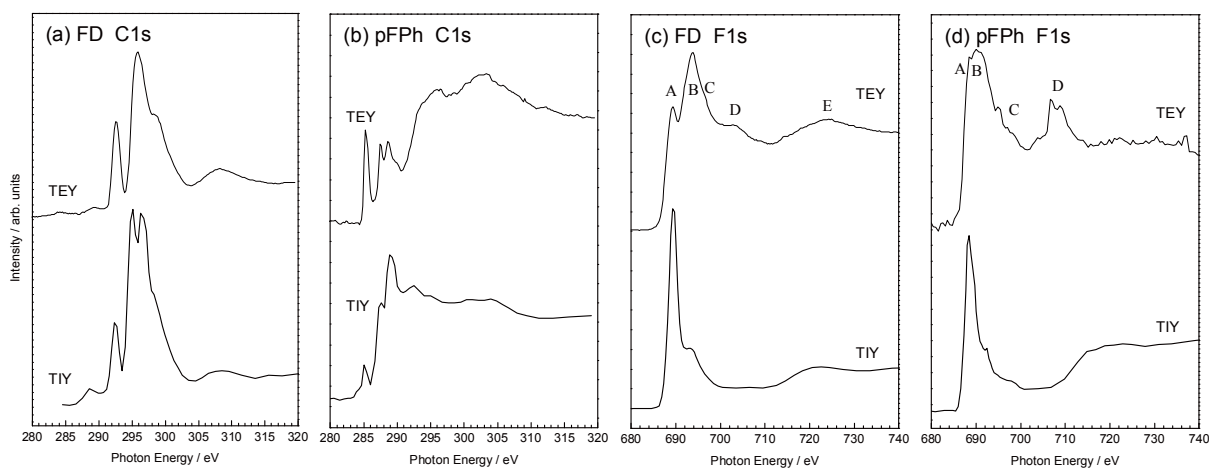


Fig. 3. TEY and TIY spectra measured for C 1s spectra of (a) FD and (b) pFPh SAMs, and F 1s of (c) FD and (d) pFPh.

Table 1: Assignments of FD and pFPh SAMs in the C 1s and F 1s edges.

Peak	Energy / eV	Assignment	Peak	Energy / eV	Assignment
FD			pFPh		
A	~289	$\sigma^*(\text{C-H})$ / Rydberg	A	285.3	$1\pi^*$ : C-H
B	292.5	$\sigma^*(\text{C-F})$ : $-\text{CF}_2-$	A'	287.6	$1\pi^*$ : C-F
B'	295.0	$\sigma^*(\text{C-F})$ : $-\text{CF}_3$	B	288.6	$2\pi^*$ : C-H
C	295.7	$\sigma^*(\text{C-C})$ : $-\text{CF}_2-$	B', C	289.5	$2\pi^*$ : C-F, $\sigma^*(\text{C-F})$
C'	296.4	$\sigma^*(\text{C-C})$ : $-\text{CF}_3$	D	293.8	$\sigma^*(\text{Ph})$
D	299.0	$\sigma^*(\text{C-F})$ : $-\text{CF}_2-$	E	297.0	$\sigma^*(\text{Ph})$
E	300.2	$\sigma^*(\text{C-C})$	F	304.0	$\sigma^*(\text{Ph})$
F	308.4	$\sigma^*(\text{C-F})$			
A	689.5	$\sigma^*(\text{C-F})$	A	688.5	$\pi^*(\text{Ph}) \rightarrow \sigma^*(\text{C-F})$
B	694.3	$\sigma^*(\text{C-C})$	B	690.0	$\sigma^*(\text{C-F})$
C	696.3	$\sigma^*(\text{C-F})$	C	695	$\sigma^*(\text{Ph})$ ?
D	704.0	$\sigma^*(\text{C-C})$	D	~708	$\sigma^*$
	720	multi-ex.			
E	724	$\sigma^*(\text{C-F})$			

## References

- [1] S. Wada et. al., J. Phys.: Condens. Matter 18, S1629 (2006).
- [2] H. Setoyama et al., Nucl. Instr. Meth. Phys. Res. B 199, 275 (2003).
- [3] A. Fujimori et al., Bull. Chem. Soc. Jpn. 76, 663 (2003).
- [4] K.K. Okudaira et al., Nucl. Instr. Meth. Phys. Res. B 199, 265 (2003).
- [5] A.P. Hitchcock et al., J. Phys. Chem. 91, 531 (1987).
- [6] J. Stöhr, NEXAFS Spectroscopy, Surface Sciences vol.25 (Springer, Berlin, 1992).

## ***In-situ* XMCD measurement system for magnetic ultrathin films at BL14**

M. Sawada

*Hiroshima Synchrotron Radiation Center, Hiroshima University*

Magnetic properties of thinfilm and multilayer have been attracted great interest from viewpoints of both fundamental science and technological applications for the few decades. With the technological progress of ultra high vacuum (UHV) and molecular beam epitaxy (MBE), well-defined structures of magnetic monolayer have been obtained on single crystal surfaces of metals and semiconductors. The microscopic magnetic property of the monatomically layered magnetic ultrathin films is a critical issue to understand interface magnetism, origin of perpendicular magnetic anisotropy (PMA) and spin-dependent transport of tunneling magnetic resistance (TMR) junctions. X-ray magnetic circular dichroism (XMCD) spectroscopy is a very powerful tool to study the local magnetic moment in the atomic sites of the magnetic ultrathin films element-specifically. So far, many XMCD studies on the thickness-dependent spin moment and the enhanced orbital moment at the interface have been carried out for various magnetic thinfilms and multilayers. However, most of them are ex-situ experiments where the samples are fabricated in separate apparatus and covered with antioxidant layers like Au cap layers. Because the crystal and magnetic structures of the monolayer films are sensitive to overlayers or adsorbates, it has been recognized that in order to determine the inner nature of magnetism in the monolayer films, *in-situ* experiments in UHV are desirable. To promote the research project on the monolayer magnetism including the interface magnetism, we have constructed an XMCD measurement system connected to the soft X-ray beamline in the synchrotron radiation facility, where various types of the magnetic ultrathin films are fabricated in monatomic layer control and their structures and magnetic properties are analyzed *in-situ*.

Our *in-situ* XMCD measurement system has been constructed at the soft X-ray beamline BL-14. The beamline is designed to provide the monochromatic polarized light whose energy ranges from 400eV to 1200eV, aimed at X-ray absorption spectroscopy (XAS) and photoelectron spectroscopy with linearly and circularly polarized light. The XMCD station is directly connected into the beamline in the first focal section behind the exit slit of the monochromator. The XMCD station consists of two UHV chambers for the measurement and the sample fabrication, whose base pressures are below  $4 \times 10^{-10}$  Torr. The measurement apparatus is composed of a sample stage connected to a 4-axis manipulator and a

permanent-magnet array joined to a motorized liner stage. The permanent-magnet array supplies magnetic field to the samples along the surface normal direction, whose magnetic flux density is 1.3 Tesla. The XMCD spectra can be measured in the total electron yield mode and in conventional transmission mode by flipping the magnetic field direction with respect to the fixed photon helicity at each energy step of the photon energy scan. In the fabrication chamber, we can conduct the sample fabrication in monatomic layer control and the structural and chemical analysis of the as-grown samples. The fabrication chamber is equipped with an ion gun with differential pumping (ULVAC-PHI FIG-5) for sample cleaning, two UHV evaporators (Omicron EFM3) for MBE deposition, a cylindrical mirror analyzer with an electron gun (ULVAC-PHI 10-155) for Auger electron spectroscopy (AES), a low energy electron diffraction (LEED) optics (Omicron SPECTALEED), an electron gun (EVC RDA-002G) and a fluorescence screen for reflection high energy electron diffraction (RHEED). The sample is mounted on a heating stage for annealing or a cryo stage cooled with liquid nitrogen, which is connected to a 4-axis manipulator. The film growth during the MBE deposition can be monitored in real time by the RHEED intensity oscillation observed with a CCD camera linked to a PC. We have achieved accurate control of film thickness within a few 0.1 ML in layer-by-layer growth mode, using the RHEED monitoring and the crosscheck on AES.

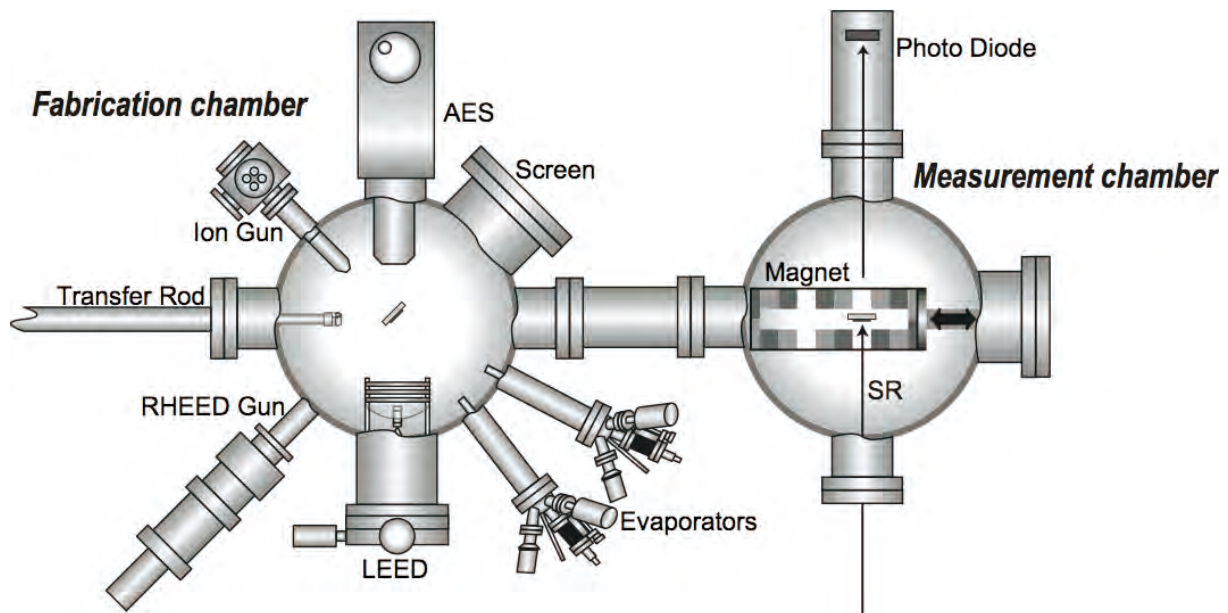


**FIG. 1** Schematic diagram of the *in-situ* XMCD measurement system installed at BL-14.



**FIG. 2** Photograph of the *in-situ* XMCD measurement system.

## Structural and magnetic properties of Cr/Fe/Cu(001)

S. Tohoda <sup>a</sup>, M. Sawada <sup>b</sup>, M. Nagira <sup>a</sup>, T. Ueno <sup>a</sup>, T. Tagashira <sup>a</sup>,

A. Kimura <sup>a</sup>, H. Namatame <sup>b</sup> and M. Taniguchi <sup>a,b</sup>

<sup>a</sup>*Graduate school of science, Hiroshima University, Higashi-Hiroshima 739-8526, Japan.*

<sup>b</sup>*Hiroshima synchrotron radiation center, Hiroshima University, Higashi-Hiroshima 739-0046, Japan*

Fe/Cr multilayers are very interesting system from viewpoints of the Giant Magnetic Resistance (GMR) effect, well known as prize-winning subject, and the junction of ferromagnetic and anti-ferromagnetic layers. The crystal structure of the conventional Fe/Cr multilayers is body centered cubic (bcc). On the other hand, Fe films with face centered cubic (fcc) like structure are realized in the ultrathin film regime, in case the films are grown on a substrate of Cu(001). The structural and magnetic properties of the Fe/Cu(001) films are classified into three phase regions depending on the Fe thickness. In the region I below 4 ML, the Fe films have face centered tetragonal (fct) structure and shows ferromagnetic and perpendicular magnetic anisotropy (PMA) behavior. In the region II between 5 ML and 11 ML, the films are obtained as fcc Fe films where the only top two layers are tetragonally distorted and ferromagnetic with PMA. In the region III above 12 ML, the Fe films become bcc structure and shows in-plane magnetic anisotropy. Since the film structure of Fe is sensitive to the film thickness and overlayers, the structural and magnetic properties of Cr/Fe/Cu(001) are unobvious and expected quite different properties from the conventional Cr/Fe multilayers.

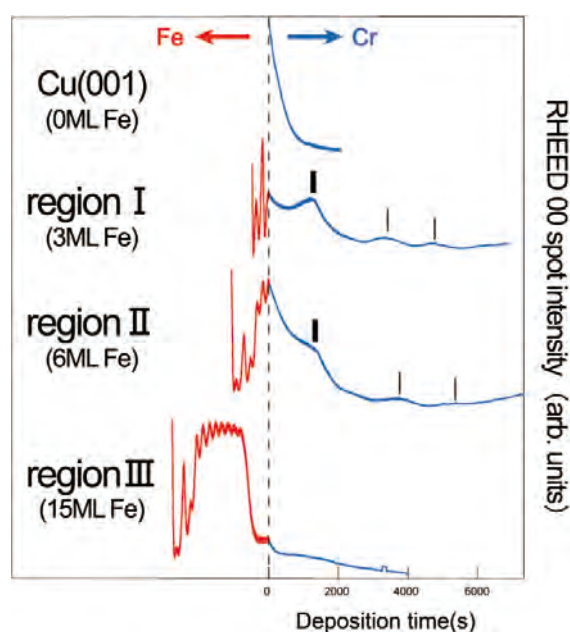


**Fig.1** RHEED intensity of (00) spot during the Cr deposition on the Fe films.

We have investigated the structure and growth mode of Cr/Fe/ Cu(001) for the three region of Fe thickness by means of Low Energy Electron Diffraction (LEED) and Reflection High Energy Electron Diffraction (RHEED) . Figure1 shows the RHEED (00) spot intensity during Fe and Cr deposition. The intensity oscillation of RHEED for region I and II are clearly observed at 1 ML Cr deposition. We conclude that the 1 ML Cr grows epitaxially on the Fe ultrathin films and we have succeeded to create the ultrathin multilayer of Fe and 1 ML Cr with a sharp interface.

We have also examined the magnetism of the Cr/Fe/Cu(001) system by means of X-ray absorption magnetic circular dichroism (XMCD). All the processes of sample preparation and XMCD experiment were performed in-situ. Figure 2 show the XMCD spectrum of Cr/ 3ML-Fe/Cu(001) at  $L_{2,3}$  edge of Fe. It is obvious that the amplitude of the XMCD signal becomes smaller with increasing Cr thickness. The intensity of the XMCD spectra at the  $L_3$  edge reaches into a certain value at the 1 ML Cr deposition. It is considered that the depression of the XMCD signals is caused by the interface formation of the Cr/Fe.

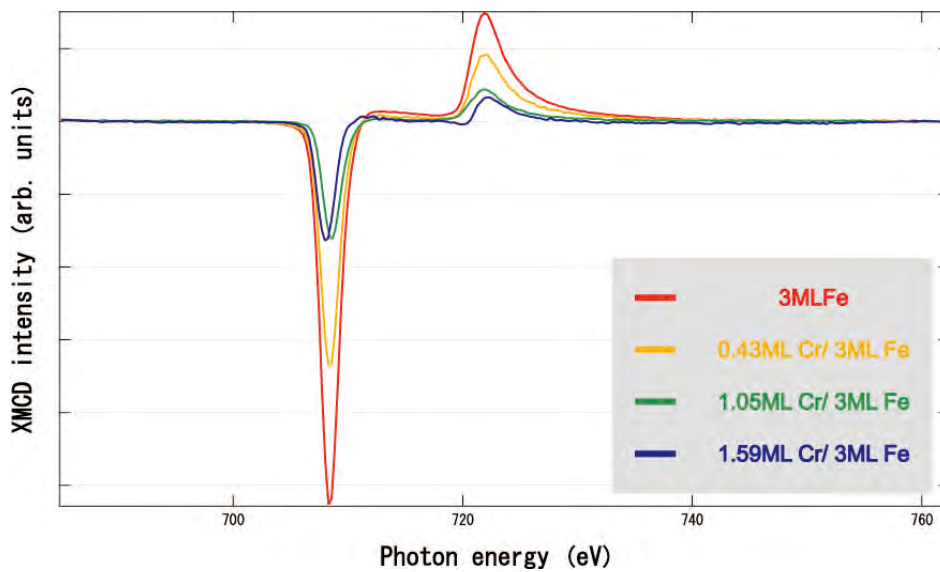


**Fig.2** Cr thickness dependence of XMCD spectra for Cr/3ML-Fe/Cu(001).

## Fabrication and *in-situ* XMCD study of Fe/Pd multilayers on Pd(001)

T. Ueno<sup>a</sup>, M. Sawada<sup>b</sup>, M. Nagira<sup>a</sup>, S. Tohoda<sup>a</sup>, T. Tagashira<sup>a</sup>, A. Kimura<sup>a</sup>,  
H. Namatame<sup>b</sup>, and M. Taniguchi<sup>a,b</sup>

<sup>a</sup>*Graduate School of Science, Hiroshima University*

<sup>b</sup>*Hiroshima Synchrotron Radiation Center, Hiroshima University*

Magnetic metal multilayers with perpendicular magnetic anisotropy (PMA) have been studied for long years, because of importance of its application to high-density magnetic recording media. Ultra-thin films or multilayers of Fe/Pd are well known as a PMA system. Previous studies using XMCD spectroscopy revealed that the orbital magnetic moment of Fe films are enhanced in Fe/Pd(001) [1]. In Fe/Pd multilayers, it is reported that Pd layers become ferromagnetic up to four monolayers (ML) from the Fe-Pd interface [2].  $L1_0$ -type ordered FePd alloy is known to have strong uniaxial magnetic anisotropy perpendicular to Fe and Pd layers [3]. Some experiments and calculations about FePd alloy thinfilms have been reported. However, most of them focus on the chemical ordering of the alloy [4, 5]. We focus on the thinnest limit of the layered PMA structures in the  $L1_0$  FePd alloy films, fabricating the monatomic Fe/Pd multilayers. We have fabricated the Fe/Pd multilayers on the Pd(001) substrate and investigated the magnetic anisotropy using X-ray magnetic circular dichroism (XMCD) spectroscopy.

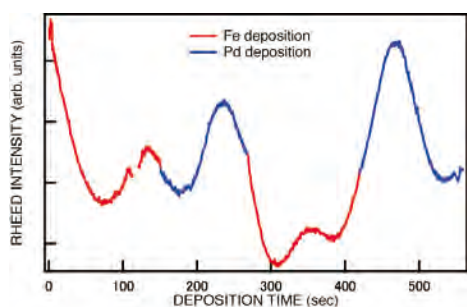


Fig. 1: RHEED [00] streak oscillation during the Fe/Pd multilayers growth. Red and blue curves correspond to the Fe and Pd layer growth, respectively.

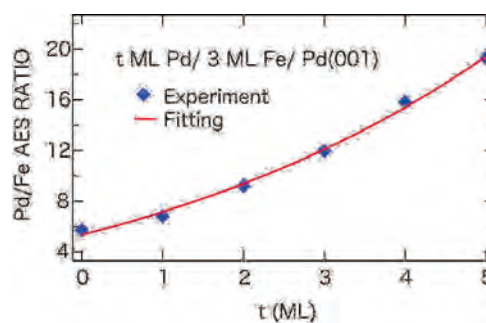


Fig. 2: Fe  $LMM$ /Pd  $MVV$  AES intensity ratio of  $t$  ML Pd/3 ML Fe/Pd(001) ( $t = 0-5$ ). Blue diamonds are experimental data, and the red curve is the fitting curve based on the model that the exponential decay of Auger electrons.

Our experiments were performed at the soft X-ray beamline BL-14, which provides linearly and circularly polarized photons for dichroic spectroscopy. The XMCD experimental system and the sample fabrication system are directly connected to the beamline under an ultra high vacuum. Single crystalline Pd(001) surface was prepared by repeated cycles of argon ion bombardment and annealing at 970 K. Several types of Fe/Pd multilayers were

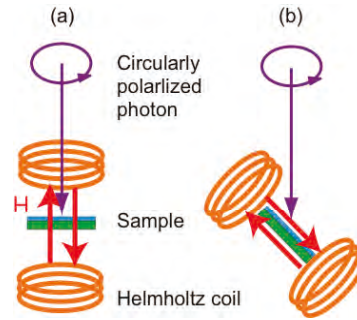


Fig.3: Schematic diagram of XMCD experimental configuration, showing sample magnetization and incident photon direction in the case of detecting (a) out-of-plane and (b) in-plane magnetization, respectively.

fabricated by alternate thermal deposition of Fe and Pd. During the sample fabrication, we observed the reflection high-energy electron diffraction (RHEED) pattern. The thickness control of Fe and Pd was achieved by the real-time observation of the intensity oscillations of the [00] RHEED streak (Figure 1). We also observed Auger spectra of Pd/3ML-Fe/Pd(001) and confirmed that the inter layer mixing between Fe and Pd layer is negligible (Figure 2). The XMCD spectra were obtained at the Fe  $L_{2,3}$  absorption edge ( $2p-3d$  transition) for the fabricated films with remanent magnetization, which was magnetized by the pulsed magnetic field generated by the Helmholtz coil. The sample magnetization was switched in parallel and anti-parallel directions to the incident photon spin. During the XMCD measurement, the sample was cooled by liquid nitrogen. Absorption signal was obtained in total electron yield method of measuring the sample drain current. We employed two different configurations in the XMCD experiments to investigate the magnetic anisotropy (Figure 3).

Figure 4 shows the Fe  $L_{2,3}$  XMCD spectra for the monatomic Fe/Pd multilayers with several stacking patterns. It is probed that the XMCD signals appear only in the grazing incidence configuration shown in Fig. 3. It means that the monatomic Fe/Pd multilayers with regular alternate stacking have the in-plane magnetic anisotropy. The XMCD intensity of the remanently magnetized samples increases with the Fe layer stacking, and close to the intensity measured under the magnetic field. Figure 5 shows the Fe  $L_{2,3}$  XMCD spectra for the different samples, whose stacking patterns are different in the thickness of the second Fe layer from that of the samples presented in Fig. 4. In contrast to the case of the regular alternate stacking, out-of-plane magnetic anisotropy was found in the particular stacking patterns as shown in Fig.5 (c). It seems that the out-of-plane magnetic anisotropy is attributed to the thickness of the topmost Fe layer. We also found that the out-of-plane anisotropy disappears when the topmost

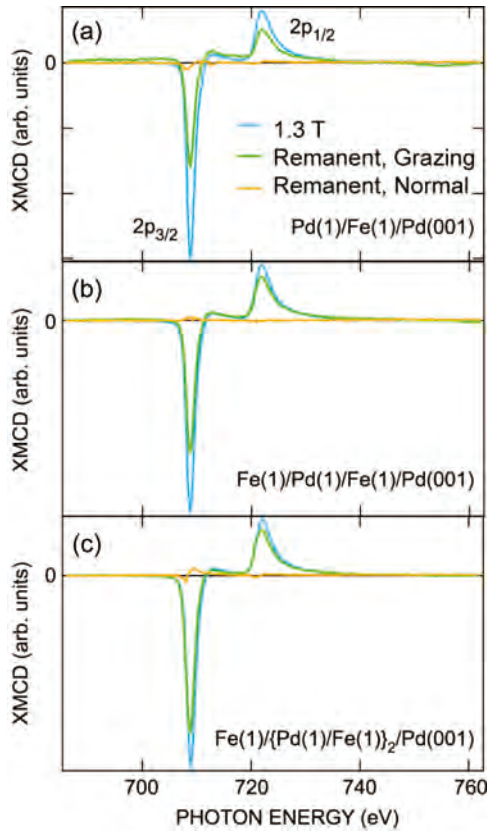


Fig. 4: Fe  $L_{2,3}$  XMCD spectra for monatomic Fe/Pd multilayer. Green and orange lines represent XMCD spectra for grazing and normal incidence, respectively. XMCD spectra taken under the magnetic field (1.3 T) are also shown for comparison (blue line).

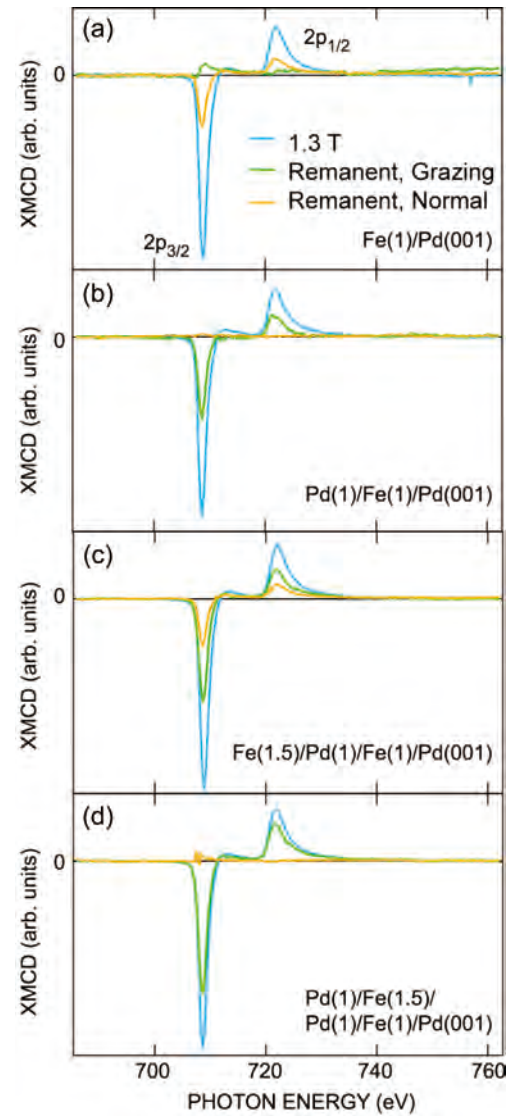


Fig.5 : Fe  $L_{2,3}$  XMCD spectra for Fe/Pd multilayer of which the second Fe layer is 1.5 ML. Green and orange lines represent XMCD spectra for grazing and normal incidence, respectively. XMCD spectra taken under the magnetic field (1.3 T) are also shown for comparison (blue line).

Fe layer is covered with the additional Pd overlayer, as shown in Fig. 5 (d). It is suggested that a part of the Fe atoms on the topmost Fe layer forms island structure, and the peculiar electronic state of Fe atoms on the island edge contribute to the out-of-plane spin reorientation.

In summary, we have fabricated several types of Fe/Pd multilayers and investigated the magnetic anisotropy using XMCD spectroscopy. We observed the in-plane magnetic anisotropy in the monatomic Fe/Pd multilayers with regular alternate stacking. On the other

hand, we observed the out-of-plane magnetic anisotropy in the Fe/Pd multilayers of particular stacking patterns, and the out-of-plane anisotropy seems to be attributed to the Fe thickness of the topmost Fe layer.

## References

- [1] X. Le Cann, C. Boeglin, B. Carrière, and K. Hricovini, *Phys. Rev. B* **54**, 373 (1996).
- [2] J. Vogel, A. Fontaine, V. Cros, F. Petroff, J.-P. Kappler, G. Krill, A. Rogalev, and J. Goulon, *Phys. Rev. B* **55**, 3663 (1997).
- [3] N. Miyata, H. Asami, T. Misushima, and K. Sato, *J. Phys. Soc. Jpn.* **59**, 1817 (1990).
- [4] P. Kamp, A. Marty, B. Gilles, R. Hoffmann, S. Marchesini, M. Belakhovsky, C. Boeglin, H. A. Dürr, S. S. Dhesi, G. van der Laan, and A. Rogalev, *Phys. Rev. B* **59**, 1105 (1999).
- [5] L. Szunyogh, J. Zabloudil, A. Vernes, P. Weinberger, B. Újfalussy, and C. Sommers, *Phys. Rev. B* **63**, 184408 (2001).

## XMCD Study of Orbital Contribution to Perpendicular Magnetization in $\text{Co}_{80}\text{Pt}_{20}$ Thin-Films

N. Ishimatsu <sup>A)</sup>, R. Ogasawara <sup>B)</sup>, T. Sone <sup>B)</sup>, Y. Tsutsui <sup>A)</sup>, H. Maruyama <sup>A)</sup>, N. Nakajima <sup>A)</sup>  
M. Sawada <sup>C)</sup>, H. Namatame <sup>C)</sup>

<sup>A)</sup> Grad. Sch. of Sci., Hiroshima Univ., <sup>B)</sup> Faculty of Sci. Hiroshima Univ.

<sup>C)</sup> HSRC, Hiroshima Univ.

Co-Pt films deposited on a Ru seed layer are one of the candidates for perpendicular recording media. It has been recently reported that uniaxial magnetic anisotropy constant  $K_u$  of the Co-Pt film exceeds  $1 \times 10^7 \text{ erg/cm}^3$  and  $K_u$  significantly increases as the film thickness  $\delta$  decreases to less than  $\delta=20 \text{ nm}$ .<sup>1,2)</sup>

We measured X-ray magnetic circular dichroism (XMCD) at the Co  $L_{2,3}$ -edges of  $\text{Co}_{80}\text{Pt}_{20}$  films and determined  $\delta$  dependence of Co  $3d$  spin ( $m_S^{\text{Co}}$ ) and orbital ( $m_L^{\text{Co}}$ ) magnetic moments using the magneto-optical sum rules. In order to investigate the relationship of  $K_u$  with anisotropy of the orbital moment (AOM), defined as a difference of  $m_L^{\text{Co}}$  between out-of-plane and in-plane magnetization, two experimental geometries were adapted<sup>3)</sup>: one for the normal incidence ( $\gamma=0^\circ$ ) and the other for glancing incidence to the sample surface ( $\gamma=60^\circ$ ). For this purpose, the films with different  $\delta$ ,  $\delta=3, 10, 20,$  and  $60 \text{ nm}$ , were prepared. Furthermore, we separately measured XMCD at the Pt  $L_{2,3}$ -edges on BL39XU of SPring-8, and  $\delta$  dependence of the Pt  $5d$  magnetic moment ( $m_S^{\text{Pt}}$  and  $m_L^{\text{Pt}}$ ) has been studied.

Figure 1 shows X-ray absorption spectrum (XAS) and XMCD spectra at the Co  $L_{2,3}$ -edges. It is found regardless of  $\delta$  that XMCD at  $\gamma=0^\circ$  geometry is larger than that at  $\gamma=60^\circ$  geometry, so that the magnitude of the Co magnetic moment depends on  $\gamma$ . AOM for  $\delta=60 \text{ nm}$  is small compared with those for the thinner films. However, a monotonous increase in the AOM is not observed in a range from  $\delta=20$  to  $3 \text{ nm}$ . On the other hand, AOM for  $m_L^{\text{Pt}}$  is almost constant as a function of  $\delta$ . It is found that the AOM for both Co  $3d$  and Pt  $5d$  are much smaller than magnitudes expected from the large  $K_u$ . The result reveals that contribution of the AOM to the large  $K_u$  is weak for the present films.

### References:

- 1) T. Shimatsu *et al.*, J. Appl. Phys. **99** (2006) 08G908.
- 2) T. Shimatsu *et al.*, IEEE Trans. Magn., **43** (2007) 2995.
- 3) W. Grange *et al.*, Phys. Rev. **B58** (1998) 6298.

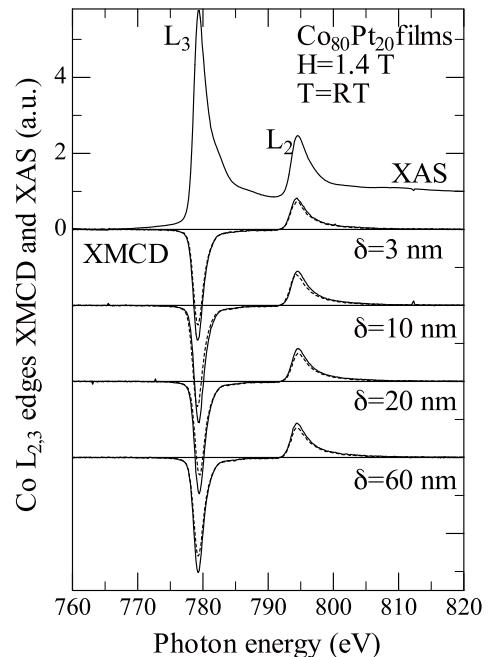


**Figure 1:** XAS and film thickness ( $\delta$ ) dependence of XMCD spectrum at the Co  $L_{2,3}$ -edges. Solid and broken lines correspond to out-of-plane ( $\gamma=0^\circ$ ) and in-plane magnetization ( $\gamma=60^\circ$ ), respectively.

**$L_{2,3}$  XAFS spectroscopy as a probe for the local symmetry of dopants (Nb, Ti) in  
 $\text{LiNi}_{1-x}\text{Co}_x\text{O}_2$**

Shinjiro Hayakawa<sup>a</sup>, Ryuta Hasuno<sup>a</sup>, Tetsutaro Hayashi<sup>b</sup>, Takefumi Sako<sup>b</sup>,  
Masahiro Sawada<sup>c</sup>, Hirofumi Namatame<sup>c</sup> and Takeshi Hirokawa<sup>a</sup>

<sup>a</sup> *Department of Applied Chemistry, Hiroshima University, Hiroshima, Japan*

<sup>b</sup> *Niihama Center Analytical Technology Dep., Sumitomo Metal Mining Co. LTD, Niihama,  
Ehime, Japan*

<sup>c</sup> *Hiroshima Synchrotron Radiation Center, Hiroshima University, Hiroshima, Japan*

$\text{LiNi}_{1-x}\text{Co}_x\text{O}_2$  (LNO) is widely used as a positive electrode material for secondary lithium cells, and the large capacity of LNO is related to its layered structure that can intercalate Li ions reversibly. It is known that charged LNO has the intrinsic thermal instabilities, and one of the solutions is the addition of Ti or Nb to substitute some of Ni sites in LNO. Though the structural change of LNO during the charging has been studied with the x-ray diffraction (XRD) and the extended x-ray absorption fine structure (EXAFS) spectroscopy, the mechanism of the thermal stabilization is still unknown.

To investigate the local structural changes of Ni and doped Ti,  $L_{23}$  edge XAFS spectra were measured on BL14. Two types of charged LNO were prepared for XAFS measurements. One was charged in the test cell, and the disk of LNO was removed just before the measurements. Another one was prepared with hydrochloric acid to extract Li ions chemically from LNO. The fraction of Li desorption was evaluated from the ICP-AES method in the case of chemical charging.

Figs. 1 and 2 show Ni and Ti  $L_{23}$  XAFS spectra of Ti doped LNO. The marked peak showed significant decrease after the Li desorption, and the resultant spectrum was quite similar to that of NiO. The result indicates the local structure of Ni has changed close to Oh symmetry.

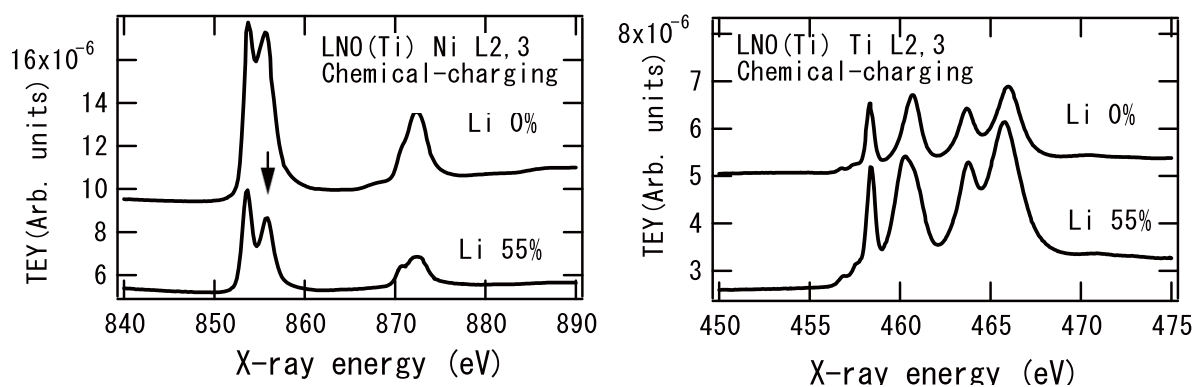


Fig.1  $L_{23}$  XAFS spectra of Ti doped LNO as a function of Li desorption.

## Improved sequence-based prediction of protein secondary structures by combining vacuum-ultraviolet circular dichroism spectroscopy with neural network

Koichi Matsuo<sup>1</sup>, Hidenori Watanabe<sup>2</sup>, and Kunihiro Gekko<sup>2</sup>

(<sup>1</sup>Synchrotron Radiation Center, <sup>2</sup>Graduate School of Science, Hiroshima University)

Synchrotron-radiation vacuum-ultraviolet circular dichroism (VUVCD) spectroscopy can significantly improve the predictive accuracy of the contents and segment numbers of protein secondary structures by extending the short wavelength limit of CD spectra (1, 2). However, VUVCD spectroscopy itself in principle yields no information on the sequence of the secondary structures, which limits the applicability of this technique to the structure analysis of proteins. In the present study, we combined the VUVCD data with neural-network (NN) method to improve the sequence-based prediction of protein secondary structures.

The 30 proteins were used as the target proteins for the sequence-based prediction of secondary structures. The VUVCD spectra of target proteins were previously measured down to 160 nm (1, 2). The secondary structures of these proteins were assigned into  $\alpha$ -helices,  $\beta$ -strands, and others using the DSSP program from their PDB codes. The secondary-structure contents and segments of the target proteins were estimated from their VUVCD spectra using the SELCON3 program (3). The contents and segment numbers of  $\alpha$ -helix and  $\beta$ -strand obtained are plotted against those determined from X-ray structures (Fig. 1). Evidently, there is good agreement between the CD and X-ray estimates for the contents and segment numbers of  $\alpha$ -helices and  $\beta$ -strands. The RMSD ( $\delta$ ) and the Pearson correlation coefficient ( $r$ ) between the X-ray and CD estimates for the overall secondary-structure contents were 0.058 and 0.85, respectively.

Two NN methods were used in this study for computational convenience (4). The first was the Holley and Karplus (NN<sub>HK</sub>) algorithm, in which the weights (output) and biases of 20 amino acids for  $\alpha$ -helices and  $\beta$ -strands were calculated using the secondary-structure information and amino-acid sequences of 48 known proteins as a training set. The second was

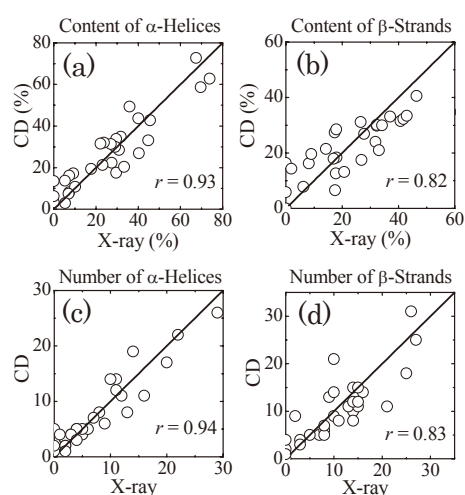


**Fig. 1. Plots of the secondary-structure contents and segment numbers of 30 target proteins predicted from the VUVCD spectra versus the X-ray estimates: (a)  $\alpha$ -helix content, (b)  $\beta$ -strand content, (c) number of  $\alpha$ -helix segments, and (d) number of  $\beta$ -strand segments.**

the Jones (NN<sub>J</sub>) algorithm, which predicts the protein secondary structures using the evolutionary sequence information based on the Position Specific Scoring Matrices generated by the PSI-BLAST algorithm. In our VUVCD-NN<sub>J</sub> method, a data set of 607 proteins was obtained as a training set for NN<sub>J</sub> algorithm. The secondary structures of these training proteins and their amino-acid sequence information were used to calculate the weights and biases of 20 amino acids for  $\alpha$ -helices and  $\beta$ -strands using the public free simulation package Stuttgart Neural Network Simulator (version 4.2).

The VUVCD data were combined with the NN<sub>HK</sub> and NN<sub>J</sub> algorithms using the computational protocol shown in Fig. 1. First, the  $\alpha$ -helix and  $\beta$ -strand weights ( $W_\alpha$  and  $W_\beta$ ) of 20 amino-acids were calculated by NN<sub>HK</sub> or NN<sub>J</sub> methods as described above (Step 1). Second, the positions of  $\alpha$ -helices and  $\beta$ -strands were assigned on the amino-acid sequence in descending order of their weights until the determined numbers of  $\alpha$ -helix and  $\beta$ -strand residues converged to those estimated from VUVCD analysis. The residues assigned as neither  $\alpha$ -helices nor  $\beta$ -strands were considered to be other (Step 2). Overlapping regions (residues) were assigned to  $\alpha$ -helices for the target protein which had more than twice as many  $\alpha$ -helix residues as  $\beta$ -strand residues, and they were assigned to  $\beta$ -strands for the target protein which had more than twice as many  $\beta$ -strand residues as  $\alpha$ -helix residues. For other target proteins, overlapping regions were assigned to either  $\alpha$ -helices or  $\beta$ -strands by directly comparing the weights of overlapped residues. Furthermore, short stretches comprising less than four  $\alpha$ -helix residues and less than two  $\beta$ -strand residues were classified as other (Step 3). The procedures from Step 2 to Step3 were repeated until the predicted numbers of  $\alpha$ -helix and  $\beta$ -strand residues agreed with those estimated from VUVCD analysis (Step 4). The assignment was complete if the two estimates were consistent, but in other cases the sequence alignment that minimized the difference between the two estimates was taken as the final solution (Step 5). The results thus predicted by combining the NN (NN<sub>HK</sub> and NN<sub>J</sub>) algorithm and the number of residues estimated from VUVCD spectroscopy (CD1) were designated as NN+CD1 (NN<sub>HK</sub>+CD1 and NN<sub>J</sub>+CD1).

Next, the numbers of  $\alpha$ -helix and  $\beta$ -strand segments estimated from VUVCD analysis were introduced into the NN calculation (Step 6). If the predicted numbers of  $\alpha$ -helix and  $\beta$ -strand segments did not agree with those estimated from VUVCD analysis, the weights ( $W_\alpha$ ) of 20 amino acids for  $\alpha$ -helices were multiplied by factors from 0.1 to 2.0 until the predicted numbers of segments converged to those obtained from the VUVCD estimation

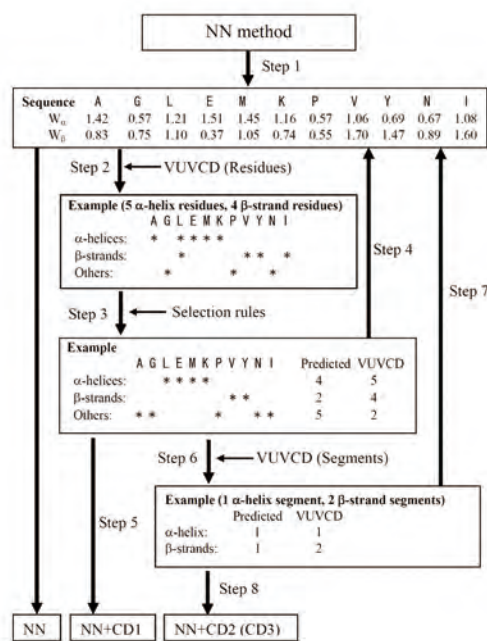


Fig. 2. Computational protocol for combining VUVCD data with the NN algorithm

(Step 7). The assignment was complete when the two estimates were consistent. If the predicted numbers of segments did not converge to the VUVCD estimates, the sequence alignment that minimized the difference between the two estimates was taken as the final solution. The predictions obtained by combining the numbers of both residues and segments (CD2) for  $\alpha$ -helices and  $\beta$ -strands were designated as  $NN_{HK}+CD2$  and  $NN_J+CD2$  (Step 8).

The improvement in sequence-based prediction by using VUVCD data was examined for  $NN_{HK}$  and  $NN_J$  algorithms using three performance indices: success rate ( $Q_3$ ), correlation coefficient ( $C$ ), and segment overlap value ( $SOV$ ). The obtained results are listed in Table 1. The total  $Q_3$  value of  $NN_{HK}$  increased from 59.5 to 60.7% by combining the  $\alpha$ -helix and  $\beta$ -strand contents estimated from VUVCD data ( $NN_{HK}+CD1$ ). Further combining the numbers of  $\alpha$ -helix and  $\beta$ -strand segments ( $NN_{HK}+CD2$ ) slightly decreased  $Q_3$  to 60.3%, but greatly increased the  $C$  and  $SOV$  scores from 0.39 to 0.51 and from 43.8 to 51.9%, respectively, by introducing the contents and segment numbers step by step. The improvement in predictive accuracy was also observed when VUVCD data were combined with the  $NN_J$  algorithm. The  $Q_3$  value of  $NN_J$  increased from 70.9 to 72.1% by introducing the  $\alpha$ -helix and  $\beta$ -strand contents ( $NN_J+CD1$ ), and further to 72.5% by adding the numbers of  $\alpha$ -helix and  $\beta$ -strand segments ( $NN_J+CD2$ ). Improvements were also evident in the  $C$  and  $SOV$  scores.

**Table 1. Accuracy ( $Q_3$ ,  $C$ , and  $SOV$ ) of predicting secondary-structure sequences of target proteins determined by the  $NN_{HK}$  and  $NN_J$  methods combined with VUVCD data**

Method	$Q_3$	$C$	$SOV$
$NN_{HK}$	59.5	0.39	43.8
$NN_{HK}+CD1$	60.7	0.43	50.7
$NN_{HK}+CD2$	60.3	0.51	51.9
$NN_J$	70.9	0.56	59.9
$NN_J+CD1$	72.1	0.59	63.6
$NN_J+CD2$	72.5	0.61	63.7
$NN_J+CD3$	73.3	0.63	65.6
$NN_J+CD4$	74.9	0.62	69.8

To facilitate comparison of the predictive accuracy of the various methods, the  $Q_3$ ,  $C$ , and  $SOV$  values in Table 1 are depicted as proportional histograms in Fig. 3. This figure indicates that the predictive accuracy of  $NN_{HK}$  and  $NN_J$  can be improved by utilizing VUVCD data. The increases in  $Q_3$ ,  $C$ , and  $SOV$  imply that the improvement is due to not only the improved prediction of the average number of residues but also those of the positions and lengths of  $\alpha$ -helix and  $\beta$ -strand segments. Thus, the VUVCD data are valuable for improving the sequence-based prediction of NN algorithm.

The results described above indicate that utilizing VUVCD data can significantly improve the secondary-structure prediction of  $NN_J$ . However, further improvements in accuracy would be required for practical application of this combination method to unknown proteins. Such improvement would be possible from both the VUVCD data and the sequence-based prediction algorithm. We have previously shown that the prediction could be improved by grouping the reference VUVCD data into  $\alpha$ -helix-rich and  $\beta$ -strand-rich proteins (2). We therefore examined whether such grouping improved the predictive accuracy of the  $NN_J+CD2$  method. The training set of 607 proteins was divided into two groups: 379 proteins with a larger  $\alpha$ -helix content than  $\beta$ -strand content were classified as  $\alpha$ -helix-rich proteins ( $\alpha$ -group),

and the remaining 228 proteins were classified as  $\beta$ -strand-rich proteins ( $\beta$ -group). The 30 target proteins were also divided with the same criterion into 17  $\alpha$ -helix-rich proteins ( $\alpha$ -group) and 13  $\beta$ -strand-rich proteins ( $\beta$ -group). The secondary-structure weights (output) of 20 amino acids obtained from the training set of the  $\alpha$ -group (or  $\beta$ -group) were used in  $NN_J$  calculations for predicting the secondary structures of the  $\alpha$ -group (or  $\beta$ -group) of target proteins ( $NN_J$ +CD3 method). The values of  $Q_3$ ,  $C$ , and  $SOV$  thus obtained are listed in Table 1 and depicted in Fig. 3, from which it is evident that classification of proteins improves the overall predictive accuracy in any scores compared with  $NN_{HK}$ +CD2 method. Because we could judge the extent to which an unknown protein was rich in  $\alpha$ -helix or  $\beta$ -strand from its VUVCD spectrum, classification of VUVCD data would be useful for improving the secondary-structure prediction of the VUVCD-NN method. Furthermore, we examined the effects of quality of VUVCD data using 16 proteins whose  $\delta$  values were smaller than the average value (0.058) for the 30 target proteins. Relative to the  $NN_J$ +CD3 method, the predictive accuracy as calculated with the 16 proteins ( $NN_J$ +CD4 method: Table 1 and Fig. 3) improved to 74.9% for  $Q_3$  and to 69.8% for  $SOV$ , but there was no improvement in  $C$ . These results suggest that the predictive accuracy of the VUVCD-NN method could be improved by raising the quality of VUVCD data, in terms of the types and numbers of target proteins.

The sequence-based prediction of protein secondary structures using the NN algorithm can be significantly improved by utilizing data obtained from VUVCD spectroscopy. The VUVCD-NN method developed here should be further improved to more accurately predict the secondary structures for the many proteins for which X-ray and NMR structures are unobtainable. The use of VUVCD data could enhance the predictive accuracy to over 80% when combined with the currently best sequence-prediction algorithm. Accumulation of VUVCD data would expand the applicability of VUVCD spectroscopy both to structural biology and computational biology.

1. K. Matsuo, R. Yonehara, and K. Gekko, *J. Biochem.*, **135**, 405–411 (2004).
2. K. Matsuo, R. Yonehara, and K. Gekko, *J. Biochem.*, **138**, 79–88 (2005).
3. N. Sreerama and R. W. Woody, *Anal. Biochem.*, **287**, 252–260 (2000).
4. K. Matsuo, H. Watanabe, and K. Gekko, *Proteins*, **73**, 104–112 (2008).

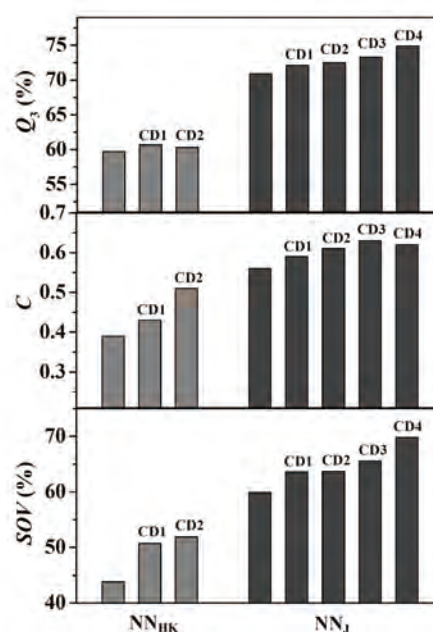


**Fig. 3. Comparison of three performance indices ( $Q_3$ ,  $C$ , and  $SOV$ ) for the  $NN_{HK}$  and  $NN_J$  methods combined with VUVCD data: CD1, number of residues; CD2, numbers of residues and segments; CD3, proteins classified as rich in  $\alpha$ -helices and  $\beta$ -strands; and CD4, 16 target proteins of high quality.**

## Secondary-Structure Analysis of Intermediate States of Apo-Myoglobin and Pepsin using a Vacuum-Ultraviolet Circular Dichroism Spectroscopy

Hidenori Watanabe<sup>1</sup>, Koichi Matsuo<sup>2</sup>, Hirofumi Namatame<sup>2</sup>, Masaki Taniguchi<sup>2</sup>,  
and Kunihiko Gekko<sup>1</sup>

<sup>1</sup> Graduate School of Science, <sup>2</sup> Synchrotron Radiation Center, Hiroshima University

The structures of the intermediates in denaturation process of proteins remain controversial although they give important information for understanding the folding mechanism and stability of proteins. A synchrotron-radiation vacuum-ultraviolet circular dichroism (VUVCD) spectroscopy is a powerful technique for the structural analysis of denatured proteins (1) as well as native ones (2, 3) because it is available for various solvent conditions and can predict accurately the secondary-structure contents and segment numbers. In the present study, we measured the VUVCD spectra of apo-myoglobin (apo-myo) and pepsin down to 170 nm at various pHs and 25°C in order to characterize the intermediate states of the proteins.

Figure 1 shows the VUVCD spectra of apo-myo at pHs 7.5, 4.2, and 2.0. From the pH dependence of the molar ellipticities at 222 nm (inset), the spectra at pHs 7.5 and 2.0 are ascribed to the native and acid-denatured states, respectively. However, the transition curve has a shoulder at around pH 4.2, suggesting the existence of an intermediate state between the native and acid-denatured states. Then, the pH 4.2 spectrum would be close to the VUVCD spectrum of the intermediate of apo-myo. Figure 2 shows the VUVCD spectra of pepsin at pHs 9.0, 4.9, and 2.0, and the pH dependence of the molar ellipticities at 215 nm (inset). The molar ellipticity at pH 2.0 is larger (more negative) than that at pH 9.0, indicating that the spectra at pHs 2.0 and 9.0 correspond to the native and alkaline-denatured states, respectively. However, the transition curve has a minimum ellipticity at around pH 4.9, suggesting the existence of an intermediate state between the native and alkaline-denatured states. Then, the pH 4.9 spectrum would be close to the VUVCD spectrum of the intermediate of this protein. Evidently, the intermediates of two proteins exhibit some characteristic CD peaks, suggesting their different secondary structures from the native and denatured states. However, these VUVCD spectra of the intermediates would involve the contributions of the coexisting native and denatured components. Therefore, we cannot directly calculate the secondary-structure contents and segment numbers of the intermediates from the observed VUVCD spectra. Detailed secondary-structure analysis of the intermediates with the SELCON3 program must await the determination of the native, intermediate, and denatured fractions, which is in progress by fitting the pH profiles of molar ellipticities (inset of each figure) to the three-state transition model.

1. K. Matsuo, Y. Sakurada, R. Yonehara, M. Kataoka, and K. Gekko, *Biophys. J.*, **92**, 4088–4096 (2007).

2. K. Matsuo, R. Yonehara, R., and K. Gekko, *J. Biochem.* **135**, 405–411 (2004).
3. K. Matsuo, R. Yonehara, and K. Gekko, *J. Biochem.*, **138**, 79–88 (2005).
4. N. Sreerama and R. W. Woody, *Anal. Biochem.*, **287**, 252–260 (2000).

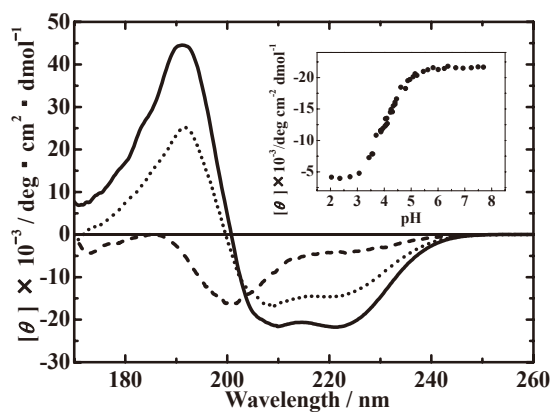


Fig. 1 VUVCD spectra of apo-myo at native (pH 7.5, solid line), intermediate (pH 4.2, dotted line), and denatured states (pH 2.0, broken line). Inset shows the plots of molar ellipticity at 222 nm against pH.

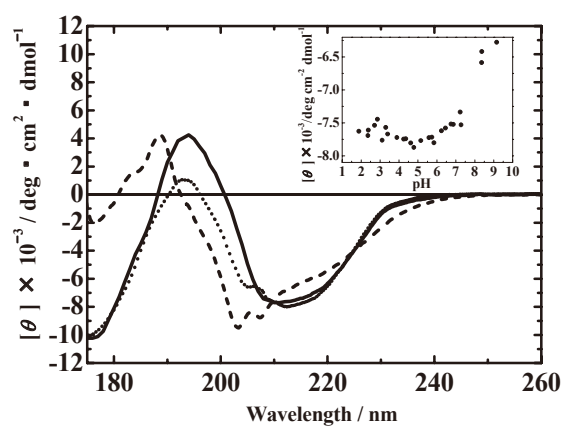


Fig. 2 VUVCD spectra of pepsin at native (pH 2.0, solid line), intermediate (pH 4.9, dotted line), and denatured states (pH 9.0, broken line). Inset shows the plots of molar ellipticity at 215 nm against pH.

## Secondary-Structure Analysis of Disulfide Variants of Lysozyme by Vacuum-Ultraviolet Circular Dichroism Spectroscopy

Koichi Matsuo<sup>1</sup>, Hidenori Watanabe<sup>2</sup>, Shin-ichi Tate<sup>2</sup>, Hideki Tachibana<sup>3</sup>,  
and Kunihiko Gekko<sup>2</sup>

<sup>1</sup>*Synchrotron Radiation Center*, <sup>2</sup>*Graduate School of Science, Hiroshima University*,  
<sup>3</sup>*Kinki University*

Disulfide bridges play an important role in the construction of the tertiary structure of proteins. However, it is unknown whether disulfide bridges force the protein into its folded form or whether other forces guide the protein into a conformation in which the disulfide bridges can form easily. Hen lysozyme contains four disulfide bridges, Cys6–Cys127 (SS1), Cys30–Cys115 (SS2), Cys64–Cys80 (SS3), and Cys76–Cys94 (SS4) (Fig. 1). In this study, to elucidate the effects of a specific disulfide bridge of Cys6–Cys127, Cys30–Cys115, Cys64–Cys80, and Cys76–Cys94 on the secondary structures of this protein, the vacuum-ultraviolet circular dichroism (VUVCD) spectra of 13 species of disulfide-deficient variants, in which Cys residues were replaced with Ala or Ser residues, were measured down to 170 nm at pH 2.9 and 25°C using a synchrotron-radiation VUVCD spectrophotometer.

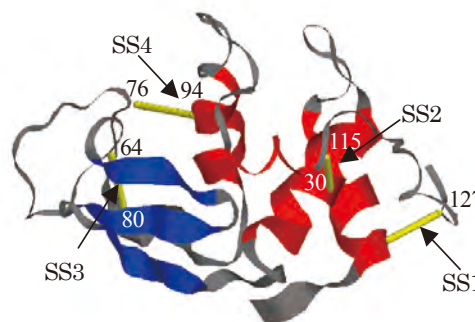


Fig. 1. X-ray structure of hen lysozyme.

As shown typically in Fig. 2, each variant exhibited a characteristic VUVCD spectrum that reflected a considerable amount of residual secondary structures depending on the position and number of deleted disulfide bridges. The contents of  $\alpha$ -helices,  $\beta$ -strands, turns, and unordered structures were estimated with the SELCON3 program using the VUVCD spectra and PDB data of 31 reference proteins (1, 2). The numbers of  $\alpha$ -helix and  $\beta$ -strand segments were also estimated from the VUVCD data. In general, the secondary structures were more effectively stabilized through entropic forces as the number of disulfide bridge increased and as

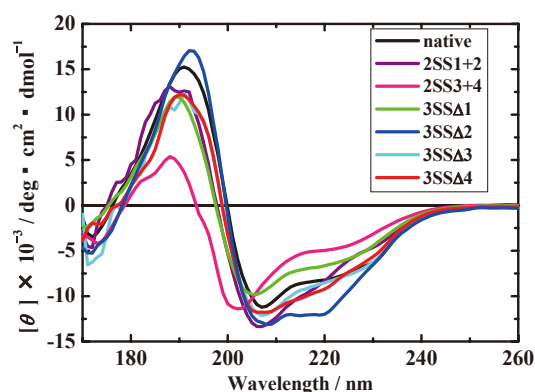


Fig. 2. VUVCD spectra of 3SS and 2SS variants of hen lysozyme at pH 2.9 and 25°C.

it was formed over a larger distance in the primary structure. The structures of three-disulfide variants were similar to that of the wild-type, but other variants diminished  $\alpha$ -helices with a border between the ordered and disordered structures around two-disulfide variants. There existed many  $\beta$ -strands in the disordered structures of one-disulfide and no-disulfide variants as well as in other denatured proteins (3). The amino-acid sequences of the secondary structures were successfully predicted for all the variants by combining the VUVCD data and the neural network algorithm, this method being recently developed in our laboratory (4). These results demonstrate that a VUVCD spectroscopy is a powerful technique for predicting comprehensively not only the contents and segment numbers of the secondary structures but also their positions in the primary structure over the native to denatured states of proteins. This study is in preparation for publication.

1. K. Matsuo, R. Yonehara, and K. Gekko, *J. Biochem.* **135**, 405–411 (2004).
2. K. Matsuo, R. Yonehara, and K. Gekko, *J. Biochem.* **138**, 79–88 (2005).
3. K. Matsuo, Y. Sakurada, R. Yonehara, M. Kataoka, and K. Gekko, *Biophys. J.* **92**, 4088–4096 (2007).
4. K. Matsuo, H. Watanabe, and K. Gekko, *Proteins* **73**, 104–112 (2008).

## Vacuum-Ultraviolet Circular Dichroism Analysis of Glycosaminoglycans by Synchrotron-Radiation Spectroscopy

Koichi Matsuo<sup>1</sup>, Hirofumi Namatame<sup>1</sup>, Masaki Taniguchi<sup>1</sup>, and Kunihiko Gekko<sup>2</sup>

<sup>1</sup>Synchrotron Radiation Center, <sup>2</sup>Graduate School of Science, Hiroshima University

Glycosaminoglycans (GAGs) are unbranched chain polymers composed of repeating a disaccharide unit containing an *N*-acetylglucosamine and a uronic acid (Fig. 1). We recently constructed a vacuum-ultraviolet circular dichroism (VUVCD) spectrophotometer at the Hiroshima Synchrotron Radiation Center (HiSOR) (1, 2), to obtain the structural information of saccharides based on the higher energy transitions such as hydroxyl and acetal groups (3). In the present study, this spectrophotometer

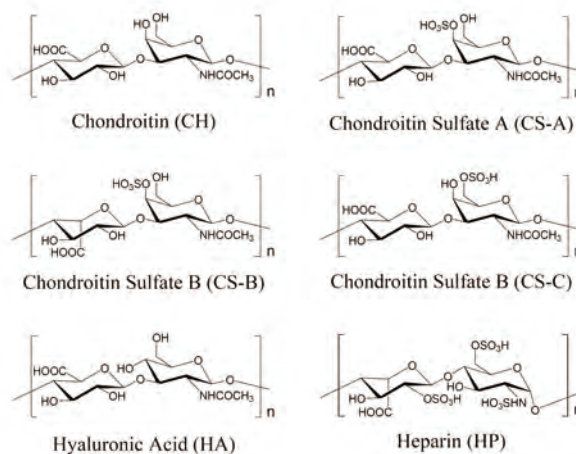


**Fig. 1. Chemical structures of the repeating disaccharide units of the GAGs used in this study.**

was used to measure the VUVCD spectra of five GAGs [chondroitin (CH), chondroitin sulfate A (CS-A), chondroitin sulfate B (CS-B), chondroitin sulfate C (CS-C), and heparin (HP)] down to 160 nm and one GAG [hyaluronic acid (HA)] down to around 185 nm in aqueous solutions at 25°C (4). The VUVCD spectra of their component sugars [*N*-acetylglucosamine (GlcNAc), *N*-acetylgalactosamine (GalNAc), *N*-acetylgalactosamine 4-sulfate (GalNAc4Sul), glucuronic acid (GlcU), and *N*-acetylglucosamine (LacNAc)] were also measured to clarify the influences of the constituent sugar residues of GAGs (4). The contributions of the constituent chromophores to the CD spectra are discussed by comparing the VUVCD spectra of GAGs and component sugars.

Figs. 2 and 3 show the VUVCD spectra of six GAGs (CH, CS-A, CS-B, CS-C, HP, and HA) and five *N*-acetylaminosugars (GlcNAc, GalNAc, GalNAc4Sul, LacNAc, GluU), respectively. For comparison, the spectra of glucose and galactose are also shown in Fig. 3. As shown in these figures, the VUVCD spectra of GAGs and their component sugars sensitively reflect the differences in their structures, although they are highly self-similar (Fig. 1). The differences in the CD spectra are larger in the VUV region than in the far-UV region, indicating that VUVCD spectroscopy provides considerably more information on the structures of GAGs in solution. The optical properties of GAGs are complicatedly affected by several factors: the number, position, and configuration of chromophores (e.g., acetamido, sulfate, carboxyl, and hydroxyl groups); the type of intersaccharide linkages (1→3 and 1→4);

the anomeric form ( $\alpha$  and  $\beta$ ) of the hydroxyl group at C-1; and the staggered orientations [gauche-gauche (GG), gauche-trans (GT), and trans-gauche (TG)] of the hydroxymethyl group at C-5.

The CH spectrum (Fig. 2) markedly differs from the sum of the spectra for GalNAc and GlcU (pH 6.7) below 200 nm, although a negative peak at 210 nm due to the  $n-\pi^*$  transitions of *N*-acetyl and carboxyl groups appears to be additive. The CS-A (Fig. 2) shows the negative CD spectrum below 205 nm compared to the CH. The difference between both CD spectra is clearly attributable to the sulfate group at position C-4 of the GalNAc residue, because CS-A and CH have the same backbone structure (Fig. 1). The CS-C (Fig. 2) shows more negative CD spectrum than CS-A at 190–210 nm, and shows less negative one than CH (Fig. 2). These differences are mainly attributable to the transfer of the sulfate group from the C-4 to the C-6 position in the GalNAc residue, because the backbone structure of CS-C is the same as those of CS-A and CH. The VUVCD spectrum of CS-B differs markedly from those of CH, CS-A, and CS-C (Fig. 2). Because CS-B has the same amino sugar (GalNAc) as CH, CS-A, and CS-C, such a large difference in VUVCD spectra is mainly attributable to the different uronic acid residue: the configuration of the carboxyl group is equatorial ( $\beta$ -D-GlcU) and axial [ $\alpha$ -L-IdoU (iduronic acid)] in CS-A and CS-B, respectively. The VUVCD spectrum of HP is more complicatedly affected by many factors that are not present in other GAGs. HP involves the IdoU unit as well as CS-B, but a striking difference is observed in the spectra of both GAGs: the positive band near 190 nm and the negative one near 173 nm in HP have the opposite sign in CS-B. However, this difference in the two spectra cannot be simply attributed to the different constituent amino sugars (GalNAc in CS-B and GlcNAc in HP), because GalNAc and GlcNAc have negative and positive CD spectra at 173 nm, respectively, and both amino sugars have a positive CD spectrum at 190 nm (Fig. 3). The overall CD spectra of HA and CH are similar

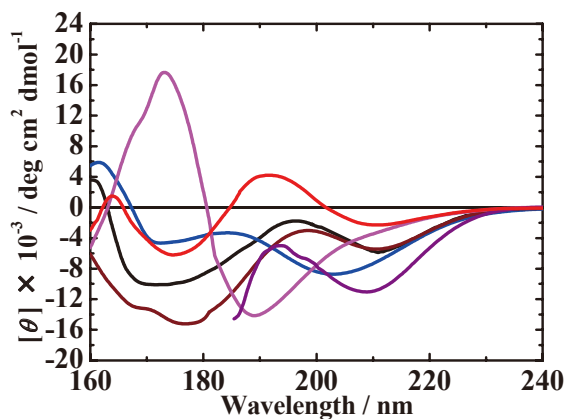


Fig. 2. VUVCD spectra of CH (black), CS-A (brown), CS-B (pink), CS-C (blue), HA (violet), and HP (red) in aqueous solutions at 30 mg/ml and 25°C.

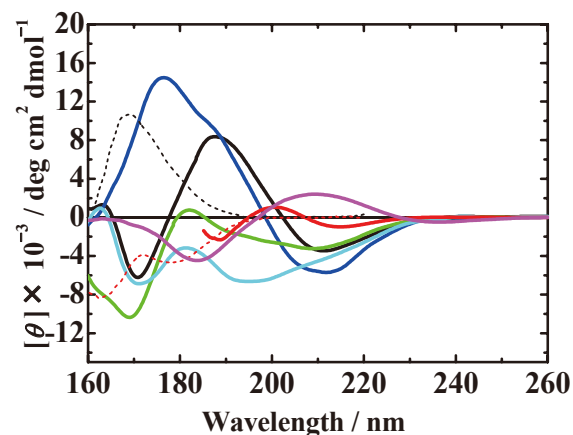


Fig. 3. VUVCD spectra of GalNAc (black), GlcNAc (blue), GalNAc4Sul (green), GlcU at pH 6.7 (red) and pH 2.4 (pink), LacNAc (light blue), Galactose (red dotted), and Glucose (black dotted) in aqueous solutions at 25°C.

above 185 nm, but the intensity of the spectrum at 210 nm of HA is about twice that of CH (Fig. 2). HA and CH differ only in the configuration of the hydroxyl group at C-4 of the amino sugars (axial in CH and equatorial in HA). The configuration of the hydroxyl group at C-4 affects the staggered conformations of the hydroxymethyl group at C-5 (3). The comparable difference in the CD-spectrum intensities between GalNAc and GlcNAc (Fig. 3) suggests that the difference in the CD spectrum at 210 nm between CH and HA is mainly due to electronic perturbation of the acetamido chromophore directly induced by the hydroxyl group at C-4 or via a modified conformational change in the hydroxymethyl group at C-5. The latter contribution would predominate since the CD spectra below 190 nm differ among GalNAc, GlcNAc, and LacNAc, and glucose (equatorial) and galactose (axial) have VUVCD spectra of different signs (Fig. 3).

As shown above, the comprehensive VUVCD spectra of GAGs and their component sugars down to 160 nm revealed the characteristic contributions of constituent chromophores to the higher energy transitions of oxygen lone-pair electrons, which are not detectable by a conventional CD spectrophotometer. Further accumulation of VUVCD data and their theoretical assignments would give important basis for understanding the detailed conformations and biological functions of GAGs.

1. Ojima, N., Sakai, K., Matsuo, K., Matsui, T., Fukazawa, T., Namatame, H., Taniguchi, M., and Gekko, K. (2001) *Chem. Lett.* **30**, 522–523.
2. Matsuo, K., Sakai, K., Matsushima, Y., Fukuyama, T., and Gekko, K. (2003) *Anal. Sci.* **19**, 129–132.
3. Matsuo, K. and Gekko, K. (2004) *Carbohydr. Res.* **339**, 591–597.
4. Matsuo, K., Namatame, H., Taniguchi, M., and Gekko, K. *Biosci. Biotech. Biochem.* (in press).

## Secondary-Structure Analysis of Human Serum Albumin and $\alpha$ -Chymotrypsinogen at Trifluoroethanol-Denatured State using a Vacuum-Ultraviolet Circular Dichroism Spectroscopy

Koichi Matsuo<sup>1</sup>, Sakurada Yoshie<sup>2</sup>, Hirofumi Namatame<sup>1</sup>, Masaki Taniguchi<sup>1</sup>,  
and Kunihiko Gekko<sup>2</sup>

<sup>1</sup>Synchrotron Radiation Center, <sup>2</sup>Graduate School of Science, Hiroshima University

A synchrotron-radiation vacuum-ultraviolet circular dichroism (VUVCD) spectroscopy is a powerful technique for the secondary-structure analysis of denatured proteins (1) as well as native ones (2, 3), because it is available under various solvent conditions and can accurately predict the contents and segment numbers of secondary structures compared with a conventional CD spectroscopy. In the present study, this technique was applied to characterize the secondary structures of human serum albumin (HSA) and  $\alpha$ -chymotrypsinogen ( $\alpha$ -CGN) denatured by trifluoroethanol (TFE).

Figure 1 shows the VUVCD spectra of HSA and  $\alpha$ -CGN down to 170 nm in TFE aqueous solutions of various concentrations (0 ~ 50%) at pH 2.0 and 25°C. As shown in the insets of the figure, the molar ellipticity at 222 nm decreases with increasing the TFE concentration and saturates in 50 % TFE, indicating that the two proteins are almost completely denatured in 50 % TFE. The TFE-denatured states have typical VUVCD spectra of  $\alpha$ -helix proteins. HSA shows an isoellipticity point at around 200 nm, while  $\alpha$ -CGN shows two isoellipticity points at around 208 and 202 nm. Further,  $\alpha$ -CGN shows characteristic VUVCD spectrum of  $\beta$ -strand proteins in 20 % TFE (Figure 1b). These results suggest that TFE induces the  $\alpha$ -helix-rich structure in HSA by the two-state transition mechanism from acid- to TFE-denatured states, but TFE denaturation of  $\alpha$ -CGN has the three-state transition involving a  $\beta$ -strand-rich intermediate state between acid- and TFE-denatured states.

The secondary structures ( $\alpha$ -helix,  $\beta$ -strand, turn, PPII, and unordered structure) of these TFE-denatured proteins were

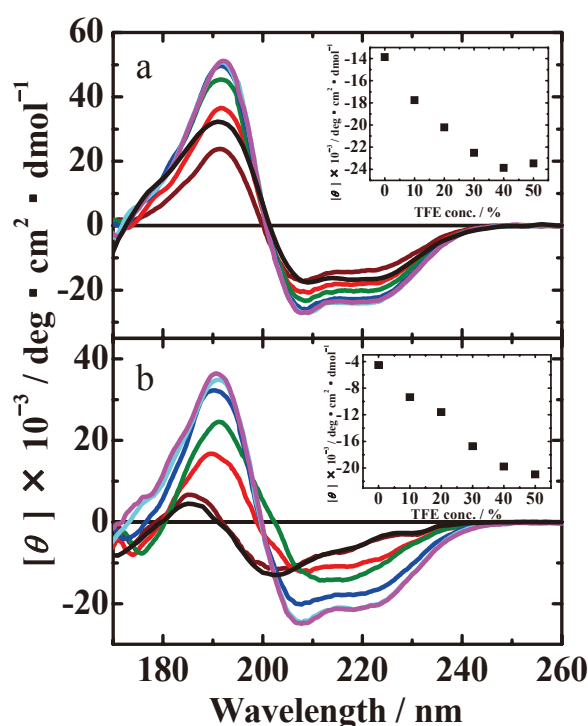


Fig. 1 VUVCD spectra of HSA (a) and  $\alpha$ -CGN (b) in TFE solutions at pH 2.0 and 25°C. Native state at neutral pH (black), TFE 0% (brown), 10% (red), 20% (green), 30% (blue), 40% (sky-blue), and 50% (pink). Insets show the plots of molar ellipticity at 222 nm against TFE concentration.

analyzed with the SELCON 3 program (5) using the PDB data and VUVCD spectra of 31 reference proteins (2, 3). The TFE-denatured structure of HSA was composed of  $\alpha$ -helix (85.6%),  $\beta$ -strand (0%), turn (11.8%), PPII (1.8%), and unordered structure (9.8%). The TFE-denatured  $\alpha$ -CGN showed similar secondary-structure contents although the  $\alpha$ -helix content (69.3%) was less than that of HSA. The number of  $\alpha$ -helix segment was estimated to be 39 and 12 for HSA and  $\alpha$ -CGN, respectively. From these results, it is speculated that the TFE-denatured states of HSA and  $\alpha$ -CGN are an ensemble of several long  $\alpha$ -helix segments connected by turns and unordered structure, as well as those of met-myoglobin and thioredoxin (4).

1. K. Matsuo, Y. Sakurada, R. Yonehara, M. Kataoka, and K. Gekko, *Biophys. J.*, **92**, 4088–4096 (2007).
2. K. Matsuo, R. Yonehara, and K. Gekko, *J. Biochem.* **135**, 405–411 (2004).
3. K. Matsuo, R. Yonehara, and K. Gekko, *J. Biochem.*, **138**, 79–88 (2005).
4. K. Matsuo, Y. Sakurada, H. Namatame, M. Taniguchi, and K. Gekko, *HiSOR Activity Report*, 97–98 (2006).
5. N. Sreerama and R. W. Woody, *Anal. Biochem.*, **287**, 252–260 (2000).

## Structural analysis of $\gamma$ -polyglutamic acids by vacuum-ultraviolet circular dichroism spectroscopy

Kunihiko Gekko,<sup>1</sup> Koichi Matsuo,<sup>2</sup> and Yoshihito Nogusa<sup>3</sup>

(<sup>1</sup>Graduate School of Science, <sup>2</sup>Synchrotron Radiation Center, Hiroshima University, <sup>3</sup>Ajinomoto Co., INC.)

$\gamma$ -Polyglutamic acid ( $\gamma$ -PGA) produced in *Bacillus natto* is a natural polypeptide which is linked at  $\gamma$ -position of the side chains of glutamic acids with the mixed composition of D- and L-isomers. This polymer is widely used in food industries for various functional properties such as water retentivity, high viscosity, and biodegradability. However, the conformation of this polymer remains unknown although  $\alpha$ -polyglutamic acid ( $\alpha$ -PGA) linked at  $\alpha$ -position forms helix structure in acidic solution. In this study, we measured the vacuum-ultraviolet circular dichroism (VUVCD) and far-UV CD spectra of  $\gamma$ -PGA under various solvent conditions to examine the helix-forming ability of this polymer.

Fig. 1 shows the VUVCD spectra of L-isomer-rich  $\gamma$ -PGA (L-PGA, L:D = 7.5:2.5) and D-isomer-rich  $\gamma$ -PGA (D-PGA, L:D = 2.5:7.5) with low and high molecular weights. L-PGA showed no negative peak around 220 nm and positive peak around 190 nm characteristic to helix structure and its spectra were rather similar to that of random coil form independent of its molecular weight. No significant changes in the far-UV CD spectra were observed at any polymer concentrations by changing pH and adding  $\text{Ca}^{2+}$  ion, lipids, and sugars in the solvent, although  $\text{Ca}^{2+}$  ion decreased the peak intensity at 215 nm probably due to its binding with  $\alpha$ -carboxyl group of the side-chain of  $\gamma$ -PGA. These results indicate that  $\gamma$ -PGA does not form helix structure under any solvent conditions examined probably because the neighboring peptide groups are too far to make peptide bonds with each other in  $\gamma$ -PGA different from  $\alpha$ -PGA. Interestingly, L-PGA and D-PGA showed asymmetric VUVCD spectra about the X-axis with different intensities although they had the opposite sign as expected. This result suggests that both  $\gamma$ -PGAs have the different arrangement of L- and D-glutamic acids although L-PGA and D-PGA consist of the mutually same composition of L- and D-isomers with the symmetrical CD. Further detailed VUVCD studies coupled with the polyelectrolyte solution theory will be necessary for elucidating the conformation of  $\gamma$ -PGA.

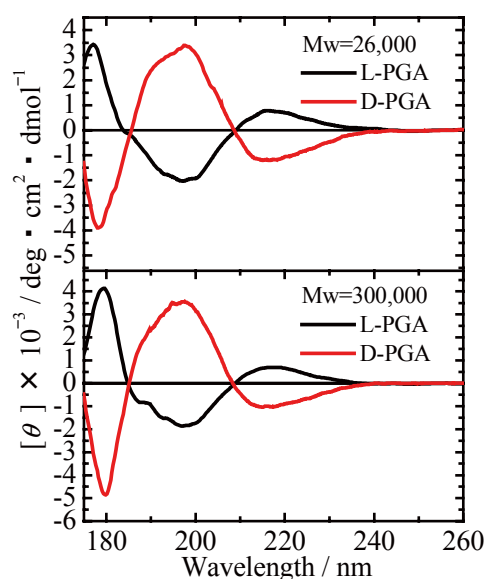


Fig. 1. VUVCD spectra of  $\gamma$ -PGAs

## Spin- and angle-resolved photoemission study of ultrathin Bi films on a silicon substrate

T. Hirahara<sup>1</sup>, K. Miyamoto<sup>2</sup>, A. Kimura<sup>2</sup>, Y. Niinuma<sup>1</sup>, G. Bihlmayer<sup>3</sup>, E. V. Chulkov<sup>4,5</sup>, T. Nagao<sup>6</sup>, I. Matsuda<sup>7</sup>, S. Qiao<sup>8</sup>, K. Shimada<sup>8</sup>, H. Namatame<sup>8</sup>, M. Taniguchi<sup>2,8</sup>, S. Hasegawa<sup>1</sup>

<sup>1</sup> *Department of Physics, University of Tokyo, Japan*

<sup>2</sup> *Graduate School of Science, Hiroshima University, Japan*

<sup>3</sup> *Forschngszentrum Jülich, Germany*

<sup>4</sup> *Donostia International Physics Center, Spain*

<sup>5</sup> *Departamento de Física de Materiales, UPV/EHU, Spain*

<sup>6</sup> *National Institute for Materials Science, Japan*

<sup>7</sup> *Institute for Solid State Physics, Japan*

<sup>8</sup> *Hiroshima Synchrotron Radiation Center, Japan*

### 1. Introduction

Spintronics, which aims at the utilization of the spin degree of freedom in addition to the charge, has attracted wide interest due to their promising potentials in realizing new functionalities in electronic devices [1]. Spin manipulation is the key factor in spintronics, and the conventional style was to develop novel ferromagnetic materials [2]. Recently, on the other hand, it was shown that by applying gate voltage (electric field), spin-split two-dimensional electron gases (2DEG) can be formed in asymmetric quantum wells of non-magnetic materials [3]. This is called the Rashba effect, due to the spin-orbit interaction and the structure inversion asymmetry (SIA) [4].

At the crystal surface, the same effect occurs due to the SIA in the surface-normal direction and spin-orbit split band structures have been found for Au(111) [5,6] and W(110)-H [7] surfaces. This splitting is caused by the spin-orbit coupling Hamiltonian

$H_{\text{SOC}} = \frac{\hbar}{4m_0^2c^2} \vec{\sigma} \cdot (\nabla V \times \vec{p})$ , where  $\vec{\sigma}$  is the spin of electrons,  $V$  is the one-electron potential,

and  $\vec{p}$  is the momentum [8]. Usually in the bulk, the time-reversal symmetry ( $E(\mathbf{k}, \uparrow) = E(-\mathbf{k}, \downarrow)$ ) and space inversion symmetry ( $E(\mathbf{k}, \uparrow) = E(-\mathbf{k}, \uparrow)$ ) lead to the Kramers degeneracy. However, at the crystal surface, due to the loss of the space-inversion symmetry the degeneracy will be lifted.

Bismuth (Bi) is a very heavy element and its electronic structure is highly influenced by the spin-orbit interaction [9]. It was reported that the surface states of single crystal Bi surfaces are highly metallic [10] and show large Rashba-type spin-orbit splitting [11]. Furthermore, using ultrathin Bi films on a Si substrate, we have previously shown from angle-resolved photoemission spectroscopy (ARPES) and relativistic *ab initio* calculations that as these Rashba-split surface-state bands overlap with the bulk projection and become quantum-well

states (QWSs), the spin-polarization will be lost [12]. However, direct experimental evidence is still lacking. Therefore in the present study, we have performed spin-resolved ARPES (SARPES) to experimentally confirm if the above fact is true or not.

## 2. Experimental

The measurements were performed in the SARPES system at Hiroshima Synchrotron Radiation Center. The spectra were recorded at  $\sim 120$  K using unpolarized He $\alpha$  radiation (21.2 eV) with a compact Mott detector operating at 25 keV [13]. In our measurement geometry, we can obtain the in-plane spin polarization of the spin component perpendicular to the plane spanned by the two vectors directed along the light incidence and electron emission. We define the spin direction as "up" and "down" with respect to this plane, which can also be thought as "left" and "right" with respect to  $k$  (Fig. 1).

Epitaxial Bi(001) films (for our film orientation we use hexagonal notation Bi(001) which is Bi(111) in rhombohedral notation) were grown on the Si(111)-7x7 surface at room temperature and annealed at  $\sim 380$  K to improve the film quality [14]. The film thickness in the present measurement was 7 BL (bilayers, 1 BL =  $1.14 \times 10^{15}$  atoms/cm $^2$ , 0.39 nm thick).

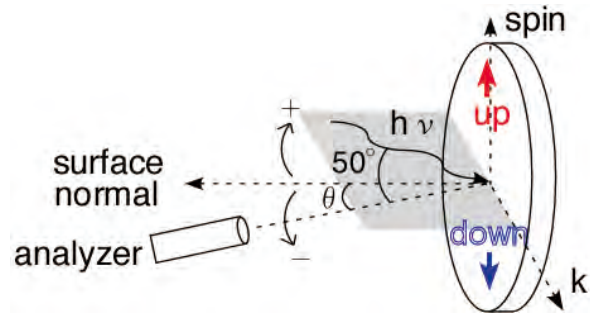


Fig 1: Schematic illustration of the spin orientation.

## 3. Results and Discussion

Figures 2 (a) and (b) show the SARPES spectra around normal emission. The red (blue) curves represent the spin-up (-down) spectra. We can obviously see that the surface states near the Fermi level are spin-split (for example, we only see a peak for the spin-up spectra at  $4.75^\circ$ ). Figure 2 (c) shows the spin-polarization map deduced from the spin-polarization curves obtained from the spectra of Figs. 2 (a) and (b). Red (blue) represents positive (negative) spin polarization. The overlapped points are the results of the first principles calculations [11,12]. Figure 2 (d) shows the band dispersion image obtained by usual ARPES measurements. Comparing Figs. 2 (c) and (d), we can say that although the features in (c) are a bit blurred due to the limited energy and angular resolutions of the SARPES instrument, the spin-split property is unequivocally observed and also consistent with the theoretical prediction; an antisymmetric spin structure with respect to  $\Gamma$ .

Figure 3 (a) shows the SARPES spectra at larger emission angles. We notice that at  $8^\circ$ , a sharp spin-up peak is present just below  $E_F$  shown by the red filled circle. As this peak disperses downwards approaching the M point, the peak width becomes broad. Furthermore, we can recognize that the spin-down spectra start to show peak features at the same energy as the spin-up spectra. This indicates that the spin-polarization is decreasing. Another spin-down peak emerges at  $14^\circ$  indicated by the blue open circle, and this state shows very small negative polarization, probably due to the effect of the Fermi-Dirac function and the limited

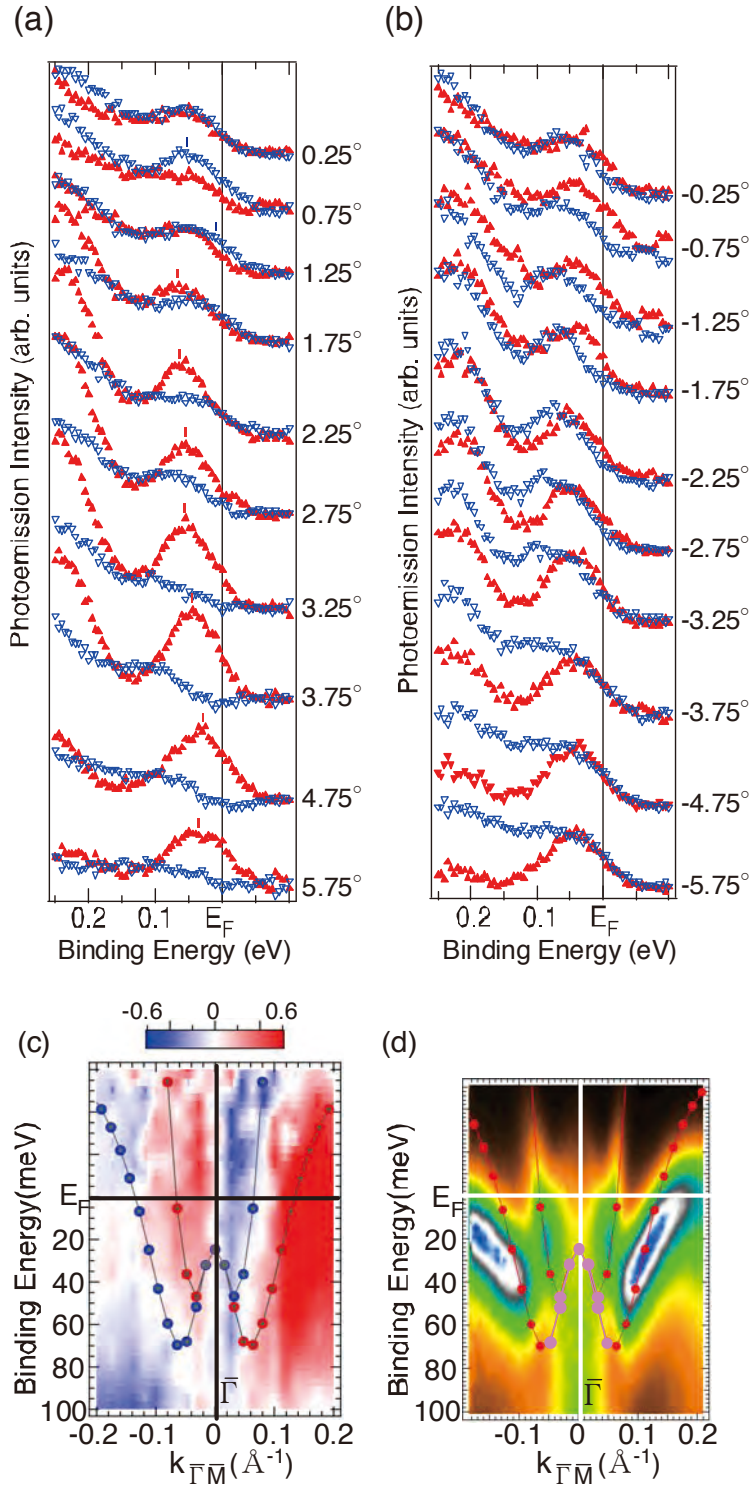


Fig 2: (a,b) SARPES spectra around normal emission for the 6 BL Bi(001) film on Si(111). (c) The spin-polarization map deduced from the spectra of (a) and (b). The overlap points represent the results of *ab initio* calculations. (d) The band dispersion image of the usual ARPES.

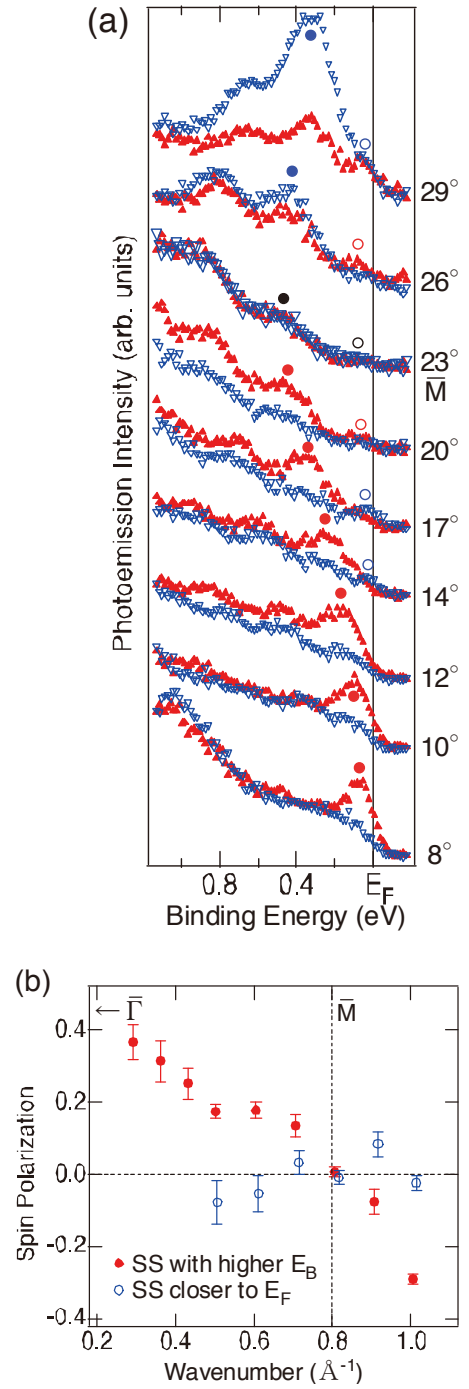


Fig 3: (a) SARPES spectra around the M point for the 6 BL Bi(001) film on Si(111). (b) The change of the spin-polarization with wavenumber deduced from the spectra of (a).

resolution in our measurement. At the M point ( $23^\circ$  spectra), the spin-up and -down spectra overlap almost completely, meaning that there is practically no spin polarization for any state at this angle. As we pass M, the shallow state near  $E_F$  now shows a peak for the spin-up spectra, while the surface state with higher binding energy is negatively polarized. The change of the spin-polarization value with wavenumber is explicitly shown in Fig. 3 (b). This shows that the spin structure is basically antisymmetric with respect to the M point. Thus we have obtained experimental evidence of our previous expectation that the spin polarization will diminish where the surface-state bands overlap with the bulk projection and become QWSs.

#### Referenes

- [1] S. A. Wolf *et al.*, *Science* **294**, 1488 (2001).
- [2] H. Ohno, *Science* **281**, 951 (1998).
- [3] T. Koga *et al.*, *Phys. Rev. Lett.* **89**, 046801 (2002).
- [4] E. I. Rashba, *Sov. Phys. Solid State* **2**, 1109 (1960).
- [5] S. Lashell *et al.*, *Phys. Rev. Lett.* **77**, 3419 (1996).
- [6] M. Hoesch *et al.*, *Phys. Rev. B* **69**, 241401(R) (2004).
- [7] M. Hochstrasser *et al.*, *Phys. Rev. Lett.* **89**, 216802 (2002).
- [8] R. Winkler, *Spin-Orbit Coupling Effects in Two-Dimensional Electron and Hole Systems*, (Springer-Verlag, Berlin, 2003)
- [9] X. Gonze *et al.*, *Phys. Rev. B* **41**, 11827 (1990).
- [10] C. R. Ast and H. Höchst, *Phys. Rev. Lett.* **87**, 177602 (2002).
- [11] Yu. Koroteev *et al.*, *Phys. Rev. Lett.* **93**, 046403 (2004).
- [12] T. Hirahara *et al.*, *Phys. Rev. Lett.* **97**, 146803 (2006).
- [13] K. Iori *et al.*, *J. Elec. Spec. Rel. Phen.* **144-147**, 997 (2005); *Rev. Sci. Inst.* **77**, 013101 (2005).
- [14] T. Nagao *et al.*, *Phys. Rev. Lett.* **93**, 105501 (2004).

## Spin polarization of spin-orbit induced electronic structures of Bi(111)

R. Nishimura<sup>1</sup>, K. Miyamoto<sup>2</sup>, T. Kadono<sup>1</sup>, K. Kanomaru<sup>1</sup>, A. Kimura<sup>1</sup>

K. Shimada<sup>2</sup>, S. Qiao<sup>3</sup>, H. Namatame<sup>2</sup>, T. Taniguchi<sup>1,2</sup>

<sup>1</sup>Graduate School of Science, Hiroshima University, Higashi-Hiroshima,  
Hiroshima, 739-8526, Japan.

<sup>2</sup>Hiroshima Synchrotron Radiation Center, Hiroshima University, Higashi-Hiroshima,  
Hiroshima, 739-0046, Japan.

<sup>3</sup>Advanced Materials Laboratory and Department of Physics, Fudan University,  
Shanghai 200433, China.

Recently, spintronics has received broad attention for the possibility as next-generation technology, where control of both spin and charge is considered as fundamental concept. One of the most striking ideas is to manipulate spin of free electron gas only by an electric field as proposed for spin- field effect transistor (spin-FET) [1], which is related to an appearance of spin-split energy band structure due to a broken space inversion symmetry. In analogy, crystal surface is expected to exhibit spin split feature of energy band structure due also to a broken space inversion asymmetry. Recently, spin-split metallic surface states of Bi(111) has been clearly observed by an angle resolved photoelectron spectroscopy [2].

In order to determine a detailed spin electronic state, we have performed spin- and angle-resolved photoemission spectroscopy of Bi(111) surface along  $\bar{\Gamma}$ - $\bar{M}$  in Hiroshima Synchrotron Radiation Center. In the present study, we have observed new spin-split bands in the larger binding energy ( $E_B$ ) region above 1 eV. Fig.1 shows energy band dispersion curves of up-spin and down-spin states, separately. As one of the most intense features, we observe a downward energy dispersion starting from  $E_B=2.6$  eV. It is noticed that the spin-up (spin-down) photoemission intensity is strong at negative (positive) wave number. For a shallower state, one finds a broad and steep energy dispersion curves from  $E_B=1.2$  eV. This also shows a strong spin dependence, which will be discussed with the one-step model photoemission calculation.

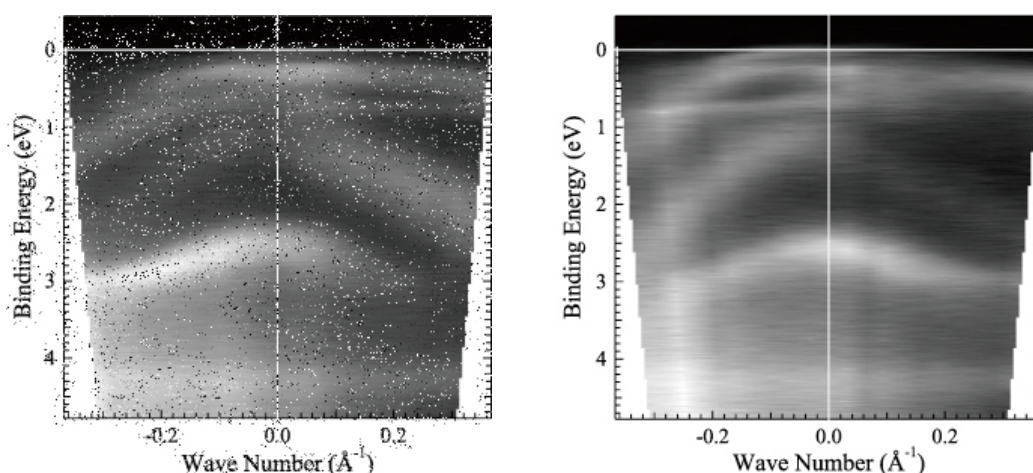


Fig.1 Experimental energy dispersion curves of up-spin (left) and down-spin (right) components.

### References

[1] S. Datta and B. Das, Appl. Phys. Lett. **56**, 665 (1990).

[2] Yu. M. Koroteev *et al.*, Phys. Rev. Lett. **93**, 046403 (2004).

## Unveiling spin characters of spin-orbit induced surface states

K. Miyamoto<sup>A</sup>, R. Nishimura<sup>B</sup>, T. Kadono<sup>B</sup>, K. Kanomaru<sup>B</sup>, K. Iori<sup>B</sup>, A. Kimura<sup>B</sup>, S. Qiao<sup>C</sup>,  
K. Shimada<sup>A</sup>, H. Namatame<sup>A</sup> and M. Taniguchi<sup>A,B</sup>

<sup>A</sup>Hiroshima Synchrotron Radiation Center, Hiroshima University

<sup>B</sup>Graduate School of Science, Hiroshima University

<sup>C</sup>Laboratory of advanced Material and Department of Physics, Fudan University  
kmiyamoto@hiroshima-u.ac.jp

Recently, “spintronics”, which manipulates a spin degree of freedom as well as charge, has attracted a great attention as a new technology in next generation. In particular, spin field effect transistor (SFET) controlled with gate voltage without external magnetic field is one of the most striking ideas as firstly proposed by Datta and Das [1]. The efficiency of SFET is dominated by spin-polarized free electrons traveling in an asymmetric spin-orbit potential induced by the external gate voltage, which is so called “Rashba effect”. A crystal surface with a broken spatial symmetry would also form a spin-split band electronic structure in a spin-orbit potential as suggested for Bi(111) and Sb(111) surfaces without spin resolution [1].

Spin-resolved ARPES is a powerful tool to enable a quantitative evaluation of spin polarizations of spin-split bands in order to see how the surface states are localized from a bulk projection and a symmetry of constituent wave functions. In the present study, we have tried to clarify the spin characters of spin-orbit induced surface state bands of Bi(111) and Sb(111) by means of spin-resolved ARPES in Hiroshima University.

Figures.1 (a) and (b) show spin resolved energy distribution curves (EDC's) as a function of binding energy ( $E_B$ ) of Bi(111) surface near  $E_F$  for positive and negative emission angles

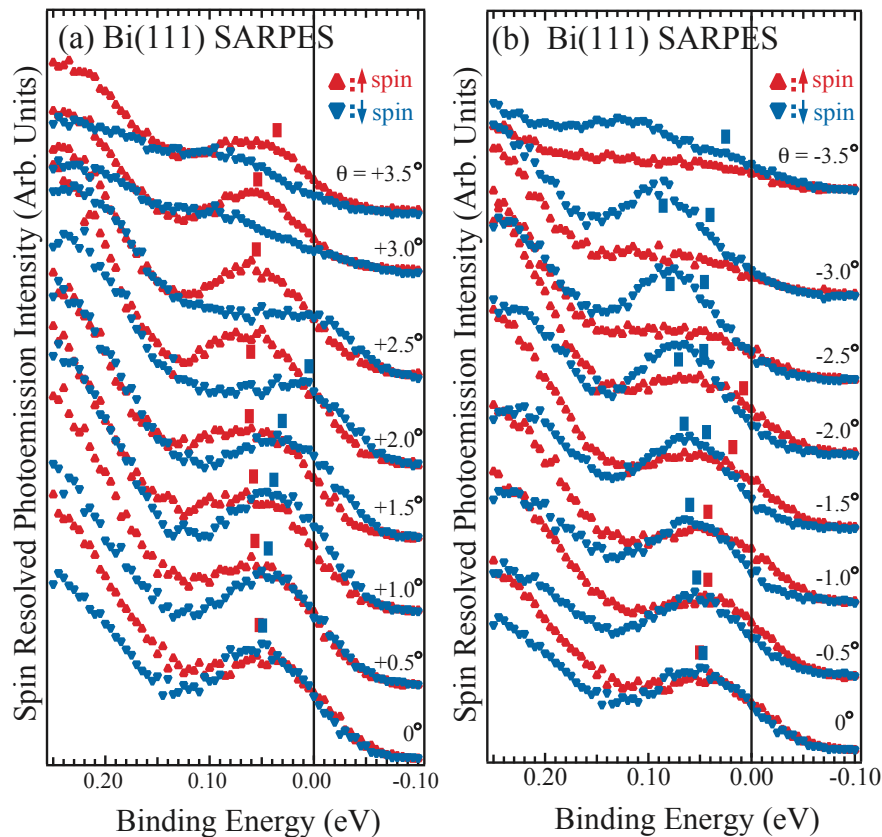


**Fig. 1** Spin-resolved EDCs of Bi(111) surface near  $E_F$  for (a) positive and (b) negative emission angles.

( $\theta$ ), respectively. At  $\theta=0^\circ$ , the peak structures are found at the same  $E_B=50\text{meV}$  in both spin-up and spin-down components, that is, the spins of the relevant state are degenerate just at  $k = 0$ . The peak position of spin-down spectra shifts from slightly below to above  $E_F$  with increasing  $\theta$  from  $+0.5^\circ$  to  $+1.5^\circ$  as marked with vertical bars and is finally crossing  $E_F$  around  $+2.5^\circ$ . In contrast to the spin-down spectra, the spectral weight of spin-up component moves to a little higher  $E_B$  from  $0^\circ$  to  $+1.5^\circ$  and shift back to  $E_F$  from  $+2^\circ$  to  $+3.5^\circ$ . If one takes a look at the spin-resolved EDCs for negative emission angles of Fig.1(b), the behavior of peak shift in spin-up (spin-down) states is similar to that in spin-down (spin-up) along positive emission angle. This result means that the spin dependent band structures originate in spin-orbit interaction.

[1] Yu. M. Koroteev et al. 2004 *Phys. Rev. Lett.* **93**. 046403. /T. Hirahara et al. 2006 *Phys. Rev. Lett.* **97**. 146803. /K. Sugawara et al. 2007 *Phys. Rev. Lett.* **96**. 046411.

## Spin-resolved ARPES of Sb(111) single crystal surface

<sup>A</sup>T. Kadono, <sup>B</sup>K. Miyamoto, <sup>A</sup>R. Nishimura, K. <sup>A</sup>Kanomaru, <sup>C</sup>M. Nagano, <sup>C</sup>T. Shishidou, <sup>C</sup>T. Oguchi, <sup>D</sup>S. Qiao, <sup>B</sup>K. Shimada, <sup>B</sup>H. Namatame, <sup>A</sup>A. Kimura, <sup>A,B</sup>M. Taniguchi  
*Grad. Sch. Sci., Hiroshima Univ.*<sup>A</sup>, *Hiroshima Univ.*, *HSRC*<sup>B</sup>,  
*ADSM, Hiroshima Univ.*<sup>C</sup>, *Dept. Phys., Fudan Univ.*<sup>D</sup>

Crystal surfaces with a strong spin-orbit coupling have attracted a great attention because it would cause a spin splitting despite of non-magnetic property. At surfaces, spin degeneracy could be lifted due to a space inversion asymmetry. Recently, energy splittings are observed in the surface states of Au(111) and Sb(111) [1,2]. Surprisingly, the size of splitting for Sb(111) is comparable to that for Au(111) although the spin-orbit coupling strength of outer p shell is much weaker for Sb [1]. In order to clarify the origin of such the marked spin-split feature, spin- and angle- resolved photoelectron spectroscopy (spin-ARPES) has been applied to Sb(111) surface.

Figure 1 shows the E- $k_{//}$  plot of spin-up component in the binding energy ( $E_B$ ) range of 0 – 0.45 eV along  $\bar{\Gamma}$ - $\bar{M}$  of surface Brillouin zone. The intensity maxima of photoemission spectra in the lower  $E_B$  region are traced with open triangles. The band shows an upward energy dispersion with a bottom ( $E_B = 0.2$  eV) at  $\bar{\Gamma}$  and crosses Fermi level ( $E_F$ ) just at  $+0.15 \text{ \AA}^{-1}$  ( $-0.05 \text{ \AA}^{-1}$ ) in the positive (negative)  $k_{//}$  region. It can be noticed that this energy dispersion is asymmetric with respect to  $\bar{\Gamma}$ , which clearly indicates the Rashba-type spin splitting due to a broken space inversion symmetry. Combined with the ab-initio slab calculation, the large spin-splitting is caused by the strong asymmetry of constituent wave function.

### References

- [1] S. LaShell *et al.*, Phys. Rev. Lett. **77**, 3419 (1996).  
 [2] K. Sugawara *et al.*, Phys. Rev. Lett. **96**, 046411 (2006).

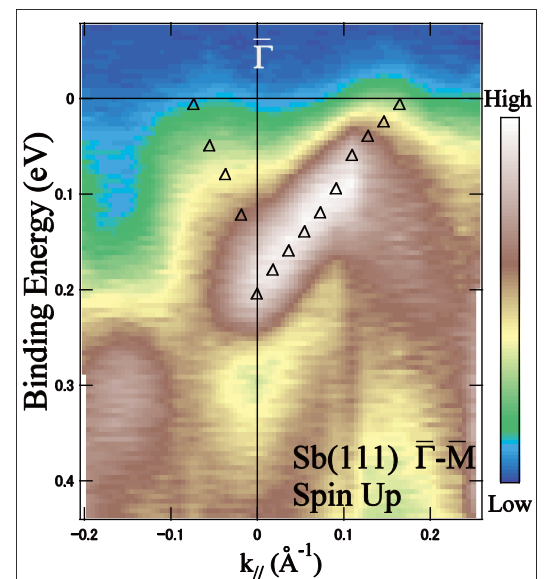


Fig. 1: Experimental E- $k_{//}$  relation of Sb(111) surface in spin-up channel. The peak maxima are traced as denoted by open triangles.

## Spin- and angle- resolved photoemission spectroscopy of a Si(111) $\sqrt{3}\times\sqrt{3}$ -Sb surface

K. Kanomaru<sup>1</sup>, K. Miyamoto<sup>1</sup>, T. Kadono<sup>1</sup>, R. Nishimura<sup>1</sup>, A. Kimura<sup>1</sup>  
S. Qiao<sup>3</sup>, K. Shimada<sup>2</sup>, H. Namatame<sup>2</sup>, M. Taniguchi<sup>1,2</sup>

<sup>1</sup>Grad. Sch. Sci., Hiroshima Univ., Higashi-Hiroshima, 739-8526, Japan

<sup>2</sup>HSRC, Hiroshima Univ., Higashi-Hiroshima, 739-0046, Japan

<sup>3</sup>Dept. Phys., Fudan Univ., Shanghai 200433, China

Spin-split band structure at surfaces is paid a lot of attention since it leads, for instance, to application of the spin field effect transistor with high performance. The spin-splitting is brought about by an asymmetric spin-orbit potential that surface state electrons feel. Since the spin-orbit potential depends on a structural property of surface, various types of superstructure would cause different spin-split bands[1]. It is known that Sb/Si(111) surface exhibits eight different surface phases obtained by a fine tuning of temperature and coverage[2]. For the purpose of investigating the adsorbate induced spin-split band structures, we have carried out a spin- and angle- resolved photoemission spectroscopy of  $\sqrt{3}\times\sqrt{3}$ -Sb/Si(111) surface.

Figure 1 shows spin-ARPES spectra at emission angles ( $\theta$ ) of  $\pm 9^\circ$  for parallel and perpendicular spin components with respect to  $\bar{\Gamma}'-\bar{M}'$  direction of  $\sqrt{3}\times\sqrt{3}$  surface Brillouin zone (SBZ). These spectra correspond to the electronic states near the middle of  $\bar{\Gamma}'-\bar{M}'$  of  $\sqrt{3}\times\sqrt{3}$  SBZ (upper part of Fig.1). As indicated with arrows in Fig. 1, the fine spin-split features are observed above the binding energy ( $E_B$ ) of 4 eV at  $\theta = \pm 9^\circ$  for the parallel spin component, whereas negligible spin polarization is found for the perpendicular spin component. Since the turns of the spin components change between Fig.1(c) and (d), it can be assigned to spin-split band induced by a broken spatial symmetry. Here, the relevant band structure comes mainly from a Si bulk-derived band. Thus, it is considered that the observed spin-split feature is derived by the interaction of Sb 5p and the Si 3s,p states.

### References

- [1] C. R. Ast *et al.*, Phys. Rev. Lett. **98**, 186807 (2007)  
[2] V. K. Paliwal *et al.*, Surf. Sci. Lett **513**, L397 (2002)

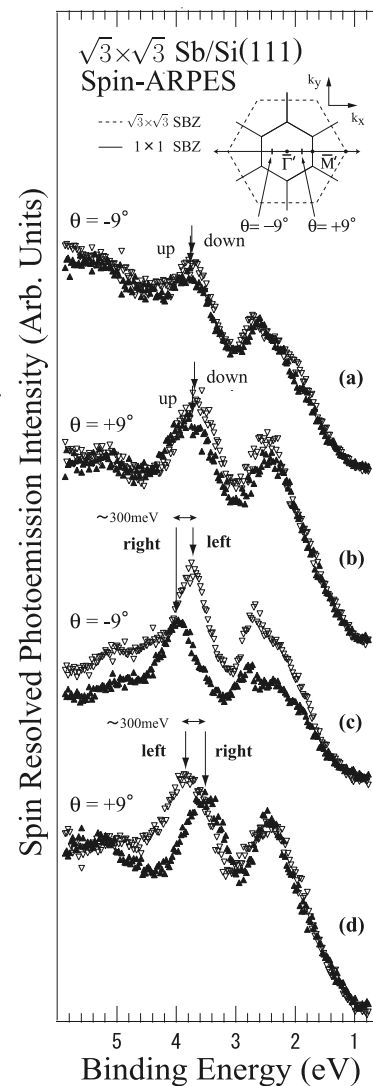


Fig.1 Spin-ARPES spectra at  $\theta = \pm 9^\circ$  for the  $\bar{\Gamma}'-\bar{M}'$  direction of  $\sqrt{3}\times\sqrt{3}$  SBZ for perpendicular(a,b) and parallel(c,d) spin components.

Spin-up (spin-right) and spin-down (spin-left) are denoted by open and solid symbols for perpendicular (parallel) spin components with respect to  $k_x$  ( $\bar{\Gamma}'-\bar{M}'$ ).

## Unoccupied band structure of 1T-TaS<sub>2</sub> investigated by angle-resolved inverse-photoemission spectroscopy

Y. Utsumi<sup>a</sup>, Y. Mukaegawa<sup>a</sup>, M. Arita<sup>b</sup>, H. Sato<sup>b</sup>, M. Sasaki<sup>c</sup>,  
A. Ohnishi<sup>c</sup>, H. Namatame<sup>b</sup> and M. Taniguchi<sup>a,b</sup>

<sup>a</sup>*Graduate School of Science, Hiroshima University, Higashi-Hiroshima 739-8526, Japan*

<sup>b</sup>*HiSOR, Hiroshima University, Higashi-Hiroshima 739-0046, Japan*

<sup>c</sup>*Faculty of Science, Yamagata University, Yamagata 990-8560, Japan*

Quasi-2D material, 1T-TaS<sub>2</sub>, has been studied for long time, because of its interesting charge density waves (CDW) phenomenon. 1T-TaS<sub>2</sub> has three CDW phases depending on temperature; incommensurate (IC) phase in the temperature range between 600 and 350 K, nearly commensurate (NC) phase with a hexagonal array of commensurate domains with typical size of 70 Å [1] between 350 and 180 K, and commensurate (C) phase with a  $\sqrt{13} \times \sqrt{13}$  superlattice below 180 K. The NC to C phase transition is accompanied by a metal-insulator transition. There are many researches on valence bands of 1T-TaS<sub>2</sub> by means of photoemission spectroscopy (PES), and the band reconstruction due to the  $\sqrt{13} \times \sqrt{13}$  superlattice and an energy gap of  $\sim 100$  meV in the C phase have been revealed [2]. However, there are few researches on unoccupied band of this material, because of experimental difficulty.

In this study, we have observed unoccupied band structures in  $\Gamma M$  and  $\Gamma K$  directions for the IC phase (380K) and C phase (100K) of 1T-TaS<sub>2</sub> single crystal, by means of angle-resolved inverse photoemission spectroscopy (ARIPES). ARIPES spectrometer used in this work consists of Erdman-Zipf electron gun with a BaO cathode, and ultraviolet emission spectrometer with non-periodic spherical gratings and CsI-coated multichannel plates [3]. The total energy resolution is 540 meV at an incidence electron kinetic energy of  $E_K=44$  eV, which is determined by Fermi edge fit of spectra for evaporated Au film measured under identical conditions as the samples. The clean surface was obtained by cleavage in the analysis chamber below  $2 \times 10^{-10}$  Torr.

We have successfully observed the clear unoccupied band dispersion in both IC and C phases of 1T-TaS<sub>2</sub>. Figure 1 shows the experimental unoccupied bands in  $\Gamma M$  direction for IC and C phase of 1T-TaS<sub>2</sub> measured at  $E_K=44$  eV. In order to compare the experimental results with band-structure calculation, theoretical bands for undistorted 1T structure in  $\Gamma M$  and AL directions calculated by Mattheiss [4] are also plotted in the IC result. In the IC phase, a

continual band near the Fermi level ( $E_F$ ), which can be attributed to the Ta  $d_{xy}$  and  $d_{x^2-y^2}$  bands, is in very good agreement with the band-structure calculation. In contrast, in the C phase, the continual band of the IC phase splits into two manifolds around M point, and the upper and lower bands exist about 3.8 and 1.5 eV, respectively. This band splitting is an evidence of band folding in the reconstructed Brillouin zone due to the  $\sqrt{13} \times \sqrt{13}$  superlattice. Band folding occurs at the boundary between the  $\sqrt{13} \times \sqrt{13}$  Brillouin zone. Since three boundaries are found around M point, the effect of the band folding is easy to be observed as the flat bands around 1.5 eV.

In comparison with the intensity near the  $\Gamma$  point of the IC and C phases, we find that intensity decreases in the C phase. We also find about 100 meV gap at  $E_F$  in the C phase, still in the unoccupied states, from the comparison of ARPES spectrum of the  $\Gamma$  point between the IC and C phases. Together with the PES results of  $\sim 100$  meV gap in the occupied states [2], the gap is considered to be the Mott-type.

## References

- [1] F. Clerc, C. Battaglia, M. Bovet, L. Despont, C. Monney, H. Cercellier, M. G. Garnier, H. Berger, L. Forro and P. Aebi, *Phys. Rev. B* **74** (2006) 155144.
- [2] M. Arita, H. Negishi, K. Shimada, F. Xu, A. Ino, Y. Takeda, K. Yamasaki, A. Kimura, S. Qiao, S. Negishi, M. Sasaki, H. Namatame and M. Taniguchi, *Physica* **351** (2004) 265.
- [3] H. Sato, T. Kotugi, S. Senba, H. Namatame and M. Taniguchi, *J. Syn. Rad.* **5** (1998) 772.
- [4] L. F. Mattheiss, *Phys. Rev. B* **8** (1973) 3719.

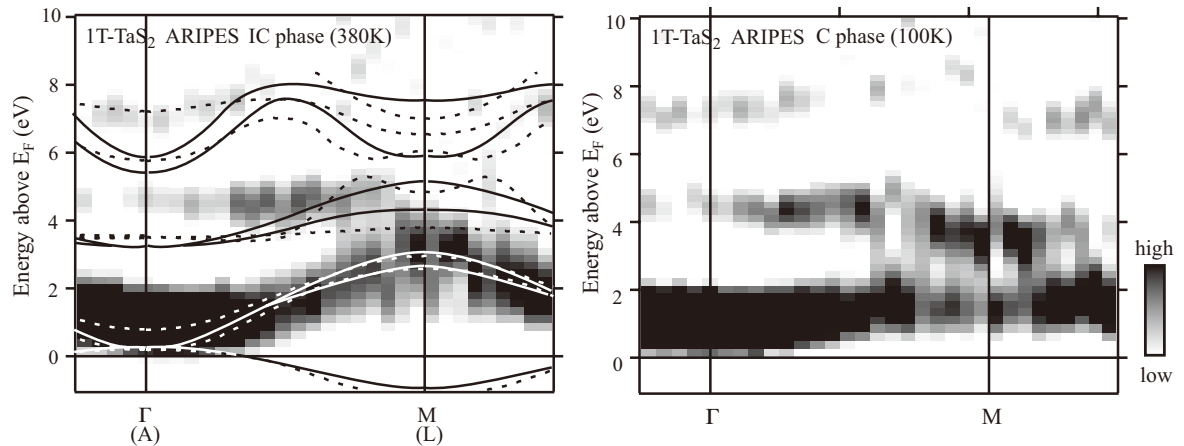


**Fig.1.** Experimental unoccupied band structures in  $\Gamma M$  direction for the IC and C phases of 1T-TaS<sub>2</sub>. Left side is the IC phase band structure with band-structure calculation [4]. The dashed line and solid line indicate the results of AL and  $\Gamma M$  directions, respectively. Right side is the C phase band structure. The band near  $E_F$  splits into two manifolds at M point.

## Surface electronic structures of ferromagnetic Ni(111) studied by scanning tunneling microscopy and spectroscopy

Yosuke Nishimura<sup>a</sup>, Hisashi Narita<sup>c</sup>, Mitsuru Kakeya<sup>a</sup>, Mitsuharu Higashiguchi<sup>a</sup>, Yuichi Miura<sup>a</sup>, Masashi Nakatake<sup>b</sup>, Akio Kimura<sup>a</sup>, Kenya Shimada<sup>b</sup>, Hirofumi Namatame<sup>b</sup>  
Masaki Taniguchi<sup>a,b</sup>

<sup>a</sup> Graduate School of Science, Hiroshima University, Higashi-Hiroshima 739-8526, Japan

<sup>b</sup> Hiroshima Synchrotron Radiation Center, Hiroshima University, Higashi-Hiroshima 739-0046, Japan

<sup>c</sup> Institute for Solid State Physics, Tokyo University, Kashiwa 277-8581, Japan

It is well known that free electron surface states, so called Shockley-type surface states, are present at (111) surface of noble metals with face centered cubic (fcc) structure like Au, Ag and Cu [1]. The Shockley-type surface state likewise exists at Ni, Pd, and Pt single crystalline surfaces. Particularly, a ferromagnetic Ni surface has attracted a considerable attention because a spin-polarized two-dimensional electron gas (2DEG) could emerge on this surface. In fact, the Shockley surface state of Ni(111) was approached using several experimental techniques, such as ARPES, STM, spin and angle resolved inverse photoemission spectroscopy [2-4]. However, the contradictory results were obtained so far. In order to resolve these discrepancies, the Shockley surface state of the Ni(111) has been investigated carefully with STM and STS.

Figure 1 shows the STM image of Ni(111) at the sample bias ( $V_s$ )=+0.35V. This image clearly shows a standing wave that is spread isotropically around point defects, which clearly indicates the existence of 2DEG on the surface. The STS spectrum shows two “rising edges” attributed to an exchange split pair of Shockley states at around -130meV and +60meV. From this spectrum, we concluded that the exchange splitting energy is 193meV.

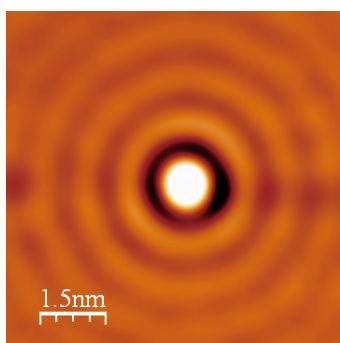


Fig. 1: The STM image of Ni(111) surface ( $V_s$ =+0.35V,  $T$ =77K)

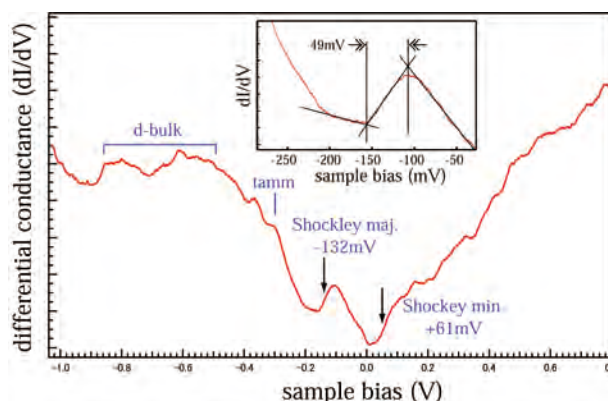


Fig. 2: STS spectrum of Ni(111) surface.

### References

- 1) M. F. Crommie et al., Nature **363** (1993) 524.
- 2) M. Higashiguchi et al., Surf. Sci. **601** (2007) 4005.
- 3) S. Pons et al., Europhys. Lett **61** (2003) 375.
- 4) M. Donath et al., Phys. Rev. Lett **70** (1993) 28.

## Atomic and local electronic structure of Co and CoSi<sub>2</sub> clusters

H. Narita, K. He, T. Okuda, A. Kakizaki, I. Matsuda

<sup>1</sup>Y. Cui, <sup>2</sup>A. Kimura, <sup>1</sup>M. Nakatake, <sup>1</sup>H. Namatame, <sup>1</sup>M. Taniguchi

*Synchrotron Radiation Laboratory, The Institute for Solid State Physics, University of Tokyo*

<sup>1</sup>*Hiroshima Synchrotron Radiation Center, Hiroshima University,*

<sup>2</sup>*Graduate School of Science, Hiroshima University*

The formation mechanism of fabricated structure on a nano-scale is an important subject in the study of the development and spread of nano technology. Especially, the nano-scale clusters attract a great deal of interest in industry and surface science as the most advanced technique, such as ultrahigh density storage media, nanocatalysis and single electron transistor [1-3].

Over the past few decades, the observation of Co/Si (111) system was carried out by scanning tunneling microscopy (STM), photoemission spectroscopy (PES) and Pseudopotential DFT calculations methods [4-6], and it was well known that the system has the flat-topped and 2×2 reconstructed triangular clusters for deposition at 320°C as shown in FIG. 1 (a) and (b). It was also suggested in some reports that these clusters show CoSi<sub>2</sub> structure with seven-fold Co coordination (interface) and so-called B-type geometry. While the clusters (Co cluster) on Al nanocluster fabricated on Si (111) 7×7 surface also have the flat-topped cluster at the same temperature, and they are seldom observed with 2×2 reconstruction as shown in FIG. 1 (c). He *et al.* [7] did not assume in detail if Co and Si atoms constitute these clusters or not. However, the interesting thing is that this Co clusters have the high perpendicular magnetic anisotropy (PMA) under 40K (Here, the cluster fabricated on Al nanocluster is described as “Co cluster” in order to differentiate the two clusters). Our final-purpose is to clarify the difference of the atomic structure between Co and CoSi<sub>2</sub> clusters and the template effect of Al nanocluster phase using photoelectron experiment [core-level photoemission spectroscopy (CL-PES), photoelectron diffraction (PED) and X-ray photoelectron diffraction (XPD)] and scanning tunneling spectroscopy (STS). In this report, we will discuss STM/STS data of CoSi<sub>2</sub> clusters fabricated on Si (111) 7×7 surface.

The experiment were carried out in an ultrahigh-vacuum (UHV) chamber with a base pressure of  $1.0 \times 10^{-10}$  mbar, using Omicron LT-STM. We used highly B-doped Si (111) wafers (p-type), and the surface was chemically treated by a modified RCA cleaning method [8]. A clean Si (111) 7×7 reconstructed surface was obtained by a standard flashing procedure up 1250 °C after outgassing at about 500 °C for several hours, and checked by LEED system. Al atoms were carefully deposited using a well-outgassed homemade evaporator, and the periodic array of Al nanocluster has been prepared by 0.24-0.3 ML-Al deposition at substrate temperature 500°C. While Co atoms were deposited at 320°C by using commercial evaporator (Omicron: EFM-3). All of STS spectra were obtained at 78K.

Figure 1 (a) shows two flat-top CoSi<sub>2</sub> clusters

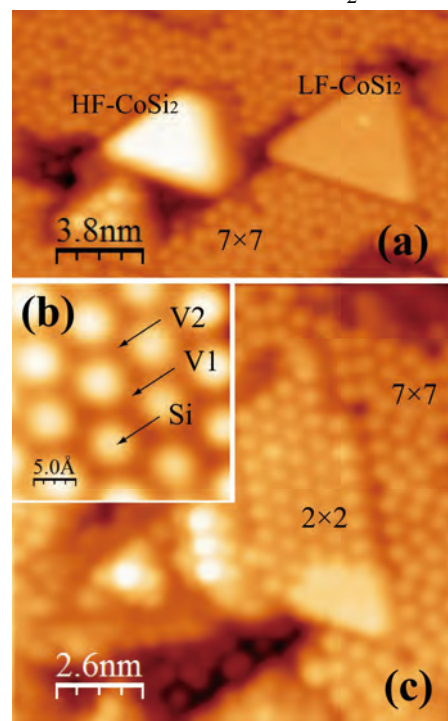


**FIG. 1** Empty state STM images of (a) flat-topped CoSi<sub>2</sub> ( $V_s = +1.8V$ ), (b) 2×2 CoSi<sub>2</sub> ( $V_s = +1.5V$ ) clusters on Si (111) 7×7 surface and (c) flat-topped Co cluster fabricated on Al nanocluster template.

fabricated on Si (111)  $7\times 7$  reconstruction surface. Here, higher  $\text{CoSi}_2$  cluster is described as HF- $\text{CoSi}_2$  and lower one is “LF- $\text{CoSi}_2$ .” While Fig. 1 (b)-(c) show the  $2\times 2$  periodical structure on cluster, and the flat area on  $2\times 2$  phase is partially formed at the corner of cluster. All of clusters is fabricated in the form of triangle shape depended on  $7\times 7$  periodicity, and the area around cluster often change from the  $7\times 7$  phase to the depressed area. According to the line-profile (*not shown here*), the depth of the depressed area is 0.23-0.30 nm, and this value says one monolayer of  $7\times 7$  DAS structure is broken. Accordingly, it should be considered that the related Si atoms diffuse toward a nearby cluster or somewhere. Actually, the depressed area is often appeared around the HF- $\text{CoSi}_2$  cluster, this phenomenon tells us that  $\text{CoSi}_2$  cluster need more Si atoms to be higher cluster.

Figure 2 shows the experimental density of state (DOS) of  $\text{CoSi}_2$  cluster formed on Si (111) and theoretical DOS of bulk  $\text{CoSi}_2$  [9]. Upper five spectra (two brown, gray, yellow and orange lines) show the STS spectra of  $2\times 2$  phase and HF/LH- $\text{CoSi}_2$  clusters, and undermost spectrum shows the theoretical DOS of bulk  $\text{CoSi}_2$ . Probing points are described in FIG.1 (a)-(c). These spectra show the different feature, and this result shows the site-resolved probing technique should be reliable. Here, we focus the difference between HF- and LF-clusters. LF-cluster has several broadened peaks in the region of  $-4 < \text{sample bias (Vs)} < 0$ . But, comparing to HF- $\text{CoSi}_2$ , these peaks become more clear, especially at  $V_s = -3.0, -1.8, -0.8\text{V}$ . While the strong peak of LF cluster at  $+0.5\text{V}$  is suppressed. Additionally, the STS spectra of HF/LF- $\text{CoSi}_2$  clusters have a double peak around  $V_s = -1.8\text{V}$ , those peak shapes and energy positions are consistent with that of calculation results. Besides, it is interesting to note, as growing from LF to HF, the characteristics of electronic structure at  $V_s = +0.5\text{V}$  gradually becomes similar to the calculated DOS. Confirming the reliability of STS spectra, the photoemission spectra of  $\text{CoSi}_2$  cluster and Si (111)  $7\times 7$  surfaces is shown in the middle of FIG. 2. The “difference” spectrum is gotten by subtracting between those spectra, and we can find the subtracted spectrum has the double peak at around  $-1.7\text{V}$  below Fermi level as the STS spectra and theoretical DOS do. Besides, the strong peak of subtracted spectra at  $-0.7\text{V}$  is consistent with that of  $2\times 2$  phase STS spectra at the same energy, therefore, it is expected that strong peak arises from the  $2\times 2$  electronic structure. As described above, we can understand that  $\text{CoSi}_2$  cluster has the same electronic state as bulk  $\text{CoSi}_2$  in spite of low dimensional structure.

For the future, we will do more accurate STM/STS experiment for  $\text{CoSi}_2$  and Co clusters.

## References

- [1] K Bromann *et al.*, Science 274 (1996) 956.
- [2] H. Brune *et al.*, Nature (London) 394 (1998) 451.
- [3] S. Sun *et al.*, Science 287 (2000) 1989.
- [4] P. A. Bennett *et al.*, J. Vac. Sci. Technol. A 11(4) (1993) 1680.
- [5] C. Pirri *et al.*, Phys. Rev. B 29 (1984) 3391.
- [6] M. A. K. Zilani *et al.*, J. Phys.: Condens. Matter 18 (2006) 6987, Phys. Rev. B 72 (2005) 193402.
- [7] Ke. He *et al.*, Surf. Interface Anal. 38 (2006) 1028.
- [8] W. Kem *et al.*, PCA Rev. 31 (1970) 187.
- [9] L. F. Mattheiss *et al.*, Phys. Rev. B 37 (1988) 10623.

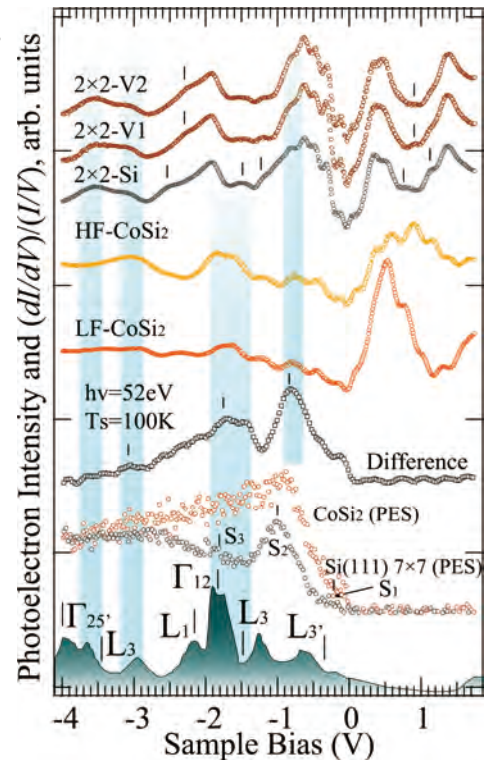


FIG. 2 Experimental and theoretical DOS of  $\text{CoSi}_2$ . STS spectra were obtained at each atomic site in FIG. 1 (a)-(c).

# Co-induced nano-structures on Si(111) surface

Y. T. Cui<sup>a</sup> T. Xie<sup>b</sup> M. Ye<sup>a</sup> A. Kimura<sup>a</sup> S. Qiao<sup>b,c</sup> H. Namatame<sup>b</sup> M. Taniguchi<sup>a,b</sup>

<sup>a</sup>Graduate School of Science, Hiroshima University Higashi-Hiroshima, 739-8526 Japan

<sup>b</sup>Hiroshima Synchrotron Radiation Center, Hiroshima University, Higashi-Hiroshima 739-0046, Japan

<sup>c</sup>Advanced Materials Laboratory, Fudan University, Shanghai 200433, China.

---

## Abstract

The interaction of cobalt atoms with silicon (111) surface has been investigated by means of scanning tunneling microscopy (STM) and low-energy electron diffraction (LEED). Besides the Co silicide islands, we have successfully distinguished two inequivalent Co-induced  $\sqrt{13} \times \sqrt{13}$  reconstructions on Si (111) surface. Our high-resolution STM images provide some structural properties of the two different  $\sqrt{13} \times \sqrt{13}$  derived phases. Both of the two phases seem to form islands with single domain. The new findings will help us to understand the early stage of Co silicide formations.

*Key words:* Co silicide; Si(111) surface; Scanning tunneling microscopy; LEED; reconstructions

*PACS:* 61.14.Hg, 61.30.Hn, 61.46.Bc, 68.35.-p, 73.20.At

---

## 1. Introduction

Transition-metal silicides have been widely investigated in recent years in terms of microelectronic industry and fundamental science. Besides the applications of transition-metal silicides (such as  $\text{CoSi}_2$ ,  $\text{NiSi}_2$ ) in integrated-circuits, the effects of adsorbed atoms on a reconstructed Si surface and the mechanisms and coefficients of surface diffusion are also fundamental subjects of surface science. Although there have been extensive studies on the growth and properties of  $\text{CoSi}_2$  epitaxial films, knowledge about the structural details of Co adatoms and the initial stages of cobalt disilicide are insufficient partly due to an appearance of very rich reconstructed phases. Si(111)- $\sqrt{7} \times \sqrt{7}$ R19.1°-Co (hereafter as  $\sqrt{7}$ ) structure has been studied by means of LEED, XPS (X-ray Photoemission Spectroscopy), ARPES (Angle-Resolved Photoelectron Spectroscopy), STM and LDA (Local Density

Approximation) based calculations (1; 2; 3). Two types of domains with  $\sqrt{13} \times \sqrt{13}$ R13.9° (hereafter as  $\sqrt{13}$ ) reconstructions and both the  $\sqrt{13}$  and  $\sqrt{19} \times \sqrt{19}$ R23.4° (hereafter as  $\sqrt{19}$ ) reconstructions were found by LEED and STM (4; 5), but the detailed structural information is still lacking. In order to investigate the detailed surface structures, STM experiment was carried out. In this paper, we will show two inequivalent Co-induced  $\sqrt{13}$  structural phases through several real space STM images together with their FFT (fast Fourier transformation) and LEED patterns.

## 2. Experimental

The Co induced surface structures were fabricated and studied with a commercial room-temperature scanning tunneling microscope (STM, RHK UHV-400) mounted in an ultrahigh-vacuum (UHV) chamber combined with a sample-preparation chamber. The base pressures of the two chambers were around  $1.0 \times 10^{-10}$  Torr. Clean Si(111) ( $p$  type,  $\geq$

---

*Email address:* yitao cui@gmail.com (Y. T. Cui).

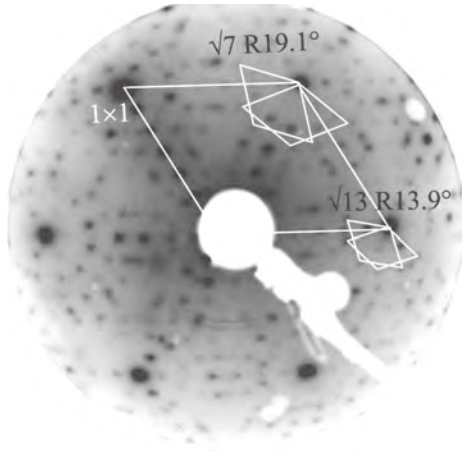


Fig. 1. LEED pattern with electron energy of 63.4 eV. The reciprocal unit cells of Si(111)- $1\times 1$ ,  $\sqrt{13}$  and  $\sqrt{7}$  reconstructed surfaces are marked.

1000  $\Omega\cdot\text{cm}$ ) surfaces were obtained by the following process. After degassed for several hours at 800 K, the sample was flashed several times to 1470 K for 5 seconds, then the sample temperature was rapidly reduced to about 1170 K, and slowly decreased to room temperature at a pace of 1~2 K/s with a pressure below  $1.0\times 10^{-9}$  Torr. The sample temperature was controlled by direct-current-heating and a nearly perfect  $7\times 7$  reconstruction was obtained by this method. Co was deposited from a water-cooled electron-beam evaporator (Omicron EFM 3) to clean  $7\times 7$ -Si(111) surface with a rate of  $\sim 0.08$  ML/min (where 1 ML =  $7.83\times 10^{14}$  atoms/cm<sup>2</sup>). The temperature of silicon substrate was kept at 800 K during the Co deposition. Auger electron spectroscopy (AES) and LEED observations were routinely carried out to check the surface cleanliness and reconstruction. All of the STM images were taken at room temperature.

### 3. Results and discussion

The LEED pattern of 0.5 ML Co on Si(111) surface is presented in Fig. 1. Besides  $1\times 1$ ,  $7\times 7$  and  $\sqrt{7}$  patterns, one can find the spots of  $\sqrt{13}$  derived structure, which are the same as those in the published results(4). It should be mentioned here that these additional spots were formerly attributed to two types of domains with  $\sqrt{13}$  phase by Dolbak et al (4), which were defined as A and B domains in their paper. The two kinds of domains are separated with respect to Si (1 $\bar{1}$ 0) mirror-image symmetry plane and they widely exist in  $\sqrt{n}$  structures such as Ni-

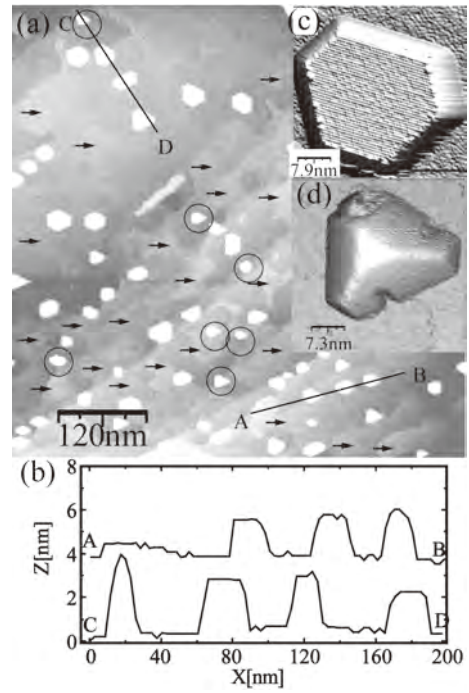


Fig. 2. Typical occupied-state STM images ( $V_S = -2.5$  V,  $I_S = 0.51$  nA) of Si (111) surface after deposition of 0.5 ML Co at a temperature of 800 K; (a) Typical topographic image in the wide area ( $600\text{nm}\times 600\text{nm}$ ); (b) The cross section profiles along the lines shown in (a); Close view of typical Co islands in three dimensional form: (c) atomically flat top island with  $2\times 2$  structure and (d) pyramid-like island.

induced  $\sqrt{19}$  twinned atomic structures(6), Si(111)- $\sqrt{21}\times\sqrt{21}$ -Ag surface with different orientations of  $[11\bar{2}]\pm 10.89^\circ$  at OPB3 (out-of-phase-boundary of the  $\sqrt{3}$ -Ag phase)(7) and so on. The present LEED pattern also indicates two domains for the  $\sqrt{7}$  surface phase as shown in Fig. 1.

Fig. 2 (a) shows the typical occupied-state STM image in the wide area ( $600\text{nm}\times 600\text{nm}$ ,  $V_S = -2.5$  V,  $I_S = 0.51$  nA). Here, one can find some islands with larger height (brighter image). The cross sections along two lines marked on Fig. 2 (a) are shown in Fig. 2 (b). The lateral size of islands is in the order of tens nanometers, and mostly in the range between 20 to 50 nm with the height of about 2~5 nm. These islands can be classified into two typical types. The major one shows approximately triangular, trapezoidal or hexagonal shape with atomically flat top that shows well-known  $\text{CoSi}_2(111)-(2\times 2)$  structure (8; 9). A typical image of this kind of island is shown in Fig. 2 (c) in three dimensional form. The minority one as marked by ellipses in Fig. 2 (a) shows pyramid-like feature without any  $\text{CoSi}_2(111)-(2\times 2)$  structure on the triangular flat top as seen

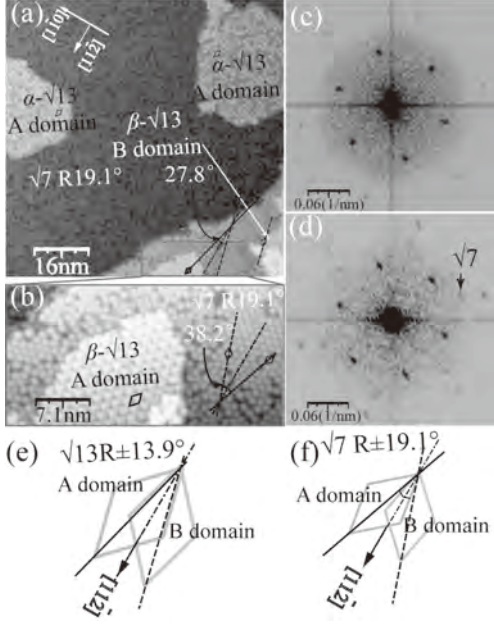


Fig. 3. (a) Occupied-state STM images of  $\alpha\text{-}\sqrt{13}$  phase with A type domain and  $\beta\text{-}\sqrt{13}$  phase with both A and B domains ( $80\text{ nm}\times 80\text{ nm}$ ). (b) Close-up view of  $\beta\text{-}\sqrt{13}$  phase with B type domain ( $35.5\text{ nm}\times 18\text{ nm}$ ,  $V_S = -2.1\text{ V}$ ,  $I_S = 0.3\text{ nA}$ ). (c) FFT pattern of Fig. (a). (d) FFT pattern of Fig. 3 (b) (The  $\sqrt{7}$  FFT spot is marked with an arrowhead (11)). Schematic diagrams of the relationships of two (A and B) domains for (e)  $\sqrt{13}$  and (f)  $\sqrt{7}$  surface phases.

in Fig. 2 (d). It is a little higher than the former type. The edges of both two types of islands are aligned parallel to those of the  $7\times 7$  unit cell, and the lengths are integer times as large as that of  $7\times 7$  unit cell as have been discussed elsewhere(8). Due to the small percentage of island relative to the whole surface, the structures of the island surface did not reflect clear corresponding spots in LEED pattern. It means that the surface structures shown in LEED pattern mainly come from the contribution of inter island.

In the inter-island regions, besides  $7\times 7$ , Co-induced  $\sqrt{7}$  and  $\sqrt{19}$  phases, one can find irregular flat areas with a height of about  $0.3\text{ nm}$  (some typical regions were marked by black arrowheads in Fig. 2 (a)). More details of the occupied-state STM images in this region are shown in Figs. 3 (a) and (b). Here, two different structures are found. One shows a  $\sqrt{13}$  surface phase, which has been observed by Löffler et al (5) (denoted as  $\alpha$  phase with A type domain). It is found that the length of unit cell is  $1.38\text{ nm}$  and its orientation is rotated by an angle of  $13.9^\circ$  relative to  $[11\bar{2}]$  direction in clockwise direction as illustrated in Fig. 3 (e). Another struc-

ture in Fig. 3 (a) and magnified in Fig. 3 (b) has not been observed before. In order to know the structural property, we have analyzed the occupied-state STM image carefully. It is found that the unit cell size is around  $1.38\text{ nm}$  and the unit cell is rotated by an angle of  $13.9^\circ$  in clockwise direction relative to  $[11\bar{2}]$  direction (illustrated in Fig. 3 (e)) indicating the same periodicity of  $\sqrt{13}$  in this new surface phase. To distinguish with  $\alpha\text{-}\sqrt{13}$  phase, this new phase is denoted as  $\beta$  phase with A type domain. The fast Fourier transformation (FFT) images of Figs. 3 (a) and (b) using WSXM software(10) are shown in Figs. 3 (c) and (d), respectively. The sharp FFT patterns of  $\sqrt{13}$  surface phases can be seen well (11), and both of them show the same orientation, which together with their corresponding STM images gives the strong evidences of the two inequivalent  $\sqrt{13}$  surface phases.

It has been mentioned above that most  $\sqrt{n}$  surface phases on Si (111) surface have two domains with a misfit angle owing to Si ( $1\bar{1}0$ ) mirror-image symmetry planes shown in LEED pattern. For easily understood the different domains the schematic diagrams of the relationship of the different domains (here, A and B domains) for  $\sqrt{13}$  and  $\sqrt{7}$  reconstructions are shown in Figs. 3 (e) and (f). So, it is reasonable to observe both domains of the two  $\sqrt{13}$  phases on the surface (not shown here). It should be mentioned that both  $\alpha$  and  $\beta$  phases seem to form islands with one domain, which is not like  $\sqrt{7}$  and  $\sqrt{19}$  structures that form twined structures with defects. The defect structures will restrain themselves from forming large islands. This feature indicates that the defect-free, single-domain  $\sqrt{13}$  island-like structures may be one kind of early-stage formation of Co silicide islands on Si (111) surface. From this point of view, the investigation of  $\sqrt{13}$  structures will help us to understand the early stage of Co silicide formations.

In order to study the detailed structures of  $\sqrt{13}$  surface phases, high-resolution STM observations have been performed. The empty- and occupied-state STM images of  $\alpha$ - (upper) and  $\beta$ - (lower)  $\sqrt{13}$  phases are presented in Fig. 4 with the unit cell indicated in the figures. The prominent feature of both  $\sqrt{13}$  surface phases is the centered hexagonal array of threefold symmetric protrusions as is evident in Fig. 4. Note that the  $\alpha$  phase seems to comprise two layers of triangular clusters on the top and another triangle with six protrusions below them as shown in the occupied-state STM image (Fig. 4 (b)). Both of them just occupies half of the unit cell (here after as HUC), the other half is a dark hole at nega-

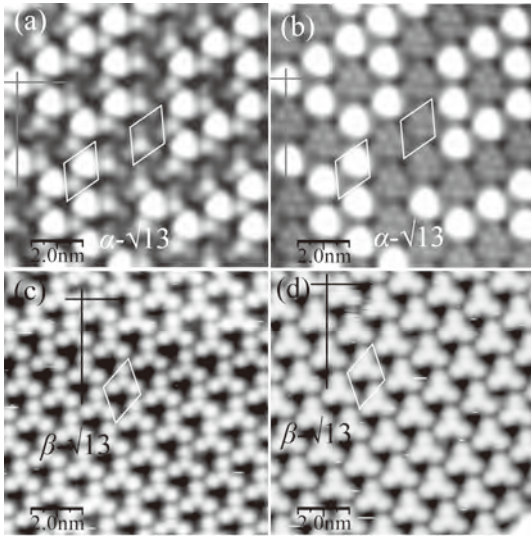


Fig. 4. High-resolution empty-(left) and occupied-(right) state STM images of  $\alpha$ - (up case) and  $\beta$ - (lower case)  $\sqrt{13}$  phases ( $10 \text{ nm} \times 10 \text{ nm}$ )  $V_S = \pm 1.5 \text{ V}$ ,  $I_S = 0.3 \text{ nA}$  for (a) and (b);  $V_S = \pm 2.0 \text{ V}$ ,  $I_S = 0.8 \text{ nA}$  for (c) and (d). The crosshairs are located in identical positions in both of the occupied- and empty-state images.

tive sample bias (shown in Fig. 4 (b)). For the lower layer, at a negative sample bias, the triangle with six protrusions and the other dark HUC can be observed, while at positive sample bias the dark HUC becomes brighter and the number of protrusions is reduced to three at the corner with a dark hole in the center. For the upper layer, it is noticed that the bright triangle always occupies the same HUC – on the top of six-protrusion triangle in occupied-states – and the positions of the bright triangle are not changed at various sample bias, which means that the protrusions of the bright triangle give the sites information of real atoms.

The expanded high-resolution  $\beta$  phase images show four protrusions (tetramers) and a dark HUC in both empty- and occupied-states. In contrast to the  $\alpha$  phase, the  $\beta$  phase exhibits a little difference in spatial distribution between empty- and occupied-state, except the protrusions in occupied-state STM images seem fatter than that in empty-state STM images. It should be mentioned that we still can not give the information of Co atoms contribution in  $\alpha$ - and  $\beta$ -  $\sqrt{13}$  surface phases just from STM image. For more information, deeper investigation and a atomic structural model need to be made and some calculated results should be helpful.

#### 4. Conclusion

In summary, self-assembled Co silicide have been fabricated on Si(111) and investigated by means of scanning tunneling microscopy (STM) and low-energy diffraction (LEED). The LEED pattern has verified the existence of  $\sqrt{13}$  phases on Si(111) surface. Our high resolution STM images show that besides the Co silicide island, there are two inequivalent  $\sqrt{13}$  surface phases in the inter-island regions. Both of the two phases seem to form islands with single domain. From this point of view, the new findings will help us to understand the early stage of Co silicide formations.

This work was supported by the Ministry of Education, Culture, Sports, Sciences and Technology.

#### References

- [1] C. Pirri, J. C. Peruchetti, G. Gewinner and J. Derrien, Phys. Rev. B **29** (1984) 3391; B **30** (1984) 6227.
- [2] P. A. Bennett, M. Copel, D. Cahill, J. Falta and R. M. Tromp, Phys. Rev. Lett. **69** (1992) 1224.
- [3] M. -H. Tsai, J. D. Dow, P. A. Bennett, D. G. Cahill, Phys. Rev. B **48** (1993) 2486.
- [4] A. E. Dolbak, B. Z. Olshanetsky, S. A. Teys, Surf. Sci. **373** (1997) 43.
- [5] M. Löffler, J. Cordón, M. Weinelt, J. E. Ortega, T. Fauster, Appl. Phys. A **81** (2005) 1651.
- [6] G. Kinoda, K. Ogawa, Surf. Sci. **461** (2000) 67.
- [7] Xiao Tong, Satoru Ohuchi, Norio Sato, Takehiro Tanikawa, Tadaaki Nagao, Iwao Matsuda, Yoshinobu Aoyagi, and Shuji Hasegawa, Phys. Rev. B **64** (2001) 205316
- [8] P. A. Bennett, S. A. Parikh, D. G. Cahill, J. Vac. Sci. Technol. A **11** (1993) 1680.
- [9] M. A. K. Zilani, Lei Liu, H. Xu, Y. P. Feng, X. -S. Wang and A. T. S. Wee, J. Phys.: Condens. Matter **18** (2006) 6987
- [10] I. Horcas, R. Fernández, J. M. Gómez-Rodríguez, J. Colchero, J. Gómez-Herrero, A. M. Baro, Rev. Sci. Instrum. **78** (2007) 013705.
- [11] One can see a large number of  $\sqrt{7}$  reconstructions from the STM images (See Figs. 3 (a) and (b)). Since there are many defects in  $\sqrt{7}$  phases, one can not get very sharp FFT spots with  $\sqrt{7}$  structure. The irregular lattices just contribute to a dark background as shown in Figs. 3 (c) and (d).

## Graphene epitaxially grown on the step with unit-cell height of 4H-SiC(0001) substrate

M. Ye<sup>1</sup>, Y. T. Cui<sup>2</sup>, S. Qiao<sup>3</sup>, A. Kimura<sup>1</sup>, M. Sawada<sup>2</sup>, H. Namatame<sup>2</sup>, M. Taniguchi<sup>1,2</sup>

<sup>1</sup>Grad. Sch. Sci., Hiroshima Univ.

<sup>2</sup>HSRC, Hiroshima Univ.

<sup>3</sup>Laboratory of advanced materials, Department of physics, and Surface physics Laboratory, Fudan Univ.

As a novel member of carbon-based materials, graphene holds promising potential for the next-generation nano-devices<sup>[1]</sup>. Especially, graphene nano-ribbons (GNRs) are highly expected for the novel spintronics<sup>[2]</sup>.

Being the substrate that allows epitaxial growth of high quality graphene film<sup>[3]</sup> and the self-assembling of periodically ordered one-dimensional system, vicinal surface of SiC(0001) has been chosen to epitaxially grow GNRs films in our present research.

4H-SiC(0001) with off-axis angle of  $4^\circ$  towards  $[1,-1,0,0]$  has been annealed in ultra-high vacuum (UHV) above  $1100^\circ\text{C}$ . The surface is characterized by scanning tunneling microscopy (STM) and low energy electron diffraction (LEED) after each different annealing temperature.

The result shows that, prior to the thermal decomposition of SiC(0001), the height of the micro-steps on the vicinal surface bunched from single atomic layer height to one unit-cell height of 4H-SiC(0001) after being annealed at  $950^\circ\text{C}$ . After the decomposition started at  $1130^\circ\text{C}$ , the vicinal surface was graphitized from the edge of the bunched steps (Fig. 1), forming well separated narrow graphene domains, which indicated a growth mode that Si atoms diffused into the vacuum through the step edges, and the carbon atoms that remained on the steps formed graphene phase from the edge regions through the surface reconstruction.

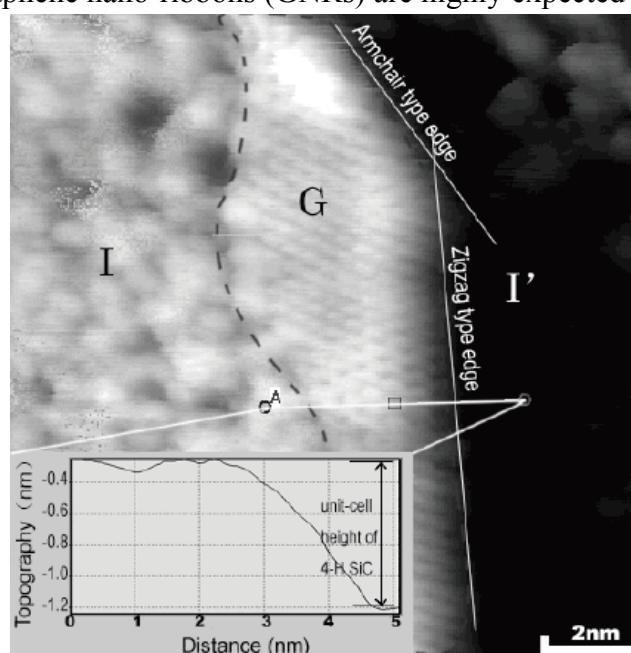


Fig.1 STM image of graphene on the stepped surface of SiC(0001),  $13\text{nm} \times 13\text{nm}$ . Sample bias voltage:  $-0.5\text{V}$ , tunneling current  $0.18\text{nA}$ . Region G (inside of the broken line): graphene phase on the step; Region I and I':  $(6\sqrt{3} \times 6\sqrt{3})R30^\circ$  C-rich phase.

### Reference:

[1]. K. S. Novoselov, *et al.*, Nature **438**, 197 (2005)

[3]. C. Berger, *et al.*, J. Phys. Chem. B **108**, 19912 (2004).

[2]. Y. W. Son, *et al.*, Nature **444**, 347 (2006).



# Appendices



# Organization

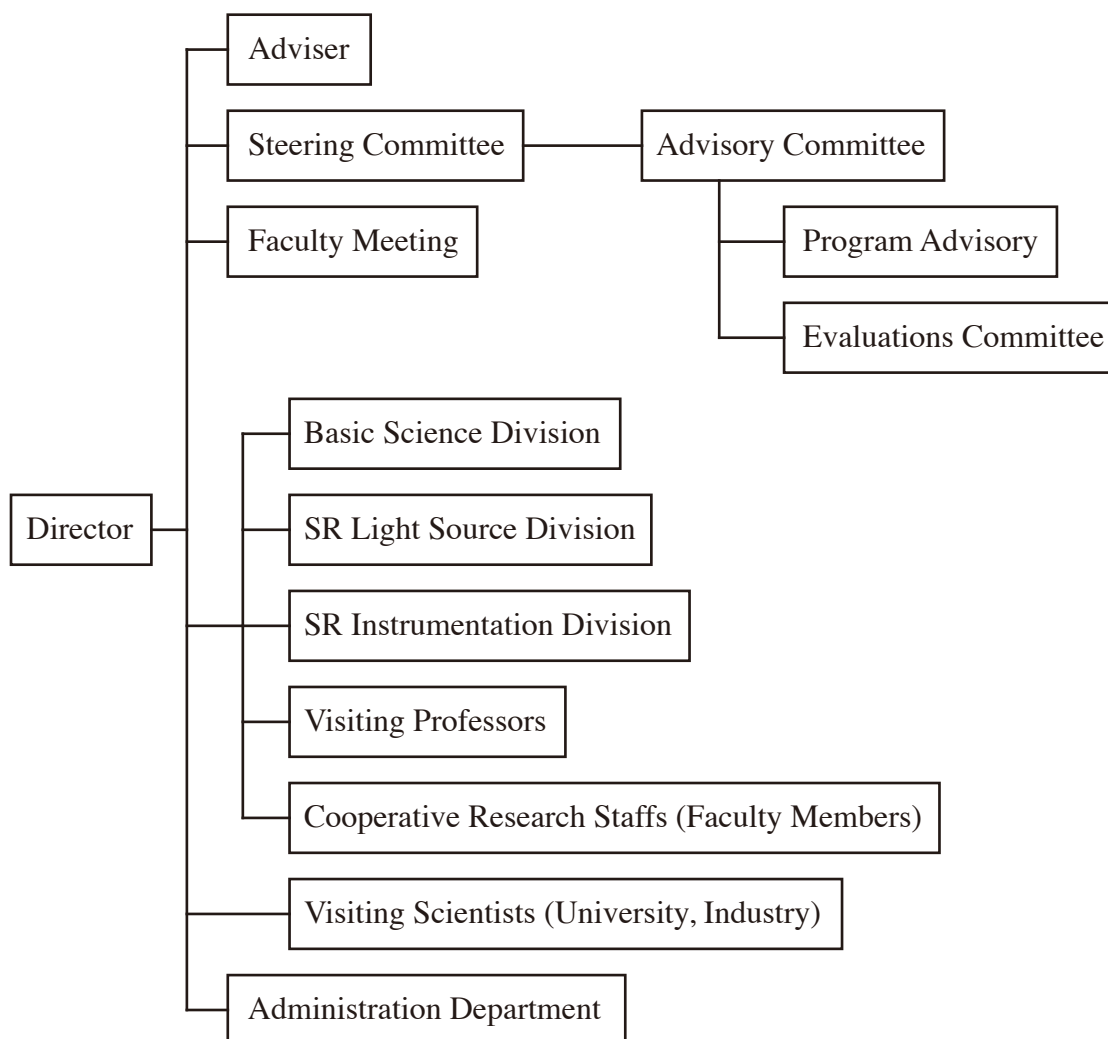


Fig. 1. Organization chart of HSRC

## Director

TANIGUCHI, Masaki

Hiroshima Synchrotron Radiation Center, HSRC,  
Graduate School of Science, Hiroshima University

## Adviser

OHTA, Toshiaki

Ritsumeikan University Emeritus Professor, University of Tokyo

SATO, Shigeru

Emeritus Professor, Tohoku University

IWAMI, Motohiro

Emeritus Professor, Okayama University

## Staff Members

TANIGUCHI, Masaki	Director, Prof.
NAMATAME, Hirofumi	Co-director, Prof.
HORI, Toshitada	Prof.
SHIMADA, Kenya	Assoc. Prof.
SATO, Hitoshi	Assoc. Prof.
KUTLUK, Galif	Visiting Assoc. Prof.
SAWADA, Masahiro	Assist. Prof.
NAKATAKE, Masashi	Assist. Prof.
MIYAMOTO, Atsushi	Assist. Prof.
GOTO, Kiminori	Engineer
ARITA, Masashi	Engineer
KASUGA, Toshio	Visiting Prof.
TSUTSUI, Hiroshi	Visiting Assoc. Prof.
MIZOKAWA, Takashi	Visiting Assoc. Prof.
NEGISHI, Saiko	Pos. Doc. Fellow
HE, Shaolong	Pos. Doc. Fellow
HONG, Cai Hau	Pos. Doc. Fellow
MORIMOTO, Osamu	Pos. Doc. Fellow
CUI, Yitao	Pos. Doc. Fellow
MATSUO, Koichi	Pos. Doc. Fellow, Japan Society for the Promotion of Science
KANEKO, Miyoko	Technical Staff
SHINNO, Naoko	Secretary
SHIMOKUBO, Harumi	Secretary

## Steering Committee

TANIGUCHI, Masaki*	HSRC
NAMATAME, Hirofumi	HSRC
HORI, Toshitada	HSRC
SHIMADA, Kenya	HSRC
SATO, Hitoshi	HSRC
INUI, Masanori	Graduate School of Integrated Arts and Sciences
MARUYAMA, Hiroshi	Graduate School of Science
KIKKAWA, Takamaro	Research Center for Nanodevices and Systems
HARIMA, Yutaka	Graduate School of Engineering
UENO, Satoshi	Graduate School of Biosphere Science
HOSHI, Seiji	Research Institute for Radiation Biology and Medicine

\*Chair Person

## **Advisory Committee**

TANIGUCHI, Masaki*	HSRC
NAMATAME, Hirofumi	HRSC
HORI, Toshitada	HSRC
SHIMADA, Kenya	HSRC
SATO, Hitoshi	HSRC
MARUYAMA, Hiroshi	Graduate School of Science
KUROIWA, Yoshihiro	Graduate School of Science
TANAKA, Kenichiro	Graduate School of Science
HIRAYA, Atsunari	Graduate School of Science
HAYAKAWA, Shinjiro	Graduate School of Engineering
FUJIMORI, Atsushi	University of Tokyo
SODA, Kazuo	Nagoya University
ISHII, Hiroyoshi	Tokyo Metropolitan University
SAITOH, Tomohiko	Tokyo University of Science
YOKOYA, Takayoshi	Okayama University
KASUGA, Toshio	High Energy Accelerator Research Organization
AIURA, Yoshihiro	Advanced Industrial Science and Technology

\*Chair Person

## **Program Advisory Committee**

NAMATAME, Hirofumi*	HSRC
HORI, Toshitada	HSRC
SHIMADA, Kenya	HSRC
SATO, Hitoshi	HSRC
SAWADA, Masahiro	HSRC
NAKATAKE, Masashi	HSRC
MIYAMOTO, Atsushi	HSRC
ARITA, Masashi	HSRC
KUTLUK, Galif	HSRC
MATSUO, Koichi	HSRC
KIMURA, Akio	Graduate School of Science
YOSHIDA, Hiroaki	Graduate School of Science
WADA, Shin-ichi	Graduate School of Science
HAYAKAWA, Shinjiro	Graduate School of Engineering

\*Chair Person

## Evaluations Committee

HORI, Toshitada*	HSRC
NAMATAME, Hirofumi	HSRC
SHIMADA, Kenya	HSRC
SATO, Hitoshi	HSRC
MARUYAMA, Hiroshi	Graduate School of Science
TSUTSUI, Hiroshi	Sumitomo Heavy Industries, Ltd.
NAKA, Yoshio	Academic Affairs Office
KANDA, Michiaki	Academic Affairs Office

\*Chair Person

## Cooperative Research Staffs (Faculty Members)

HOSHINO, Kozo	Faculty of Integrated Arts and Sciences
KOJIMA, Kenichi	Faculty of Integrated Arts and Sciences
INUI, Masanori	Faculty of Integrated Arts and Sciences
TANAKA, Kenichiro	Graduate School of Science
HIRAYA, Atsunari	Graduate School of Science
MARUYAMA, Hiroshi	Graduate School of Science
KUROIWA, Yoshihiro	Graduate School of Science
TABAYASHI, Kiyohiko	Graduate School of Science
SEKITANI, Tetsuji	Graduate School of Science
KIMURA, Akio	Graduate School of Science
OKADA, Masakazu	Graduate School of Science
NAKAJIMA, Nobuo	Graduate School of Science
TAKAHASHI, Yoshio	Graduate School of Science
YOSHIDA, Hiroaki	Graduate School of Science
WADA, Shin-ichi	Graduate School of Science
ISHIMATSU, Naoki	Graduate School of Science
MORIYOSHI, Chikako	Graduate School of Science
INO, Akihiro	Graduate School of Science
TAKAHAGI, Takayuki	Graduate School of Advanced Sciences of Matter
TAKABATAKE, Toshiro	Graduate School of Advanced Sciences of Matter
JO, Takeo	Graduate School of Advanced Sciences of Matter
MIYAZAKI, Seiichi	Graduate School of Advanced Sciences of Matter
OGUCHI, Tamio	Graduate School of Advanced Sciences of Matter
TAKAHASHI, Toru	Graduate School of Advanced Sciences of Matter
IGA, Toshifumi	Graduate School of Advanced Sciences of Matter
TANAKA, Arata	Graduate School of Advanced Sciences of Matter

YAMANAKA, Shoji	Graduate School of Engineering
HIROKAWA, Takeshi	Graduate School of Engineering
SHIZUMA, Kiyoshi	Graduate School of Engineering
SASAKI, Gen	Graduate School of Engineering
HAYAKAWA, Shinjiro	Graduate School of Engineering
SATO, Kiyotaka	Faculty of Applied Biological Science
UENO, Satoshi	Faculty of Applied Biological Science
HOSHI, Seiji	Research Institute for Radiation Biology and Medicine
KAMIYA, Kenji	Research Institute for Radiation Biology and Medicine
YOKOYAMA, Shin	Research Center for Nanodevices and System

### **Visiting Scientists**

SUMIDA, Hirosuke	Technical Research Center, Mazda Motor Co.
MIYADE, Hiroki	Sumitomo Heavy Industries, Ltd.
SENBA, Shinya	Ube National College of Technology
YAMAMOTO, Yasukazu	Ritsumeikan University SR Center
YOKOYA, Takayoshi	Graduate School of Nature Science and Technology, Okayama University
HIRAI, Masaaki	Graduate School of Nature Science and Technology, Okayama University
MURAOKA, Yuji	Graduate School of Nature Science and Technology, Okayama University
YAGI, Shinya	Graduate School of Engineering, Nagoya University
AOKI, Kenichi	Sumitomo Heavy Industries, Ltd.
AIURA, Yoshihiro	Advanced Industrial Science and Technology
SASABE, Jun	Hamamatsu Photonics Central Research Laboratory
OBA, Akira	Hamamatsu Photonics Central Research Laboratory
SATOZONO, Hiroshi	Hamamatsu Photonics Central Research Laboratory
SHAN, Qiao	Lawrence Berkeley National Laboratory, USA
DONGLAI, Feng	Fudan University, China

## List of Publications

S. He, M. Arita, H. Namatame, M. Taniguchi, H.-N. Li, H.-Y. Li

*Angle-dependent oscillations in valence-band photoemission intensity of C-60*

JOURNAL OF PHYSICS-CONDENSED MATTER **19**(2) 26202 (2007)

S. Nagaoka, G. Prumper, H. Fukuzawa, M. Hino, M. Takemoto, Y. Tamenori, J. Harries, I.H. Suzuki, O. Takahashi, K. Okada, K. Tabayashi, X.-J. Liu, T. Lischke, K. Ueda

*Electron-ion-ion triple-coincidence spectroscopic study of site-specific fragmentation caused by Si : 2p core-level photoionization of F<sub>3</sub>SiCH<sub>2</sub>CH<sub>2</sub>Si(CH<sub>3</sub>)<sub>3</sub> vapor*

PHYSICAL REVIEW A **75**(2) 020502 (2007)

J. Chaboy, Laguna-MA. Marco, C. Piquer, H. Maruyama, N. Kawamura, N. Ishimatsu, M. Suzuki, M. Takagaki

*Relationship between the magnetic moment of Lu and the magnetic behavior of (Y<sub>y</sub>Lu<sub>1-y</sub>)(Co<sub>1-x</sub>Al<sub>x</sub>)<sub>2</sub> from x-ray absorption spectroscopy and x-ray magnetic circular dichroism*

PHYSICAL REVIEW B **75**(6) 064410 (2007)

J.F. Douglas, H. Iwasawa, Z. Sun, A.V. Fedorov, M. Ishikado, T. Saitoh, H. Eisaki, H. Bando, T. Iwase, A. Ino, M. Arita, K. Shimada, H. Namatame, M. Taniguchi, T. Masui, S. Tajima, K. Fujita, S.-I. Uchida, Y. Aiura, D.S. Dessau

*Superconductors - Unusual oxygen isotope effects in cuprates?*

NATURE **446** E5 (2007)

B.-P. Xie, K. Yang, D.-W. Shen, J.F. Zhao, H.-W. Ou, J. Wei, S.Y. Gu, M. Arita, S. Qiao, H. Namatame, M. Taniguchi, N. Kaneko, H. Eisaki, K.-D. Tsuei, C.-M. Cheng, I. Vobornik, J. Fujii, G. Rossi, Z.-Q. Yang, D.-L. Feng

*High-energy scale revival and giant kink in the dispersion of a cuprate superconductor*

PHYSICAL REVIEW LETTERS **98**(14) 147001 (2007)

T. Yamasaki, K. Yamazaki, A. Ino, M. Arita, H. Namatame, M. Taniguchi, A. Fujimori, Z.-X. Shen, M. Ishikado, S. Uchida

*Unmasking the nodal quasiparticle dynamics in cuprate superconductors using low-energy photoemission*

PHYSICAL REVIEW B **75**(14) 140513 (2007)

J. Chaboy, M.A. Laguna-Marco, H. Maruyama, N. Ishimatsu, Y. Isohama, N. Kawamura

*X-ray magnetic circular dichroism study of the decoupling of the magnetic ordering of the Er and Co sublattices in Er<sub>1-x</sub>Y<sub>x</sub>Co<sub>2</sub> systems*

PHYSICAL REVIEW B **75**(14) 144405 (2007)

O. Takahashi, T. Matsui, A. Kawano, K. Tabayashi, K. Yamasaki

*Systematics of the gradient on the resonant core-hole state*

JOURNAL OF MOLECULAR STRUCTURE-THEOCHEM **808** 35–40 (2007)

- K. Matsuo, Y. Sakurada, R. Yonehara, M. Kataoka, K. Gekko  
*Secondary-structure analysis of denatured proteins by vacuum-ultraviolet circular dichroism spectroscopy*  
BIOPHYSICAL JOURNAL **92**(11) 4088–4096 (2007)
- K. Mimura, M. Arita, K. Wakita, N. Mamedov, G. Orudzhev, Y. Taguchi, K. Ichikawa, H. Namatame  
*Angle-resolved photoemission study of quasi-one-dimensional TlInSe<sub>2</sub>*  
JOURNAL OF ELECTRON SPECTROSCOPY AND RELATED PHENOMENA **156–158** 379–382 (2007)
- K. Yoshikawa, H. Sato, M. Arita, M. Higashi, K. Hiraoka, K. Kojima, H. Namatame, M. Taniguchi  
*Low-energy excited photoemission spectroscopy of Y<sub>x</sub>Yb<sub>1-x</sub>InCu<sub>4</sub>*  
JOURNAL OF ELECTRON SPECTROSCOPY AND RELATED PHENOMENA **156–158** 361–364 (2007)
- H. Sato, K. Tsuji, K. Yoshikawa, Y. Tezuka, S. Nishimoto, M. Higashi, F. Iga, M. Tsubota, M. Takemura, T. Takabatake, M. Taniguchi  
*Ti 2p soft X-ray emission spectroscopy of Ti<sub>2</sub>O<sub>3</sub>*  
JOURNAL OF ELECTRON SPECTROSCOPY AND RELATED PHENOMENA **156–158** 365–368 (2007)
- S. Hosokawa, H. Sato, K. Mimura, N. Happo, Y. Tezuka, T. Ichitsubo, E. Matsubara, N. Nishiyama  
*Soft X-ray emission study of Pd-Ni-Cu-P bulk metallic glass*  
JOURNAL OF ELECTRON SPECTROSCOPY AND RELATED PHENOMENA **156–158** 426–429 (2007)
- N. Ishimatsu, S. Miyamoto, H. Maruyama, J. Chaboy, M.A. Laguna-Marco, N. Kawamura  
*Experimental evidence of pressure-induced suppression of the cobalt magnetic moment in ErCo<sub>2</sub>*  
PHYSICAL REVIEW B **75**(18) 180402 (2007)
- M. Arita, H. Sato, M. Higashi, K. Yoshikawa, K. Shimada, M. Nakatake, Y. Ueda, H. Namatame, M. Taniguchi, M. Tsubota, F. Iga, T. Takabatake  
*Unoccupied electronic structure of Y<sub>1-x</sub>Ca<sub>x</sub>TiO<sub>3</sub> investigated by inverse photoemission spectroscopy*  
PHYSICAL REVIEW B **75**(20) 205124 (2007)
- S. Hosokawa, H. Sato, N. Happo, K. Mimura, Y. Tezuka, T. Ichitsubo, E. Matsubara, N. Nishiyama  
*Electronic structure of N<sub>42.5</sub>N<sub>7.5</sub>Cu<sub>30</sub>P<sub>20</sub>, an excellent bulk metallic glass former: Comparison to the Pd<sub>40</sub>Ni<sub>40</sub>P<sub>20</sub> reference glass*  
ACTA MATERIALIA **55**(10) 3413–3419 (2007)
- N. Ishimatsu, H. Maruyama, N. Kawamura, M. Suzuki, Y. Ohishi, O. Shimomura  
*Stability of ferromagnetism in Fe, Co, and Ni metals under high pressure*  
JOURNAL OF THE PHYSICAL SOCIETY OF JAPAN **76**(6) 64703 (2007)

S. Kaneyoshi, H. Iwasawa, T. Saitoh, Y. Aiura, D. Satoh, T. Katsufuji, I. Hase, M. Higashiguchi, K. Shimada, H. Namatame, M. Taniguchi, M. Kubota, K. Ono

*Independent control of charge and spin density in  $\text{Sr}_{1-(x+y)}\text{La}_{x+y}\text{Ti}_{1-x}\text{Cr}_x\text{O}_3$  probed by photoemission spectroscopy*

JOURNAL OF MAGNETISM AND MAGNETIC MATERIALS **310**(2) Part 2 E278–E280 (2007)

T. Saitoh, D. Ishii, A. Hachimura, M. Hirose, TS. Naing, Y. Kobayashi, K. Asai, M. Nakatake, M. Higashiguchi, K. Shimada, H. Naniataine, M. Taniguchi

*Electronic structure of  $\text{La}_{1-x}\text{Pr}_x\text{CoO}_3$  and  $\text{NdCoO}_3$  studied by photoemission spectroscopy*

JOURNAL OF MAGNETISM AND MAGNETIC MATERIALS **310**(2) Part 2 981–983 (2007)

K. Terai, K. Yoshii, Y. Takeda, S. Fujimori, Y. Saitoh, K. Ohwada, T. Inami, T. Okane, M. Arita, K. Shimada, H. Namatame, M. Taniguchi, K. Kobayashi, M. Kobayashi, A. Fujimori

*Electronic structure and magnetism of  $\text{CaMn}_{1-x}\text{Ru}_x\text{O}_3$  thin films*

JOURNAL OF MAGNETISM AND MAGNETIC MATERIALS **310**(2) Part 2 1070–1072 (2007)

Y. Miura, K. Shimada, M. Hoesch, M. Higashiguchi, N. Tobita, XY. Cui, Y. Aiura, H. Namatame, M. Taniguchi

*High-resolution angle-resolved photoemission study of the spin-polarized Fermi surface of Ni(100)*

JOURNAL OF MAGNETISM AND MAGNETIC MATERIALS **310**(2) Part 2 1082–1083 (2007)

XY. Cui, K. Shimada, M. Hoesch, Y. Sakisaka, H. Kato, Y. Aiura, S. Negishi, M. Higashiguchi, Y. Miura, H. Namatame, M. Taniguchi

*High-resolution angle-resolved photoemission spectroscopy of iron: A study of the self-energy*

JOURNAL OF MAGNETISM AND MAGNETIC MATERIALS **310**(2) Part 2 1617–1619 (2007)

N. Tobita, K. Emi, N. Nakajima, H. Maruyama, Y. Miura, M. Higashiguchi, K. Shimada, H. Namatame, M. Taniguchi

*Valence-band photoemission spectroscopy of a single-crystal  $\text{FePt}_3$*

JOURNAL OF MAGNETISM AND MAGNETIC MATERIALS **310**(2) Part 2 1642–1644 (2007)

K. Shimada, M. Higashiguchi, M. Arita, H. Namatame, M. Taniguchi, S. Fujimori, Y. Saitoh, A. Fujimori, Y. Takata, S. Shin, K. Kobayashi, E. Ikenaga, M. Yabashi, K. Tamasaku, Y. Nishino, D. Miwa, T. Ishikawa, T. Sasakawa, T. Takabatake

*High-resolution photoemission study of the hybridization gap in the Kondo semiconductor  $\text{CeRhAs}$*

JOURNAL OF MAGNETISM AND MAGNETIC MATERIALS **310**(2) Part 1 E57–E58 (2007)

M. Higashiguchi, K. Shimada, M. Arita, Y. Miura, N. Tobita, XY. Cui, Y. Aiura, H. Namatame, M. Taniguchi

*High-resolution photoemission study of electron-electron interaction in the Ni(111) surface state*

JOURNAL OF MAGNETISM AND MAGNETIC MATERIALS **310**(2) Part 3 E743–E744 (2007)

M. Arita, H. Sato, M. Higashi, K. Yoshikawa, K. Shimada, M. Sawada, Y. Ueda, H. Namatame, M. Taniguchi, SI. Fujimori, Y. Saitoh, M. Tsubota, F. Iga, T. Takabatake

*X-ray absorption and inverse photoemission study of  $Y_{1-x}Ca_xTiO_3$*

JOURNAL OF THE PHYSICAL SOCIETY OF JAPAN **76**(7) 74720 (2007)

H. Kato, S. Takemura, Y. Watanabe, A. Ishii, I. Tsuchida, Y. Akai, T. Sugiyama, T. Hiramatsu, N. Nanba, O. Nishikawa, M. Taniguchi

*X-ray photoemission spectroscopy and Fourier transform infrared studies of electrochemical doping of copper phthalocyanine molecule in conducting polymer*

JOURNAL OF VACUUM SCIENCE & TECHNOLOGY A **25**(4) 1147–1151 (2007)

H. Narita, A. Kimura, M. Taniguchi, M. Nakatake, T. Xie, S. Qiao, H. Namatame

*Intermediate surface structure of Al nanoclusters restricted to Si(111) half-unit cells observed via scanning tunneling microscopy*

PHYSICAL REVIEW B **76**(11) 115405 (2007)

A. Kimura, S. Asanao, T. Kambe, T. Xie, S. Watanabe, M. Taniguchi, S. Qiao, E. Hashimoto, H. Namatame, T. Muro, S. Imada, S. Suga

*Electron correlation and magnetic properties of  $c(2\times 2)CuMn/Cu(001)$  two-dimensional surface alloys*

PHYSICAL REVIEW B **76**(11) 115416 (2007)

T. Hirahara, K. Miyamoto, I. Matsuda, T. Kadono, A. Kimura, T. Nagao, G. Bihlmayer, E.V. Chulkov, S. Qiao, K. Shimada, H. Namatame, M. Taniguchi, S. Hasegawa

*Direct Observation of Spin Splitting in Bismuth Surface States*

PHYSICAL REVIEW B **76**, 153305 (2007)

SI. Fujimori, Y. Saitoh, T. Okane, H. Yamagami, A. Fujimori, K. Shimada, H. Namatame, M. Taniguchi, H. Shishido, D. Aoki, S. Ikeda, Y. Haga, E. Yamamoto, Y. Onuki

*Photoemission study on heavy fermion superconductors*

PHYSICA C-SUPERCONDUCTIVITY AND ITS APPLICATIONS **460** Part 1 657–658 (2007)

JF. Zhao, HW. Ou, G. Wu, BP. Xie, Y. Zhang, DW. Shen, J. Wei, LX. Yang, JK. Dong, M. Arita, H. Namatame, M. Taniguchi, XH. Chen, DL. Feng

*Evolution of the electronic structure of  $1T-Cu_xTiSe_2$*

PHYSICAL REVIEW LETTERS **99**(14) 146401 (2007)

S. He, M. Nakatake, M. Arita, X. Cui, S. Qiao, H. Namatame, M. Taniguchi, H. Li, H. Li

*Temperature-dependent photoemission spectroscopy study of  $RE_xC_{60}$  (RE=Yb and Sm) films*

APPLIED PHYSICS LETTERS **91**(14) 143103 (2007)

H. Iwasawa, Y. Aiura, T. Saitoh, H. Eisaki, H. Bando, A. Ino, M. Arita, K. Shimada, H. Namatame, M. Taniguchi, T. Masui, S. Tajima, M. Ishikado, K. Fujita, S. Uchida, JF. Douglas, Z. Sun, DS. Dessau  
*A re-examination of the oxygen isotope effect in ARPES spectra of Bi2212*

PHYSICA C-SUPERCONDUCTIVITY AND ITS APPLICATIONS **463–465** 52–55 (2007)

T. Nomoto, K. Miura, S. Yagi, G. Kutluk, H. Sumida, K. Soda, E. Hashimoto, H. Namatame, M. Taniguchi

*Spectroscopic study on thermal reaction and desorption of sulfur/Rh(100) induced by oxygen-containing molecules*

SURFACE SCIENCE **601**(18) 3784–3787 (2007)

S. Wada, M. Takigawa, K. Matsushita, H. Kizaki, K. Tanaka

*Adsorption and structure of methyl mercaptoacetate on Cu(111) surface by XPS and NEXAFS spectroscopy*

SURFACE SCIENCE **601**(18) 3833–3837 (2007)

T. Ashida, K. Miura, T. Nomoto, S. Yagi, H. Sumida, G. Kutluk, K. Soda, H. Namatame, M. Taniguchi  
*Synthesis and characterization of Rh(PVP) nanoparticles studied by XPS and NEXAFS*

SURFACE SCIENCE **601**(18) 3898–3901 (2007)

H. Kizaki, Y. Matsumoto, H. Ban, K. Morishita, SI. Wada, K. Tanaka

*Configuration dependence of photon stimulated ion desorption from methyl ester compounds induced by core excitation*

SURFACE SCIENCE **601**(18) 3956–3960 (2007)

M. Higashiguchi, K. Shimada, M. Arita, Y. Miura, N. Tobita, X. Cui, Y. Aiura, H. Namatame, M. Taniguchi

*High-resolution angle-resolved photoemission study of Ni(111) surface state*

SURFACE SCIENCE **601**(18) 4005–4009 (2007)

XY. Cui, K. Shimada, M. Hoesch, Y. Sakisaka, H. Kato, Y. Aiura, M. Higashiguchi, Y. Miura, H. Namatame, M. Taniguchi

*Angle-resolved photoemission spectroscopy study of Fe(110) single crystal: Many-body interactions between quasi-particles at the Fermi level*

SURFACE SCIENCE **601**(18) 4010–4012 (2007)

M. Nagira, M. Sawada, M. Higashiguchi, K. Yaji, T. Mao, T. Ueno, U. Miura, K. Shimada, A. Kimura, H. Namatame, M. Taniguchi

*Surface quantum well state at the striped Cu(110)(2×1)O surface studied by angle resolved photoemission spectroscopy*

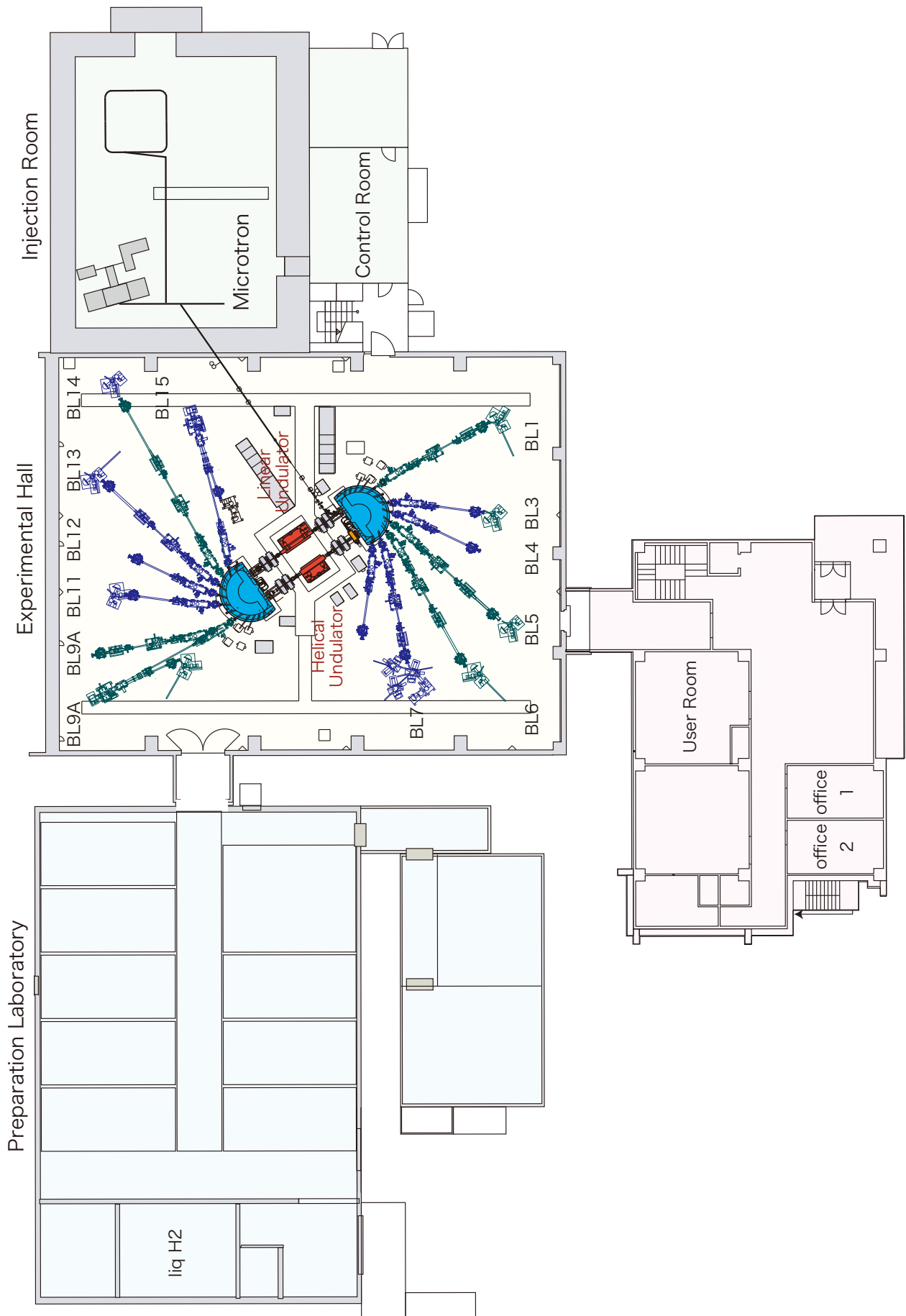
SURFACE SCIENCE **601**(18) 4041–4044 (2007)

- S. Yagi, Y. Matsumura, T. Nomoto, K. Soda, E. Hashimoto, H. Namatame, M. Taniguchi  
*Liquid-solid interface of L-cysteine/TM (TM = Ni and Cu) in aqueous solution by means of sulfur K-edge NEXAFS*  
SURFACE SCIENCE **601**(18) 4154–4157 (2007)
- M. Kotsugi, FZ. Guo, M. Taniguchi, N. Ishimatsu, H. Maruyama  
*Easy-axis rotation in meteoritic iron probed by photoelectron emission microscope (PEEM)*  
SURFACE SCIENCE **601**(18) 4326–4328 (2007)
- T. Kinoshita, E. Ikenaga, J. Kim, S. Ueda, M. Kobata, JR. Harries, K. Shimada, A. Ino, K. Tamasaku, Y. Nishino, T. Ishikawa, K. Kobayashi, W. Drube, C. Kunz  
*How is it possible to obtain buried interface information through very thick films using a hard-X-ray PEEM?*  
SURFACE SCIENCE **601**(20) 4754–4757 (2007)
- M. Kotsugi, T. Wakita, N. Kawamura, T. Taniuchi, K. Ono, M. Suzuki, M. Oshima, N. Ishimatsu, M. Taniguchi, H. Maruyama  
*Application of photoelectron emission microscopy (PEEM) to extraterrestrial materials*  
SURFACE SCIENCE **601**(20) 4764–4767 (2007)
- M. Nagira, M. Sawada, M. Higashiguchi, K. Yaji, T. Moko, T. Ueno, Y. Miura, K. Shimada, A. Kimura, H. Namatame, M. Taniguchi  
*Temperature dependent quantum well state on Cu(110)(2×1)O striped surface studied by angle resolved photoelectron spectroscopy*  
SURFACE SCIENCE **601**(22), 5254–5257 (2007)
- K. Shimada, Edited by S. Huefner  
*High-resolution Photoemission Spectroscopy of Solids Using Synchrotron Radiation, in Very High Resolution Photoelectron Spectroscopy*  
Lecture Notes in Physics **715**, Chap. 4, pp. 85-112. (Springer-Verlag, Berlin-Heidelberg, 2007)

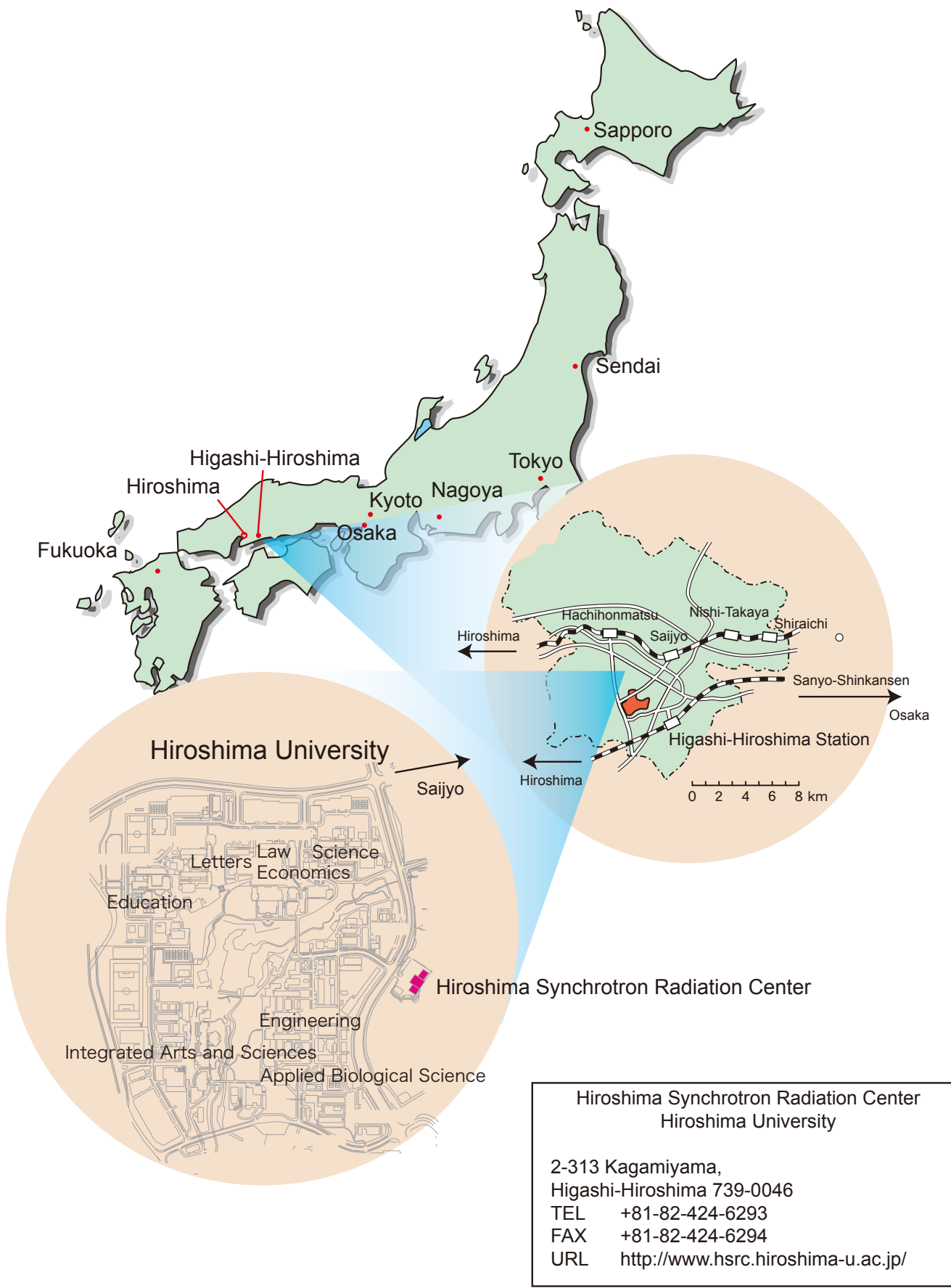
# **Symposium**

The 12th Hiroshima International Symposium on Synchrotron Radiation  
March 13–14, 2007

# Plan of the Building



# Location



**Hiroshima Synchrotron Radiation Center**  
**Hiroshima University**  
 2-313 Kagamiyama,  
 Higashi-Hiroshima 739-0046  
 TEL +81-82-424-6293  
 FAX +81-82-424-6294  
 URL <http://www.hsrc.hiroshima-u.ac.jp/>



